NBS SPECIAL PUBLICATION 460

U.S. DEPARTMENT OF COMMERCE / National Bureau of Standards

Use of Monte Carlo Calculations in Electron Probe Microanalysis and Scanning Electron Microscopy

NATIONAL BUREAU OF STANDARDS

The National Bureau of Standards[1] was established by an act of Congress March 3, 1901. The Bureau's overall goal is to strengthen and advance the Nation's science and technology and facilitate their effective application for public benefit. To this end, the Bureau conducts research and provides: (1) a basis for the Nation's physical measurement system, (2) scientific and technological services for industry and government, (3) a technical basis for equity in trade, and (4) technical services to promote public safety. The Bureau consists of the Institute for Basic Standards, the Institute for Materials Research, the Institute for Applied Technology, the Institute for Computer Sciences and Technology, the Office for Information Programs, and the Office of Experimental Technology Incentives Program.

THE INSTITUTE FOR BASIC STANDARDS provides the central basis within the United States of a complete and consistent system of physical measurement; coordinates that system with measurement systems of other nations; and furnishes essential services leading to accurate and uniform physical measurements throughout the Nation's scientific community, industry, and commerce. The Institute consists of the Office of Measurement Services, and the following center and divisions:

Applied Mathematics — Electricity — Mechanics — Heat — Optical Physics — Center for Radiation Research — Laboratory Astrophysics[2] — Cryogenics[2] — Electromagnetics[2] — Time and Frequency[2].

THE INSTITUTE FOR MATERIALS RESEARCH conducts materials research leading to improved methods of measurement, standards, and data on the properties of well-characterized materials needed by industry, commerce, educational institutions, and Government; provides advisory and research services to other Government agencies; and develops, produces, and distributes standard reference materials. The Institute consists of the Office of Standard Reference Materials, the Office of Air and Water Measurement, and the following divisions:

Analytical Chemistry — Polymers — Metallurgy — Inorganic Materials — Reactor Radiation — Physical Chemistry.

THE INSTITUTE FOR APPLIED TECHNOLOGY provides technical services developing and promoting the use of available technology; cooperates with public and private organizations in developing technological standards, codes, and test methods; and provides technical advice services, and information to Government agencies and the public. The Institute consists of the following divisions and centers:

Standards Application and Analysis — Electronic Technology — Center for Consumer Product Technology: Product Systems Analysis; Product Engineering — Center for Building Technology: Structures, Materials, and Safety; Building Environment; Technical Evaluation and Application — Center for Fire Research: Fire Science; Fire Safety Engineering.

THE INSTITUTE FOR COMPUTER SCIENCES AND TECHNOLOGY conducts research and provides technical services designed to aid Government agencies in improving cost effectiveness in the conduct of their programs through the selection, acquisition, and effective utilization of automatic data processing equipment; and serves as the principal focus wthin the executive branch for the development of Federal standards for automatic data processing equipment, techniques, and computer languages. The Institute consist of the following divisions:

Computer Services — Systems and Software — Computer Systems Engineering — Information Technology.

THE OFFICE OF EXPERIMENTAL TECHNOLOGY INCENTIVES PROGRAM seeks to affect public policy and process to facilitate technological change in the private sector by examining and experimenting with Government policies and practices in order to identify and remove Government-related barriers and to correct inherent market imperfections that impede the innovation process.

THE OFFICE FOR INFORMATION PROGRAMS promotes optimum dissemination and accessibility of scientific information generated within NBS; promotes the development of the National Standard Reference Data System and a system of information analysis centers dealing with the broader aspects of the National Measurement System; provides appropriate services to ensure that the NBS staff has optimum accessibility to the scientific information of the world. The Office consists of the following organizational units:

Office of Standard Reference Data — Office of Information Activities — Office of Technical Publications — Library — Office of International Standards — Office of International Relations.

---

[1] Headquarters and Laboratories at Gaithersburg, Maryland, unless otherwise noted; mailing address Washington, D.C. 20234.

[2] Located at Boulder, Colorado 80302.

Use of Monte Carlo Calculations in Electron Probe Microanalysis and Scanning Electron Microscopy

Proceedings of a workshop held at the
National Bureau of Standards
Gaithersburg, Maryland, October 1-3, 1975

Edited by

Kurt F. J. Heinrich
Dale E. Newbury
Harvey Yakowitz

Sponsored by

Analytical Chemistry Division
Institute for Materials Research
National Bureau of Standards

U.S. DEPARTMENT OF COMMERCE, Elliot L. Richardson, Secretary
Edward O. Vetter, Under Secretary
Dr. Betsy Ancker-Johnson, Assistant Secretary for Science and Technology
NATIONAL BUREAU OF STANDARDS, Ernest Ambler, Acting Director

Issued December 1976

Library of Congress Catalog Card Number: 77-608002

National Bureau of Standards Special Publication 460
Nat. Bur. Stand. (U.S.), Spec. Publ. 460, 169 pages (Dec. 1976)
CODEN: XNBSAV

U.S. GOVERNMENT PRINTING OFFICE
WASHINGTON: 1976

For sale by the Superintendent of Documents, U.S. Government Printing Office, Washington, D.C. 20402
(Order by SD Catalog No. C13.10:460). Stock No. 003-003-01737-0 Price $2.35
(Add 25 percent additional for other than U.S. mailing).

Foreword

The Analytical Chemistry Division of the Institute for Materials Research, National Bureau of Standards, seeks to develop new techniques of chemical analysis and improve existing techniques. Part of the mission of NBS is to disseminate knowledge in the scientific and technical community. To aid in reaching this objective, the Analytical Chemistry Division has sponsored a series of workshops on various topics in analytical chemistry. The workshop topics are chosen to fulfill current needs for detailed discussions on sharply defined subjects in a wide variety of specialist areas. The objective is to bring together specialists from throughout the world to concentrate intensively on a particular subject in order to advance the state-of-the-art. It is often very difficult to achieve this goal at large international meetings where the size and diversity of topics presented often limits detailed discussion of special subjects. Past topics of these workshops and the published proceedings include: Quantitative Electron Probe Microanalysis (NBS Special Publication 298, available from editors), Aerosol Measurements (NBS Special Publication 412), Oil Pollution Monitoring (NBS Special Publication 409), and Secondary Ion Mass Spectrometry (NBS Special Publication 427). These proceedings are available from the Superintendent of Documents, Government Printing Office, Washington, DC 20402. Further information on the workshops can be obtained by writing to the Division Office, Analytical Chemistry Division, National Bureau of Standards, Washington, DC 20234.

This volume contains the proceedings of a Workshop on the Use of Monte Carlo Calculations in Electron Probe Microanalysis and Scanning Electron Microscopy. The three-day meeting involved participants from the United States and Europe. The workshop format consisted of a keynote talk on each topic followed by extensive discussions. The papers in this volume are based on the keynote talks augmented with some points raised in the discussion.

The extensive development of electron beam instrumentation for the microscopy and analysis of samples of diverse scientific interest has resulted in a need for detailed studies of the origin and characteristics of the signals involved. This publication provides a detailed view of one approach to the study of such signals, namely the Monte Carlo technique for electron trajectory calculation. The publication should be of value to the numerous workers who utilize the scanning electron microscope and electron probe microanalyzer.

John D. Hoffman
Director
Institute for Materials Research
National Bureau of Standards

Preface

The utility of electron probe microanalysis and scanning electron microscopy is demonstrated by the fact that more than 2500 such instruments costing from $25,000 to $200,000 are now in use worldwide, and more instruments are constantly being added. Moreover, the instruments are at work in fields as diverse as biology, metallurgy, electronics, chemistry, and forensic science. Simultaneously with the development and distribution of the instrumentation, much work has been devoted to the study of electron interactions with solids with the purpose of characterizing the signals which are utilized in microscopy and analysis. One approach which has proven especially useful in both qualitative and quantitative studies of electron interactions is that of Monte Carlo electron trajectory simulation. Monte Carlo calculations have enabled scientists to visualize the electron interaction volume in solids as to size and shape, to predict the parameters characterizing the secondary and back-scattered electrons, the x-rays, and the Auger electrons, and to analyze factors which determine resolution in micrographs.

The purpose of the present workshop was to bring together a number of workers in Monte Carlo trajectory techniques to assess the current state of development and to look for areas of future development. The list of participants in the meeting does not include all active workers in the field, but we hope that this document contains a reasonably complete description of the subject. By examining the areas of application, including particulate analysis, thin film analysis, and magnetic domain imaging, some idea can be obtained of the future directions which the Monte Carlo technique may follow.

December 10, 1976

K. F. J. Heinrich
H. Yakowitz
D. E. Newbury

Abstract

This book is the formal report of the Workshop on the Use of Monte Carlo Calculations in Electron Probe Microanalysis and Scanning Electron Microscopy held at the National Bureau of Standards, October 1-3, 1975. The papers cover a wide range of topics within the field: the history and development of Monte Carlo methods for use in x-ray microanalysis; the study of the distribution of electron and x-ray signals by Monte Carlo techniques; the effect of the choice of scattering models on the calculations; techniques for considering the distribution of energies of the beam electrons propagating in the specimen; evaluation of ionization cross-section models; and applications of Monte Carlo techniques to the study of particles, thin films, and magnetic domain images. The contributions include reviews of general interest as well as papers treating specific topics. The volume should be of wide interest to workers in the fields of scanning electron microscopy, electron probe microanalysis, electron physics, and other fields involving the interaction of electrons with solids.

Key Words: Electron probe microanalysis; electron-solid interactions, magnetic domains; Monte Carlo electron trajectory calculations; particle analysis; scanning electron microscopy; thin film analysis.

Contents

National Bureau of Standards Special Publication 460. Proceedings of a Workshop on the Use of Monte Carlo Calculations in Electron Probe Microanalysis and Scanning Electron Microscopy held at NBS, Gaithersburg, Maryland, October 1-3, 1975. Issued December 1976.

THE ROLE OF MONTE CARLO CALCULATIONS IN ELECTRON PROBE MICROANALYSIS AND SCANNING ELECTRON MICROSCOPY

Kurt F. J. Heinrich

Analytical Chemistry Division
National Bureau of Standards
Washington, DC 20234

1. Introduction

The emission of characteristic x-rays, on which electron probe microanalysis is based, depends on the deceleration and scattering of the primary electrons and the x-ray production as a function of the energy of the primary electron. In the ZAF methods applicable to flat, electron-opaque targets, Bethe's theories are used to calculate the electron deceleration and the ionization cross-sections of the target atoms. The effects of scattering on the generated x-ray intensities are taken into account by an empirical correction factor based on the measurement of the energy distribution of backscattered electrons, and the absorption losses of the emerging x-rays are also determined by a semi-empirical approach due to Philibert, or by empirical generalizations of experiments by Green and by Castaing, et al. Further corrections must be applied to account for the effects of indirect (fluorescent or photon-photon) x-ray excitation. (For references on various aspects of the ZAF method see reference [1][1].)

Although some aspects of the ZAF procedure are still open to improvement, the achievable accuracy is of the order of magnitude of the measurement or standardization errors and is considered satisfactory. The application of the ZAF method cannot, however, be extended with rigor to the analysis of specimens which are not flat, homogeneous and electron-opaque, because the empirical adjustments in this method cannot be used to treat such geometrical configurations. Yet, many important analytical situations fall into the categories which are not considered by the ZAF method. These include the analysis of supported and unsupported thin layers, of inclusions and free particles, and thin sections of biological specimens (fig. 1).

A related problem arises in analysis by means of x-rays of large wavelengths in which the observed x-radiation emerges from a shallow region of the excited volume adjacent to the specimen surface. In this case, most of the x-ray absorption models commonly used in ZAF procedures do not adequately predict the observable x-ray intensities. For the prediction of the x-ray emission from such targets, we must choose a method which follows more closely the chain of events within the specimen with particular reference to the spatial distribution of these events. A procedure commonly used to this effect is the Monte Carlo calculation.

The study of spatial distribution of the points of origin of signals is equally important to scanning electron microscopy, in which high spatial resolution ($\sim$100 Å) is desirable, and specimen surfaces are not usually flat. With the rapid development and diffusion of scanning electron microscopy, the contributions of the Monte Carlo method to the knowledge of the physical foundations of scanning electron microscopy become increasingly significant. Such contributions are presented in paper by Myklebust, et al., Wells, and Newbury et al.

---

[1]Figures in brackets indicate literature references at the end of this paper.

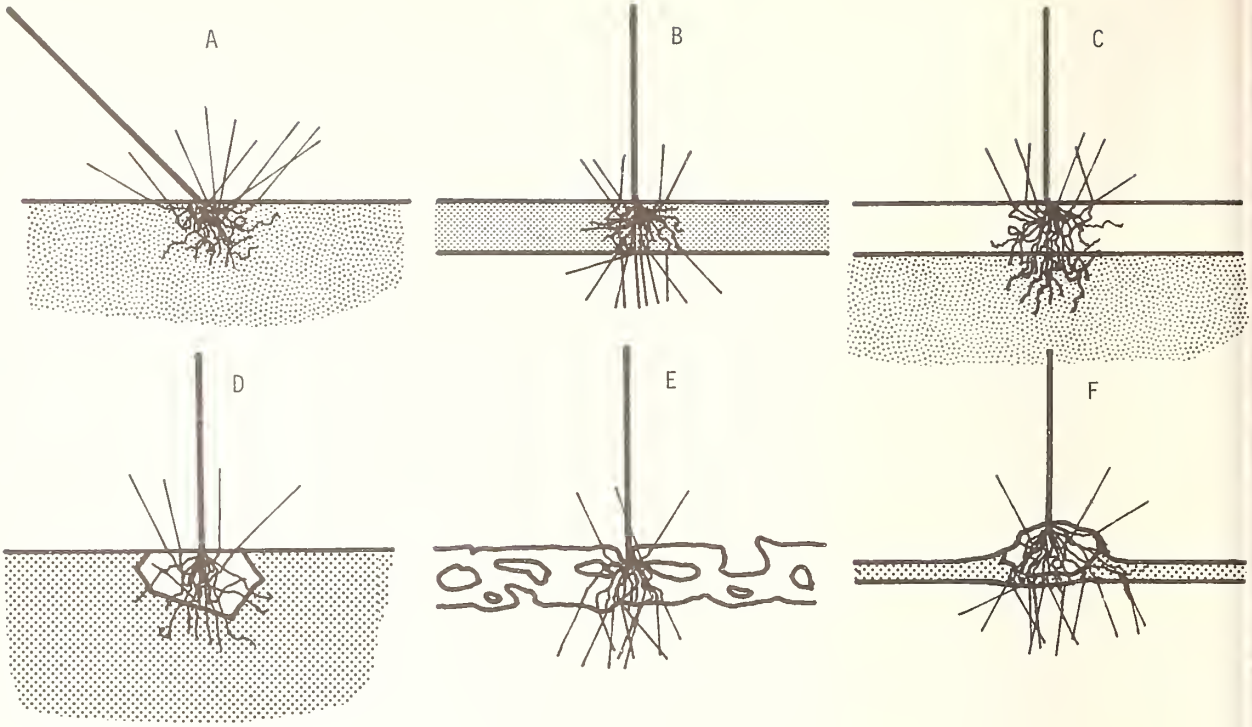

Figure 1. Some configurations not considered in the usual ZAF procedure. A: inclined electron beam; B: unsupported foil; C: supported coating; D: small inclusion; E: thin section of biological material; F: particle mounted on thin foil.

2. The Monte Carlo Model

This evaluation is based on the summation of the events occurring in a large number of simulated electron trajectories within the specimen. In principle, the interactions between the electron and the target material should all be treated individually. Where elements of randomness enter the decisions concerning the occurrence and nature of an event, a random number is used to choose from among a series of equally possible outcomes. Each trajectory is terminated when the primary (beam) electron has lost too much energy to produce the signal of interest, or when the electron leaves the target material (backscattered or transmitted electrons). Hence, by changes in the equation representing the specimen surface, the method can be adapted to diverse geometric configurations.

The observed intensity of any signal--such as x-rays and secondary electrons--depends on at least four parameters: the distribution in depth of the primary electrons, their energy distribution, the cross-section for signal generation as a function of electron energy (see paper 6 for x-ray production), and the attenuation of the signal by the target, and where applicable, by the surrounding force fields. In some cases, such as secondary electron and fluorescent (or indirect) x-ray emission, intermediate mechanisms of energy transmission must also be described. If all mechanisms are known from theory, then the Monte Carlo procedure can be based entirely on these theoretical premises. If the results so obtained are not fully satisfactory, empirical adjustments can be made. As will be shown in the ensuing papers, it is one of the strengths of the Monte Carlo procedure that such empirical adjustments can lead to simple yet accurate models.

3. Simplifications

It is sometimes assumed in the literature of microprobe analysis that the use of Monte Carlo techniques circumvents the uncertainties which plague the ZAF method; thus, the results

of the Monte Carlo method are often cited as paragons in the evaluation of variants of ZAF. This assumption does not, however, hold. A full event-by-event treatment of the electron-target interaction would exceed the capacity of most computers and be economically untenable. Moreover, the interactions of electrons with lattice regions and large molecules are mathematically intractable. Therefore, all existing Monte Carlo models contain important simplications, and the choice of the simplifications may significantly affect the results (see paper 5).

For instance, it is common practice to ignore the effects of target structure, and to treat the electron deceleration as a continuous process due to interactions with orbital electrons of an amorphous medium consisting of free atoms. When the stopping power equation of Bethe is used for this effect, the uncertainty in the values of the mean excitation potentials creates exactly the same problem as ZAF procedure [2]. Further inaccuracies which arise from straggling are discussed by Hénoc and Maurice.

Another problem arises from the choice of scattering parameters. According to Reimer (paper 4), the use of the Rutherford model leads to large errors in scattering angles. Even more startling is the observation by Reimer that indirect excitation due to secondary electrons of high energy is a significant source of x-rays (about 30% for AlKα!) in aluminum. Such a mechanism has not been taken into account in any earlier model for x-ray excitation, either of the ZAF or the Monte Carlo type.

Further complications may arise in the so-called multiple-scattering models, in which the electron trajectory is arbitrarily divided into segments, and the scattering acts within each segment are replaced by a single hypothetical scattering event. In some of these models, the results depend upon the number of intervals into which the trajectories are divided. The effects of inelastic large-angle scattering are also ignored in most Monte Carlo models. Finally, if an insufficient number of trajectories is calculated, statistical errors may arise regardless of the fit of the model.

Only a small fraction of electron trajectories produce characteristic x-ray photons (10^{-2} to 10^{-3} for Kα lines of elements under typical conditions). For this reason, one must sum fractional probabilities of x-ray production within individual trajectories, to effectively decrease the statistical uncertainties in x-ray production, or use scaling procedures which, in turn, may produce artifacts (clusters) in the graphic representation of the distribution of sites of x-ray generation.

The effects of simplifications in the model depend to a large degree on the intended applications. For instance, when the measurement of thin layers or of single large-angle scattering is of prime interest, the first segments of the trajectory must be treated carefully, and it may be inadequate to assume that the first scattering interaction always occurs at the mid-depth of the first interval of integrations. On the other hand, such an arbitrary assumption will have little effect on the depth distribution of the short-wavelength x-radiation from electron-opaque targets. It is thus possible, with judicious selection of procedures and fitting adjustments where needed, to obtain models of relative simplicity which are in satisfactory agreement with a wide variety of experiments (as shown in paper 8).

4. Conclusions

We hope that these proceedings will not only illustrate the wide range of objectives that can be attained by the Monte Carlo calculations, but also the complexity of the problem and the diversity of possible solutions. An understanding of the options which are available should help in the selecting the procedure which is most appropriate for a given purpose. We also trust that we have provided the proper historical perspective and shown some of the limitations of this versatile technique.

References

[1] Reed, S. J. B., *Electron Microprobe Analysis*, Cambridge University Press, London, 1975.

[2] Heinrich, K. F. J. and Yakowitz, H., *Mikrochim. Acta*, 1970, 123-134.

National Bureau of Standards Special Publication 460. Proceedings of a Workshop on the Use of Monte Carlo Calculations in Electron Probe Microanalysis and Scanning Electron Microscopy held at NBS, Gaithersburg, Maryland, October 1-3, 1975. Issued December 1976.

THE HISTORY AND DEVELOPMENT OF MONTE CARLO METHODS FOR USE IN X-RAY MICROANALYSIS

H. E. Bishop

Materials Development Division
AERE Harwell
Didcot, Oxon, England

Green in 1963 first demonstrated the usefulness of Monte Carlo calculations to the understanding and development of the theory of x-ray microanalysis. As his calculations was based on experimental scattering data it was of relatively limited application. By 1965, at the 4th International Conference on X-Ray Optics and Microanalysis in Paris, papers from Japan and the United Kingdom demonstrated that a more general approach based on theoretical cross-sections was possible. Since then many further developments have been reported and a number of Fortran programs have become available.

Monte Carlo calculations may be divided conveniently into two classes; those aimed at a general understanding of the electron scattering process leading to x-ray production and those intended to solve particular problems. For conventional quantitative microprobe analysis of a flat specimen, uniform over the analyzed volume, the first class is the most important as it should lead to improvements in the conventional ZAF procedures. In a situation where there are special boundary conditions, such as thin surface films or particles, the second class is useful in predicting or interpreting the observed results. In this paper, the various approaches to Monte Carlo calculations are reviewed and their suitability for different applications is discussed.

Key Words: Electron probe microanalysis; Electron scattering; electron-specimen interactions; Monte Carlo electron trajectory calculations; scanning electron microscopy; x-ray microanalysis

1. Introduction

Electron scattering in a solid is a complex multi-dimensional problem that is quite intractable to analytical solutions. The first attempts to describe the phenomenon were thus based on empirical relationships and simplified scattering models, leading to a good qualitative understanding of the scattering process which was sufficiently quantitative for many purposes. The development of electron probe x-ray microanalysis, however, was found to require a much more exact approach if the technique was to achieve its full quantitative potential. Fortunately, the demand for more precise theory coincided with the computer revolution so that direct simulation of electron scattering by Monte Carlo techniques became feasible, and as increasingly powerful computers have become available, so have more ambitious Monte Carlo calculations.

The first application of Monte Carlo techniques to the problems of electron probe microanalysis was by Green [1][1], who used experimental results from thin films as a basis for his calculation. His paper showed clearly the potential of the method, but was rather limited in its scope by the need for detailed experimental data. By 1965 a more general approach based on theoretical scattering cross-sections was reported at the 4th Interna-

[1]Figures in brackets indicate literature references at the end of this paper.

tional Conference on X-Ray Optics and Microanalysis in Paris by workers from both Japan [2] and the United Kingdom [3]. This approach, although relatively simple, required what was, at that time, a large computer. Small computers soon became increasingly common in laboratories and, in 1971, Curgenven and Duncumb [4] described a very much simplified calculation based on the same general approach that has proved very successful. Since then, the rate of publication of Monte Carlo calculations has increased, many of these aimed at explaining contrast effects in the scanning electron microscope rather than at microanalysis problems. More exact scattering cross-sections have been tried and the effects of replacing the continuous energy loss approximation by individual inelastic events have been explored.

This paper does not set out to be a comprehensive review of Monte Carlo calculations relating to electron probe microanalysis, but rather to examine the various approaches that may be taken and to relate them to the problems that the calculations are setting out to solve. In the main, the calculations may be divided into two classes: those aimed at providing a general understanding of the electron scattering processes leading up to x-ray production; and those intended to solve particular problems. For example, in the conventional microprobe analysis of a flat, uniform specimen, the first class may be used to evaluate and develop the ZAF correction procedures. The second class finds its main application in dealing with situations where there are special boundary conditions such as thin surface films or particles where generalized empirical relationships, such as are used for the ZAF correction, cannot easily be applied.

2. General Discussion of Electron Scattering Problem

Before discussing the different Monte Carlo approaches that have been used, it is instructive to discuss the electron scattering problem in general. Electron scattering occurs through two distinct processes: (1) elastic scattering by the nucleus which is responsible for most of the angular scattering and (2) electron-electron scattering that causes the incident electron to lose energy, but causes relatively little angular deflection. In a typical case met in x-ray analysis, where one wishes to investigate the characteristic x-rays produced by an electron beam in a solid, with the beam energy three times the critical ionization potential, each incident electron would suffer several hundred elastic scattering events and a similar number of inelastic events before its energy dropped below the ionization potential and ceased to be of interest. Given that the efficiency of characteristic x-ray production per incident electron is usually less than 10^{-2}, a vast computation would be required if a direct simulation approach were to be used even if all the individual scattering cross-sections were adequately known. The art of setting up a Monte Carlo calculation is to introduce as many simplifications to the scattering process as possible without affecting significantly the end result.

The first simplification that is common to all calculations, so far, is to ignore the structure of the solid. To take full account of electron diffraction effects would be completely impracticable for the thick specimens of interest in x-ray production, although some empirical allowance may be possible. The uncertainties introduced by this necessary approximation will limit the precision that is worth aiming for in any calculation.

Having replaced real matter with a continuum approximation, electron scattering may be approached as a diffusion problem. That is, the scattering distribution in the target may be represented as a function, $f(\underline{r}, \underline{v}, E, s)$ where $\underline{r}$ and $\underline{v}$ are position and direction vectors and E and s are electron energy and total distance traveled in the target. No general solution to this problem has been published but if one introduces the continuous energy loss approximation based on the Bethe [5] energy loss equation, that is, E is directly related to s, the scattering problem can be written as a Boltzmann equation [6] which can yield solutions for two particular cases:

(1) thin films in the small angle approximation--the multiple scattering theories used for electron transmission; and

(2) infinite targets for which Lewis [6] has derived integral equations for the moments of electron scattering distributions, from which electron energy loss distributions and the depth dose curve distribution could also be obtained [7].

The significance of these two solutions to Monte Carlo calculations is that the first allows elastic scattering events to be grouped together giving a fixed number of steps in a condensed path--rather than treating each elastic scattering event individually--with a corresponding saving in computing time. The second gives an accurate solution for the particular case of an infinite target, against which the Monte Carlo results may be checked to reveal any systematic errors that may be introduced by the calculation procedure.

The Boltzmann equation may, of course, be solved by purely numerical methods similar to those used for diffusion problems with the added complication of a varying diffusion coefficient. Dashen [8] has applied such an approach but the calculation is very unwieldy and would appear to be much less efficient than a comparable Monte Carlo calculation. Ogilvie and Brown [9] have solved a simplified transport equation formulated by Bethe, Rose and Smith [10] by numerical methods and applied the results to x-ray production. This approach appears very attractive but essentially neglects large angle single scattering events. It is likely, therefore, that the method will give reasonable results for electron penetration (within the limits of the continuous energy loss approximation) but will be less reliable near the specimen surface and for electron back-scattering where single large angle scattering events are very important.

The continuous energy loss approximation is extremely valuable in reducing the complexity of Monte Carlo calculations, and for most microanalysis problems it is quite acceptable. Its use produces two main systematic errors:

(1) energy spectra obtained from the calculation are more strongly peaked than is found experimentally; and

(2) spatial distributions are similarly affected to a lesser extent. The effect is only really significant in the tail of the distribution and so the continuous loss approximation should not be used if an accurate calculation of x-ray production in the region of boundaries is required. In these cases, it is necessary to take some account of so-called "energy straggling" effects. On the whole, however, it is usually desireable to retain as far as possible the framework used in the continuous loss calculations rather than using individual scattering cross-sections. Landau [11] has extended the Bethe approach giving loss distribution rather than mean energy loss. Alternatively, a purely empirical distribution function may be employed.

3. Monte Carlo Calculation

In this section, the main types of Monte Carlo calculation used in relation to microprobe analysis are discussed. By the time Green started his work, the Monte Carlo technique was well established and about this time there were a number of publications devoted to the general problems associated with Monte Carlo calculations [12]. The one of most relevance was a paper by Berger [13] which reviewed the use of Monte Carlo techniques for high energy electrons. The development of Monte Carlo calculations for microprobe analysis is considered below under three headings: experimental scattering; multiple scattering; and finally, single scattering and other improvements.

3.1 Experimental Scattering Approach

Once the continuous energy loss approximation has been accepted, the main problem in setting up a Monte Carlo calculation is how to represent the angular scattering of the electron. Green overcame this problem very simply by taking the experimental data of Thomas [14] for electron scattering in a 1000 Å copper film. With his calculation, Green was able to get very encouraging agreement with experimental data for electron backscattering and the depth distribution of characteristic x-ray production. This approach is clearly limited in its scope because of the need for accurate experimental data, and the main significance of Green's work was to demonstrate the significance of the Monte Carlo technique to the theory of microprobe analysis. Bishop [15] carried out further work based on Green's approach again showing good agreement with experiment. In this paper, a comparison was also made with calculations of the moments of electron scattering distribution from the Monte Carlo calculation with those calculated from the Lewis equations [6]. Both this calculation and

that of Green were made before Cambridge University had acquired a really modern computer. As a result a great deal of attention had to be given to the efficiency of the computer program and to presenting the results in as concise a form as possible. In particular, it would not have been possible to run a full calculation for every different ionization potential, so a set of complete trajectories was produced and stored in the form of a scattering matrix f(z,s) where z is the depth below the surface and s the actual distance traveled in the target. Electron scattering distributions obey a well-known scaling law [7,16], i.e., for a given element the function f(z/r, s/r), where r is the Bethe range, is almost independent of incident beam energy. Owing to this property, the scattering matrix once evaluated for a particular element and beam specimen geometry contains all the information necessary to calculate x-ray production for any critical ionization potential over a wide range of beam energies. An example of such a matrix for copper is shown in Table 1.

3.2 Multiple Scattering Approach

Following Green's pioneering work, the next stage was clearly to replace experimental scattering data by theoretically based scattering distributions that could then be applied more generally. A suitable multiple scattering formalism had been developed by Goudsmit and Sanderson [17] and two papers based on this approach were presented by Bishop [3] and by Shimizu, et al. [2], to the 4th International Conference on X-Ray Optics and Microanalysis in Paris in 1965. The only substantial difference between these two calculations was that Bishop [2] retained a fixed step length as this was more convenient to use in conjunction with the scattering matrix method of recording the results while Shimizu, et al., used a reducing step length Δs_i, where

$$\Delta s_i = \frac{E_i}{E_o} \Delta s_o \ .$$

This is, in general, a better choice than a fixed step as it allows for increased scattering as the electron loses energy. As many subsequent calculations are based on the same approach it is worth considering it in rather more detail.

Inelastic scattering is represented by the Bethe equation

$$-\frac{dE}{ds} = \frac{2\pi e^4 N}{E} \frac{Z}{A} \ln \frac{1.166E}{J} \qquad (1)$$

where N is Avogadro's number, Z and A are the atomic number and atomic weight of the target, respectively, and J is the mean ionization potential. Integration of this relationship gives the Bethe range, r, of the electron and a relationship between s, the distance traveled in the specimen and residual electron energy, E.

The elastic scattering can be represented by a screened Rutherford cross-section

$$\frac{d\sigma}{d\Omega} = \frac{Z^2 e^4}{16E^2(1+2\alpha-\cos\theta)^2} \qquad (2)$$

where α is a screening factor, e the electronic charge and θ the scattering angle.

The screening factor α, like the mean ionization potential, may be treated as an adjustable parameter to give a good fit to experimental data. A typical expression is that used by Bishop

$$\alpha = 3.4\ Z^{2/3}/E \qquad (3)$$

(E is in electron volts).

The angular scattering distribution $f(p,\theta)$ for each step is determined by the Goudsmit-Sanderson formula which is expressed as a Legendre series

$$f(p,\theta) = \frac{1}{4\pi} \sum_{n=0}^{\infty} (2n+1)\ e^{(-p(1-a_n))} P_n(\cos\theta) \qquad (4)$$

Table 1. Scattering of 30 keV electrons in a copper target for normal beam incidence [18].

Step	1	2	3	4	5	6	7	8	9	10	11	12	13	14	15	16	17	18	19	20	21	22	23	24	25
%																									
0	145	92	88	104	120	122	121	120	113	99	115	105	105	100	80	81	76	72	60	66	43	52	55	44	34
1	4832	1027	524	425	386	389	362	326	323	344	320	298	286	255	254	267	232	210	207	181	187	173	158	151	149
2		3822	1974	960	718	583	522	496	474	429	401	383	347	345	327	269	285	292	270	263	259	246	224	237	226
3			2290	2191	1192	871	703	595	542	486	440	420	411	389	377	395	334	321	316	313	294	290	306	290	293
4				1130	1809	1128	875	717	583	532	511	471	447	403	381	353	381	372	349	369	367	354	322	313	315
5					497	1341	1025	808	687	601	506	453	412	426	417	405	395	374	400	358	338	336	338	323	311
6						187	835	841	693	617	549	507	465	425	405	393	376	358	326	334	347	335	315	339	337
7							70	483	627	581	549	501	443	410	401	359	349	335	336	337	324	343	340	331	319
8								19	262	403	435	419	426	409	369	350	340	354	348	322	314	304	320	307	319
9									5	127	253	309	313	315	320	322	303	290	279	299	298	275	298	291	282
10										0	54	144	200	220	230	253	255	246	227	206	214	246	230	234	230
11											0	21	81	119	142	136	151	167	193	176	180	164	164	158	161
12												0	5	35	59	89	91	105	113	139	124	119	119	122	126
13													0	1	16	32	50	52	59	62	80	87	92	96	101
14														0	0	8	19	23	33	38	40	45	45	50	48
15															0	0	2	10	13	20	20	23	21	22	29
16																0	0	2	3	7	6	8	11	14	14
17																	0	0	0	1	4	4	5	5	4
18																		0	0	0	1	3	3	3	4
19																			0	0	0	0	1	2	2
20																				0	0	0	0	0	1
21																					0	0	0	0	0
22																						0	0	0	0
23																							0	0	0
24																								0	0
Backscattering	23	36	65	66	88	101	108	108	96	90	86	102	90	89	74	66	73	56	51	41	51	33	40	35	27

where the a_n are the Legendre coefficients for the single scattering distribution and p is the mean number of elastic scattering events in the step Δs given by

$$p = \frac{\rho N}{A} \sigma_t \Delta s \tag{5}$$

where σ_t is the total elastic cross section and ρ is the density.

The Rutherford cross-section is particularly useful in evaluating eq. (4) because the Legendre coefficients may be obtained from a simple recurrence relationship, although precautions must be taken to overcome rounding errors [18]. There is however, no reason why a more precise cross-section should not be used, although the generation of the Legendre coefficients will be more complicated.

Equation (4) as it stands can give problems with convergence as it includes the unscattered proportion of the beam. Shinoda, et al. [19], have found that this effect limits the mininum step that can be used. However, this convergence problem may be simply avoided by recasting the equation in the form

$$F(p,\theta) = e^{-p} \left[\delta(\theta) + \frac{1}{4\pi} \sum_{0}^{\infty} (2n+1) \left(e^{pa_n}-1\right) P_n(\cos\theta)\right] \tag{4b}$$

where $\delta(\theta)$ is a delta function [18]. Even so, several hundred terms may be necessary for the light elements where the screening function is small. Equation (4) allows angles of equal scattering probability to be evaluated for each step in the electron trajectory and these are subsequently used in the Monte Carlo program.

The multiple scattering approach essentially replaces the effects of a number of single scattering events that may befall an electron traveling a distance Δs in the target by a single scattering event occurring at some arbitrary point (selected at random) within the step. Provided the step length is chosen such that the chances of two large angle scattering events (say greater than 20°) is small, this approach is a very good approximation. A good criterion for choosing the step length is to set it equal to the mean free path for single scattering through an angle greater than say 10 or 15°. It may not be possible to satisfy this criterion easily for heavy elements or at low voltages, in which case it may be necessary to work out some corrective strategy based on an effective step length.

Calculations based on this approach give very good general agreement with experiment with the exception that energy spectra are rather too narrow and that the tails of scattering distributions are much smaller than experimental ones--both predictable consequences of the continuous energy loss approximation. Agreement is best for the light elements and rather poorer for the heavy elements. This again is to be expected as the Rutherford cross-section is a very poor approximation for the heavy elements.

Subsequently, a number of papers based on this general approach have appeared specifically aimed at microanalysis problems. For instance, Pascal [20], Hénoc and Maurice [21] have used the fixed step length approach, while the paper by Shimizu, et al. [22], using a variable step length, is representative of a number of relevant Japanese papers. Although this method is successful and relatively efficient, a fairly large computer is required to handle the tables containing angles of equal scattering probability. As small computers have become more common within the laboratory, there is a need for a much simpler type of calculation. Such a calculation was described by Curgenven and Duncumb [4] and is probably the best small computer calculation available. Although often referred to as a single scattering calculation, it is more strictly a multiple scattering approach with a fixed step length. The Bethe equation is again used for energy loss and the Bethe range is divided into between 25 and 100 steps. The Rutherford cross section in its simplest form may be written as

$$\cot(\theta/2) = \frac{2\alpha}{b}$$

where $b = 1.44 \times 10^{-2}\ Z/E$ (E in kV) and α is an impact parameter. In each step, the angular deflection is determined from a random number n, such that

$$\cot(\theta/2) = \frac{2\sqrt{n}}{b}\alpha .$$

The impact parameter α is chosen so the calculated back-scattering coefficient matches the experimental value.

At first sight, this approach appears over-simplified but, in practice, the approximations are not all poor provided a sufficiently short step length is used. When one bears in mind the approximate nature of the Rutherford cross-section, this greatly simplified approach may give results very comparable in accuracy to calculations based on the Goudsmit-Sanderson multiple scattering theory. It would be interesting to see a systematic test of this approach against experiment and other Monte Carlo calculations.

A further development within this general category is the "single scattering" model of Murata, Matsukawa, and Shimizu [23]. In this model, the step length is chosen equal to the elastic mean free path and angular deflection selected from the screened Rutherford cross-section. A true single scattering model would have step lengths selected at random. With a fixed step length, a multiple scattering distribution should always be used in principle but, in practice. the error involved in using the single scattering cross section is probably negligible. Although this approach requires substantially more computing time, the authors have shown that it is more appropriate for the heavy elements than a full multiple scattering approach.

3.3 Single Scattering and Other Improvements

The calculations described in the previous section are subject to two major approximations. First, the continuous energy loss approximation and second, the use of the Rutherford scattering cross-section. The former is for many applications quite acceptable, but in the energy range of importance in microprobe analysis the Rutherford cross-section is a very poor approximation particularly for the heavy elements. Krefting and Reimer [24] have been able greatly to improve agreement with experiment by using the exact Mott elastic cross-section for scattering greater than 10° using a true single scattering approach for elastic scattering. Energy loss was also partly treated in a single scattering mode. Low energy losses were described by a modified Bethe equation, but higher losses (greater than about 100 eV) were treated as single scattering events. Any calculations attempting to achieve absolute accuracy, particularly for the heavy elements and lower beam energies, will have to incorporate these more precise cross-sections, although the multiple scattering formalism may still be used if required.

There are a number of ways in which the continuous energy loss approximation may be replaced. The most obvious is to include all the possible inelastic interactions in a single scattering calculation. This approach however, would lead to a very lengthy calculation and it is doubtful whether the cross-sections are well enough known in many cases to justify the expense. A simpler alternative is to take the mean energy loss for each step as predicted by the Bethe formula, but to determine the actual energy loss by sampling from some distribution about the mean energy loss using either the Landau equation [11] or some empirical formula. Both these alternatives have been adopted in recent papers, Hénoc and Maurice [25] using the Landau formula, and Shimizu, et al. [26] using an empirical expression. These two papers do demonstrate clearly the effects of the continuous loss approximation and where it is acceptable. Shimizu et al. were investigating the energy spectra of electrons transmitted through thin foils. The spectra given in a calculation based on the continuous loss approximation are quite unrealistic (although the mean energy loss is correct). By introducing energy straggling, good agreement was obtained with experiment. On the other hand, Henoc and Maurice did not find that straggling had a very significant effect on the overall distribution of characteristic ionization in a solid except in the tail of the distribution. Thus, for most microanalytical applications, the continuous loss approximation is satisfactory.

4. Presentation of Results

A Monte Carlo calculation is essentially a statistical experiment. How the results are treated will depend on the aims of the calculations which for microanalysis fall into two categories:

(1) a direct simulation to solve a specific problem; and

(2) calculations aimed at gaining a general understanding of electron scattering in solids.

The first category presents no real problem. The simplest Monte Carlo calculation that will give an acceptable result is employed to give the desired information directly. In this application, the Curgenven and Duncumb method [4] is the obvious first choice. Monte Carlo calculations have been incorporated within correction programs to determine atomic number and absorption corrections, for instance by Shimizu et al. [27]; however, the length of Monte Carlo calculations makes them unsuitable for general use in such applications.

Improvements to the standard ZAF correction procedures are better approached via the second category using the results of the calculation to test procedures and to suggest the correct parameters to use, subsequently confirming the absolute value of any parameters by experiment. Monte Carlo calculations have not had as much impact in this field as they should in spite of the excellent agreement that has been demonstrated between the calculations and experiment. This is probably because of the difficulty of presenting the results in such a way that other workers can make use of them without setting up identical calculation. The author has found the f(z,s) matrix described earlier to be a very convenient method of saving the results of a Monte Carlo calculation and he has been able in this way to develop ideas using data from Monte Carlo calculations carried out some eight years previously [28]. A more general use of this means of presenting results would lead to a much more effective and widespread use of Monte Carlo calculation.

5. Suggested Aims for Future Work

The basic framework for the ZAF correction for microprobe analysis is well founded and the inherent approximations involved, for instance using an average value for the stepping power, are acceptable. However, there are three areas in which Monte Carlo calculations could make further significant contributions:

(1) effects of the angle of incidence of the electron beam;

(2) choice of the mean ionization potential, J; and

(3) an improved absorption correction.

With the extensive use of energy dispersive x-ray detectors in the scanning electron microscope, there is a growing requirement for a careful examination of the variation of the absorption and atomic number correction with the angle of beam incidence. This requires a straightforward application of one of the well-proved calculations.

Of more fundamental importance is the choice of the mean ionization potential, J. There is currently a great deal of uncertainty about what value is best, particularly for the very light elements and also for the very heavy elements where the incident beam energy is less than the binding energy of the more tightly bound atomic electrons. A series of Monte Carlo calculations for different elements using the appropriate single inelastic scattering cross-sections to calculate energy loss as a function of distance traveled (ignoring angular scattering altogether) could well throw invaluable light on this problem.

The Philibert absorption correction formula owes its success to the fact that $f(\chi)$ is extraordinarily insensitive to the depth distribution of characteristic ionization for $f(\chi)>0.8$. It may be shown to be quite inadequate, even in its full form, for lower values of $f(\chi)$. Monte Carlo calculations have already been used to show the form a more accurate approach should take [28], but more work is required to establish a procedure for routine use.

References

[1] Green, M., *Proc. Phys. Soc.* 82, 204 (1963).

[2] Shimizu, R., Murata, K., and Shinoda, G., *X-Ray Optics and Microanalysis*, R. Castaing, P. Descamps, and J. Philibert, eds., p. 127 (Hermann, Paris, 1966).

[3] Bishop, H. E., see ref. [2], p. 112.

[4] Curgenven, L., and Duncumb, P., Tube Investments Research Report 303 (1971).

[5] Bethe, H. A., *Ann. Phys. Leipzig* 5, 325 (1930).

[6] Lewis, H. W., *Phys. Rev.* 78, 526 (1950).

[7] Spencer, L. V., *National Bureau of Standards Monograph No. 1* (1959).

[8] Dashen, R. F., *Phys. Rev.* 134A, 1025 (1964).

[9] Ogilvie, R. E. and Brown, D. B., see ref. [2], p. 139.

[10] Bethe, H. A., Rose, M. E., and Smith, L. P., *Proc. Am. Phil. Soc.* 78, 573 (1938).

[11] Landau, L., *J. Phys. USSR* 8, 201 (1944).

[12] Hammersley, J. M. and Handscomb, D. C., *Monte Carlo Methods* (Methuen, London, 1964).

[13] Berger, M. J., *Methods in Computational Physics, Vol. 1*, B. Alder, S. Fernback, and M. Rotenberg, eds. (Academic Press, New York and London, 1963).

[14] Thomas, R. N., Ph.D. Thesis, University of Cambridge (1961).

[15] Bishop, H. E., *Proc. Phys. Soc.* 85, 855 (1965).

[16] Gruen, A. E., *Z. Naturforsch.* 12a, 89 (1957).

[17] Goudsmit, S. and Sanderson, J. L., *Phys. Rev.* 57, 24 (1940).

[18] Bishop, H. E., Ph. D. Thesis, University of Cambridge (1966); *Brit. J. Appl. Phys.* 18, 703 (1967).

[19] Shinoda, G., Murata, K., and Shimizu, R., *Quantitative Electron Probe Microanalysis*, K. F. J. Heinrich, ed., p. 155 (National Bureau of Standards Special Publication 298, Washington, D.C. 1968).

[20] Pascal, B., *X-Ray Optics and Microanalysis*, G. Mollenstedt and K. H. Gaukler, eds., p. 137 (Springer, Tübingen, Berlin, 1969).

[21] Hénoc, J. and Maurice, F., *Proceedings of the Sixth International Conference on X-Ray Optics and Microanalysis*, G. Shinoda, K. Kohra, and T. Ichinodawa, eds., p. 113 (Univeristy of Tokyo, 1972).

[22] Shimizu, R., Ikuta, T., and Murata, K., *J. Appl. Phys.* 43, 4233 (1972).

[23] Murata, K., Matsukawa, T., and Shimizu, R., *J. Appl. Phys. Japan* 10, 678, (1971).

[24] Krefting, E. and Reimer, L., *Quantitative Analysis With Electron Microprobe and Secondary Ion Mass Spectroscopy*, E. Preuss, ed., p. 114 (Julich: Zentralbibliothek der KFA, Julich GmbH, 1973).

[25] Hénoc, J. and Maurice, F., CEA-R-4615, (Commisariat à l'Energie Atomic, France, 1975).

[26] Shimizu, R., Kataka, Y., Matsukawa, T., Ikuta, T., Murata, K., and Hashinoto, H., *J. Phys. D* 8, 820 (1975).

[27] Shimizu, R., Nishigori, N., and Kurata, K., see ref. [21], p. 95.

[28] Bishop, H. E., *J. Phys. D* 7, 2009 (1974).

National Bureau of Standards Special Publication 460. Proceedings of a Workshop on the Use of Monte Carlo Calculations in Electron Probe Microanalysis and Scanning Electron Microscopy held at NBS, Gaithersburg, Maryland, October 1-3, 1975. Issued December 1976.

STUDIES OF THE DISTRIBUTION OF SIGNALS IN THE SEM/EPMA BY MONTE CARLO ELECTRON TRAJECTORY CALCULATIONS

AN OUTLINE

Dale E. Newbury and Harvey Yakowitz

Institute for Materials Research
National Bureau of Standards
Washington, DC 20234

Monte Carlo electron trajectory calculations provide a powerful technique for the study of the characteristics and distributions of the various signals generated in electron-specimen interactions. This paper is a review of the diverse applications of Monte Carlo techniques to the calculation of signal distributions. The following topics will be considered: extent of the primary interaction volume; lateral, depth, angular and energy distributions of backscattered and secondary electrons; the extent of the x-ray generation volume, and the depth distribution of characteristic and continuum x-rays. Numerous examples of these calculated distributions are drawn from the literature and compared, when possible, with appropriate experimental results.

Key Words: Backscattered electrons; electron probe microanalysis; Monte Carlo electron trajectory simulation; scanning electron microscopy; secondary electrons; x-rays.

1. Introduction

The techniques of Monte Carlo electron trajectory simulation have been applied by many authors to the problem of determining signal distributions arising from electron-specimen interactions. In this paper, we shall review examples of calculations of the following signal distributions: (1) extent of the primary interaction volume; (2) lateral and depth distributions of backscattered electrons; (3) angular and energy distributions of backscattered electrons; (4) lateral and depth distributions of secondary electrons; (5) angular and energy distributions of secondary electrons; (6) extent of x-ray generation volume; and (7) the depth distribution of x-ray production. Examples of these distributions, as calculated by Monte Carlo techniques, will be presented, taken from the literature as well as our own work. This paper is intended as an outline review, highlighting the areas in which Monte Carlo techniques have been used, rather than a comprehensive review of all work. Therefore, we will not attempt to list all citations of a particular type of calculation; instead, representative examples of each calculation will be given.

2. Extent of the Primary Interaction Volume

Direct experimental visualization of the primary electron-target interaction volume is only possible in certain targets such as gases or liquids. Indirect visualization is possible for some solid organic compounds such as polymethylmethacrylate, where chemical etching following electron beam irradiation produces a pit which reveals the extent of primary electron interaction. For many targets of interest to the microscopist/analyst, e.g., solid elemental or compound targets, experimental determination of the interaction volume can only be carried out indirectly through sequential measurements of a series of films of different thicknesses so as to determine the fractional electron transmission.

The Monte Carlo electron trajectory calculation is directly applicable to the problem of determining the interaction volume. Since the coordinates (X, Y, Z) of the electron are calculated at each scattering point, a plot of these successive points traces the path of the electron through the solid. By superimposing many trajectories on the same plot, a picture is built up of the interaction volume. Such a plot must necessarily be two-dimensional; and therefore, the true trajectory path in three dimensions is actually projected onto the particular section selected.

Curgenven and Duncumb [1][1] presented a series of trajectory plots revealing the extent of the primary interaction volume (figs. 1-4). The trajectories plotted by the Curgenven and Duncumb program show sharp angular changes, a result of their use of a multiple scattering approximation. Plots of trajectories with single scattering models are much smoother, a result of the small step length used in these calculations and the small angle of scattering. The interaction volume in copper as a function of increasing beam energy (fig. 1) shows an increase in size. This increase is expected since the elastic scattering cross-section is proportional to $1/E^2$, and the stopping power, which is related to the rate of energy loss with distance traveled in the specimen, goes as log E/E. Thus, both the elastic scattering cross-section and the stopping power decrease with increasing energy, leading to an increase in the size of the interaction volume with increasing energy. Note that the interaction volume at 20 keV is roughly spherical and more than 1 μm in diameter.

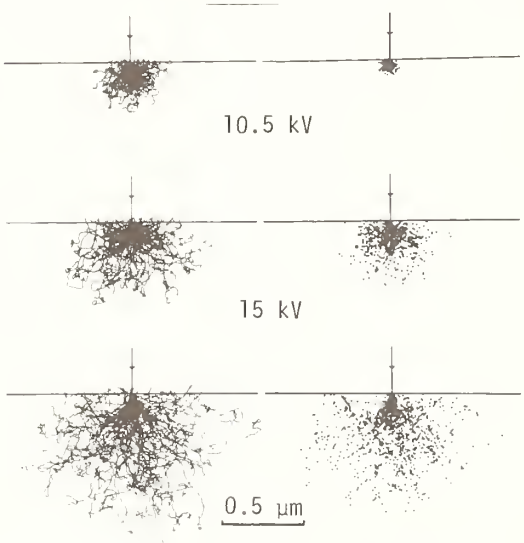

Figure 1. Interaction volume in copper with normal beam incidence at various accelerating voltages (Curgenven and Duncumb [1]).

The effect of the atomic number of the target upon the interaction volume is illustrated in figure 2, where aluminum and gold are compared assuming a beam energy of 20 keV. The interaction volume has a diameter of approximately 3 μm for aluminum and 0.4 μm for gold. The reduction in the physical size of the interaction volume with increasing atomic number, Z, is a result of the dependence of the elastic scattering cross-section upon Z^2. From figure 2, one can also observe the increased number of trajectories which exit the specimen; i.e., backscatter, for gold as compared to aluminum. Furthermore, examination of figure 2 shows a basic difference in the shape of the interaction volume in the low Z material (aluminum) as compared to the high Z material (gold). The dense region of interaction volume in aluminum is pear-shaped, with a narrow neck near the surface, whereas the interaction volume in gold resembles a sphere partially submerged below the specimen surface. The interaction volume for an element of intermediate atomic number, copper, shows a transition structure containing the neck characteristic of the pear shape, while showing a more spherical shape (fig. 3). Note that even in aluminum, the region over which x-rays are produced is spherical, but the density of production varies greatly. In gold, the density is more uniform.

[1]Figures in brackets indicate literature references at the end of this paper.

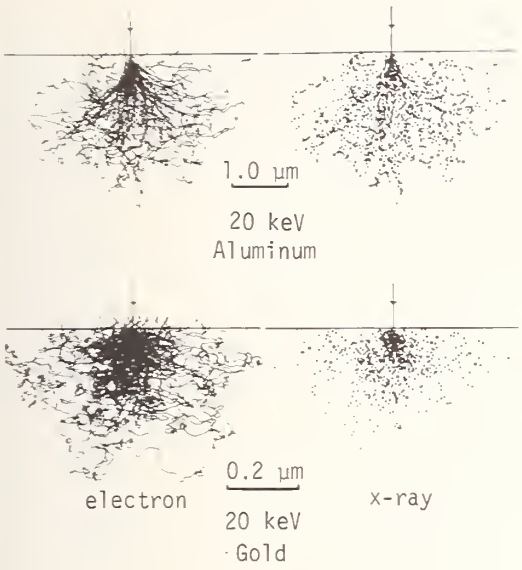

Figure 2. Comparison of the interaction volume in aluminum and gold at normal beam incidence and 20 keV beam energy (Curgenven and Duncumb [1]).

The effect of the angle of beam incidence on the interaction volume is shown in figures 3 and 4 for copper bombarded with a beam having energy of 20 keV. As the specimen tilt increases and the beam approaches grazing incidence, the interaction volume decreases in size and the path density increases near the surface. These effects result from the tendency of electrons to scatter in the forward direction. The angular distribution of elastic scattering is strongly peaked in the forward direction; at grazing incidence, the forward scattering keeps the electrons near the surface. The increased tendency for electrons to escape the specimen can also be observed in figures 3 and 4; thus, the backscattering coefficient increases as a function of tilt.

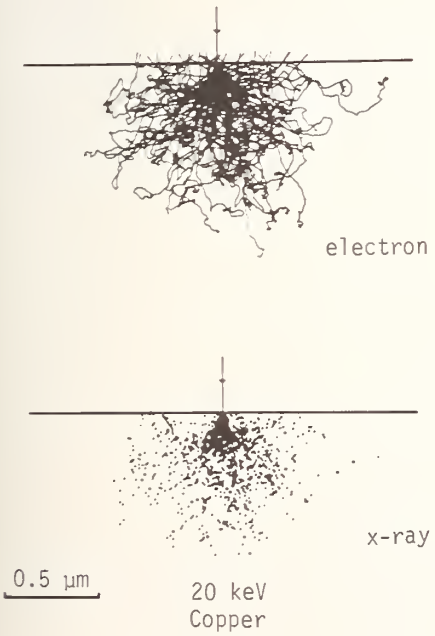

Figure 3. Interaction volume in copper at normal incidence and 20 keV beam energy (Curgenven and Duncumb [1]).

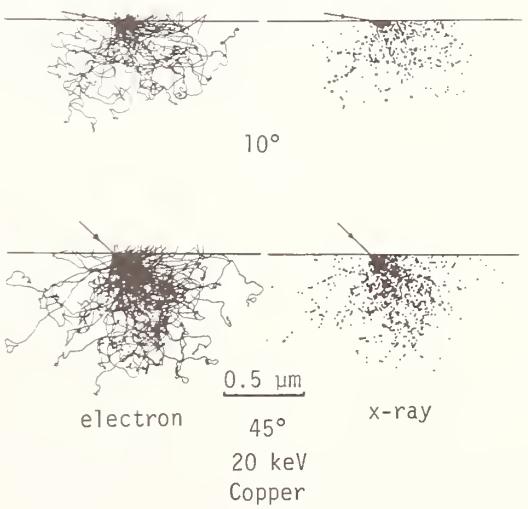

Figure 4. Interaction volume in copper with 20 keV beam energy at beam incidence angles of 45° and 10°; compare with figure 3 (Curgenven and Duncumb [1]).

The density of plotted trajectories in figures 1-4 makes individual trajectories difficult to discern; the poor resolution results from the superposition of trajectories in two dimensions. By calculating the scattering events within a radial segment, the radial distribution function can be obtained (fig. 5). For quantitative evaluation of the interaction volume, a plot such as that in figure 5 is more useful than a drawing of superimposed trajectories.

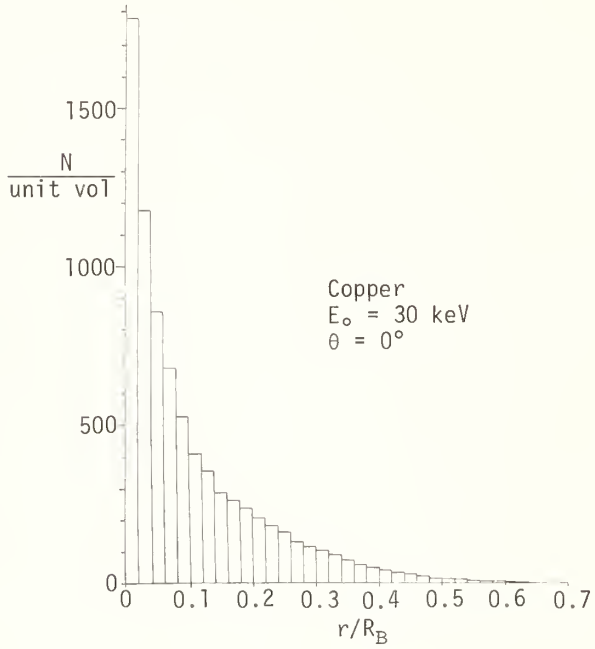

Figure 5. Lateral extent of the interaction volume indicated by the emission of backscattered electrons.

At normal beam incidence, the sections Y-Z and X-Z (coordinate system: Z perpendicular to surface, positive going into the specimen; X,Y orthogonal and contained in the surface plane, X the axis of tilt; Y pointing down a tilted specimen) are equivalent because of the radial symmetry of scattering. For tilted specimens, the Y-Z and X-Z sections are not equivalent because of forward scattering. This asymmetry is illustrated in figures 6 and 7, where the Y-Z and X-Z sections for iron tilted 55° (beam incidence 35°) and a beam energy of 30 keV are given. The high path density portion of the interaction volume is more compact in the X-Z section than in the Y-Z section.

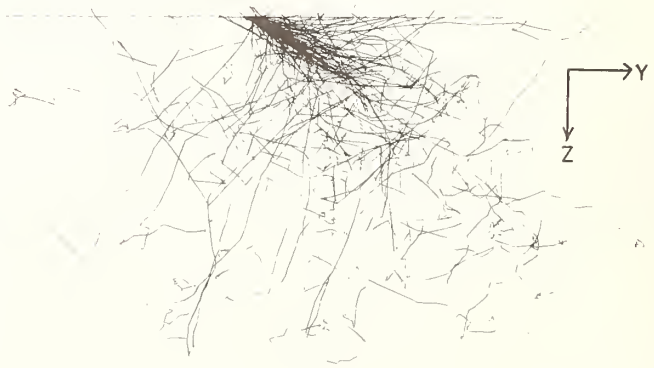

Figure 6. Section of interaction volume perpendicular to the tilt axis for iron at a tilt angle of 55°, and a beam energy of 30 keV (Myklebust, et al. [3]).

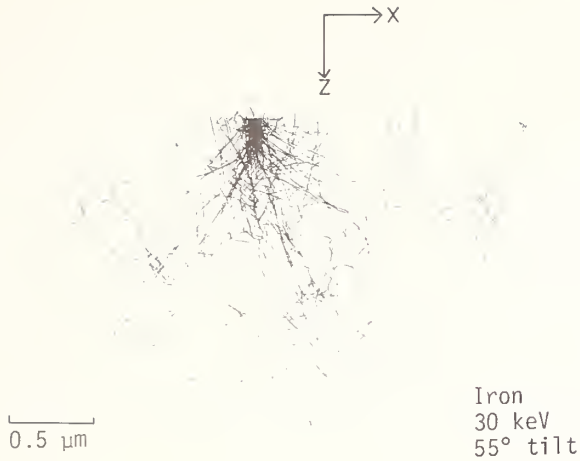

Figure 7. Section of the interaction volume containing the axis of tilt for iron at a tilt angle of 55° and a beam energy of 30 keV (Myklebust, et al. [3]).

The analysis of particles is gaining increasing importance. This class of objects provides one of the most difficult analysis situations, and quantitative analysis is frequently impossible by conventional techniques when the particle size approaches the x-ray interaction volume. The techniques of Monte Carlo electron trajectory simulation are well suited to analysis when the geometry of the target becomes important, and calculations for particles are in progress [4]. The effects of finite particle size relative to the interaction volume are shown for aluminum spheres in figure 8, illustrating the enhanced loss of electrons from particles.

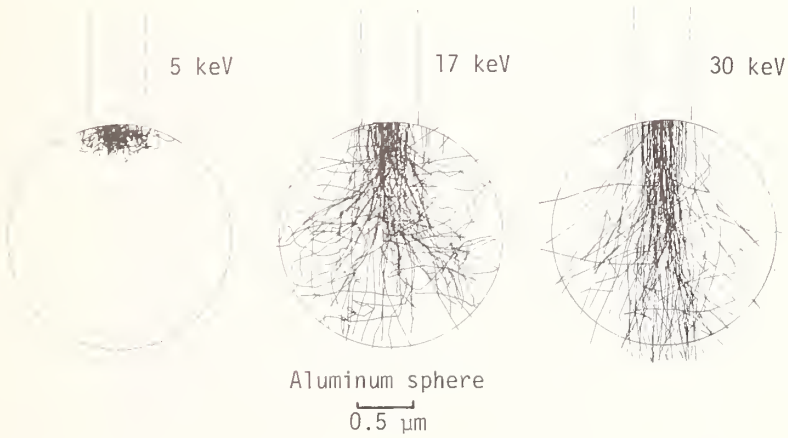

Figure 8. Interaction volume in aluminum spheres at different beam energies (Myklebust, et al. [3]).

When the specimen thickness is below the diameter of the interaction volume, electron transmission occurs. This transmission causes a change in the lateral dimension because backscattering is reduced. Curgenven and Duncumb [1] illustrated this effect by plotting the trajectories of 20 keV electrons passing through 0.25 μm and 1.3 μm thick films of aluminum (fig. 9). The transmission through the 0.25 μm film is nearly complete and the interaction volume is small. For the 1.3 μm film, backscattering is significant, and the interaction volume is quite similar to that observed in the top 1.3 μm slice of the interaction volume of the bulk target. The work of Krefting and Reimer [5] has shown that the

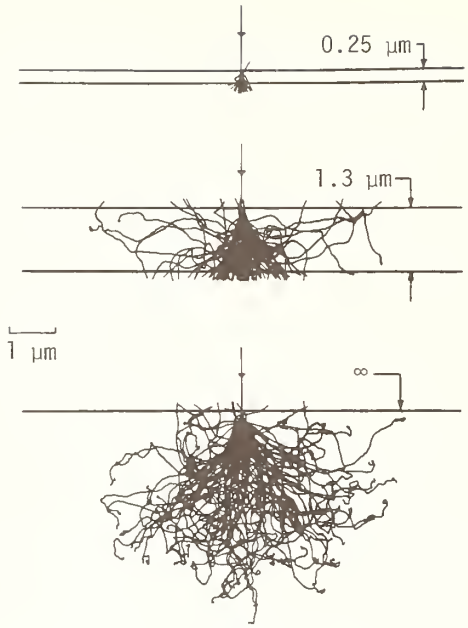

Figure 9. Interaction volume as a function of specimen thickness for aluminum with normal beam incidence and 20 keV beam energy (Duncumb and Curgenven [1]).

transmission coefficient, τ, can be accurately calculated by Monte Carlo techniques (fig. 10). Shinoda, et al. [6], have shown that the angular distribution of electrons transmitted through a thin foil calculated by Monte Carlo techniques is in good agreement with the experiment (fig. 11).

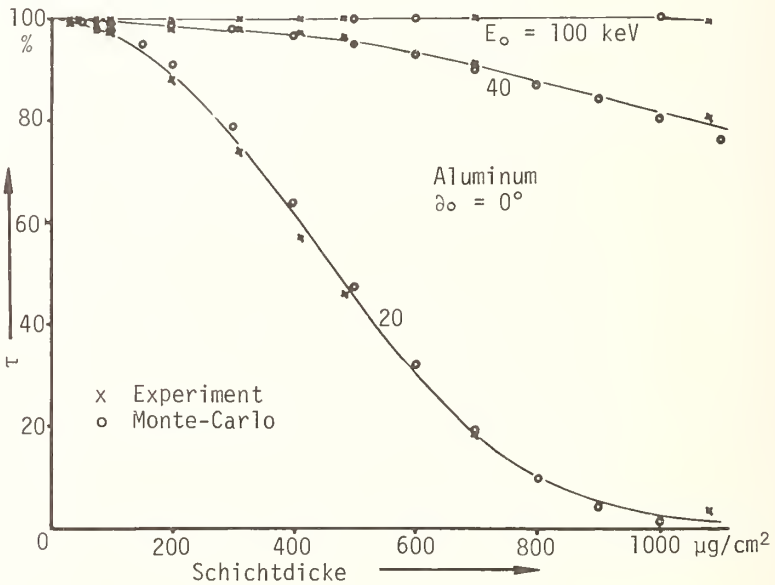

Figure 10. Coefficient of transmission of electrons, τ, through thin films, Monte Carlo and experimental values (Krefting and Reimer [5]).

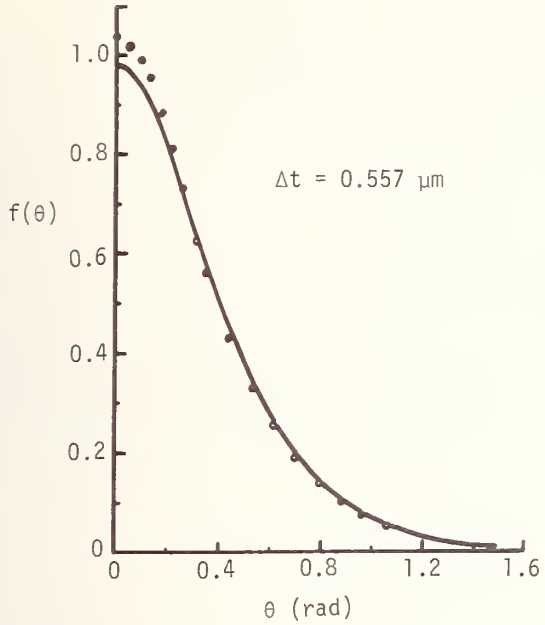

Figure 11. Angular distribution of electrons transmitted through an aluminum foil of 0.557 μm thickness. Monte Carlo calculations by Shinoda, et al. [6]; experimental points by Thomas [7].

Several authors [8,9,10] have carried out experiments involving irradiation of polymethylmethacrylate, followed by etching, to reveal the contours of the energy deposition (fig. 12). Comparison of Monte Carlo calculations of the energy deposition contours with the experimental results show good agreement (fig. 13).

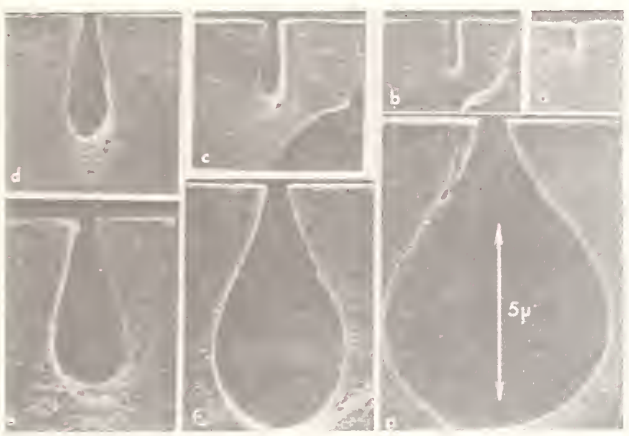

Figure 12. SEM images of polymethylmethacrylate following increasing chemical etching times to reveal deposited energy contours (Everhart, et al. [10]).

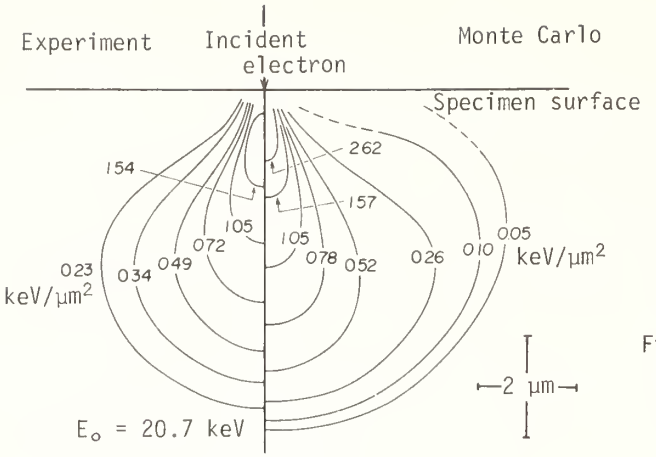

Figure 13. Comparison of energy dissipation profiles in polymethylmethacrylate determined experimentally and by Monte Carlo calculation (Shimizu, et al. [8]).

3. Properties of Backscattered Electrons

Beam electrons which exit the specimen after scattering through a large angle, or else after undergoing several small angle collisions which reverse the direction of flight, are collectively referred to as backscattered electrons. These electrons provide an important source of information in scanning electron microscopy. Many authors have used Monte Carlo techniques to calculate the properties of backscattered electrons. It is well known experimentally that the backscatter coefficient, η, increases with increasing atomic number, Z, of the target (fig. 14). This dependence can be used as a test to adjust the parameters of the

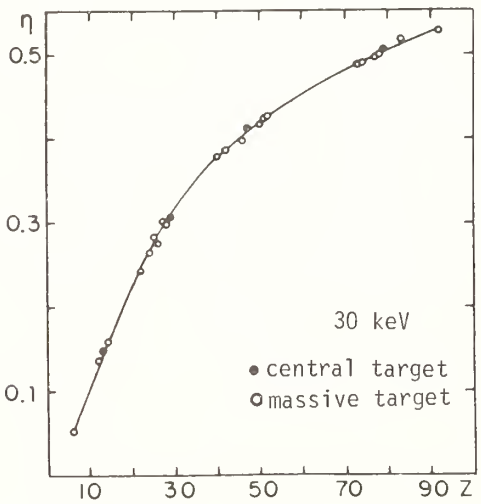

Figure 14. Backscatter coefficient, η, as a function of atomic number; experimental data determined by Heinrich [11]. Central and massive targets refer to the experimental techniques.

Monte Carlo techniques so that realistic values will be calculated for other parameters of interest. For example, the backscatter coefficient increases as a function of increasing specimen tilt, and Monte Carlo calculations show good correspondence to experimental measurements of this effect (fig. 15).

Of particular interest in determining the depth of sampling of the backscattered electron signal is the escape probability of incident beam electrons which have penetrated to various depths. Calculations of the escape probability for 30 keV electrons incident on

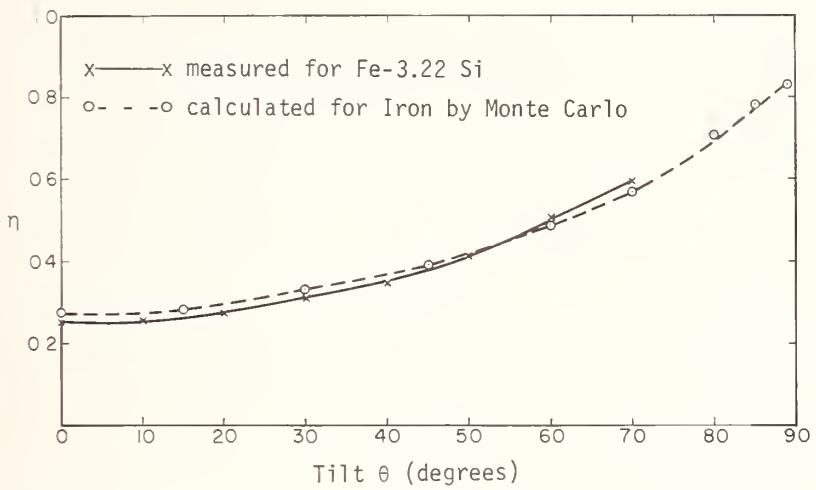

Figure 15. Backscatter coefficient as a function of specimen tilt for iron with a beam energy of 30 keV; experimental values for iron--3.22% silicon (Myklebust, et al. [3]).

copper reveal a rapidly decreasing probability of escape with depth (fig. 16). Elaboration of this calculation gives the fraction of escaped electrons, η_B, and absorbed electrons, η_A, as a function of depth (fig. 17). Although the absorption of electrons takes place at a greater mean depth than the mean penetration of the backscattered electrons, the absorbed

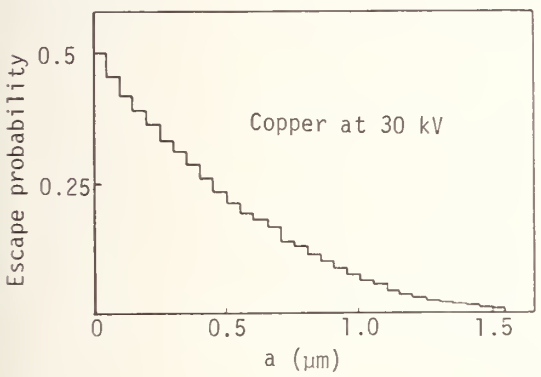

Figure 16. Probability of escape of incident 30 keV electrons which have penetrated to various depths, a, in copper (Schimizu and Murata [12]).

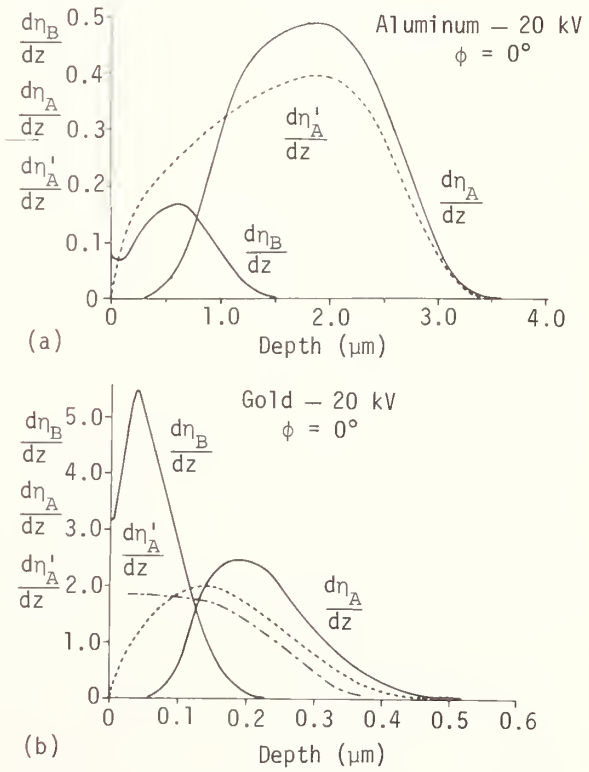

Figure 17. Maximum penetration depth of backscattered and absorbed electrons for aluminum and gold (Murata [2]). η'_A dashed line from Thomas [6].

(specimen) current signal does not contain information from deeper within the specimen than does the backscattered electron signal. Contrast formation in the specimen current signal depends only on the fact that electrons have excited the specimen and, thus, the specimen current signal has a depth of sampling identical to that of the backscattered electrons. The depth distribution of backscattered electrons is affected by the proximity of an edge, which leads to enhanced escape because of the lateral extent of the interaction volume (fig. 18).

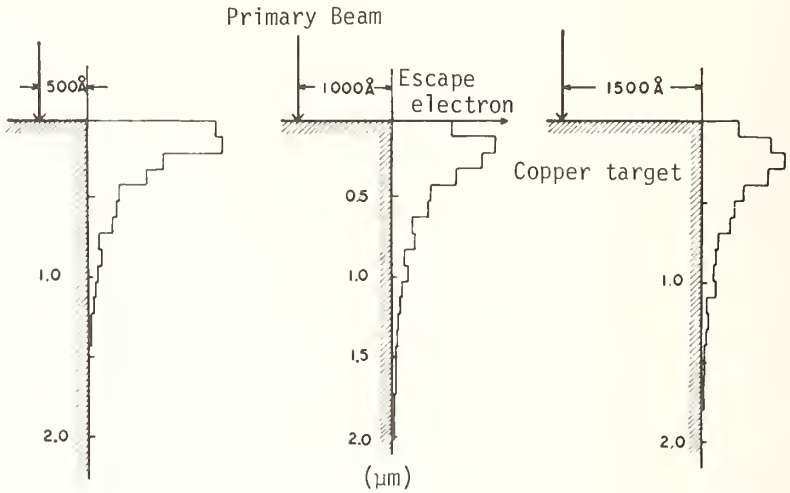

Figure 18. Depth distribution of maximum penetration of backscattered electrons with a point beam incident near an edge (Shimizu and Murata [12]). The histogram indicates the number of electrons which have penetrated to a given depth before backscattering.

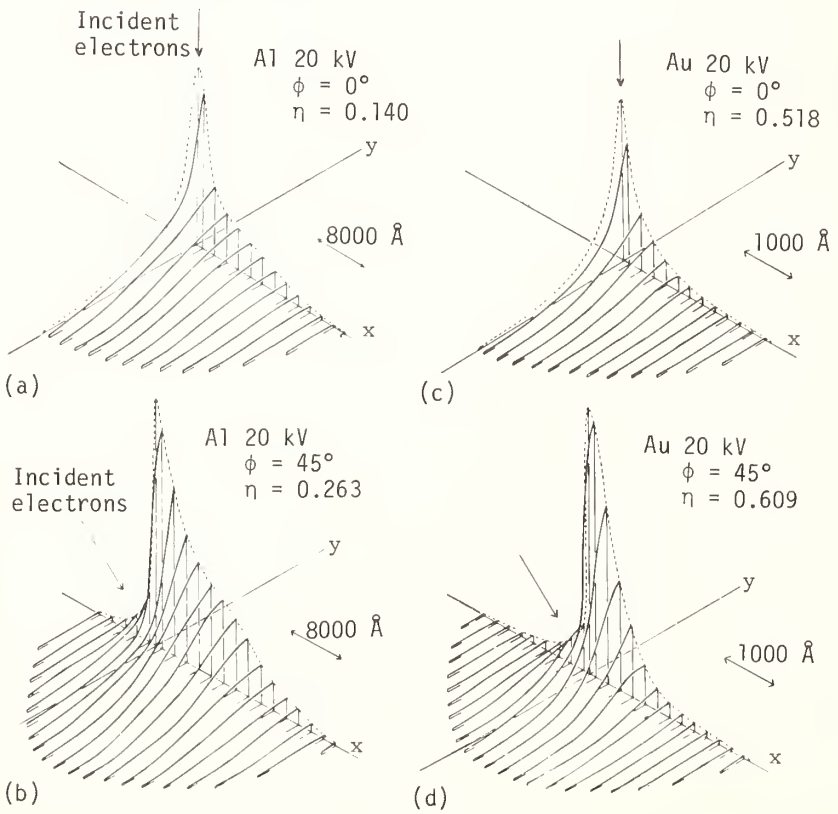

Figure 19. Intensity distribution of backscattered electrons as a function of position of escape from the surface (Murata [2]).

In determining the spatial resolution of the backscattered electron signal, the escape of electrons remote from the beam impact area must be considered as a result of the lateral extent of the interaction volume. Murata [2] has calculated the lateral escape area of backscattered electrons for different atomic number targets and for conditions of normal and tilted specimens (fig. 19). For normal incidence, a strong central peak is observed, with the lateral extent reduced in the case of high atomic number. For a tilted specimen, the central peak is enhanced and sharper for gold. The area distribution becomes asymmetric, with the forward lobe enlarged. The extent of the forward lobe is quite similar to the lateral range observed at normal incidence. All of these observations are in keeping with the characteristics of the interaction volume noted previously.

The angular distribution of the backscattered electrons can be calculated by recording the angle of elevation of the electron trajectory above the surface. A histogram of such exit angles is shown in figure 20. Experimentally, the angular distribution is found to follow a cosine law because of the state of nearly complete diffusion or randomness of the electron trajectories following many elastic scattering acts. A cosine law distribution is superimposed on the histogram of figure 20, and the correspondence is very good.

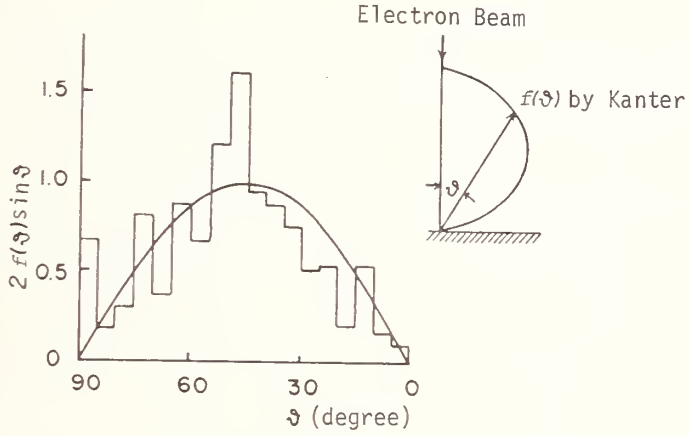

Figure 20. Angular distribution of backscattered electrons relative to surface normal and a cosine distribution [12]; experimental results of Kanter [13].

Wells has reported the angular distribution of low energy-loss electrons which scatter out of the specimen after one or two elastic collisions [14]. The measurements were made with the specimen highly tilted (i.e., beam incidence nearly grazing) to enhance forward scattering out of the specimen. Wells' results are shown in figure 21 (barred points) and are compared with the angular distribution for single-event electrons predicted by a Monte Carlo technique.

The energy distribution of the backscattered electrons has been calculated by means of Monte Carlo techniques by several authors [3,4,12,15,16,17]; examples of these distributions are shown in figure 22 along with experimental results. Usually, the correspondence is very good, although the position of the high energy peak and the shape of the distribution is somewhat dependent on the form chosen for the scattering model.

Wells has demonstrated the great value of forming SEM images with those electrons which have lost only a small fraction of the incident energy (low-loss electrons) [14]. The image derived from these electrons, which have traveled a limited distance in the solid, is particularly sensitive to surface structure. The information is localized near the impact point of the beam, making this signal especially useful for high resolution microscopy. Murata [19] has carried out Monte Carlo calculations to study characteristics of such backscattered electrons. A comparison is shown of the surface emission function of backscat-

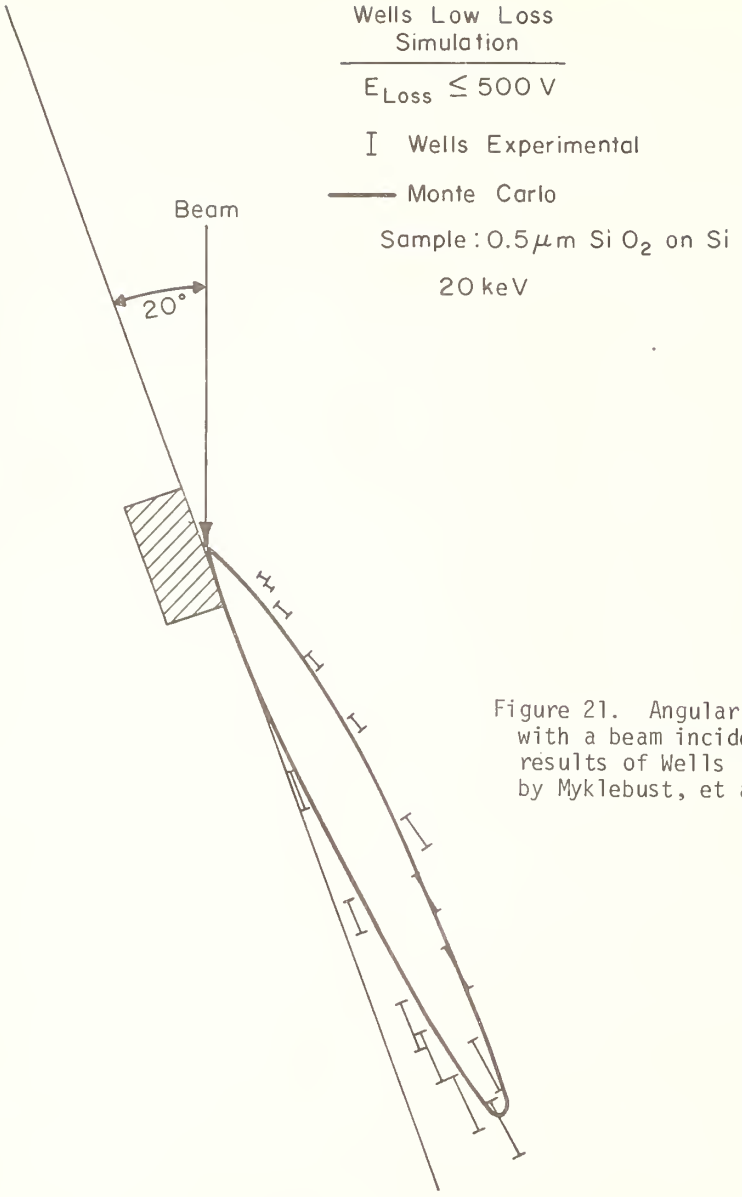

Figure 21. Angular distribution of low loss electrons with a beam incidence angle of 20°. Experimental results of Wells [14]; Monte Carlo calculations by Myklebust, et al. [3].

tered electrons with consideration of (a) all energies (fig. 23), and (b) low energy losses (fig. 24). Even at normal beam incidence, the low-loss electrons show a stronger and more sharply defined central peak. Murata further calculated the surface emission area of back-scattered electrons selected by the angle of elevation along which they exited the specimen (fig. 25(a)). For a specimen tilt of 45°, the electrons emitted at an elevation angle less than 30° come from about 25 percent of the area of emission of electrons with elevation angles in the range 60-90°. Moreover, the mean electron penetration depth was found by the Monte Carlo calculations to be strongly dependent upon the elevation angle of the back-scattered electron, especially for tilted specimens (fig. 25(b)). The utility of (a) tilting the specimen, (b) accepting only a limited angular evelation range, and (c) energy selection is thus confirmed by the Monte Carlo calculations.

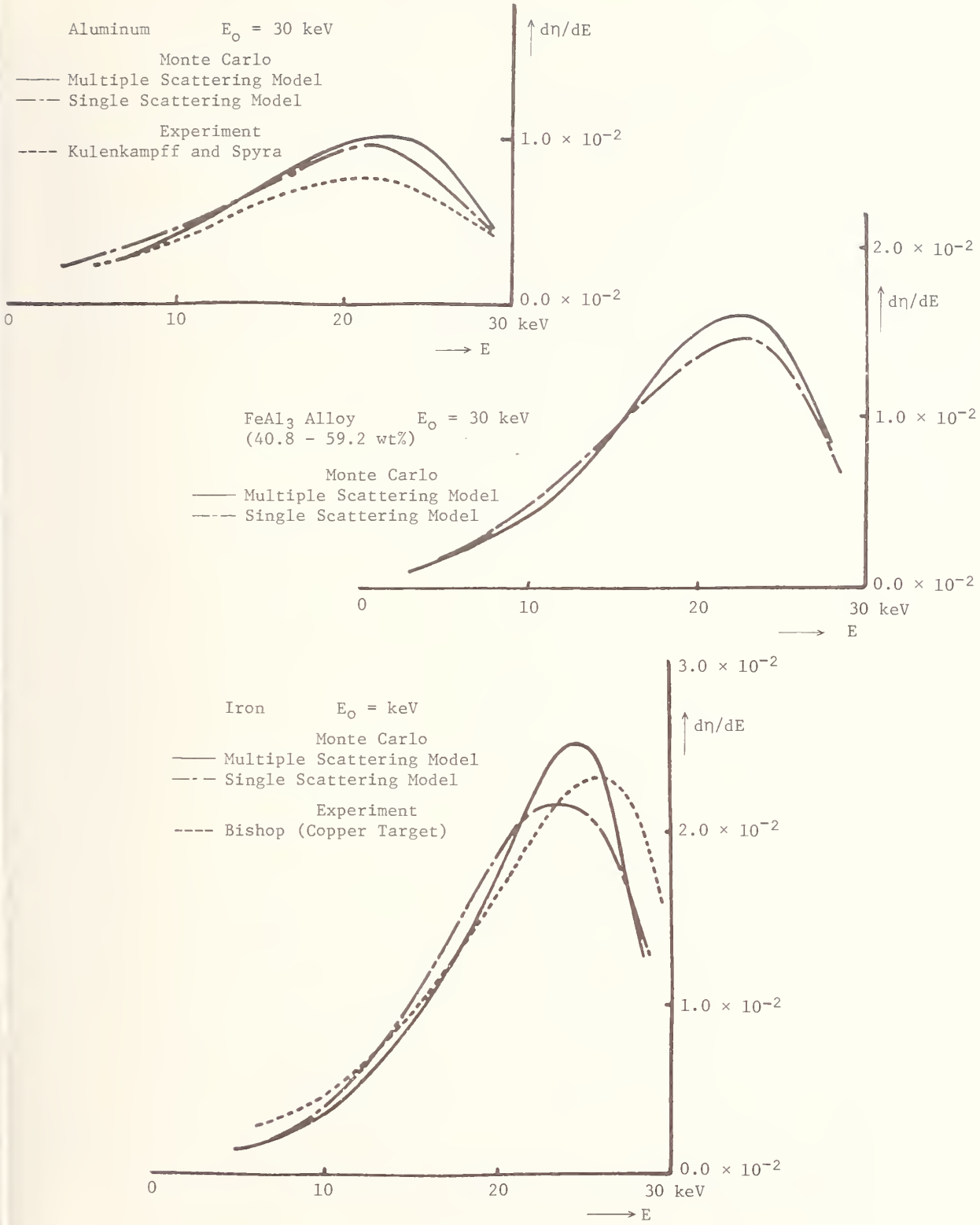

Figure 22. Energy distributions of backscattered electrons calculated by Monte Carlo techniques with single scattering and multiple scattering models, Shimizu, et al. [16]; experimental results of Bishop [18].

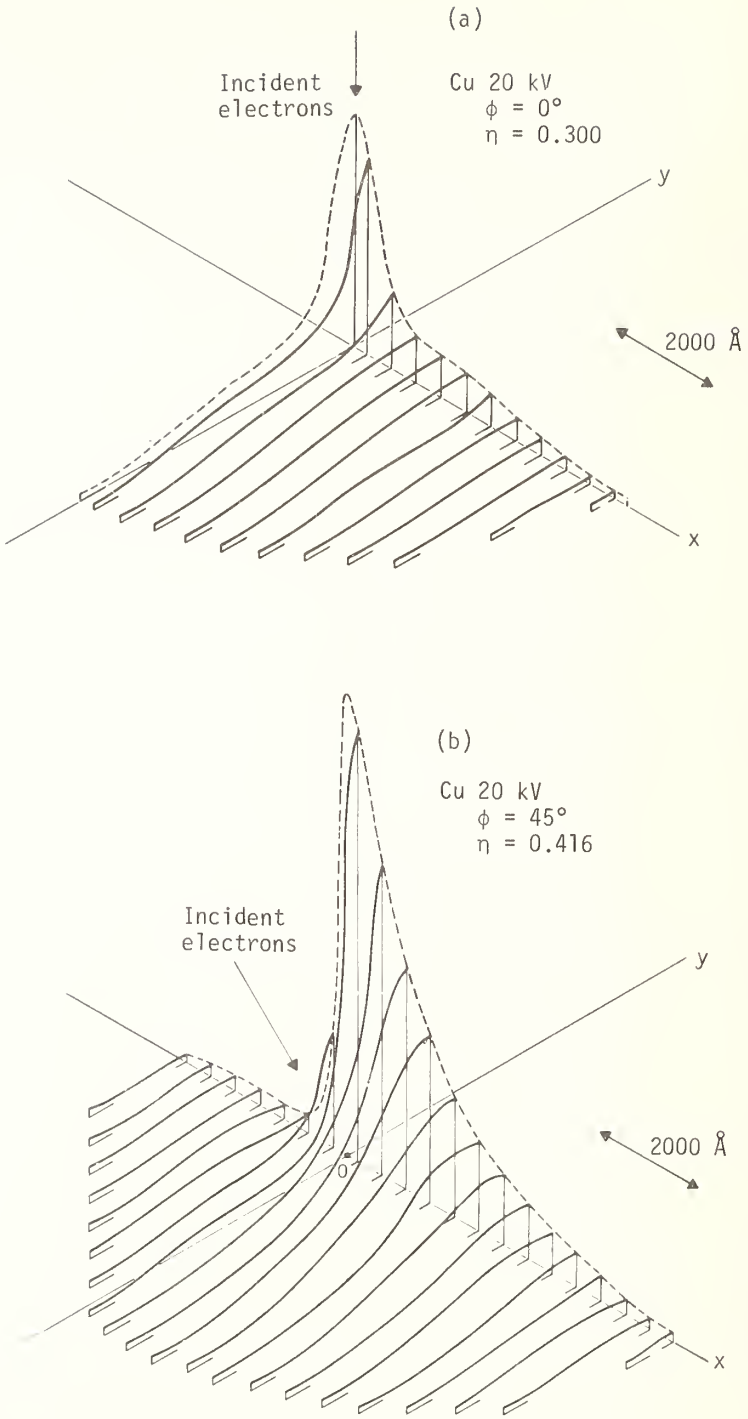

Figure 23. Surface distribution of backscattered electrons of all energies; copper target, beam energy 20 keV (Murata [19]).

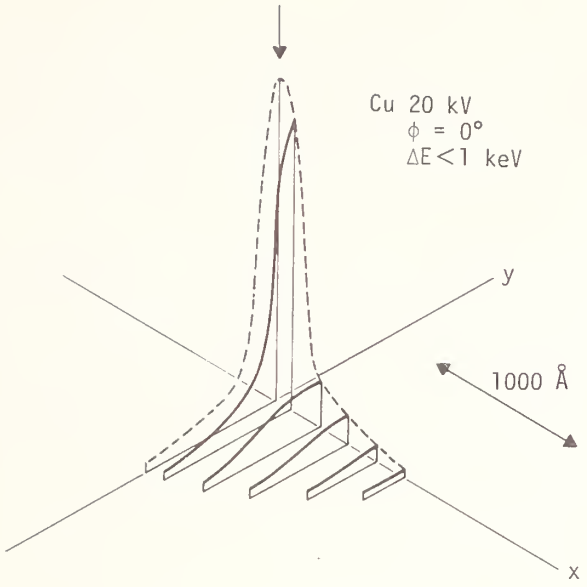

Figure 24. Surface distribution of backscattered electrons which have lost less than 1 keV; copper target, beam energy 20 keV (Murata [19]).

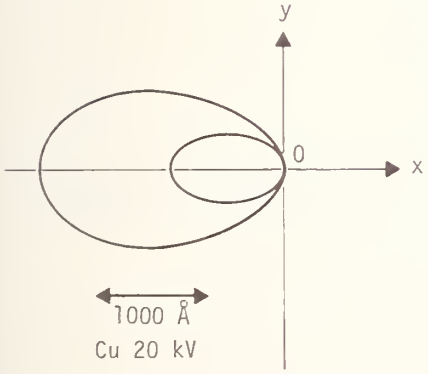

Inside: Low exit angles (0°-30°)
Outside: High exit angles (30°-90°)

(a)

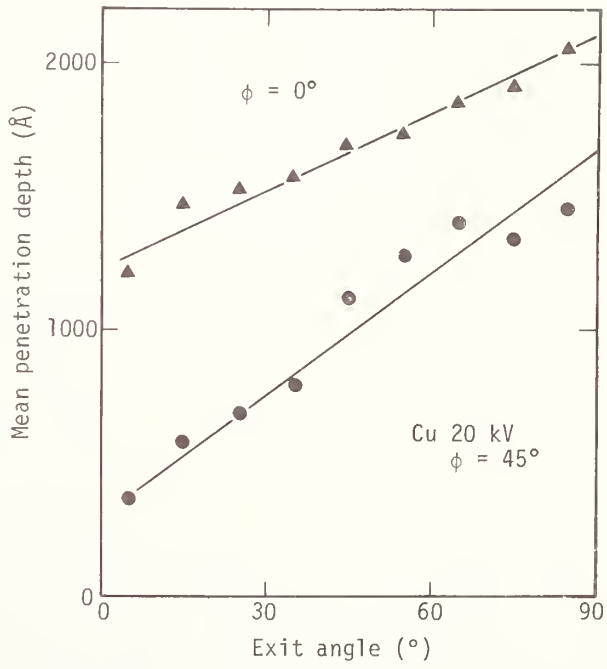

(b)

Figure 25. (a) Surface emission area for backscattered electrons which have been emitted with low (0-30°) or high (30-90°) exit angles relative to the surface. (b) Mean penetration depth as a function of exit angle (Murata [19]).

4. Properties of Secondary Electrons

The most common signal used by scanning electron microscopists for obtaining images of three-dimensional objects has been the secondary electron signal. The low energy of these electrons (< 50 eV) allows for their efficient collection by means of a suitably biased grid. Moreover, because of their low energy, they can only escape from near the surface of the specimen, and thus convey information concerning approximately the top 50 Å layer of the specimen.

The most extensive study to date of secondary electrons by Monte Carlo techniques is that by Koshikawa and Shimizu [20], and most examples given here will be drawn from that paper. These authors used the energy excitation function of Streitwolf [21] to describe the energy distribution of the production of secondary electrons. The primary beam was considered to penetrate--without scattering or significant energy loss--to a depth of 75 Å, while producing secondary electrons along this path. Secondary electrons produced by the exiting backscattered electrons were ignored. Since secondary electron production by the backscattered electrons is more efficient than production by primary electrons, this simplification restricts strict interpretation of the results of Koshikawa and Shimizu [20] to the case of primary electrons incident on thin films where backscattering is negligible.

The energy of the secondary electrons produced along the path of the primary electrons was then adjusted for energy loss during passage through the solid prior to escape. The mean free path was deduced from results of Kanter [22] and of Palmberg [23]. Moreover, the slow electrons undergo energy loss and scattering in collisions with conduction band electrons. The authors considered the loss of energy from the slow electron, its change in direction due to scattering, and the energy and direction of the conduction electron after the interaction (fig. 26). Finally, they considered the refraction of the slow electrons by the surface potential barrier.

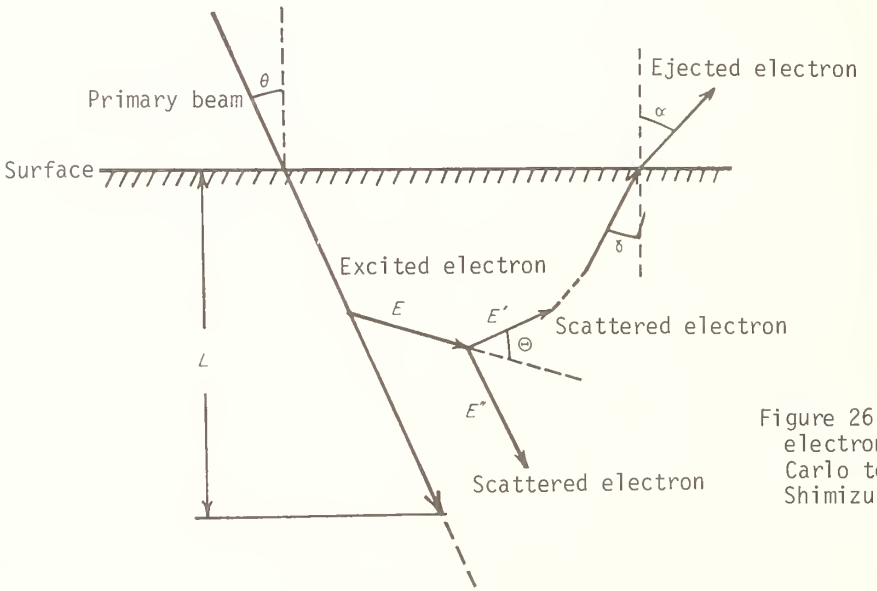

Figure 26. Schematic of secondary electron calculation by Monte Carlo techniques (Koshikawa and Shimizu [20]).

Taking into account all of these effects, Koshikawa and Shimizu [20] determined the energy distribution of the emitted secondary electrons from copper. This distribution is compared with the experimentally observed distribution in figure 27. The shapes of the distributions are similar, with the peak energy slightly higher for the Monte Carlo calculation.

The angular distribution of the emitted secondary electrons calculated by the Monte Carlo technique is shown in figure 28 with a cosine law distribution superimposed on the calculated points. Good agreement is found, indicating that the secondary electrons are generated in random directions by the incident beam.

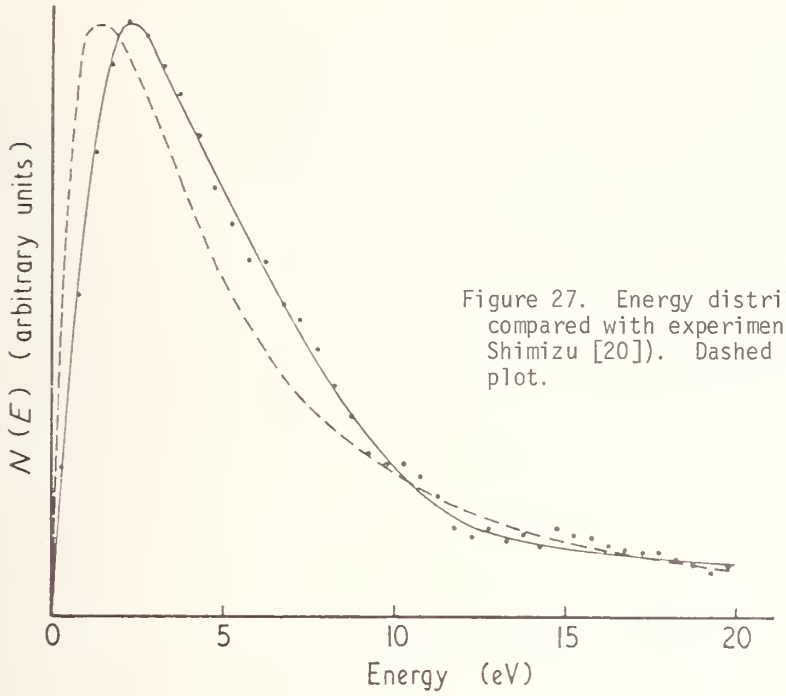

Figure 27. Energy distribution of secondary electrons compared with experimental values (Koshikawa and Shimizu [20]). Dashed line is the experimental plot.

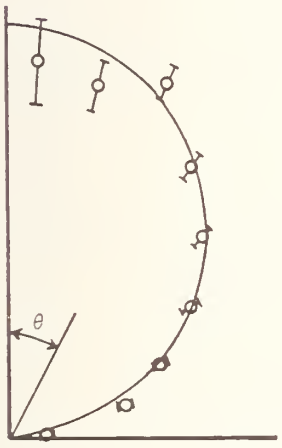

Figure 28. Angular distribution of secondary electrons and a superimposed cosine law (Koshikawa and Shimizu [20]). Horizontal line is the surface, vertical line is the normal to the surface. Polar coordinate plot (r,θ).

The calculated lateral distribution of the secondary electrons with an incident point beam is shown in figure 29. The distribution at normal incidence is about 10 Å wide, full width, half maximum, indicating the limiting spatial resolution which can be expected. As the specimen tilt is increased, the distribution becomes skewed in the forward direction, and the strong central peak is diminished.

The distribution in depth of the origin of the emitted secondary electrons is shown in figure 30. The function shows a rapid decrease with only a few percent of the signal originating at a depth of 75 Å. Examination of the lateral distribution of the secondary electrons as a function of depth (fig. 31), reveals that the strong central peak observed in figure 29 originates with those secondary electrons formed near the surface. This behavior occurs because the secondaries produced deeper in the specimen are more likely to scatter laterally while propagating back toward the surface.

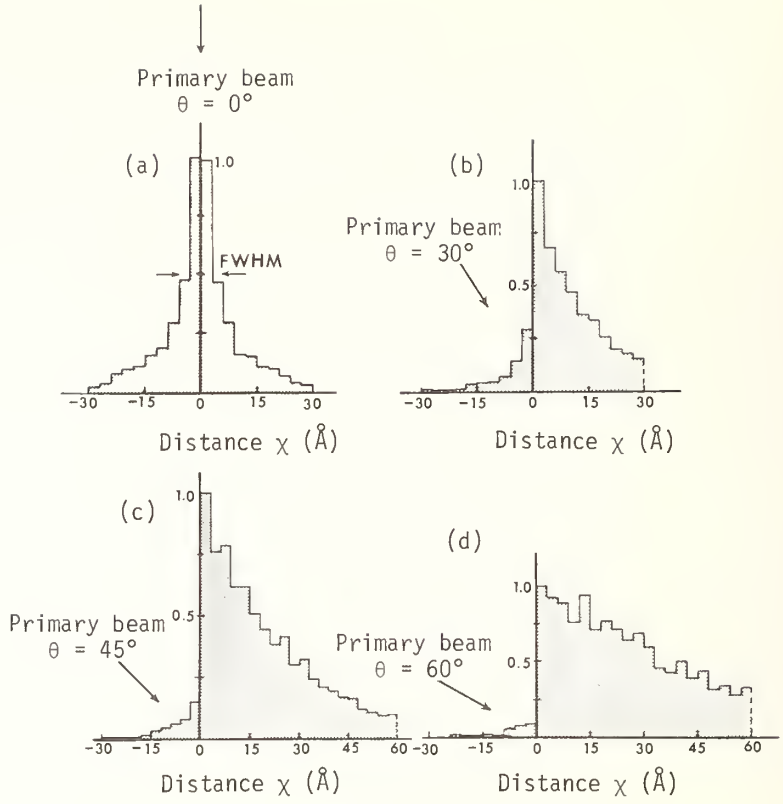

Figure 29. Lateral distribution of secondary electrons with a point beam at various incidence angles to the surface (Koshikawa and Shimizu [20]).

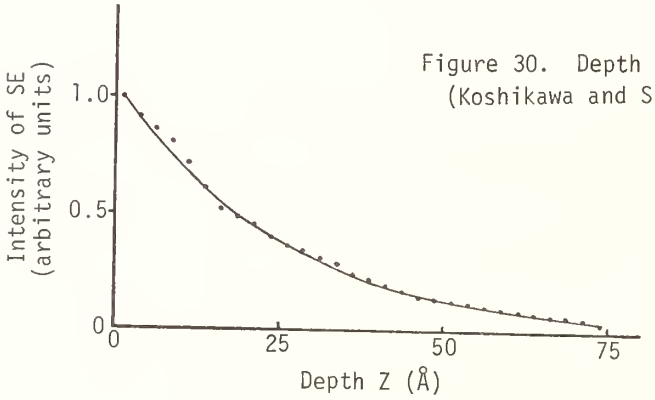

Figure 30. Depth distribution of secondary electrons (Koshikawa and Shimizu [20]).

Considering the emergence distance from the primary beam impact point and the depth origin of the secondary electrons, the authors obtained figure 32; a depth distribution strongly peaked near the surface occurs at the beam impact point. As the distance of emergence from the impact point is increased, the depth distribution becomes relatively flat.

Koshikawa and Shimizu also considered the excitation of characteristic Auger electrons, and a plot of the depth distribution for the copper MMM transition (E = 58 eV) is shown in figure 33. Virtually all of these electrons originate from less than 20 Å in depth since the energy loss processes rapidly cause deviation from the characteristic energy.

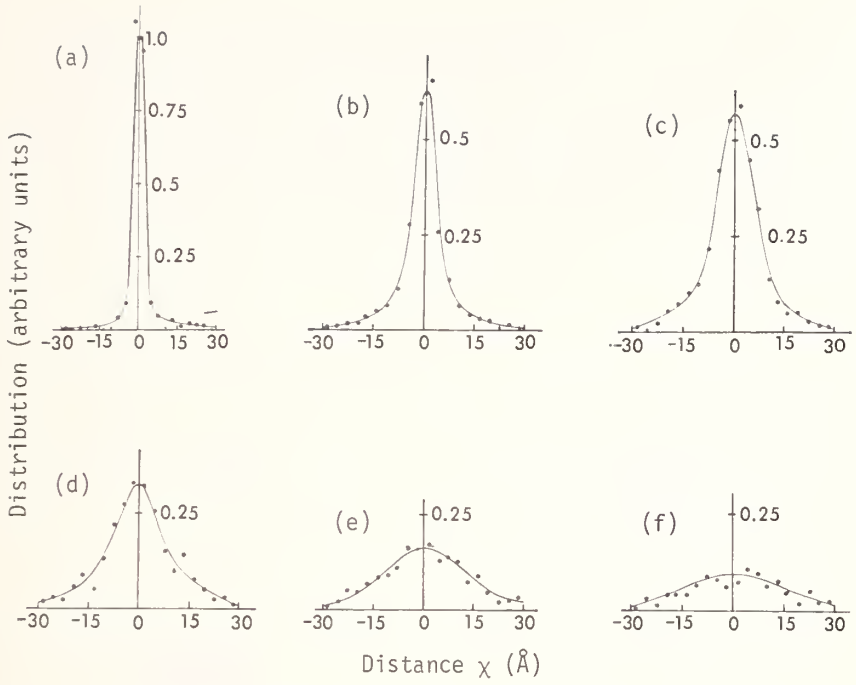

Figure 31. Lateral distribution of secondary electrons as a function of excitation depth below the surface. (a) 0-5 Å; (b) 5-10 Å; (c) 10-20 Å; (d) 20-30 Å; (e) 30-40 Å; (f) 40-50 Å (Koshikawa and Shimizu [20]).

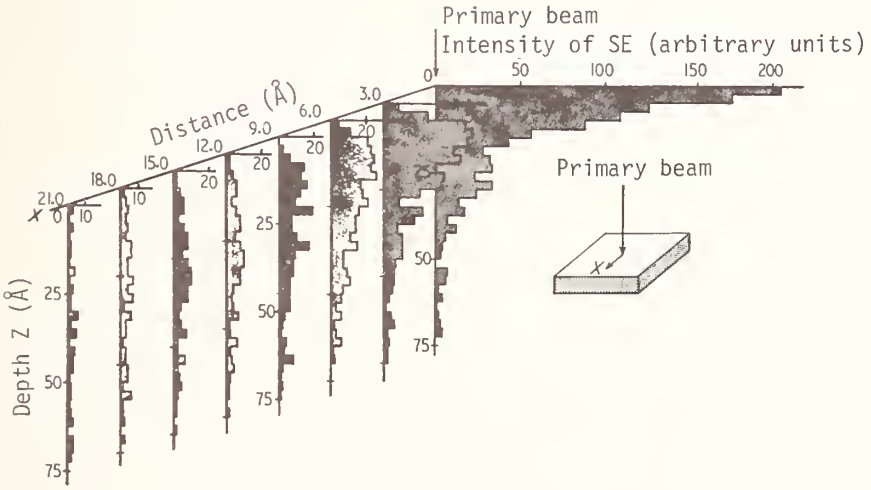

Figure 32. Depth distribution of secondary electrons as a function of position of emission relative to beam impact point (Koshikawa and Shimizu [20]).

Shimizu and Murata considered the contribution of secondary electron production by the exiting backscattered electrons [12]. Their results for the spatial distribution of emitted secondary electrons are shown in figure 34. The same sharp central peak is again observed, with the number of secondary electrons falling off rapidly with distance from the beam impact point. The contribution of backscattered electrons is found to be small, remaining relatively constant with distance from the beam impact point. Near the beam impact position,

the secondaries produced by backscattered appear to be insignificant. But, backscattered electrons can exit thousands of angstroms from the impact point; and, hence, the secondary electron intensity integrated over this emission area becomes very large.

Shimizu and Murata [12] calculated the emission of secondary electrons as a function of specimen tilt; the results yielded the behavior shown in figure 35. The Monte Carlo calculations follow most closely the experimental formula of Bruining [24]. The secant law usually assumed for tilt behavior underestimates the actual value significantly at tilt of 40°.

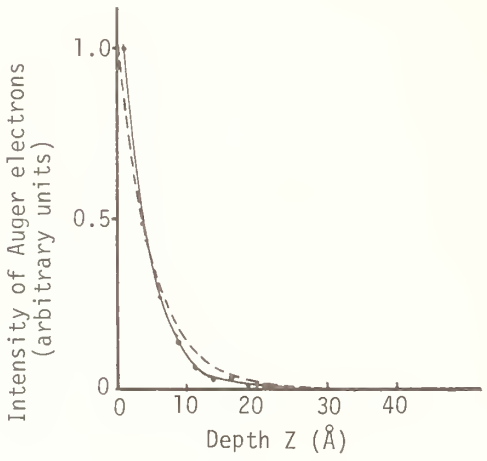

Figure 33. Depth distribution of copper MMM type Auger electrons (E = 58 eV) as calculated by Monte Carlo techniques; and exponential decay law is also shown (dashed line (Koshikawa and Shimizu [20]).

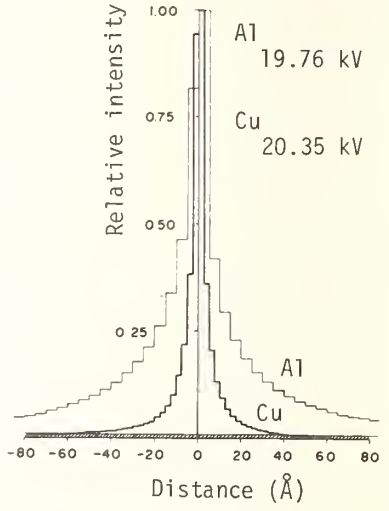

Figure 34. Laterial distribution of secondary electrons emitted from copper and aluminum; contribution of secondaries created by backscattered electrons for copper (hatched area) (Shimizu and Murata [12]).

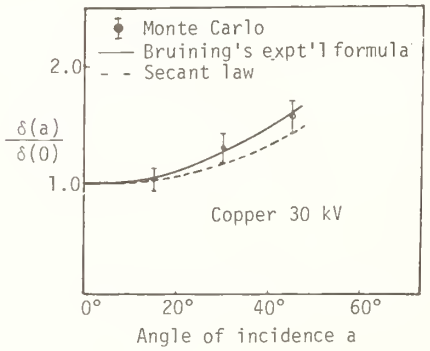

Figure 35. Emission of secondary electrons as a function of specimen tilt. An experimental formula of Bruining [24] and a secant dependence are also shown (Shimizu and Murata [12]).

5. Distribution of X-ray Signals by Monte Carlo Methods

The typical outputs of the Monte Carlo technique as applied to x-rays produced by electron-solid interactions are: (1) two-dimensional plots of the distribution of ionization in the solid, (2) the computation of the distribution in depth $\phi(z)$ of the x-rays generated by the primary electron beam, (3) the computation of the absorption correction factor $f(\chi)$ for x-ray microanalysis based on the $\phi(z)$ calculation, and (4) the distribution in depth of continuum x-radiation of a given energy. The major achievement is the ability to predict x-ray outputs from geometrical configurations which classical theory is not capable of handling.

Plots of the ionization distribution were first presented by Curgenven and Duncumb; some of their results are reproduced in figures 1-4. The method used was to compute the probability of an ionization at any location of the electron along its trajectory. If the Monte Carlo model indicated that an ionization should occur at that location, then a dot was plotted. This procedure was carried out for all electrons at all positions. The resulting plots give a qualitative idea of the x-ray distribution in the solid as a function of atomic number, Z, incident beam energy, E_0 (keV), and incident beam angle [1,25].

Bolon and Lifshin, and Bolon, et al., extended the work of Curgenven and Duncumb to include the effects of finite beam size and to analyze thin film specimens with and without substrates [26,27]. Again, the resulting plots yield a qualitative view of the processes taking place in the solid as shown in figures 36 and 37.

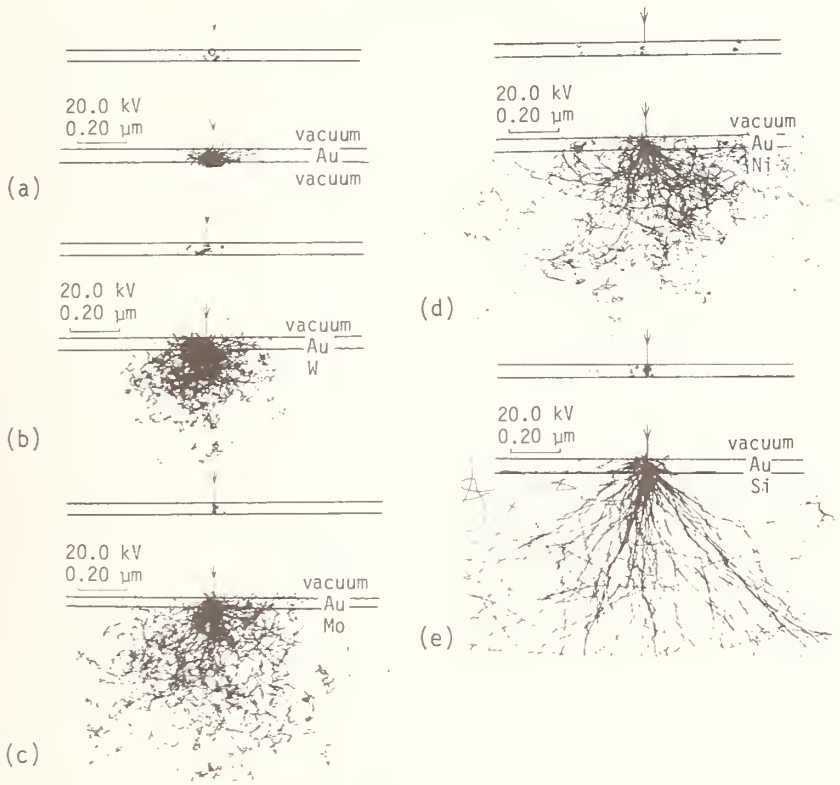

Figure 36. Monte Carlo calculated electron and x-ray distributions in 500 Å gold films on various substrates (Bolon, et al. [27]).

In addition to plotting the results of the ionization distribution, the Monte Carlo technique can be used to calculate the distribution in depth of the x-rays generated by the primary electron beam. Several papers have reported the results of such computations [2-6,8,9,12,15,16,21,28]. Typically, a plot of the parameter $\phi(z)$ against z, the mass thickness, is obtained. The parameter $\phi(z)$ represents the number of x-rays generated at depth z normalized by the number of x-rays which would be generated from a "free layer" of the specimen, i.e., a free standing layer of vanishingly small thickness [29]. A typical plot of $\phi(z)$ against z for normal electron beam incidence is shown in figure 38. The maximum in this function occurs because the lateral spread of electron paths increases the probability of ionization per unit of depth, and because some electrons scatter back toward the surface, producing ionizations along the path. If the incident beam angle is altered, the $\phi(z)$ plot against z changes; figure 39 shows the results of a Monte Carlo calculation for a copper target [25]. The peak of the distribution moves to lower z values as the electron backscatter coefficient increases; the peak is primarily dependent on this parameter.

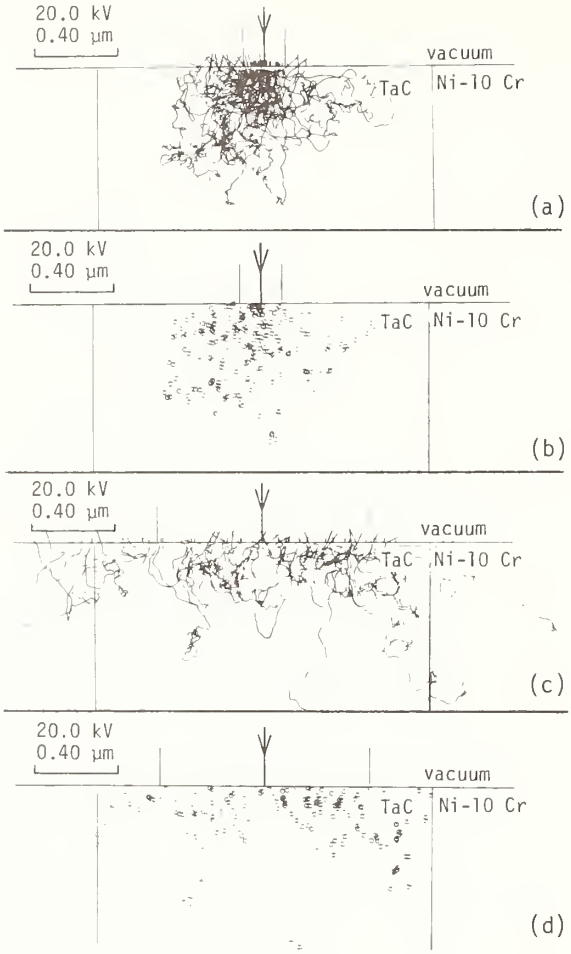

Figure 37. Simulated electron and x-ray distributions for: (a,b) focused (0.2 μm) electron beam and (c,d) defocused (1.0 μm) electron beam; TaMα x-radiation (Bolon, et al. [27]).

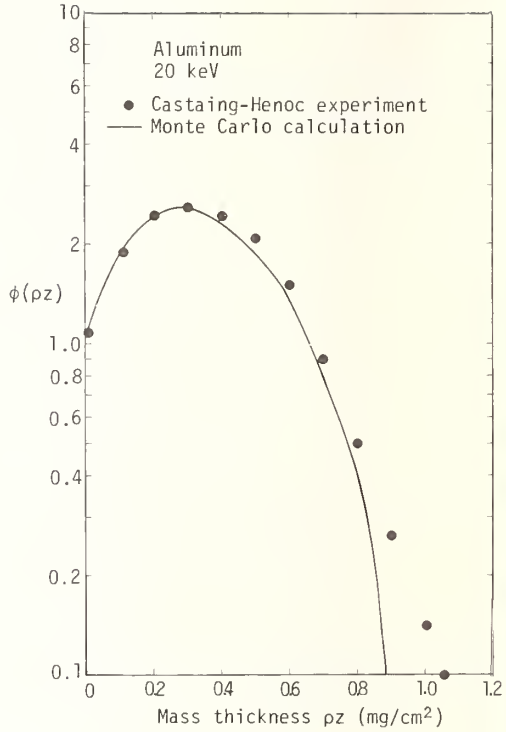

Figure 38. Distribution in depth of AlKα x-rays in Al matrix. Experimental data [32] are compared with Monte Carlo results calculated using the NBS program (this volume, p.). Note that mass thickness is indicated as ρz.

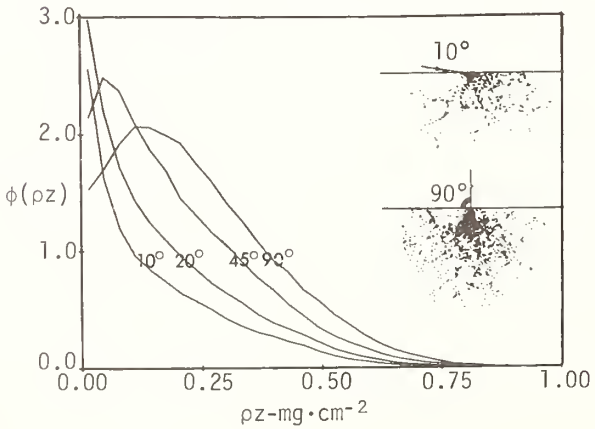

Figure 39. Variation of distribution in depth of CuK x-rays in Cu matrix, assuming E_0 = 20 keV, as a function of beam incidence angle (Duncumb [25]). Mass thickness is indicated as ρz.

The $\phi(z)$ function can be used to predict the absorption effect [29] and atomic number effect [29], thus facilitating quantitative x-ray microanalysis. The generated x-ray intensity is:

$$I_{GEN} = F(0) = \int_0^\infty \phi(z)dz \tag{1}$$

while the emitted intensity is

$$I'_{EMIT} = F(\chi) = \int_0^\infty e^{-\chi z}\phi(z)dz \tag{2}$$

where $\chi = \mu \csc\psi$, μ being the x-ray mass attenuation coefficient of the specimen for the monitored x-ray line, and ψ the average x-ray emergence angle from the specimen with respect to the detector. If the specimen has an average atomic number, Z*, while the standard has atomic number Z, then in the conventional ZAF notation [30]:

$$C = k\, k_Z\, k_A\, k_F \tag{3}$$

where C is the mass fraction, k is $I^{*\prime}_{EMIT}/I'_{EMIT}$, i.e., the measured intensity ratio of sample to standard, k_Z is the atomic number correction accounting for differences in electron backscatter and retardation between a sample of atomic number Z* and a standard of atomic number Z, k_A is the absorption correction factor accounting for differences in absorption of the x-ray line of interest along its path within the target for the specimen and standard, and k_F accounts for secondary emission (fluorescence) effects. The terms k_Z and k_A have been examined in great detail both experimentally and theoretically by many authors in an effort to obtain the most accurate quantitative analysis scheme possible as outlined in reference [30].

The definition of the primary absorption correction factor $f(\chi)$ (also designated f_p) is I_{EMIT}/I_{GEN}; i.e., from eqs. (1) and (2):

$$f(\chi) = F(\chi)/F(0). \tag{4}$$

For the specimen, likewise, $f^*(\chi) = F^*(\chi)/F^*(0)$ and

$$k_A = \frac{f(\chi)}{f^*(\chi)}\ . \tag{5}$$

The term k_Z in eq. (3) is defined as the ratio I_{GEN}/I^*_{GEN}, i.e., the ratio of primary beam x-rays generated in a target of atomic number Z, divided by those generated in target of atomic number Z*. Hence,

$$k_Z = \frac{1}{C} \cdot F(0)/F^*(0). \tag{6}$$

Therefore, the product

$$k_Z k_A = \frac{f(\chi)}{f^*(\chi)}\,\frac{F(0)}{F^*(0)}\,\frac{1}{C} = \frac{1}{C}\,\frac{F(\chi)}{F(0)} \cdot \frac{F^*(0)}{F^*(\chi)} \cdot \frac{F(0)}{F^*(0)} = \frac{1}{C}\,\frac{F(\chi)}{F^*(\chi)}\ . \tag{7}$$

The usefulness of the $\phi(z)$ distribution is now clear; with $\phi(z)$, one can obtain the number of photons generated by the primary beam, the terms k_Z and k_A, their product, and the absorption correction factor $f(\chi)$. Indeed, Castaing pointed this fact out in his thesis [29]. However, relatively few $\phi(z)$ distributions have been determined experimentally; the experiment is tedious, difficult, and experimental errors are potentially very large [31-33].

Therefore, the Monte Carlo method was seen as a means to obtain $\phi(z)$ distributions and, hence, all of the useful by-products for x-ray microanalysis. All of the $\phi(z)$ curves so calculated depend upon the specific Monte Carlo simulation model employed. Thus, while the $\phi(z)$ distributions can be calculated, the result is subject to all of the uncertainties in the model, e.g., scattering law, continuous slowing down approximation, etc. Crucial questions then, are how sensitive to model changes is the distribution and how well do calculated $\phi(z)$ distributions agree with experimental findings?

Reimer and Krefting have indicated that the calculated $\phi(z)$ distribution is not particularly sensitive to the scattering model selected nor is $\phi(z)$ greatly affected by fairly large changes in model input parameters [34]. The effect of using one or the other of two different mean ionization potentials to calculate $\phi(z)$ for Au-Mα is shown in figure 40. Hénoc and Maurice have indicated that electron straggling effects play only a minor role in altering the calculated $\phi(z)$ distribution [35].

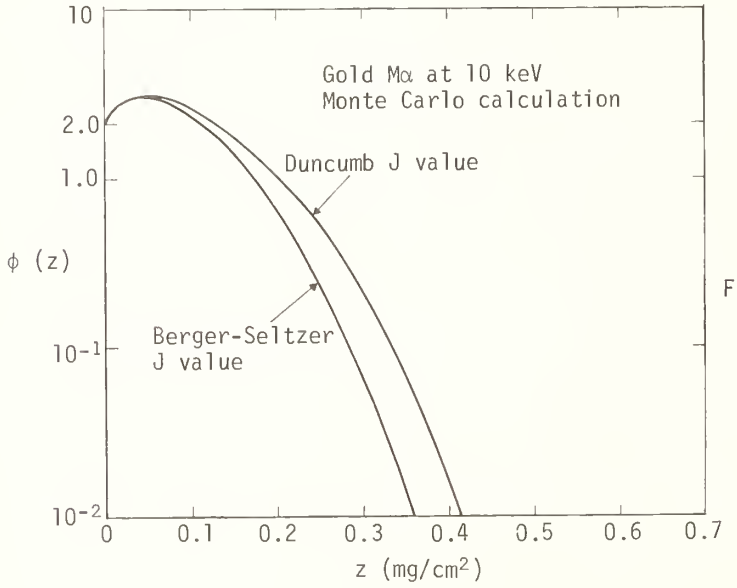

Figure 40. Variation of Monte Carlo calculated distribution in depth of AuMα x-rays in Au, assuming E_0 = 10 keV, as a function of mean ionization potential used for calculation.

Agreement of calculated $\phi(z)$ distributions with experimental results is fairly good, especially at low z values [3,5,6,15,28]. Hence, the Monte Carlo results for $\phi(z)$, $f(\chi)$, k_A, and k_Z are probably no worse than those derived by other methods. Indeed, Shimizu, et al. [16], used the Monte Carlo method for correcting raw data for quantitative x-ray microanalysis. The results were comparable to ZAF results for a variety of materials and experimental conditions.

So far as $f(\chi)$ vs χ curves derived from Monte Carlo methods are concerned, Duncumb compared Monte Carlo results for Cu-Kα with those calculated by the Philibert-Duncumb-Heinrich relation [25]; results are shown in figure 41. This figure indicates the effect of tilt on the result as well thus illustrating the potential value of the Monte Carlo method in dealing with a wide variety of experimental arrangements. Figure 42 shows $1/f(\chi)$ plotted against χ for Ta-Lα as calculated by Monte Carlo procedures, but using two sources for mean ionization potential [36,37] for comparison with Green's [38] experimental results. It is difficult to believe that, since the Monte Carlo $\phi(z)$ distribution is not greatly sensitive to model, but is affected by input parameters, significant improvement in conventional x-ray microanalysis will result from Monte Carlo calculations. However, intractable experimental arrangements can be attacked by means of the Monte Carlo method.

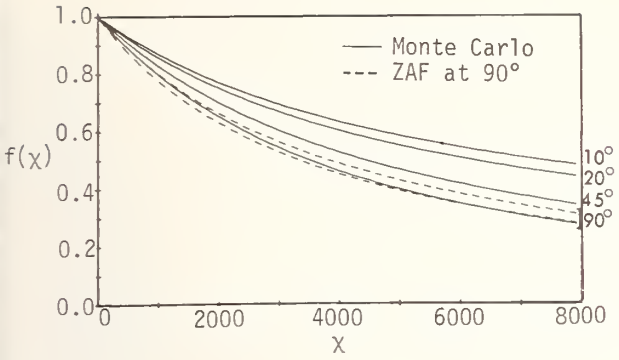

Figure 41. Variation Monte Carlo calculated absorption correction factor $f(\chi)$ vs. χ as a function of tilt (Duncumb [25]). The dashed lines indicate the effect of varying the mean ionization potential.

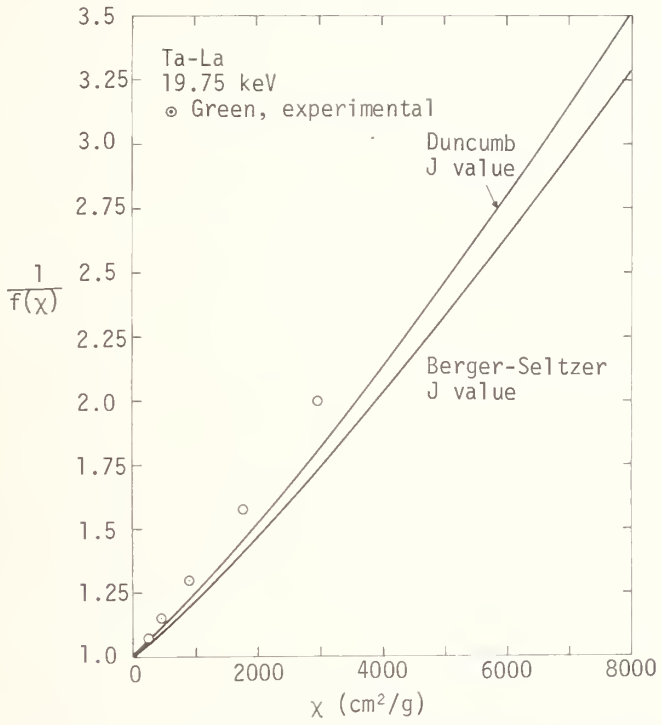

Figure 42. Monte Carlo calculated value of $1/f(\chi)$ vs. χ for TaLα using two values of mean ionization potential. Experimental results of Green [38] are shown as well.

Among these difficult specimen geometries is the case of a thin film on a substrate. Kyser and Murata have used Monte Carlo calculations to derive intensity against thickness curves for Si, Cu and Au on Al_2O_3 substrates for a wide variety of incident beam energies [9]. Agreement with experimental results was very good (fig. 43). Furthermore, these authors were able to quantitatively analyze binary thin films of Co-Pt and Mn-Bi on SiO_2 substrates; neither composition nor film thickness was known. The Monte Carlo method was used to establish calibration curves for several thicknesses as shown in figure 44; the final results were graphically interpolated from these curves and the measured intensities. Agreement with nuclear backscatter measurements was good [9].

Bolon and co-workers were able to measure Ta content in square TaC rods a few micrometers across in a directionally solidified TaC-NiCr eutectic alloy. Monte Carlo calculations agreed with experimental findings within a few percent. These authors also successfully investigated thin film specimens with the aid of Monte Carlo computations [26,27].

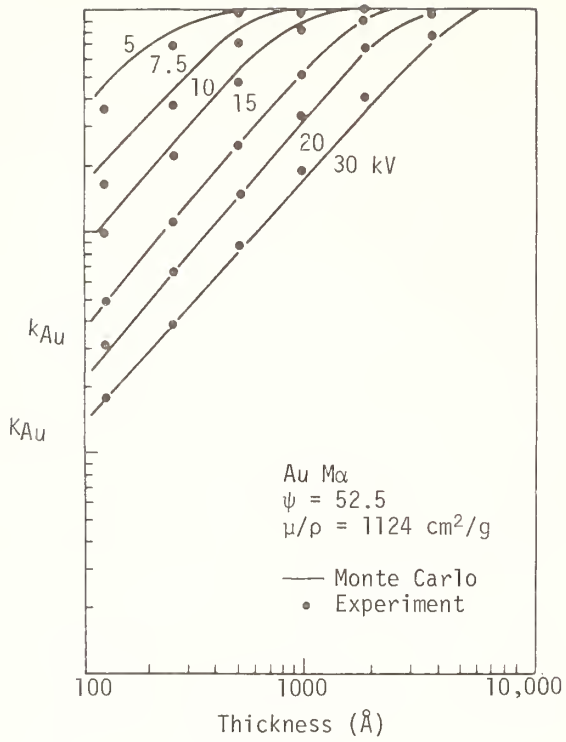

Figure 43. Monte Carlo intensity ratios as a function of thickness and incident beam energy for Au films on Al_2O_3 as compared with experimental results (Kyser and Murata [9]).

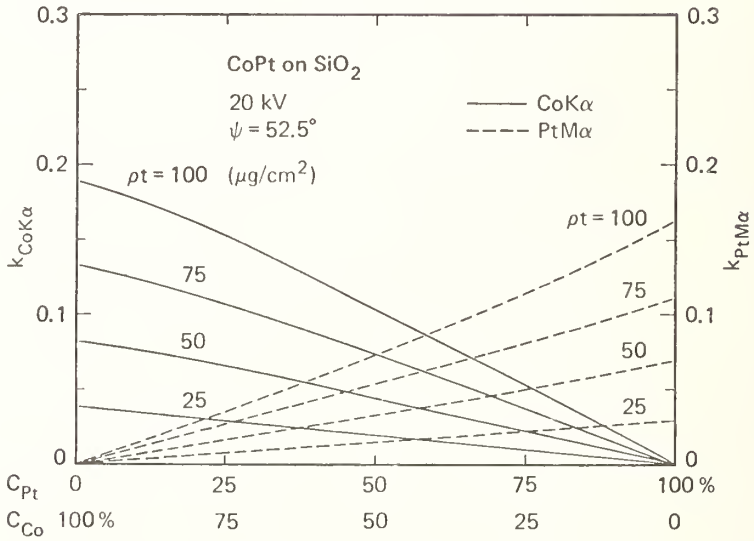

Figure 44. Monte Carlo calculated calibration curves for Co and Pt x-ray emission from thin films on SiO_2 substrate (Kyser and Murata [9]).

X-ray computations based on the Monte Carlo method have been made for spherical and cylindrical particles [3,4]. Results are in good agreement with experimental findings (fig. 45), thus indicating that the Monte Carlo method can be used to handle certain of the problems involved with particulate analysis.

Apparently, only one attempt to derive the distribution of continuum x-rays as a function of z by means of Monte Carlo methods has been carried out. Reed obtained this distri-

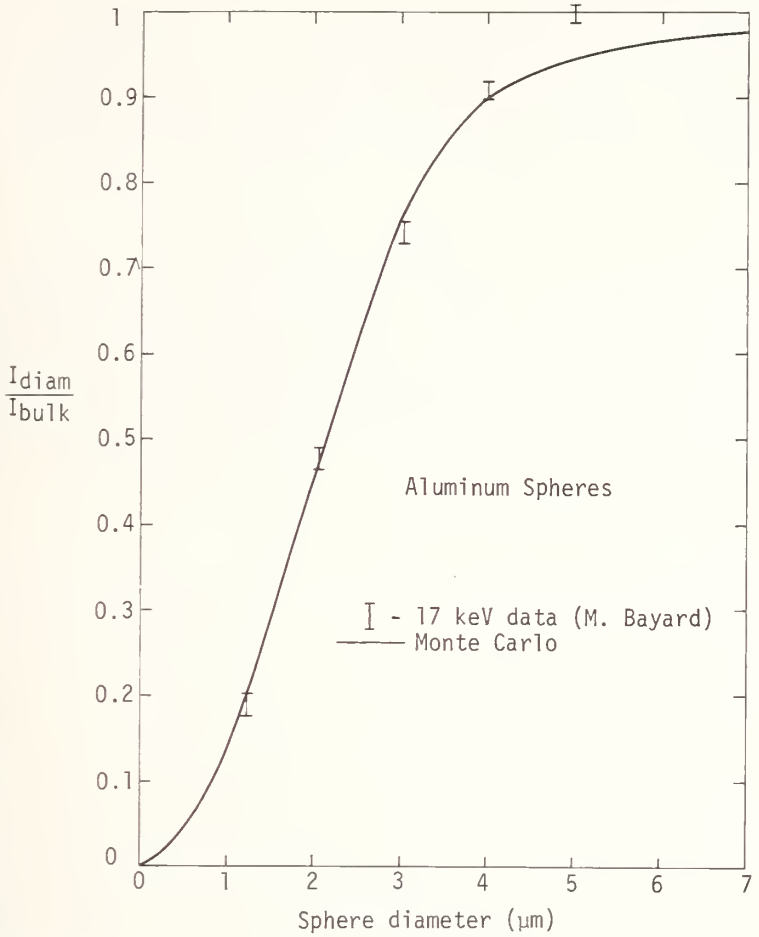

Figure 45. Comparison of Monte Carlo calculated intensity ratios from Al spheres with experimental findings of Bayard [43]. I_{bulk} is the intensity from pure, bulk aluminum. I_{diam} is the intensity from a sphere of a particular diameter.

bution for 8.04 keV continuum x-rays in a copper target assuming E_o = 29 keV [40]. The cross-section for continuum x-ray production was obtained from results reported by Kirkpatrick and Weidmann [39]. The Monte Carlo results were obtained from the work of Bishop [44]. The combination resulted in the distribution reproduced as figure 46. Apparently, the distribution of characteristic and continuum x-rays of like energy is similar--not an altogether surprising result.

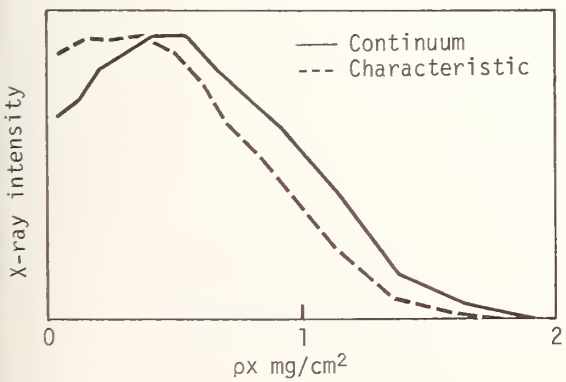

Figure 46. Distribution of 8.04 keV continuum and characteristic x-ray production with depth for Cu target, E_o = 29 keV (Reed [40]).

The study of the continuum distribution would be useful in studying background effects in energy dispersive x-ray detectors [41]. Monte Carlo calculations of this distribution might also be useful for analytical situations in which a small quantity of heavy material (high atomic number) resides in a light (low atomic number) matrix. In such cases, most of the observed x-ray intensity from the heavy component will be produced by continuum x-rays [42].

6. Summary

Monte Carlo electron trajectory calculations can be used to obtain diverse information about the distribution of signals in the SEM/EPMA. In the examples reviewed in this paper, the characteristics of the interaction volume, backscattered electrons, of secondary electrons, and of x-rays have been calculated. Where experimental measurements are available, the agreement between the Monte Carlo calculations and experimental values is generally very good. The Monte Carlo calculations can be carried out in many cases where experiments are difficult or intractable. Monte Carlo calculations provide a powerful tool for both the microscopist and the analyst.

References

[1] Curgenven, L. and Duncumb, P., *Simulation of Electron Trajectories in a Solid Target, by a Simple Monte Carlo Technique*, Report 303 (Tube Investments Research Laboratories, Saffron Walden, Essex, England, July 1971).

[2] Murata, K., *J.A.P.* 45, 4110 (1974).

[3] Myklebust, R. L., Yakowitz, H., Newbury, D. E., and Heinrich, K. F. J., this volume, p.

[4] Yakowitz, H., Newbury, D. E., and Myklebust, R. L., in *SEM/1975, Proceedings of the 8th Annual SEM Symposium*, O. Johari, ed., p. 93 (IITRI, Chicago, 1975).

[5] Krefting, E. R. and Reimer, L., in *Quantitative Analysis with Electron Microprobes and Secondary Ion Mass Spectrometry*, E. Preuss, ed., p. 114 (Kernforschungsanlage, Julich, 1973).

[6] Shinoda, G., Murata, K., and Shimizu, R., in *Quantitative Electron Probe Microanalysis*, K. F. J. Heinrich, ed., p. 155 (National Bureau of Standards Special Publication 298, Washington, D.C., 1968).

[7] Thomas, R. N., Ph.D. Thesis (Cambridge University, 1961).

[8] Shimizu, R., Ikuta, T., Everhart, T. E., and Devore, W. J., *J.A.P.* 46 (1975).

[9] Kyser, D. F. and Murata, K., *Monte Carlo Simulation of Electron Beam Scattering and Energy Loss in Thin Films on Thick Substrates*, IBM Research Report, RJ 1404 (June 1974).

[10] Everhart, T. E., Herzog, R. F., Chung, M. S., and DeVore, W. J., in *Proceedings Sixth International Conference on X-ray Optics and Microanalysis*, G. Shinoda, K. Kohra, and T. Ichinokawa, eds., p. 81 (University of Tokyo Press, 1972).

[11] Heinrich, K. F. J., in *X-ray Optics and Microanalysis*, R. Castaing, P. Deschamps, and J. Philibert, eds., p. 159 (Hermann, Paris, 1966).

[12] Shimizu, R. and Murata, K., *J.A.P.* 42, 387 (1971).

[13] Kanter, H., *Ann. Physik* 20, 144 (1957).

[14] Wells, O. C., in *Sem/1975, Proceedings Eighth Annual SEM Symposium*, O. Johari, ed., (IITRI, Chicago, 1975).

[15] Murata, K., Matsukawa, T., and Shimizu, R., *Jap. J.A.P.* 10, 678 (1971).

[16] Shimizu, R., Nishigori, N., and Murata, K., in *Proceedings Sixth International Conference on X-ray Optics and Microanalysis*, G. Shinoda, K. Kohra, and T. Ichinokawa, eds., p. 95 (University of Tokyo Press, Tokyo 1972).

[17] Shimizu, R., Ikuta, T., and Murata, K., *J.A.P.* 43, 4233 (1972).

[18] Bishop, H., *Brit. J.A.P.* 1, series 2, 673 (1968).

[19] Murata, K., in *SEM/1973, Proceedings Sixth Annual SEM Symposium*, O. Johari, ed., p. 268 (IITRI, Chicago, 1973).

[20] Koshikawa, T. and Shimizu, R., *J. Phys. D.: Appl. Phys.* 7, 1303 (1974).

[21] Streitwolf, H., *Ann. Phys. Lpz.* 3, 189 (1959).

[22] Kanter, H., *Phys. Rev.* B1, 522 (1970).

[23] Palmberg, P., *Anal. Chem.* 45, 549A (1973).

[24] Bruining, H., *Physica* 3, 1046 (1936).

[25] Duncumb, P., in *Electron Microscopy and Analysis*, W. C. Nixon, ed., Conf. Series 10, p. 132 (Inst. Phys., London, 1971).

[26] Bolon, R. B. and Lifshin, E., in *SEM/73, Proceedings Sixth Annual SEM Symposium*, O. Johari, ed., p. 285 (IITRI, Chicago, 1973).

[27] Bolon, R. B., Lifshin, E., and Ciccarelli, M. F., in *Practical Scanning Electron Microscopy*, J. I. Goldstein and H. Yakowitz, eds., p. 299 (Plenum Press, New York, 1975).

[28] Hénoc, J. and Maurice, F., in *Proceedings Sixth International Conference of X-ray Optics and Microanalysis*, G. Shinoda, K. Kohra, and T. Ichinokawa, eds., p. 113 (University of Tokyo Press, Tokyo 1972).

[29] Castaing, R., Ph.D. Thesis, University of Paris (1951).

[30] Yakowitz, H., in *Practical Scanning Electron Microscopy*, J. I. Goldstein, and H. Yakowitz, eds., p. 327 (Plenum Press, New York, 1975).

[31] Castaing, R. and Deschamps, J., *J. Phys. Radium*, 16, 304 (1955).

[32] Castaing, R. and Hénoc, J., in *Proceedings Fourth International Congress on X-ray Optics and Microanalysis*, R. Castaing, P. Deschamps, and J. Philibert, eds., p. 120 (Hermann, Paris, 1966).

[33] Brown, J. D. and Parobek, L., in *Proceedings Sixth International Conference on X-ray Optics and Microanalysis*, G. Shinoda, K. Kohra, and T. Ichinokawa, eds. p. 163 (University of Tokyo Press, Tokyo 1972).

[34] Reimer, L. and Krefting, R., this volume, p. .

[35] Hénoc, J. and Maurice, F., this volume, p. .

[36] Duncumb, P. and Reed, S. J. B., in *Quantitative Electron Probe Microanalysis*, K. J. Heinrich, ed., p. 133 (National Bureau of Standards Special Publication 298, Washington, D.C., 1968).

[37] Berger, M. J. and Seltzer, S. M., *Natl. Acad. Sci., Natl. Res. Council Publ. 1133*, 205 (Washington, D.C., 1964).

[38] Green, M., Ph.D. Thesis, University of Cambridge (1962).

[39] Kirkpatrick, P. and Wiedmann, L., *Phys. Rev.* 67, 321 (1945).

[40] Reed, S. J. B., *X-ray Spectrometry* 4, 14 (1975).

[41] Fiori, C. E., Myklebust, R. L., Heinrich, K. F. J., and Yakowitz, H., *Anal. Chem.* 48, 172 (1976).

[42] Myklebust, R. L., Yakowitz, H., and Heinrich, K. F. J., *Proceedings Fifth National Conference MAS,* paper No. 11 (New York, 1970).

[43] Bayard, M., in *Microprobe Analysis,* C. A. Andersen, ed., p. 323 (Wiley, New York, 1973).

[44] Bishop, H. E., *Proc. Phys. Soc.* 85, 855 (1965).

National Bureau of Standards Special Publication 460. Proceedings of a Workshop on the Use of Monte Carlo Calculations in Electron Probe Microanalysis and Scanning Electron Microscopy held at NBS, Gaithersburg, Maryland, October 1-3, 1975. Issued December 1976.

THE EFFECT OF SCATTERING MODELS ON THE RESULTS OF MONTE CARLO CALCULATIONS

L. Reimer and E. R. Krefting

Physikalisches Institut
Universität Münster, Germany

A special Monte Carlo model is presented considered Mott scattering for scattering angles $\zeta>10°$, a mean angular deviation caused by multiple scattering for $\zeta<10°$, individual inelastic scattering events with energy loss $\Delta E>200$ eV and a continuous energy loss for $\Delta E<200$ eV. Results of the Monte Carlo calculations are compared with experimental results of the backscattering coefficient, the angular and energy distribution of backscattered electrons and the transmission of thin films. Some calculations of the depth distribution of x-ray emission are reported. Parts of the program are changed to see which parts of the model influence the results.

Key Words: Monte Carlo electron trajectory simulation; scanning electron microscopy; electron probe microanalysis; electron-specimen interactions; electron microscopy; x-ray generation.

1. Introduction

The results of Monte Carlo calculations (MC) depend on the model used. It is not possible to consider all collisions individually, especially the inelastic ones, because this increases the computation time. One has to use approximations, for example, a Bethe law, for the energy loss along the electron trajectories.

Our complete model consists of the following parts:

(1) use of single elastic collisions with the exact Mott scattering cross-sections for large angle scattering ($\zeta > 10°$) instead of the Rutherford cross-sections;

(2) treatment of small angle scattering ($\zeta < 10°$) by a mean angular deviation of the electron trajectory with a formula of Lewis for multiple scattering;

(3) taking into account single inelastic electron-electron collisions and the generated fast secondary electrons (FSE) with energies larger than 200 eV, using a formula of Gryzinski; and

(4) use of continuous energy loss along the electron trajectory by the Bethe formula, subtracting the energy losses caused by the single inelastic collisions considered in (3).

If one wants to calculate the backscattering coefficient, η, of bulk material at normal incidence, the result is rather insensitive to the model. One obtains, for example, reasonable values if only Rutherford scattering at angles $\zeta > 10°$ and a continuous energy loss by the Bethe formula are used [1][1]. But if one tries to get agreement between MC and experiments for the increase of η with increasing film thickness or the energy and angular distribution of backscattered electrons, one obtains systematic deviations. In Section 6, we report calculations omitting or changing some of the above-mentioned parts of the program and how such omissions influence some results.

[1]Figures in brackets indicate the literature references at the end of this paper.

2. Single and Multiple Scattering Data

2.1 Single cross-sections for scattering angles $\zeta > 10°$

Figure 1 demonstrates the relative differences if Mott cross-sections $(d\sigma/d\Omega)_M$ calculated by Bühring [2], Badde, et al., [3], and Reimer, et al. [4], are used instead of Rutherford cross-sections $(d\sigma/d\Omega)_R$. These cross-sections were verified in experiments on Hg

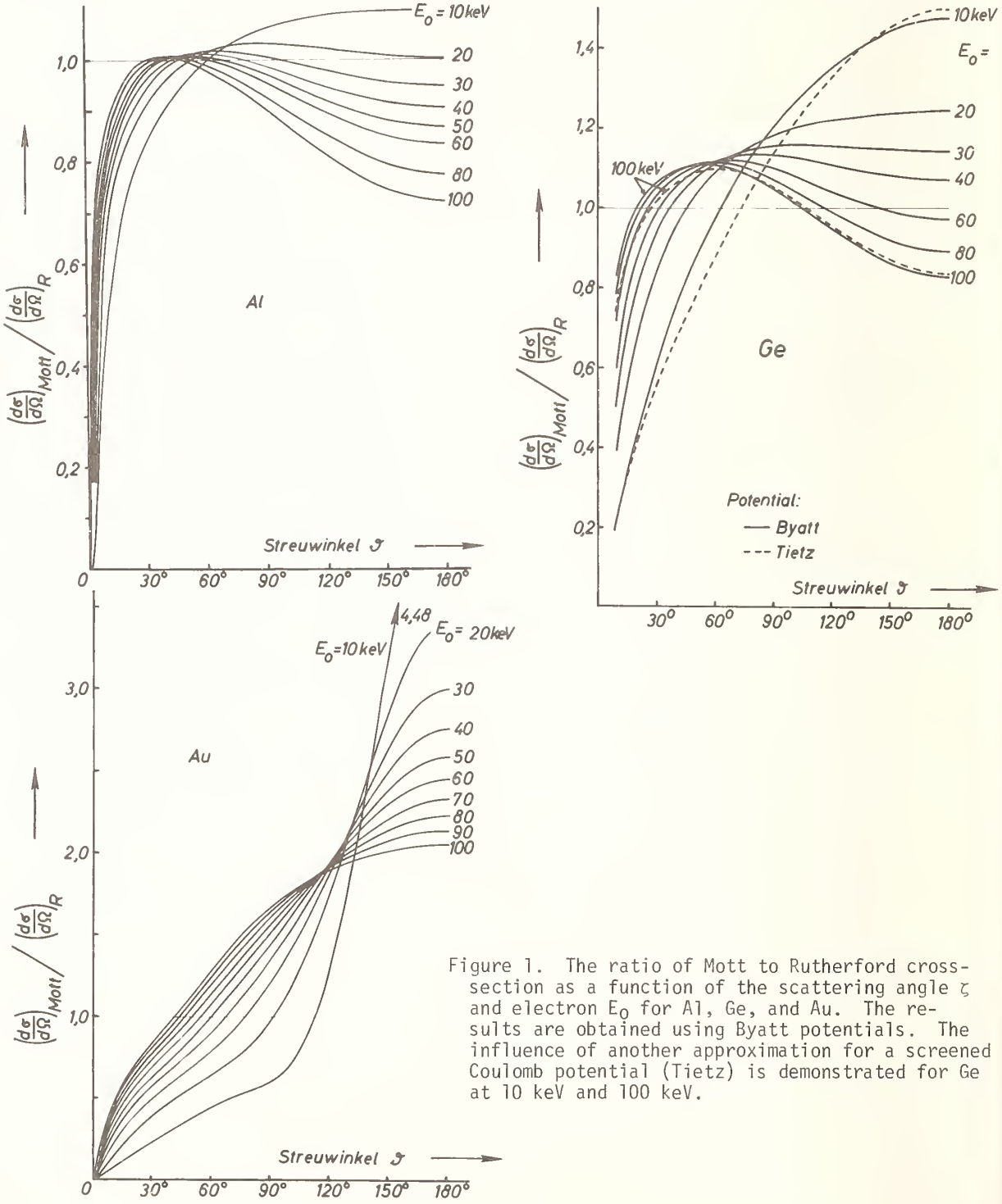

Figure 1. The ratio of Mott to Rutherford cross-section as a function of the scattering angle ζ and electron E_0 for Al, Ge, and Au. The results are obtained using Byatt potentials. The influence of another approximation for a screened Coulomb potential (Tietz) is demonstrated for Ge at 10 keV and 100 keV.

vapor (40-200 keV) by Kessler and Weichert [5]. Because of the rapid decrease, proportional to $1/\sin^4 \zeta/2$, of the Rutherford cross-section, the results are represented as a ratio of $(d\sigma/d\Omega)_M/(d\sigma/d\Omega)_R$. The relativistic Rutherford cross-section is

$$\left(\frac{d\sigma}{d\Omega}\right)_R = \frac{Z^2 e^4}{(8\pi\varepsilon_o)^2 E_o^2} \left(\frac{E_o + m_o c^2}{E_o + 2m_o c^2}\right)^2 \frac{1}{\sin^4 \zeta/2} \quad . \tag{1}$$

Values of $d\sigma/d\Omega$ for scattering angles $\zeta < 10°$ are strongly influenced by the screening of the Coulomb potential of the nucleus; these have been determined by WKB calculations [6]. In addition to this influence of screening at low scattering angles, deviations occur at large scattering angles increasing with increasing atomic number Z. The screening is expressed by exponential terms in the Coulomb potential [7]. Figure 1 for Ge shows no large deviations (dotted lines) if the screening parameters proposed by Tietz [8] are used.

One needs the total cross-section

$$\sigma_{el} = \int_{10°}^{\pi} \left(\frac{d\sigma}{d\Omega}\right)_M \cdot 2\pi \sin \zeta d\zeta \tag{2}$$

for the calculation of the free path, s, between collisions. These collisions with scattering angles $\zeta > 10°$ were calculated individually. They represent a fraction of about 10 percent of all elastic collisions.

2.2 Small angle elastic scattering

We used a mean scattering angle for collisions with scattering angles $\zeta < 10°$. The mean value $\langle \cos \zeta \rangle$ which depends upon the free electron path, s, was calculated by means of a formula of Lewis [9]

$$\langle \cos\zeta \rangle = \exp\left[-\int_o^s 2\pi N \left(\int_o^{10°} \frac{d\sigma}{d\Omega} (1-\cos \zeta)\sin \zeta d\zeta\right) ds\right] \tag{3}$$

with N = number of atoms per mass thickness (s in $g \cdot cm^{-2}$).

2.3 Single inelastic scattering

Electron-electron collisions cause scattering as well as energy losses, W. We considered all inelastic collisions as single events resulting in an energy loss W larger than a limit W_{min}

$$W > W_{min} = E_{nl} + 200 \text{ eV} \tag{4}$$

(E_{nl} = ionization energy of an atomic shell with quantum numbers n,l). This means that the generated fast secondary electrons (FSE) reach at least a kinetic energy $E_{kin} > 200$ eV. We used the semi-empirical formula of Gryzinski [10]

$$\frac{d\sigma}{dW} = \frac{e^4 E_{nl}}{W^3 E} \left(\frac{E}{E+E_{nl}}\right)^{3/2} \left(1 - \frac{W}{E}\right)^{E_{nl}/E_{nl}+W} \left[\frac{W}{E_{nl}} \left(1 - \frac{E_{nl}}{E}\right) + \frac{4}{3} \ln\left(2.7 + \left(\frac{E-W}{E_{nl}}\right)^{1/2}\right)\right] \tag{5}$$

for the differential cross-section as a good approximation for nonrelativistic energies. One obtains for the classical collision between two free nonrelativistic electrons

$$\frac{d\sigma}{dW} = \frac{\pi e^4}{EW^2} \tag{6}$$

and the incident electron is then scattered through an angle

$$\sin^2 \zeta = \frac{W}{E} \quad . \tag{7}$$

The classical formula (6) for large W is a good approximation to formula (5) of Gryzinski for large W. We therefore used eq. (7) for calculating the scattering angle.

The FSE with $E_{kin} > 200$ eV can contribute to electron backscattering, the transmission of electrons through thin films and K-shell ionization. We treated the diffusion of such FSE in the solid by means of a simplified model: the FSE are assumed to be emitted isotropically and to penetrate in a straight line up to a ζ range r from their origin (point P) of generation. If a sphere of radius r around P is drawn, all those electrons lying on the area F of the sphere outside the specimen will leave the specimen and the probability of escape is

$$w = F/4\pi r^2 = \begin{cases} (r-z)/2r & \text{for } z < r \\ 0 & \text{for } z > r \end{cases} . \tag{8}$$

The range r is calculated by the empirical formula [11]:

$$r = a\, E^b (\mu g \cdot cm^{-2}) \text{ with } a = 10,\ b = 1.43 \text{ (E in keV)}. \tag{9}$$

2.4 Continuous energy losses

Bethe [12] obtained the formula

$$\left(\frac{dE}{ds}\right)_{Bethe} = \frac{N_L \pi e^4}{AE} \sum_{n,l} f_{nl} \ln \left(\frac{E}{E_{nl}}\right)^2 \tag{10}$$

for the energy loss per unit path length. We used this formula with the approximation $f_{nl} = Z_{nl}$ for the oscillator strength f_{nl}. A portion of the inelastic collisions was however considered in 2.3:

$$\left(\frac{dE}{ds}\right)_{single} = \frac{N_L}{A} \sum_{n,l} Z_{nl} \int_{W_{min}}^{E} W \frac{d\sigma}{dW}\, dW. \tag{11}$$

Therefore, only

$$\frac{dE}{ds} = \left(\frac{dE}{ds}\right)_{Bethe} - \left(\frac{dE}{ds}\right)_{single} \tag{12}$$

is used as a continuous decrease of energy proportional to the mean free path, s, between the two single collisions considered (elastic or inelastic). The energy loss by single inelastic collisions is of the order of 50% of the whole energy loss. We included no further angular deviation by this kind of inelastic scattering because the inelastically scattered electrons having small energy losses are concentrated at very small scattering angles.

3. The Organization of the Program

In the MC, one obtains a free path s, scattering angle ζ, azimuth angle ψ, or energy loss W by means of a random number $0 < R < 1$. If n(x) is the probability distribution (x = s, ζ, ψ, or W) the following relationship exists:

$$R = \int_0^x n(x)dx \quad \int_0^\infty n(x)dx. \tag{13}$$

The free path, s, between two collisions, for example, is obtained from the total cross-section

$$\sigma_t = \sigma_{el} + \sigma_{inel}. \tag{14}$$

and $\exp[-N\sigma_t s]$ is the probability that the electron experiences no collisions along the path s. The probability that s has values between s and s + ds is therefore

$$n(s)ds = -N\sigma_t \exp[-N\sigma_t s]ds \tag{15}$$

and (13) becomes

$$R = 1 - \exp[-N\sigma_t s]. \tag{16}$$

Since R' = 1 - R is also a random number, solving for s gives

$$s = \frac{-\ln R'}{N\sigma_t}. \tag{17}$$

In the case of the azimuth angle ψ, one gets the simple relation

$$\psi = 2\pi R. \tag{18}$$

Analogous equations are obtained for ζ and W, respectively, by using the expressions $(d\sigma/d\Omega)_R$ or (5) for $n(\zeta)$ and n(W). Solving for ζ or W can only be done by numerical methods.

Figure 2 shows the flow chart of a MC program for the calculation of the backscattering coefficient η and the transmission τ in terms of film thickness z and angle of incidence ζ_0. The calculation starts at the target surface with the initial conditions x,y,z = 0, $E = E_0$ and $\zeta,\psi = 0$. The electron has the position $\vec{r}_n = (x_n,y_n,z_n)$ at the n^{th} collision and the direction (ζ_n, ψ_n) after this collision, and a free path s is calculated by eq. (17). The new position $\vec{r}_{n+1} = (x_{n+1},y_{n+1},z_{n+1})$ of the electron following collision is

$$\begin{aligned} x_{n+1} &= x_n + s \sin\zeta_n \cos\psi_n \\ y_{n+1} &= y_n + s \sin\zeta_n \sin\psi_n \\ z_{n+1} &= z_n + s \cos\zeta_n. \end{aligned} \tag{19}$$

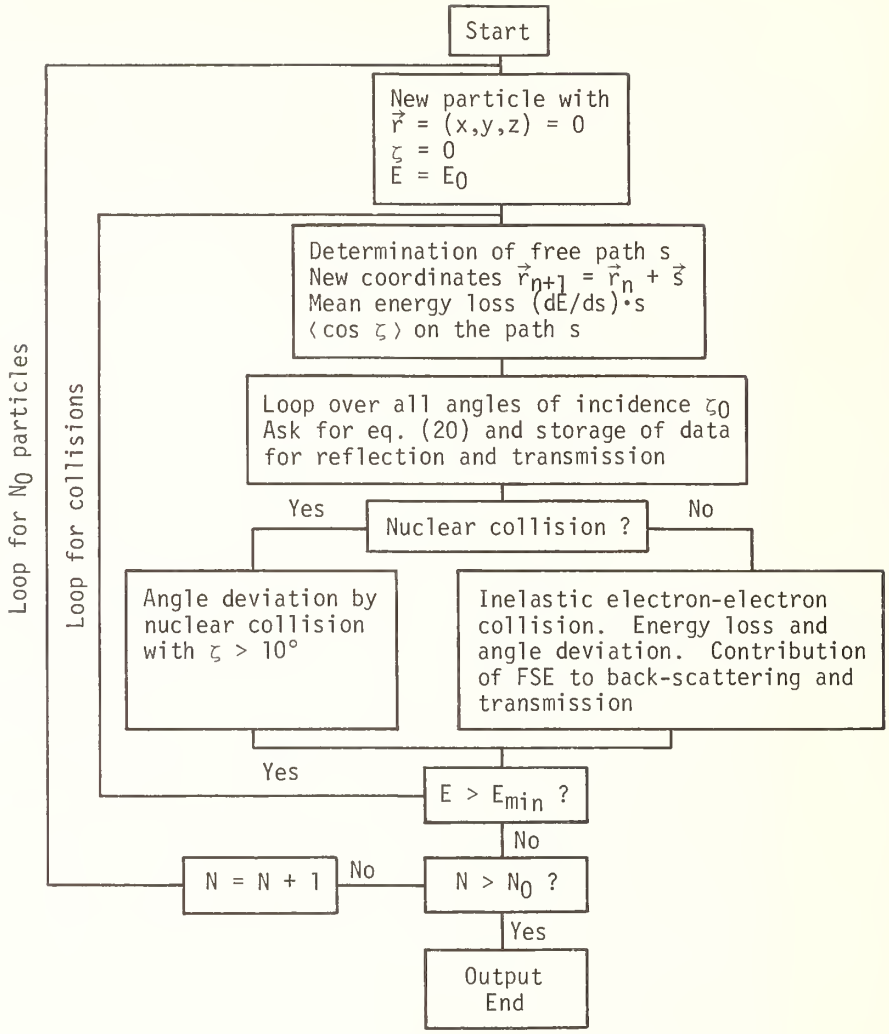

Figure 2. Monte Carlo Program.

Then ⟨ cos ζ ⟩ on the free path s caused by collisions with ζ < 10 is calculated by eq. (3) and (ζ,ψ) are changed for this small angle contribution. The mean energy loss (dE/ds)·s on the free path s (eq. (12)) is subtracted from E. Then interrogation for penetration through different thicknesses z* or for backscattering follows:

$$z_{n+1} \cos \zeta_0 - x_{n+1} \sin \zeta_0 \quad \begin{cases} > z^* : & \text{transmission} \\ < 0 : & \text{backscattering} \end{cases} \tag{20}$$

(ζ_0 = angle of incidence; ζ_0 = 0: normal incidence). If this is the case, the desired parameters such as energy, exit position or angle, are stored.

A further random number, R, selects either a nuclear collision (ζ > 10°) or an inelastic electron-electron collision:

$$\frac{\sigma_{el}}{\sigma_{el} + \sigma_{inel}} \quad \begin{cases} < R: & \text{nuclear collision} \\ > R: & \text{electron-electron collision.} \end{cases} \tag{21}$$

In the case of a nuclear collision, a scattering angle ζ is determined by a random number R. ζ-values are stored for 1000 R-values in 10 keV intervals of energy values E. This high number--1000--is the minimum required to obtain enough scattering angles in the interval $\zeta > 90°$. For R-values near 1, there must be a more dense distribution of $\zeta(R)$. An azimuthal angle ψ is obtained from eq. (18) and the sine and cosine of the new directions $(\zeta_{n+1}, \psi_{n+1})$ are calculated by

$$\begin{aligned} \cos \zeta_{n+1} &= \cos \zeta_n \cos \zeta - \sin \zeta \cos \psi \sin \zeta_n \\ \sin \zeta_{n+1} &= (1 - \cos^2 \zeta_{n+1})^{1/2} \\ \cos \psi_{n+1} &= [\cos \psi_n (\sin \zeta \cos \psi \cos \zeta_n + \cos \zeta \sin \zeta_n) \\ &\quad - \sin \psi_n \sin \zeta \sin \psi]/\sin \zeta_{n+1} \\ \sin \psi_{n+1} &= [\sin \psi_n (\sin \zeta \cos \psi \cos \zeta_n + \cos \zeta \sin \zeta_n) \\ &\quad + \cos \psi_n \sin \zeta \sin \psi]/\sin \zeta_{n+1}. \end{aligned} \tag{22}$$

In the case of an electron-electron collision the first random number determines the ionized shell; the second one, the energy loss W and the scattering angle ζ by eqs. (5) and (7); with an azimuth angle ψ, one obtains a new direction $(\zeta_{n+1}, \psi_{n+1})$ analogously to (22).

The kinetic energy E_{kin} of the generated FSE is

$$E_{kin} = W - E_{n1}. \tag{23}$$

The range r follows from eq. (9), and using the probability w of eq. (8), a contribution to backscattering or transmission is obtained.

If the remaining energy of the electron is large enough ($E > E_{min}$), the calculation will be continued with the next collision; otherwise, the contribution of this primary electron to backscattering, transmission and ionization of an atomic shell is treated like a FSE. Usually, the energy E_{min} is 0.25 E_o.

4. Results of the Monte Carlo Calculations and Comparison with Experiments on Backscattering and Transmission

A few examples will be shown to demonstrate the agreement between experiments and MC calculations for Al and Au as typical representatives for materials with low and high atomic numbers.

4.1 Backscattering of films at normal incidence

If we assume single scattering only, the backscattering coefficient of very thin films due to single collisions with scattering angles $\zeta > \pi/2$ is:

$$\eta = \frac{N_L z}{A} \int_{\pi/2}^{\pi} \frac{d\sigma}{d\Omega} 2\pi \sin\zeta \, d\zeta. \tag{24}$$

Values calculated with eq. (24) and experimental values of the initial slope $d\eta/dz$ are listed in table 1, which shows that the experimental values are much larger. Therefore, one must consider multiple scattering even in very thin films.

Table 1. Values of $d\eta/dz$ for very thin films of Au (E_0=40 keV)

Single scattering calculated with (24):	$d\eta/dz$ ($g^{-1} \cdot cm^2$)
Rutherford, non-relativistic	195
Rutherford, relativistic	210
Mott cross-sections	380
Experiments:	
Niedrig and Sieber [13]	465
Seidel [14]	560
Drescher [15]	520

Figures 3a and b show MC calculations and experimental results for relatively thin films of Al and Au at E_0 = 40 kev and normal incidence ($\cos \zeta_0 = 1$). The use of Mott scattering cross-sections alone cannot explain the increase of η with increasing film thickness z. One gets much better agreement if the generated fast secondary electrons (FSE) are also considered. There remains a constant difference between MC and experimental values, which is nearly independent of film thickness. Therefore, we assume that this difference is caused by FSE with energies between 50 and 200 eV, because only secondary electrons with E < 50 eV are suppressed in the retarding field experiment.

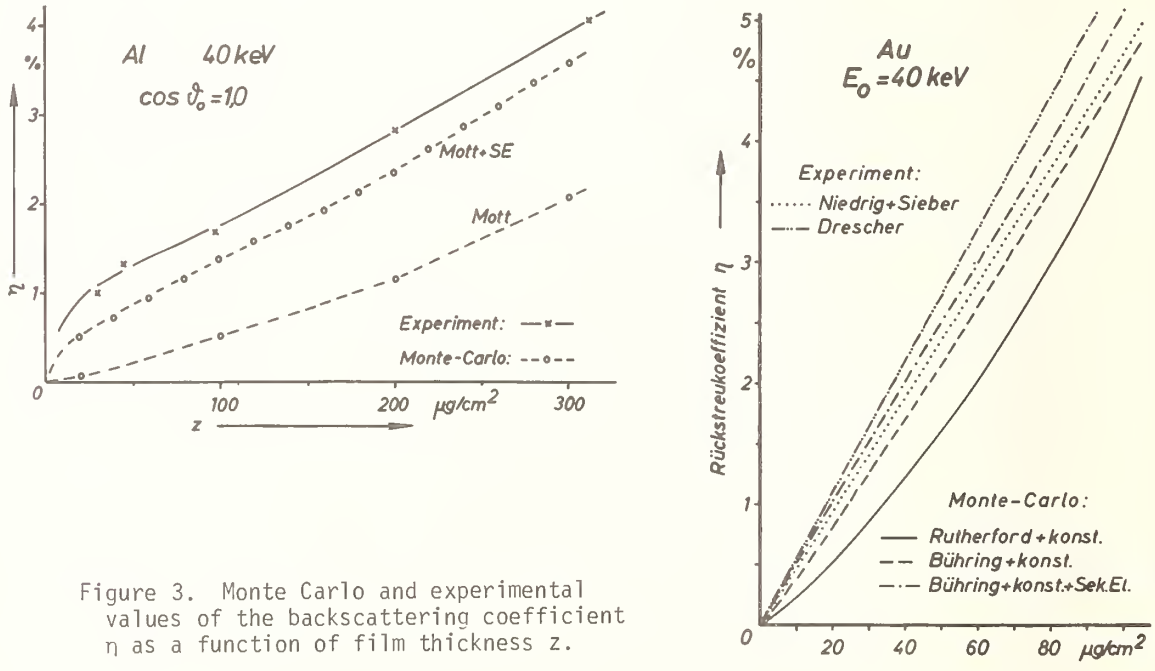

Figure 3. Monte Carlo and experimental values of the backscattering coefficient η as a function of film thickness z.

Figures 4a and b show the calculated values and experimental data obtained for greater thicknesses. The indicated values in percent are added to the MC values to give a best fit to the experimental data. The need for this adjustment is attributed to the FSE with E = 50-200 eV. Figure 4 shows three curves for comparison for Au at 40 keV: (a) a straight line obtained with eq. (24) using relativistic Rutherford cross-sections; (b) MC calculations with Rutherford cross-sections for $\zeta > 10°$; and (c) calculations using Mott cross-sections.

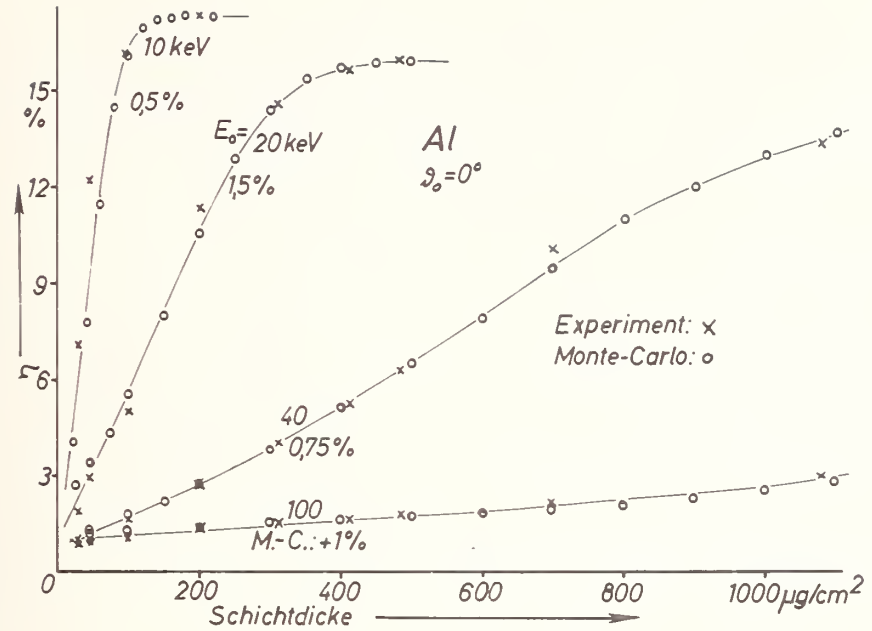

(a)

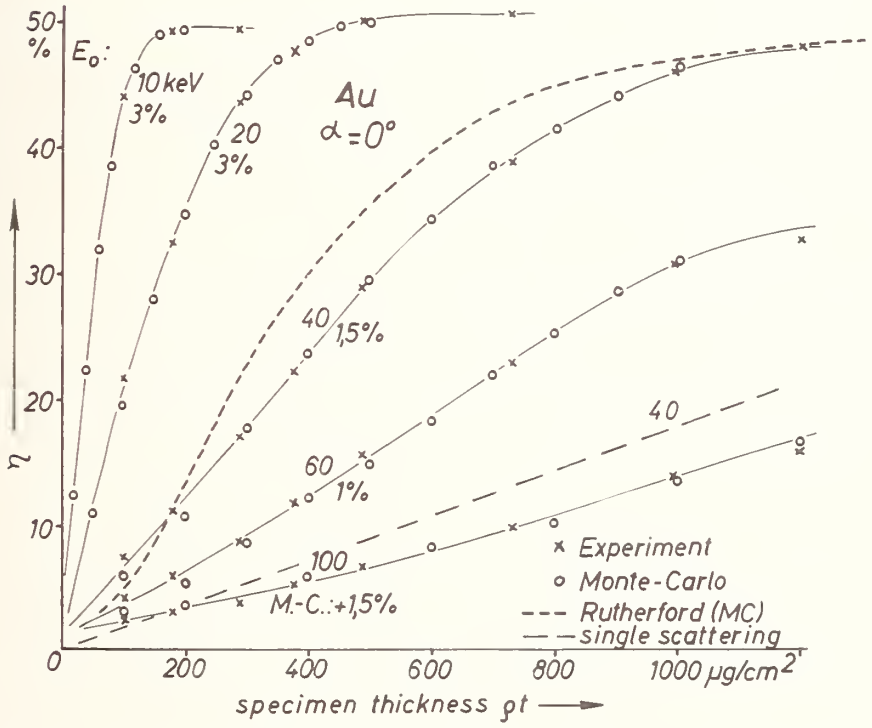

(b)

Figure 4. Comparison of MC and experimental values of the backscattering coefficient η as a function of film thickness for thick specimens.

4.2 Backscattering of bulk material for oblique incidence

Figures 5a and b show the backscattering coefficient η of bulk material for different angles of incidence ζ_0 versus cos ζ_0 (cos ζ_0 = 1; normal incidence). There is quite good agreement between MC and experiment for the increase of η with increasing ζ_0. The curves for Al show no large differences for different electron energies. MC calculations for both Al and Au show somewhat larger values at 100 keV.

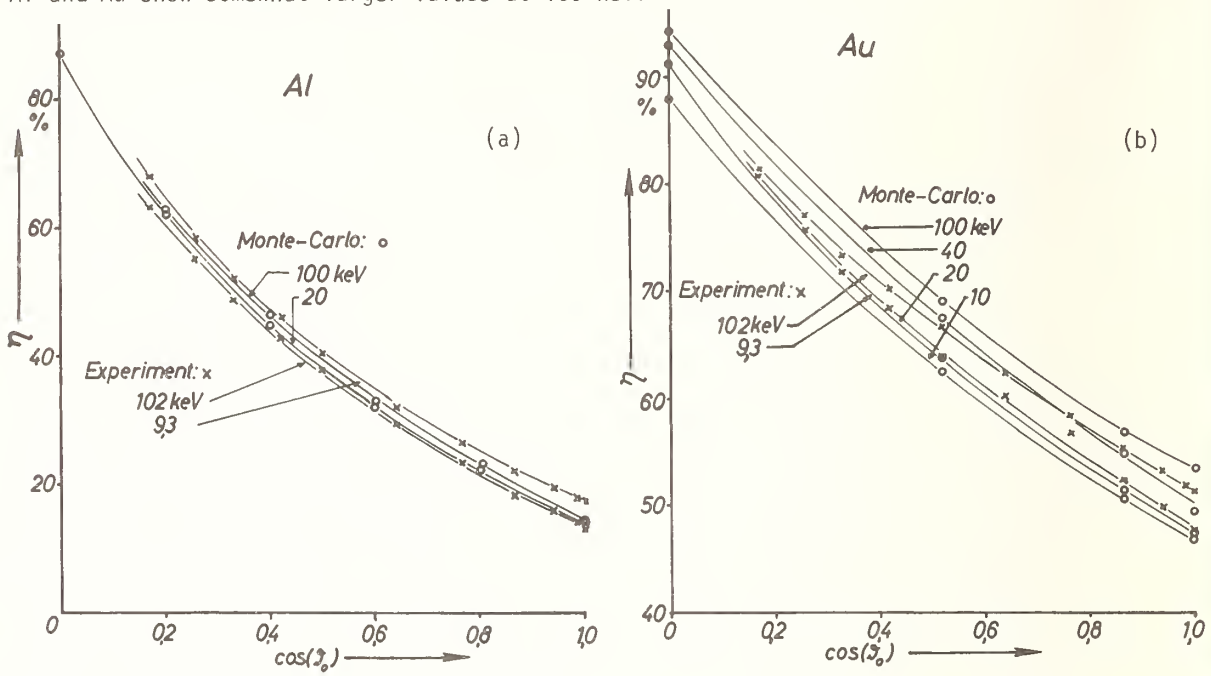

Figure 5. Dependence of backscattering coefficient η of bulk material on the angle of incidence ζ_0 for different electron energies.

4.3. Angular distribution of backscattered electrons

The angular distribution $d\eta(\zeta)/d\Omega$ of backscattered electrons for bulk material shows roughly a cosζ dependence. This is a circle in a polar diagram or a straight line if plotted against cos ζ(cos ζ = 1: backscattering into $\zeta = \pi$). There should be larger deviations for thin films at low cosζ near $\zeta = 90°$, caused by pronounced single elastic scattering into these directions. Figure 6 shows experimental results and the MC calculations.

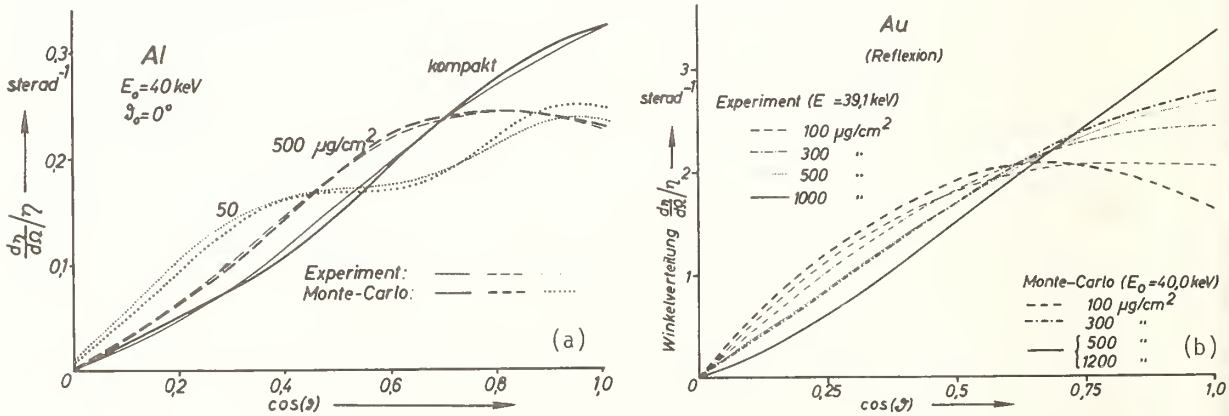

Figure 6. Angular distribution $d\eta/d\Omega$ as a function of cos ζ for thin films of: (a) Al, and (b) Au.

4.4. Energy distribution of backscattered electrons

The energy distribution of backscattered electrons shows for Al a broad maximum with a most probable energy $E_p/E_0 = 0.7$ (see experiments of Kulenkampff and Spyra [16] in fig. 7). The MC calculation in figure 7 gives results for the contribution of different depths to this energy distribution. For bulk material, our MC values show a shift of E_p/E_0 to somewhat smaller values. This will be further discussed in Section 6.2.

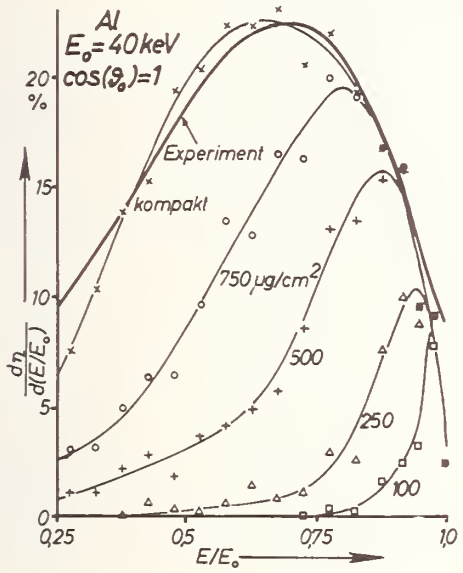

Figure 7. Energy distribution of backscattered electrons for Al. MC calculations about the contribution of different depths. Full curve: experiments of Kulenkampff and Spyra [16].

4.5. Transmission of films

A good agreement is also obtained (fig. 8) between experiments and MC values of the transmission τ through thin films measured over the range $0 < \zeta < \pi/2$.

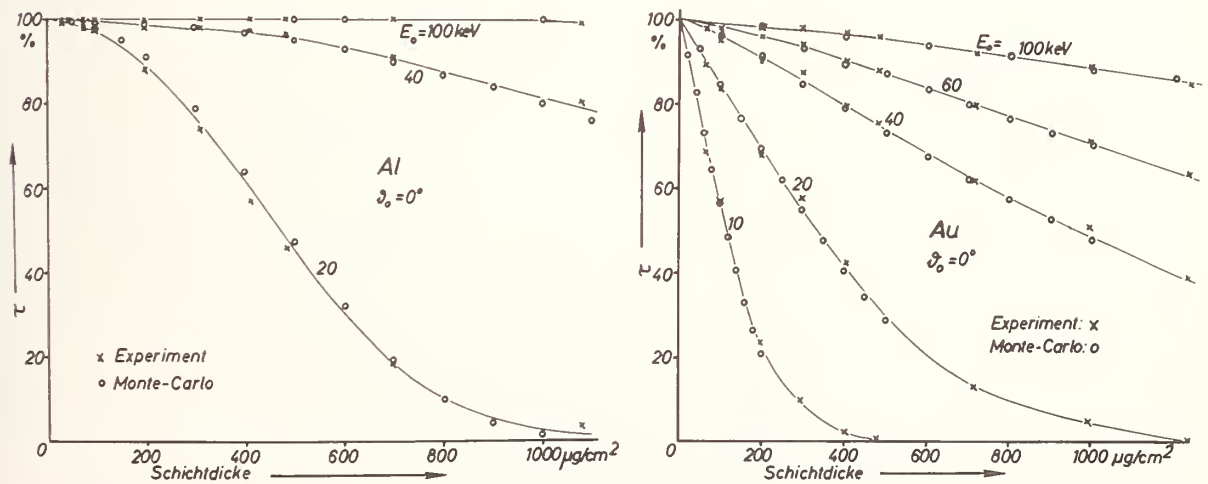

Figure 8. Transmission τ as a function of film thickness.

5. The Calculation of X-Ray Emission

Characteristic x-ray emission can be calculated by two methods. In the first, the numbers of electron-electron collisions with E_{nl} are summed. To obtain absolute values, one must also consider that there are several possibilities for filling the nl-shell; for example, emission of Kα- and Kβ-lines. FSE also can contribute to ionization if their energy $E > E_{nl}$. There is a probability

$$w = \int_0^x \frac{d\sigma}{dx}\, dx = \int_{E_{nl}}^{E} \left(\frac{d\sigma}{dE}\right)_{nl} dE \qquad (25)$$

for ionization. The contribution of FSE to the ionization of the K-shell of Al is of the order of 30%. To a first approximation this does not, however, cause a change in the depth distribution and can be neglected for relative calculations. It is a disadvantage of this method that the probability of an ionization, especially of the K-shell, is too low. The tallying of K-shell ionizations in the form of integer numbers requires very large numbers of incident electrons in the MC calculation. Therefore, it is better to sum up the probabilities of K-shell-ionization along the path s between two collisions as real numbers smaller than 1. In this case, the single electron-electron collisions with electrons of the nl-shell must be taken into consideration only for their contribution to the electron diffusion and not for their contribution to x-ray emission. In both cases, the absorption can be taken into account by multiplying with an exponential term $\exp[-\chi z]$ ($\chi = \mu/\sin\beta$, β = take-off angle). One obtains also the $f(\chi)$ correction curves used in microanalysis.

Figures 9-11 show calculated results for Al and Au assuming E_0 = 20 and 40 keV and different values of the angle of incidence ζ_0. The results for Al in figure 9 are calculated for the K-shell ionization while those of Au in figure 11 are for different ionization energies E_{nl} of spurious elements in an Au matrix. A more extensive program for comparison of experimental data of x-ray emission and MC calculations is being undertaken in our laboratory.

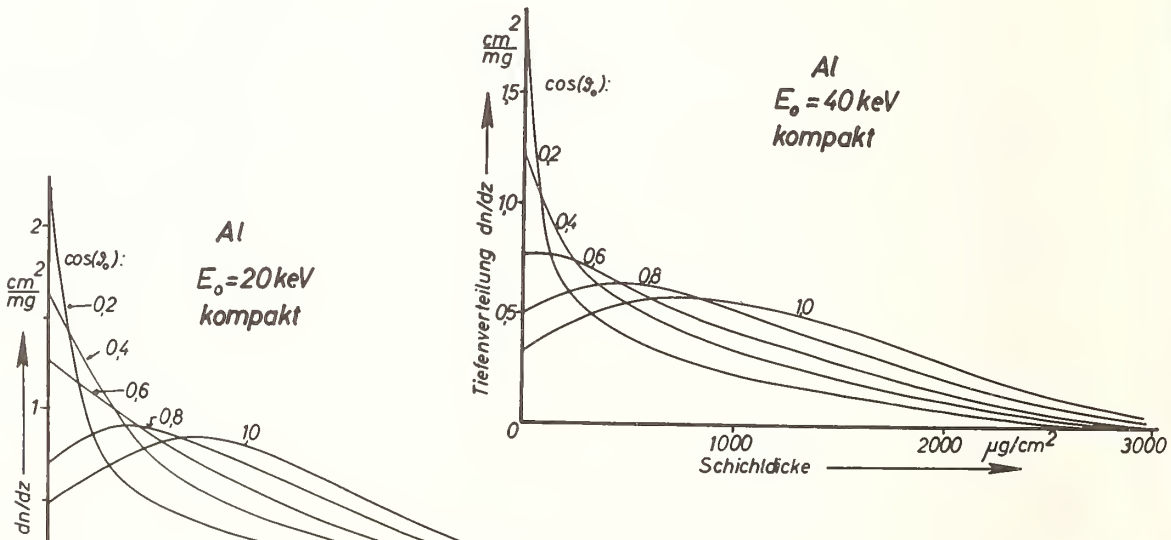

Figure 9. Calculated depth distributions of k-shell ionization for Al at E_0 = 20 and 40 keV and different angles of incidence ζ_0.

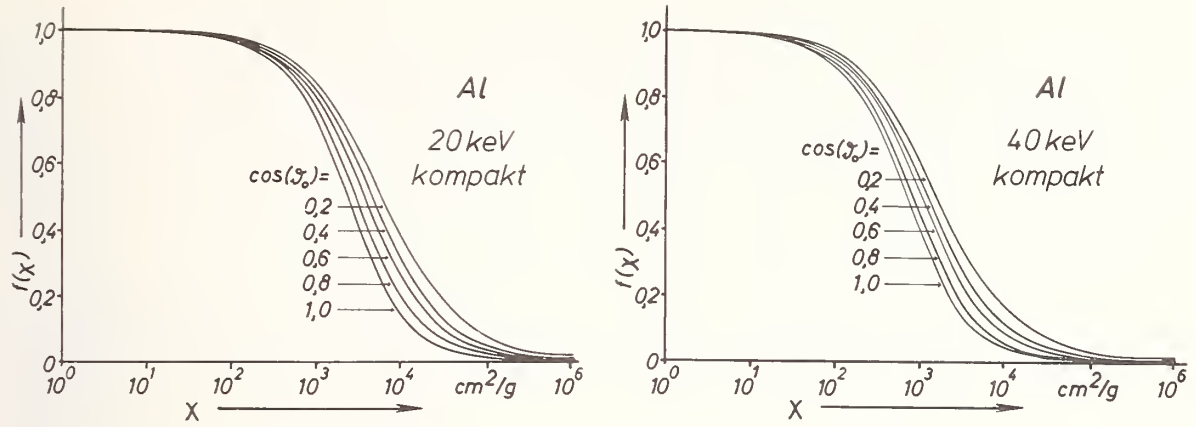

Figure 10. Calculated $f(\chi)$ correction factors for Al Kα at E_0 = 20 and 40 keV and different angles of incidence ζ_0.

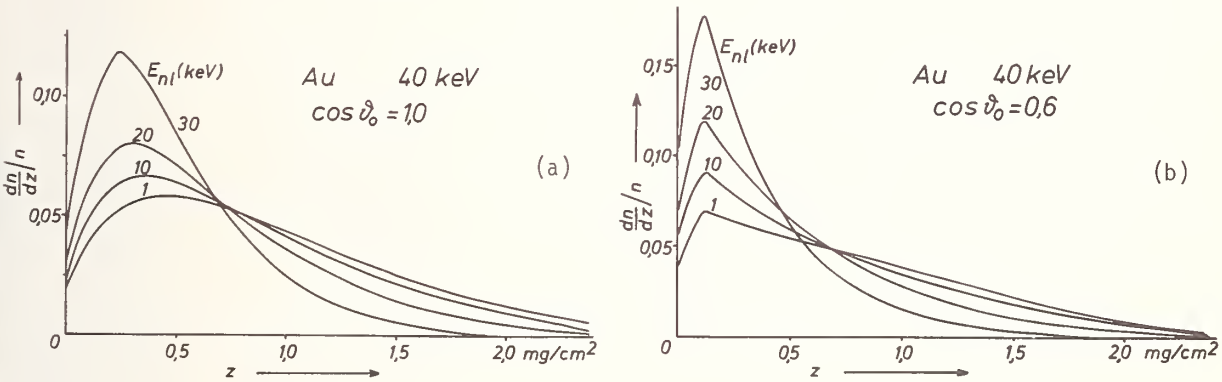

Figure 11. Calculated depth distributions for x-ray emission of trace elements with an ionization energy E_{nl} in an Au matrix for: (a) normal, and (b) 53°-incidence.

6. Influence of Changing Different Parameters of the Monte Carlo Model

We changed some parts of our normal program (see Section 1) to see which parts of the model influence the results of the calculation.

6.1. Backscattering of Au for 40 keV incident energy (fig. 12)

The full curve represents the results of the normal MC program including the FSE. The experimental values are somewhat higher because in this diagram no additional percentages were added to account for the FSE between 50 and 200 eV as in figure 4. In the curve with (dE/ds)x 1.5, the continuous Bethe energy losses are increased by a factor 1.5. Because we considered about 50% of the total mean energy loss as single electron-electron collisions, the mean energy loss is increased by 25%. This change has no influence for thin films, but saturation is reached at smaller film thicknesses because the total path length is shorter than before. Increasing the energy loss also causes more frequent elastic collisions because $d\sigma/d\Omega$ increases with increasing energy. If the cross-section for elastic scattering with $\zeta > 10°$ is increased by a factor 1.5, the backscattering coefficient of thin films increases by the same factor because this coefficient is built up by single and multiple elastic scattering. The curve, indicated by σ(Ruth), was calculated with unscreened Rutherford

cross-section ($\zeta > 10°$ only). For very thin films, the backscattering is smaller because $(d\sigma/d\Omega)_R < (d\sigma/d\Omega)_M$ for $\zeta > 90°$. There is a steeper increase with increasing film thickness caused by multiple scattering because $(d\sigma/d\Omega)_R > (d\sigma/d\Omega)_M$ for medium scattering angles. Compared to the results of Rutherford scattering in figure 4b, the FSE are included in this calculation, so that η for bulk material is larger than the experimental value.

Corresponding changes occur in the transmission curve (fig. 13).

6.2. Energy distribution of backscattered electrons (fig. 14)

There is a good agreement between our normal model (RE in fig. 14) and the experiments of Kanter [17]. One gets the same "most probably energy" $E_p/E_0 = 0.97$. Deviations occur at small E/E_0, since we only considered the FSE in the scattering model but not in the calculation of the energy spectrum. The latter requires further assumptions about the energy distribution of the FSE. If this contribution to ionization by single electron-electron collisions is omitted ($\sigma(\text{ioni}) = 0$ in fig. 14), a shift to $E_p/E_0 = 0.93$ occurs. Because omitting single electron-electron collisions increases the continuous Bethe losses, (see eq. (12)), a factor of 1.5 for the Bethe losses results from the same tendency, whereas E_p/E_0 increases to 0.96 if the single elastic scattering is increased by a factor 1.5.

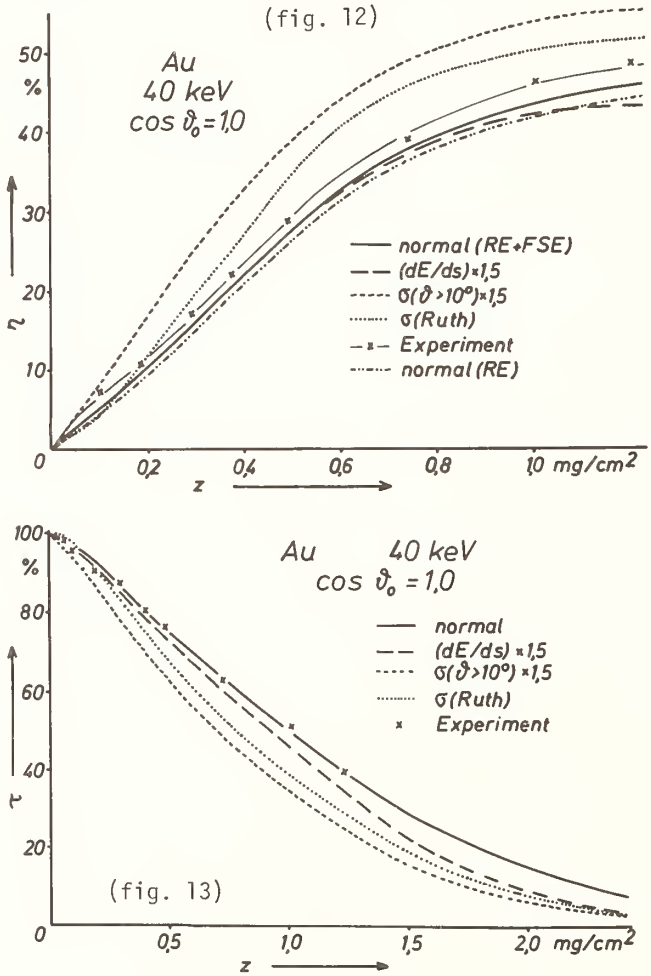

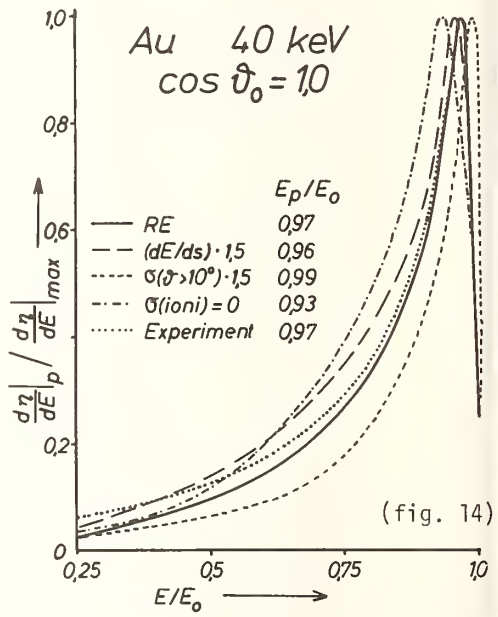

Figure 12-14. Influence of changing different parts of the MC program on the results of the backscattering coefficient η (fig. 12), the transmission τ (fig. 12), the transmission τ (fig. 13), and the energy distribution of backscattered electrons for Au and E_0 = 40 deV (fig. 14).

6.3 X-ray emission (fig. 15)

Figure 11 shows the depth distribution of shells with different ionization energies E_{nl} in a gold matrix assuming normal electron beam incidence. Figure 15 demonstrates for E_{nl} = 1 and 30 keV, the influence of the previously discussed alterations of the model. The corresponding $f(\chi)$-curves are very insensitive to these relatively large changes of the depth distribution and show differences of only 2-5 percent. This means that one should not calculate depth distributions from measured values of $f(\chi)$.

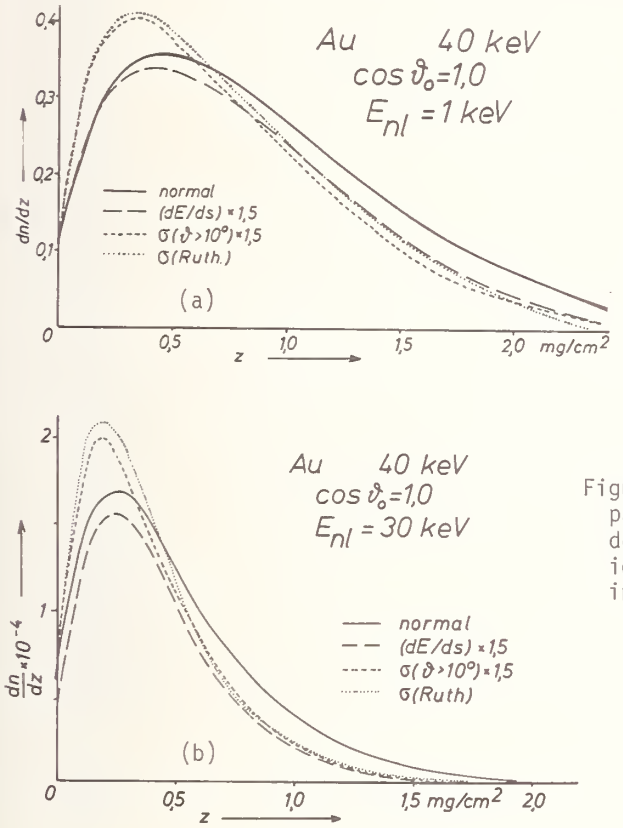

Figure 15. Influence of changing different parts of the MC program on the results of the depth distribution for x-ray emission with an ionization energy of: (a) 1, and (b) 30 keV in a gold matrix.

7. Monte Carlo Calculations of Low Angle Scattering Problems

There are many problems in conventional transmission (CTEM) and scanning transmission electron microscopy (STEM) in which one needs all the elastic and inelastic scattering collisions. If one only looks at the angular distribution of transmitted electrons through thick films, it is possible to solve the problem by means of multiple scattering integral [6,18]. Also, if the spatial distribution normal to the electron probe after passing a thick film is required, a corresponding multiple scattering integral can be calculated [19,20]. But if one wants information about the spatial broadening of the electron beam for a limited detector aperture in STEM, one must know the electron distribution as a function of angle as well as the spatial distribution. This is not possible by a multiple scattering formula. Therefore, MC calculations are useful for this problem and also for the calculation of multiple energy losses (chromatic error in CTEM).

Because only low scattering angles are of interest, the MC calculations can be simplified. With the calculated scattering angle ζ and the azimuthal angle ψ, two angular coordinates $\zeta_x = \zeta\cos\psi$ and $\zeta_y = \zeta\sin\psi$ are obtained and eqs. (19) and (22) become, respectively,

$$x_{n+1} = x_n + s\zeta_x;\ y_{n+1} = y_n + s\zeta_y;\ z_{n+1} = z_n + s$$

$$\zeta_{x,n+1} = \zeta_{x,n} + \zeta_x;\ \zeta_{y,n+1} = \zeta_{y,n} + \zeta_y. \qquad (26)$$

The elastic and inelastic cross sections are described by the Lenz formula [18], but with empirical parameters x_a and ζ_o [6], which are also in good agreement with WKB calculations. The energy losses can be calculated by a formula fitting experimental distributions of plasma energy losses. Results of this method have been reported for the spatial broadening of the electron probe [20,21] and the chromatic error [22].

References

[1] Reimer, L., *Optik*, 27, 86 (1968).

[2] Bühring, W., *Z. Physik*, 212, 61 (1968).

[3] Badde, H. G., Drescher, H., Krefting, E. R., Reimer, L., Seidel, H., and Bühring, W., *Proceedings 25th Annual Meeting of EMAG*, p. 74 (Institute of Physics, London, Bristol, 1971).

[4] Reimer, L., Badde, H. G., Seidel, H., and Bühring, W., *Z. Angew. Physik*, 31, 145 (1971).

[5] Kessler, J. and Weichert, N., *Z. Physik*, 212, 48 (1968).

[6] Reimer, L. and Sommer, K. H., *Z. Naturforschung*, 23a, 1569 (1968).

[7] Byatt, W. J., *Phys. Rev.* 104, 1298 (1956).

[8] Tietz, T., *Nuovo Cimento*, 36, 1365 (1965).

[9] Lewis, H. W., *Phys. Rev.* 78, 526 (1951).

[10] Grysinski, M., *Phys. Rev.* 138, A336 (1965).

[11] Drescher, H., Reimer, L., and Seidel, H., *Z. Angew. Physik*, 29, 331 (1970).

[12] Bethe, H., *Ann. Physik*, 5, 325 (1930).

[13] Niedrig, H. and Sieber, P., *Z. Angew. Physik*, 31, 27 (1971).

[14] Seidel, H., Ph.D. thesis (Münster, 1969).

[15] Drescher, H., Ph.D. thesis (Münster, 1970).

[16] Kulenkampff, H. and Spyra, W., *Z. Physik*, 137, 416 (1954).

[17] Kanter, H., *Ann. Physik*, 20, 144 (1957).

[18] Lenz, F., *Z. Naturforschung*, 9a, 185 (1954).

[19] Jost, K. and Kessler, J., *Z. Physik*, 176, 126 (1968).

[20] Reimer, L., Gilde, H., and Sommer, K. H., *Optik*, 30, 590 (1970).

[21] Gentsch, P., Gilde, H., and Reimer, L., *J. Microscopy*, 100, 81 (1974).

[22] Reimer, L. and Gentsch, P., *Ultramicroscopy*, 1, 1 (1975).

[23] Krefting, E. R. and Reimer, L., *Quantitative Analysis with Electron Microprobes and Secondary Ion Mass Spectroscopy*, Report Jul-Conf-8, p. 114 (E. Preuss Kernforschungsanlage, Jülich, Germany, 1974).

National Bureau of Standards Special Publication 460. Proceedings of a Workshop on the Use of Monte Carlo Calculations in Electron Probe Microanalysis and Scanning Electron Microscopy held at NBS, Gaithersburg, Maryland, October 1-3, 1975. Issued December 1976.

CHARACTERISTICS OF A MONTE CARLO PROGRAM FOR MICROANALYSIS STUDY OF ENERGY LOSS

J. Heńoc

C.N.E.T.
Bagneux, France

and

F. Maurice

C.E.N.
Saclay, France

The x-ray depth distribution curves obtained by the Monte Carlo method are in disagreement with the experiment. For this reason, Bishop [2][1] proposed in his thesis the use of the theory of Landau, which takes into account the statistical nature of the energy loss of the electrons. This procedure gives a more realistic description of the events. We have taken into account, in this way, the effects of electron straggling upon the function $\phi(\rho Z)$ and the energy loss distribution of electrons passing through thin films. The general solution of the problem of electron trajectory simulation is straightforward, but it requires lengthy and expensive calculations. The procedure can be reduced in length by means of two simplifications, one of which was proposed by Bishop.[2] Different treatments affect in different ways the statistical distributions of the variables which are being studied. In addition, the importance of the parameters and physical models which govern the diffusion of electrons (step length, diffusion model, screening parameter, etc.) will be discussed.

Key Words: Electron energy loss; Landau electron deceleration theory; microanalysis; Monte Carlo electron trajectory calculations; scanning electron microscopy; x-ray microanalysis.

1. Introduction

It is well known that, while traveling through a target, electrons lose their energy by creating ionizations which are the origin of radiative transitions; x-ray photons resulting from these transitions provide the signal used in x-ray microanalysis. It is also known that primary electrons are progressively scattered from their initial direction; consequently, x-ray emission is a three-dimensional phenomenon. Because of the small penetration of the electrons in matter, x-ray microanalysis is considered to be a surface analysis technique; thus, it is easy to understand why, initially, the theory has dealt only with the calculation of the total number of ionizations produced by electrons as their energy decreases to the minimum excitation energy. The spatial distribution of the phenomenon is only implicit in the absorption correction [4], but becomes explicit in the fluorescence correction. The simplest model appears quickly to become inadequate when the field of application of the method widens, because each theoretical treatment of x-ray emission implies the knowledge of the spatial distribution.

---

[1]Figures in brackets indicate literature references at the end of this paper.
[2]H. E. Bishop, personal communication.

Experiments made by Castaing and Descamps [5] on the depth distribution of characteristic x-ray production were the first to clearly show the limits of the original method, while they also suggest directions for further improvement.

Some semi-empirical attempts have been made at analytical treatments, such as that of Philibert [16], later improved by Heinrich [10]. However, the Monte Carlo method introduced by Green [9], and developed independently by Bishop [2] and Shimizu [18], appears to be the only way to take into account the different variables in competition in the x-ray production of targets of any shape.

This method consists of a sampling of electron trajectories determined by means of a certain number of random variables; the statistical distribution of these variables being known and usually deduced from the theoretical cross-section. The expression "Monte Carlo calculations" covers a great number of calculation techniques with the same common basis. In the present work, we have chosen to deal with the statistical energy distribution of electrons transmitted through a thin metal foil. This example allows the comparison between the Monte Carlo statistics and a simple probability calculation.

From this basic concept, we describe the simulation method of electron trajectories in any target, in order to derive the matrix that gives the energetic and spatial distribution of the electrons. Such a matrix supplies the necessary information which is needed in microanalysis.

To show the flexibility of the model, after using the classical continuous Bethe deceleration law [1], we will turn to the Landau statistical energy loss theory [14].

2. Basis of the Monte Carlo Technique

2.1 Background (principle)

The Monte Carlo technique consists in sampling a random variable x by selecting at random from a set $\{x_i\}$ of values of equal probability of this variable. The values of equal probability must be previously determined as follows:

(i) let f(x)dx be the probability density function, i.e., the probability for x to be included between x and x+dx

(ii) let F(x) be the distribution function that represents the probability that x, whose extreme values are x_1 and x_2, is lower than a given value x

$$F(x) = \int_{x_1}^{x} f(x)dx \quad . \tag{1}$$

This function takes its values on the [0-1] interval, which is divided into N equal intervals (fig. 1). One element x_i of the set of equal probability values is defined by:

$$F(x_i) = \frac{i-1}{N} + \frac{1}{2N} \tag{2}$$

where i is an integer and $1 < i < N$.

2.2 Example of application

In this paragraph, we put the emphasis on the statistical behavior of the energy of electrons transmitted through a thin metal foil. The physical principles of the Landau theory will be discussed in Appendix 1. The probability density function, $f(\Delta)$, for the electrons of initial energy E, to suffer an energy loss included between Δ and $\Delta+d\Delta$,

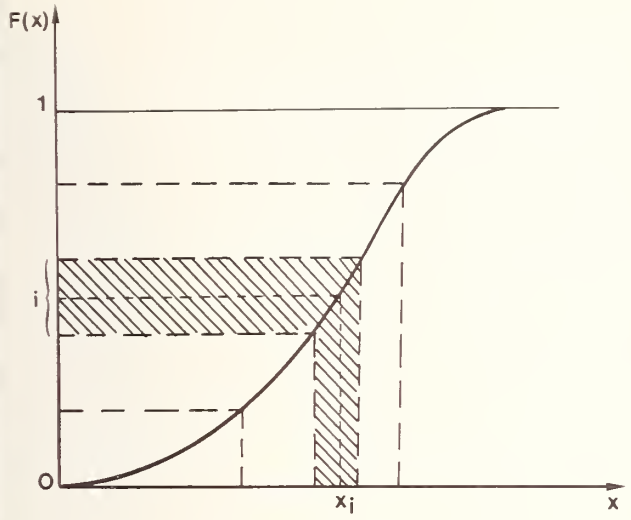

Figure 1. Determination of the set of values of equal probability.

while crossing a foil of thickness $\rho s(g/cm^2)$, may be expressed by means of an integral in terms of a universal parameter λ:

$$f(\lambda) = \frac{1}{2i\pi} \int_{-i\infty+\sigma}^{i\infty+\sigma} \exp\{u[\ln(u) + \lambda]\}du \qquad (3)$$

provided that $f(\Delta)d\Delta = f(\lambda)\frac{d\lambda}{d\Delta}d\Delta$.

λ is linked to the initial energy E of the electron and to the characteristics of the specimen by:

$$\lambda = \frac{\Delta - \xi[1 - C + \ln(4E\xi / J^2)]}{\xi} \qquad (4)$$

with

$$\xi = \frac{\pi N e^4}{E} \rho s \frac{Z}{A}$$

in which Z is the atomic number of the target element, A is the atomic mass, and J is the mean ionization potential. C, e, & N are, respectively, the Euler constant, the electron charge, and the Avogadro number.

The associated distribution function is then defined by:

$$F(\lambda) = \int_{\lambda_0}^{\lambda} f(\lambda)d\lambda \qquad \lambda_0 < \lambda < \infty . \qquad (5)$$

A set $\{\lambda_i\}$ of N values of equal probability has been derived by integrating (5), then interpolating by using (2). Afterwards we have made a sampling of λ using a pseudo-random number generator of uniform distribution. According to (4), each of these λ_i values corresponds to an energy loss Δ_i.

In figure 2 are shown two histograms of the energy losses suffered by primary electrons of 1000 keV passing through a 4.5 μm thick aluminum film. Sevely, et al. [15], used the same physical conditions in their experiment, also quoted in the same figure. The sampling

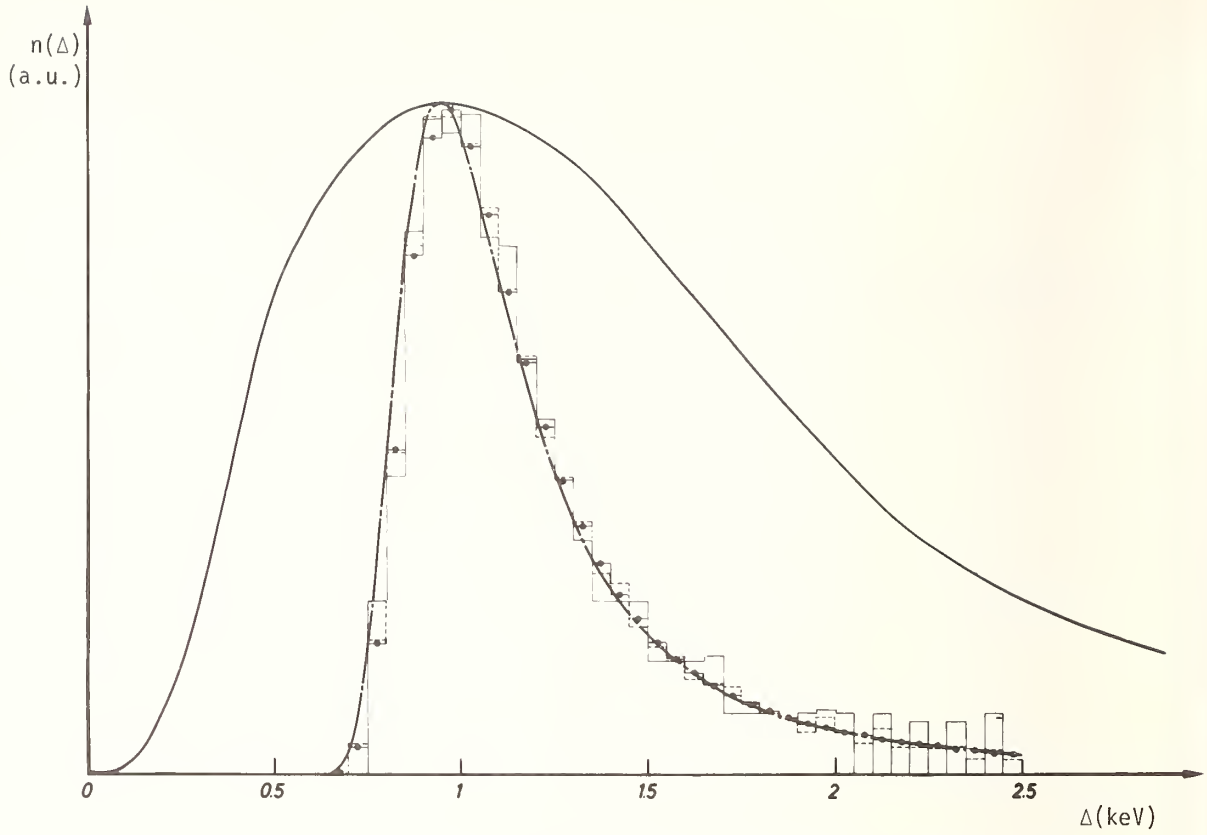

Figure 2. Energy loss distribution of 1000 keV electrons transmitted through a 4.5 μm thick aluminum foil. ——— experiment; ——— Monte Carlo calculation--5000 trajectories 128 λ values of equal probability; ---- Monte Carlo calculation--5000 trajectories 512 λ values of equal probability; —•— discrete probability distribution--50 eV class width; — - — continuous probability distribution.

is made with 5000 trajectories and the number of values of equal probability is either 128 or 512; the width of a class is always 50 eV.

In this particular case, which is a single probability problem, we can also obtain the histogram of energy losses by calculating:

$$n(\Delta_i) = \frac{\int_{\lambda_i}^{\lambda_{i+1}} f(\lambda)d\lambda}{|\Delta_{i+1} - \Delta_i|} \qquad (6)$$

$n(\Delta_i)$ represents the relative weight of every class and $|\Delta_{i+1}-\Delta_i|$ has the same value as in the Monte Carlo calculation. The distribution $n(\Delta)$ is also plotted in figure 2. The continuous curve represents $n(\Delta)$ when the width of the class vanishes. If the difference between two adjacent values of λ of equal probability is spread over several energy classes, as it is the case for strong energy losses, the histogram produces accumulations and holes. The histogram shown in figure 3 is obtained by increasing the width of the class by a factor of 3; the above-mentioned shortcoming disappears, but the accuracy for weak losses is poor. The width of the class must be adjusted for the number of values of equal probability in order to get a good sampling of the variable. If this condition is fulfilled, the direct calculation and the Monte Carlo approach will fit, provided that the number of trials is sufficiently high. In our case, 512 values of λ of equal probability and a class width of 50 eV are suitable enough to reach the goal. With regard to the number of

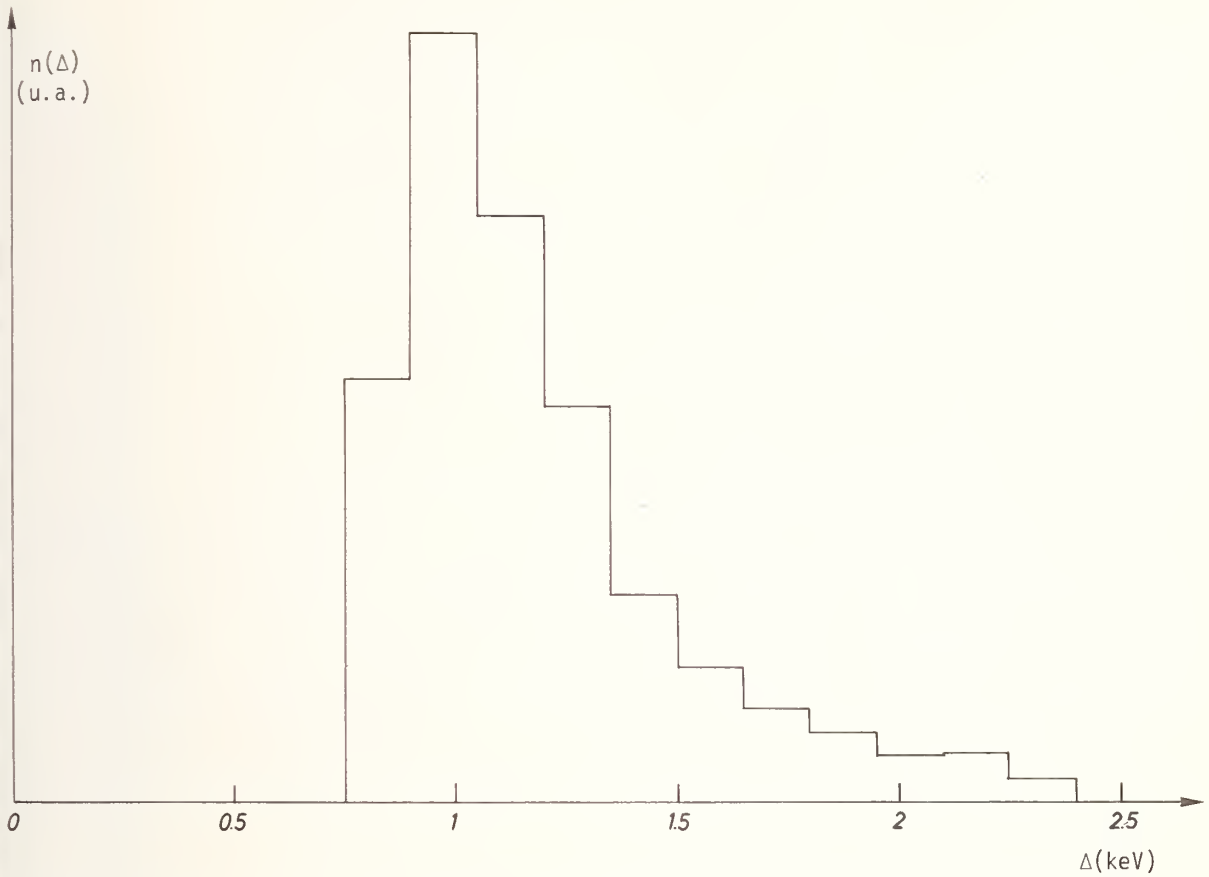

Figure 3. Energy loss distribution of 1000 keV electrons transmitted through a 4.5 μm thick aluminum foil. Monte Carlo distribution 5000 trajectories--128 λ values of equal probability--150 eV class width.

trials, we must keep in mind that it should be optimized in order to achieve the required accuracy at the lowest cost.

In practice, when many random variables compete, so that only the Monte Carlo technique can be used, it is obvious that the choice of the working conditions is quite arbitrary. The justification can only be made *"a posteriori."*

3. Description of a Versatile Monte Carlo Calculation for Microanalysis

3.1 Main Outlines

We know that along its trajectory in the target, an electron is slowed down and scattered from its original direction. The trajectory is then simulated as a succession of broken lines such as AA'A" (fig. 4) generally called steps; $ds_i = ds_{i,1} + ds_{i,2}$ denotes the path length of AA'A". The energy decrease along the elementary path, depends only upon the path length ds_i, assuming the Bethe continuous energy loss law holds; furthermore, a one-to-one relationship may be established between the path length S_i

$$S_i = \sum_{j=1}^{j=i} ds_j$$

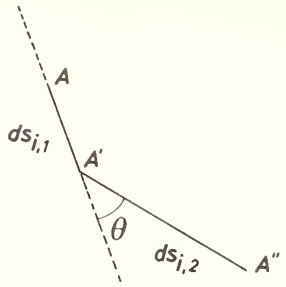

Figure 4. Elementary path.

and the mean electron energy E_i for a given step:

$$S_i = S(E_i)$$

In particular, the Bethe range R which is taken as unity is defined by R = S(0).

To consider the statistical part of the treatment we will start with Shimizu's point of view [19], which uses a single scattering cross-section. This means that the elementary path must have such a length ds_i that the electron undergoes, on the average, only one scattering event while traveling through. In other words, ds_i must be equal to the mean free path Λ_i of the electron for the actual energy E_i. The point A' where this event effectively takes place is selected at random (1st random variable). The new direction is self-determined by two angles selected at random (fig. 5): α has an uniform distribution in $(0,2\pi)$ (2nd random variable) and θ is taken out of a set $\{\theta_i^j\}$ of angles of equal probability built from the single scattering cross-section. The scattering cross-section is indeed the probability density function for an electron to be scattered in the θ direction in solid angle $d\Omega$.

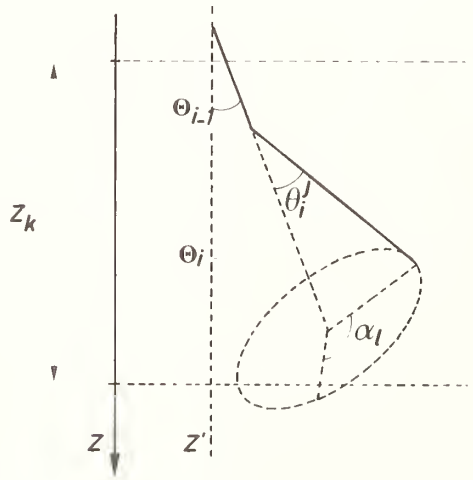

Figure 5. Definition of electron coordinates.

Bishop's method [2] is a simplification of this elementary model because it uses the convolution of Goudsmit and Saunderson [8], which allows the calculation of the angular deviation resulting from multiple interactions. The elementary path ds_i may thus be increased and the cost is lowered at the same time. The previous scheme is retained for the calculation even if the justification is less obvious than in the single scattering approach.

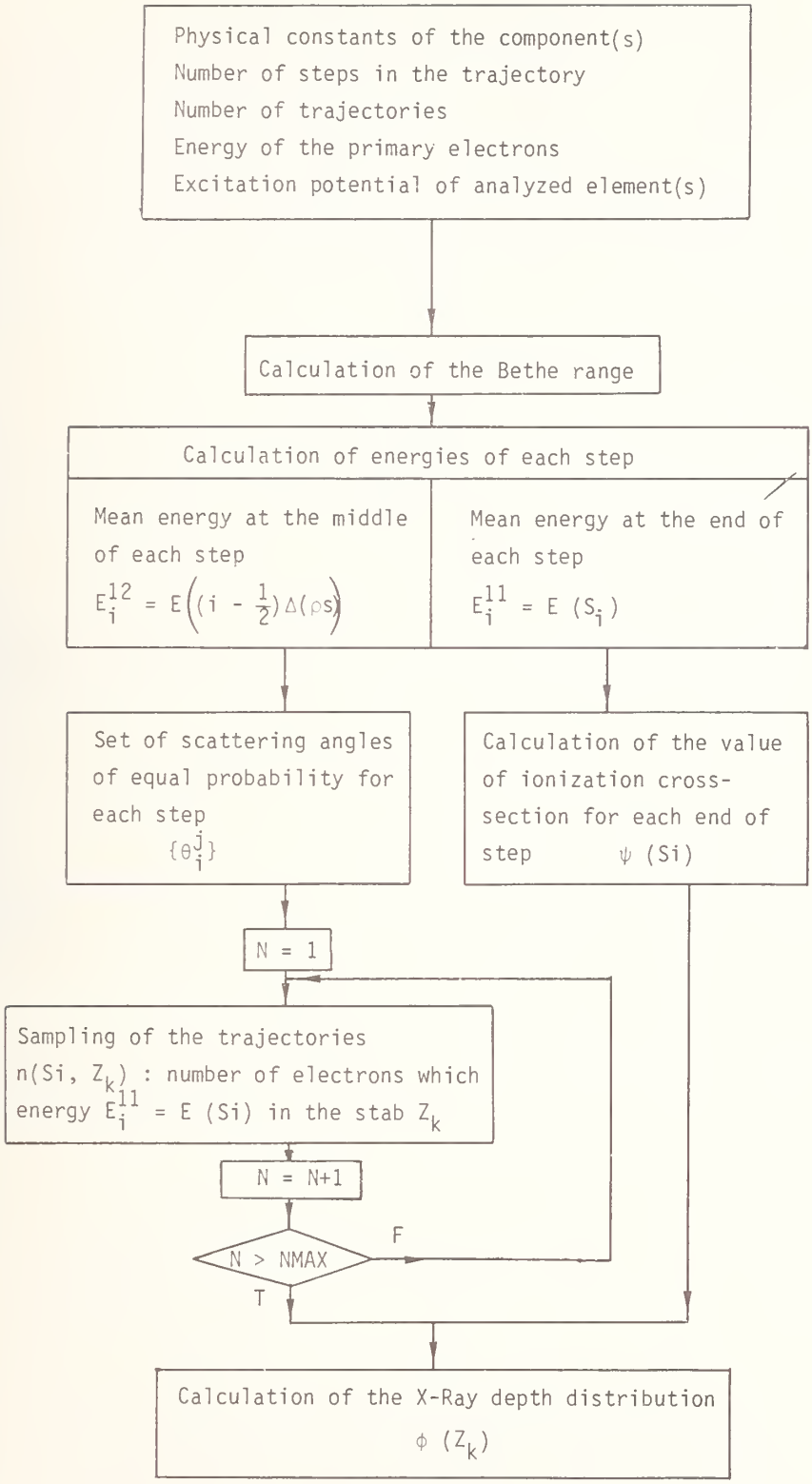

Figure 6. Schematic flow chart of a conventional treatment for the electron trajectory simulation with continuous energy losses.

3.2 Diagram of the Monte Carlo calculation

The main lines of Bishop's Monte Carlo calculation which we have used (1972) are shown in figure 6. The process contains three phases. Preliminary operations are performed in the first of these: calculation of the Bethe range and subdivision of this range into a certain number of steps, computation of energies for every half-step, and end of step. Some mean values may also be computed, for instance, the mean value of the ionization cross-section. This phase is ended when the set of scattering angles of equal probability has been determined. The second phase is the actual Monte Carlo calculation with the setting of the matrix $n(S_i, Z_k)$ which gives the number of electrons with a known energy (subscript i) belonging to a given slab of the target (subscript k). In the last phase the computation of any particular quantity that is significant in microanalysis is made.

3.2.1 Preliminary operations

3.2.1.1 Range calculation

The Bethe range is defined by Bethe's deceleration law [1], which links the mean energy loss dE to the path length $d(\rho s)$ with familiar symbols:

$$dE = \frac{-2\pi e^4 N}{E} \frac{Z}{A} \ln\left(1.66 \frac{E}{J}\right) d(\rho s).$$

Inversion of this formula gives the range by integrating between E_o and $E_j = 1.03\ J$; the upper limit is chosen so that the integral is convergent:

$$R = \int_{E_o}^{E_j} dE \Big/ \left[\frac{2\pi e^4 N}{E} \frac{Z}{A} \ln\left(1.66 \frac{E}{J}\right)\right].$$

For practical purpose, we use:

$$R(g/cm^2) = \frac{J^2}{7.85 \cdot 10^4} \frac{A}{Z} \quad EI\left[2 \ln\left(1.166 \frac{E_o}{J}\right)\right] - EI\left[2 \ln\left(1.166 \frac{E_j}{J}\right)\right]$$

where EI is the exponential integral function and energies are given in keV. R, which is used as the unit path length, is divided into I intervals of constant length $\Delta(\rho s) = R/I$. After the i^{th} step the electron has traveled the distance $S_i^{11} = i\frac{R}{I} = i\Delta(\rho s)$ we also define $S_i^{12} = (i-\frac{1}{2})\frac{R}{I} = (i-\frac{1}{2})\Delta(\rho s)$ as the distance traveled up to the middle of the i^{th} step.

3.2.1.2 Half-step and end-of-step energies

Assuming continuous energy loss, the Bethe equation holds and we can find for the mean energy at the middle and at the end of the i^{th} step:

$$E_i^{12} = E_o + \int_o^{(i-\frac{1}{2})\Delta(\rho s)} dE/d(\rho s) \qquad E_i^{11} = E_o + \int_o^{i\Delta(\rho s)} dE/d(\rho s).$$

These values are found by successive approximations, applying the RUNGE-KUTTA method; they are stored for further use.

3.2.1.3 Mean value of the ionization cross-section

We wish to calculate the mean number of ionizations when the electron has traveled through $(i-\frac{1}{2})R/I < \rho s < (i+\frac{1}{2})R/I$ with $1 < i < I$. Let $\psi(E)$ be the ionization cross-section; thus:

$$\psi_i = \int_{(i+\frac{1}{2})R/I}^{(i-\frac{1}{2})R/I} \psi(E)\, dE/d(\rho s)\, d(\rho s) \ .$$

For the ionization cross-section, the expression:

$$\psi(E) \simeq \frac{1}{E^2} \frac{\ln (U)}{U}$$

is commonly used, U being the overvoltage.

3.2.1.4 Setting of scattering angles of equal probability

The multiple scattering is treated by the Goudsmit and Saunderson theory as the convolution of the angular distribution given by the single scattering cross-section. This theory is summarized in Appendix 2. Let us simply say that the probability $F(\theta,p)$ for an electron to be scattered within angle θ after any number m of scattering events is $F(\theta,p)$, given by:

$$F(\theta,p) = \sum_{m=0}^{\infty} f_m(\theta)\pi(m)$$

where $f_m(\theta)$ is the probability for an electron to be scattered with an angle θ after m collisions and $\pi(m)$ is the probability for the electron to undergo m collisions. $\pi(m)$ obeys a Poisson distribution law:

$$\pi(m) = \frac{p^m}{m!} \exp(-p)$$

with p denoting the mean number of collisions suffered by the electron along the elementary path; p depends on the inverse of the square of the energy. For every energy $E_i^{1/2}$ at the half-step, we get a distribution function:

$$G(\theta,E_i^{1/2}) = \int_0^{\theta} F(\theta)d\Omega \ . \qquad (7)$$

The equal probability angles θ_i^j are calculated from (7) according to eq. (2); $\sin \theta_i^j$ are stored in the memory or in a special file. The subscript i refers to the energy.

3.2.2 Monte Carlo calculation

When a new electron impinges onto the target, its energy is E_0 and its coordinates are $X_0 = Y_0 = Z_0 = \Theta_0 = 0$. But, as far as the depth distribution is concerned, the Z coordinate is sufficient to locate the electron in the forward direction. In addition, we must make sure that the electron number is not greater than N, the maximum number of trajectories to be described; otherwise the control is transmitted to the next phase. At

the end of the $(i-1)^{th}$ step, (fig. 5) the electron behavior is characterized by the distance travelled $S_{i-1} = (i-1)R/I$, the energy E^{11}_{i-1}, the cartesian coordinate Z_{i-1} and the angle Θ_{i-1} between the trajectory and the forward direction. At the beginning of the i^{th} step, a randomly selected fraction r of the elementary path is added to the electron path length without any change in direction; consequently, the new coordinate is:

$$Z'_i = Z_{i-1} + r \cos \Theta_{i-1} \, R/I$$

The remaining part (1-r) of the elementary path then takes place after the electron has been scattered in a direction given by selecting at random two angles θ^j_i and α_1. θ^j_i is taken from the set of angles of equal probability $\{\theta^j_i\}$ determined in 3.2.1.4 for $E = E^{12}_i$. The new electron coordinates are calculated using

$$\cos \Theta_i = \cos \Theta_{i-1} \cos \theta^j_i + \sin \Theta_{i-1} \sin \theta^j_i \cos \alpha_1$$

$$Z_i = Z'_i + (1-r) \cos \theta_i \, R/I = Z_{i-1} + \left[r \cos \theta_{i-1} + (1-r) \cos \Theta_i \right] R/I.$$

If we can find a value of k, with $1 < k < I$ such that:

$$\left(k - \frac{1}{2}\right) R/I < Z_i < \left(k + \frac{1}{2}\right) R/I,$$

the matrix element $n(S_i, Z_k)$ is increased by 1.

If $Z_i \leq 0$, the electron is backscattered and the $n_S(S_i)$ component of the n_S vector is incremented by 1.

If $0 < Z_i \leq \frac{1}{2} R/I$, the matrix element $n(S_i, Z_o)$ is incremented by 1.

The vector $n_S(S_i)$ gives the energy distribution of the backscattered electrons and the $n(S_i, Z_o)$ row is used to determine the scattering properties of the surface layer.

3.2.3 Characteristic x-ray depth distribution

As a result of the previous paragraph the number of ionizations produced in the k^{th} slab is proportional to

$$\sum_{i=1}^{I} n(S_i, Z_k)\psi_i \, .$$

Under the same physical conditions, the same number, N, of electrons striking a self-supported film of thickness R/I, made of the same material would produce a number of ionizations proportional to $N \psi (E_o)$. Therefore the relative intensity of the characteristic radiation ϕ_k emitted by the embedded slab may be expressed by:

$$\phi_k = \sum_{i=1}^{I} \frac{n(S_i, Z_k)\psi_i}{N \psi (E_o)} \, .$$

For the emission at the surface layer, the enhancement produced by both the progressive diffusion and the backscattering is given by:

$$d\phi_o = \sum_{i=1}^{I} \frac{n(S_i \, Z_o)}{N \psi (E_o)} \, .$$

Figures 7, 8, and 9 show the depth distribution of Kα radiation emitted by a copper target, the acceleration voltage being 29 kV, and by an aluminium target, the acceleration voltage being 15 and 29 kV.

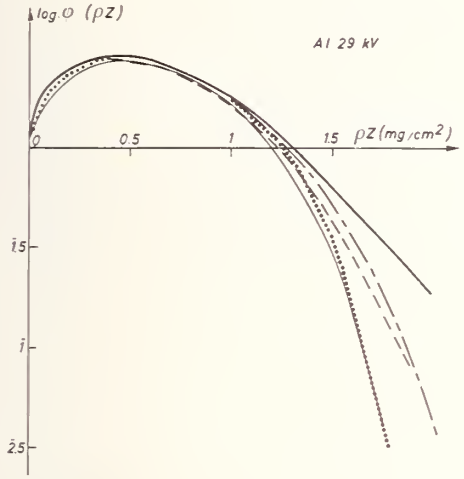

Figure 7. Characteristic x-ray depth distribution for a copper target at 29 kV. ——— experiment (Castaing and Descamps, (1955); ..... conventional calculation, 15000 trajectories, 45 steps; ——— conventional calculation with the mean Landau energy substituted for the Bethe energy, 5000 trajectories, 25 steps; — — — full treatment, 2000 trajectories, 45 steps; —·— alternative treatment, 15000 trajectories, 45 steps.

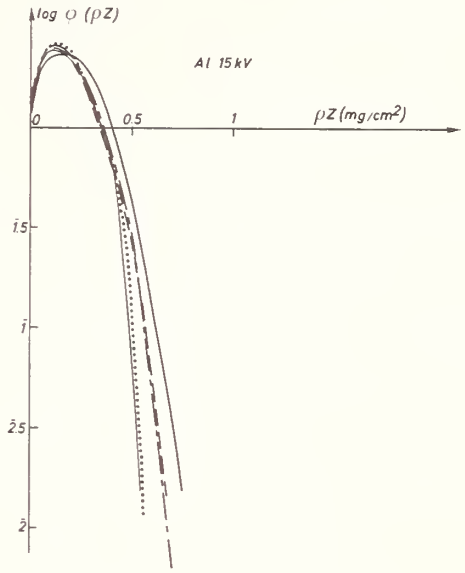

Figure 8. Characteristic x-ray depth distribution for an aluminum target at 15 kV. ——— experiment (Castaing and Hénoc, 1966); ..... conventional calculation, 15000 trajectories, 20 steps; ——— conventional calculation with the mean Landau energy substituted for the Bethe energy, 5000 trajectories, 25 steps; — — — full treatment, 2500 trajectories, 20 steps; ——— alternative treatment, 15000 trajectories, 20 steps.

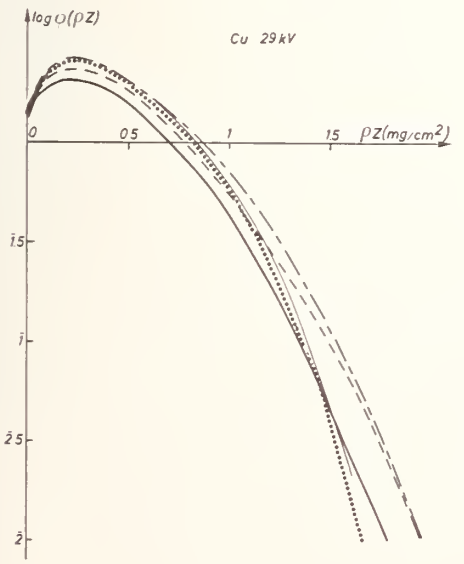

Figure 9. Characteristic x-ray depth distribution for aluminum target at 29 kV. ——— experiment (Castaing and Hénoc, 1966); ..... conventional calculation, 15000 trajectories, 25 steps; — — — full treatment, 2000 trajectories, 45 steps; —·— alternative treatment, 15000 trajectories, 45 steps.

4. Introduction of Statistical Energy Losses into the Monte Carlo Calculation

It has been shown both by experiment and theory that the energy losses are of statistical nature. Before describing a general approach of electron penetration with regard to the statistical energy losses, we will try to keep the scheme given above.

4.1 Mean energy losses deduced from the Landau distribution

In an exploratory Monte Carlo calculation, Bishop [2] had already determined the electron mean energy loss using the Landau theory [14]. The elementary path length being R/I, the residual energy E_1 of the electron after traveling R/I, is computed as in paragraph 2.2. This has been done by selecting at random from the set of λ of equal probability which allows a E_1 value to be found when E_0 is known. The process is continued to find E_2 from E_1 for the second step and so on until E_j vanishes to the minimum excitation potential. We must note at this point that the maximum value of j may be greater than I. If $E_{i,n}$ denotes the energy of electron number n at step number i, the mean energy E_i^m for the i^{th} step may be defined by:

$$E_i^m = \frac{\sum_{n=1}^{N} E_{i,n}}{N}$$

The mean energy defined above is then substituted for the Bethe energy without changing anything else in the schematic diagram of figure 6. The x-ray depth distributions obtained are also plotted on figures 7, 8, and 9; they fit closely with those obtained with the Bethe law. This is not surprising because it seems that the mean value of the Landau distribution must agree with the Bethe formula. This method relates the continuous deceleration law to the mean of the statistical distribution; however it lacks homogeneity. Moreover, the notion of mean energy is not significant in the neighbourhood of the excitation potential.

4.2 General treatment of the simulation of electron trajectories

We now consider the diffuse penetration of electrons into matter in a more realistic fashion by introducing a new random variable, i.e., energy. Figure 10 shows a diagram of the employed method. The first block represents the input of data: physical constants of the target component(s), number of trajectories, energy of primary electrons, and minimum excitation voltage of the calculated element(s). The calculation of the Bethe range (taken as unity) and the length of each step is performed in the second block. The values of λ of equal probability, which have been already calculated and saved on a file, are input into the computer memory. Represented next in the diagram is the trajectory description. When the electron impinges onto the target, the coordinates are initialized to zero as usual and the number of trajectories already made, contained in a storage register, is tested. If this number is greater than the input maximum value, the trajectory description is ended. Otherwise, one more trajectory is started. Let us now suppose that the electron coordinate is Z_{i-1} at the end of the $(i-1)^{th}$ step, the trajectory making a Θ_{i-1} angle with the forward direction; the electron energy E_i^{12} at the half i^{th} step is computed by selecting at random a λ value and using the relationship which links λ, E_{i-1}^{11} and E_i^{12}. The set of scattering angles $\{\theta_i^j\}$ of equal probability is calculated for $E = E_i^{12}$; one of those elements θ_i^j is selected at random and so is α. Furthermore another selection at random of a new λ value gives the end-of-step energy E_i^{11}. If E_i^{11} is lower than the minimum excitation potential, the trajectory is ended and the control is transmitted to the beginning of one more trajectory. Otherwise, the continuation of the i^{th} step proceeds to get Z_i, Θ_i, as previously mentioned in paragraph 2.2.2. The electron is backscattered if $Z_i \leq 0$ or Z_i is located in the appropriate slab of subscript k in which the target has been divided, the contribution of this electron to the $\phi_k(\rho Z)$ depth distribution is calculated for the actual value $\psi(E_i^{11})$ of the ionization cross-section. The results of this general procedure are also plotted in figures 7, 8 and 9.

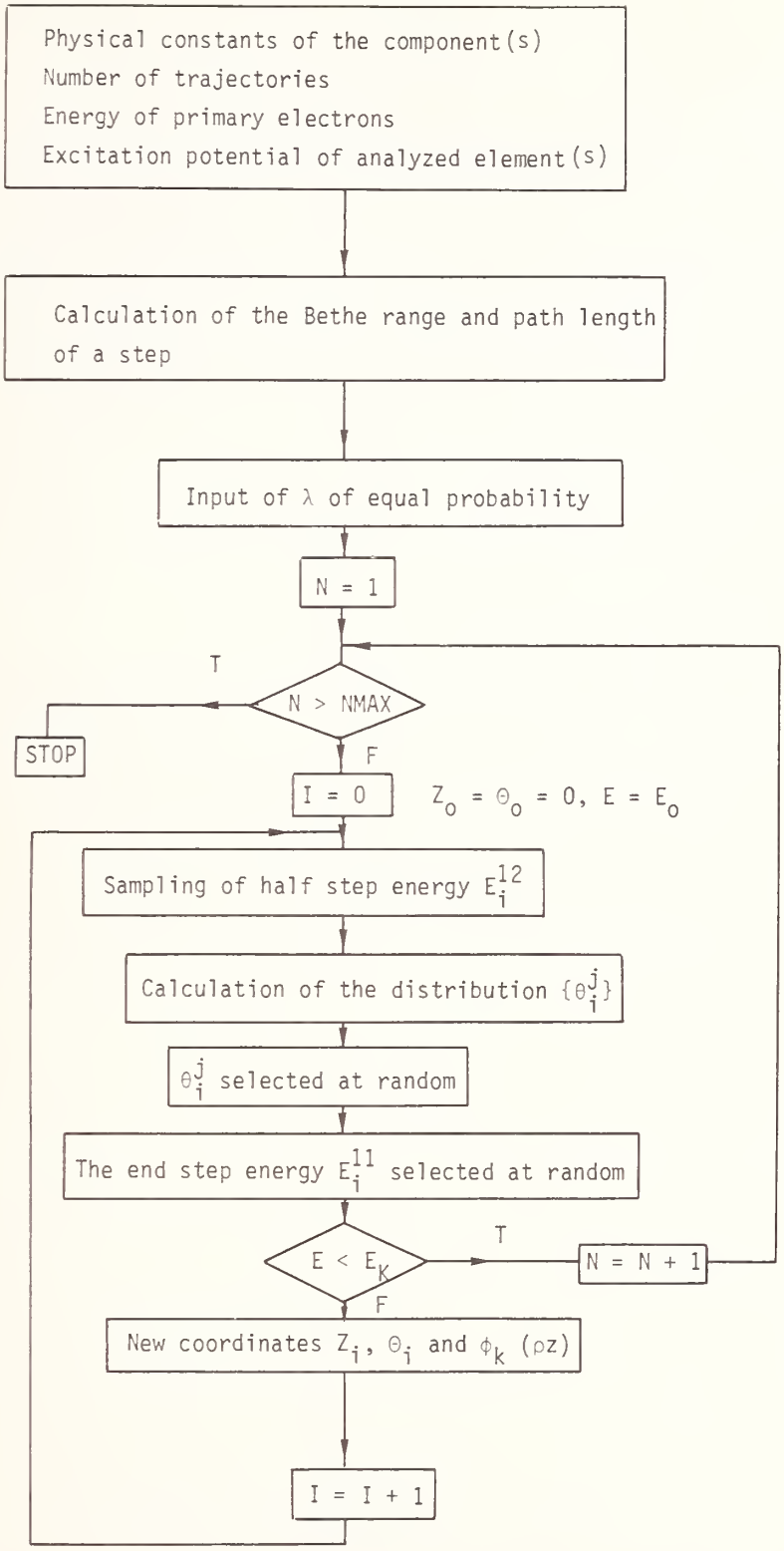

Figure 10. Schematic flow chart of the full treatment for the electron trajectory simulation with statistical energy losses.

4.3 Some alternatives

The general method we have just described is lengthy and computer-time-consuming because the angular scattering distribution depends upon energy which is a random variable. A simpler alternative consists in defining a discrete set $\{\varepsilon_m\}$ of energy values for which the angular distribution is computed once and for all and saved in a file. Let us suppose the electron has the actual energy E_i^{12}; the scattering angle is thus selected at random in the distribution corresponding to the ε_m energy value provided that $|\varepsilon_m - E^{12}|$ is minimum for $E=\varepsilon_m$. As a matter of fact, this induces a slight modification of statistical distribution. Another way to use the set $\{\varepsilon_m\}$ and the related set $\{\theta_m^j\}$ of equal probability scattering angles is to determine the elementary path length $\Delta(\rho s)$ so that the energy decreases from ε_{i-1} to ε_i during the i^{th} step. Consequently, the step lengths are different and the selection at random of a small λ leads to a rather large $\Delta(\rho s)$ and, consequently, to an overestimate of the penetration depth when the multiple scattering theory is used. Finally in a extreme simplification, Shimizu [19] uses an exponential distribution for the statistical energy losses.

On figures 7, 8, and 9 are plotted the depth distributions corresponding to the model first described.

Programs of the different methods used in the present paper are listed and described by Hénoc and Maurice [12].

5. Conclusion

We have reviewed some possibilities of simulating the penetration of electrons in matter according to the Monte Carlo technique. The validity of this method may be tested by comparing theoretical values and experimental curves (Castaing and Descamps, [5]; Castaing and Hénoc, [6]) of the characteristic x-ray depth distribution. The general agreement which is observed allows the use of this technique with some confidence in spite of the differences existing for great depths. Moreover, these differences are somewhat reduced by introducing the statistical energy losses.

The accuracy requirements in routine microanalysis do not justify the expense of the more detailed treatment, and the ZAF method is quite convenient. Nevertheless, the Monte Carlo method is an essential tool for thin specimen analysis. In this field, the computer cost will always be lower than the amount of labor required to get experimental calibration curves.

References

[1] Bethe, H. A., Handb. Phys. 24, 273, (Springer Verlag, Berlin, 1933).

[2] Bishop, H., Thesis, Cambridge University (1966).

[3] Börsch-Supan, W., NBS J. of Research, 65 B n°4, (Oct.-Dec.) 245 (1961).

[4] Castaing, R., Thesis Paris, Publication ONERA N°55 (1951).

[5] Castaing, R. and Descamps, J., J. Phys. Radium 18, 304, (1955).

[6] Castaing, R. and Hénoc, J., 4° Congrès International sur l'Optique des Rayons X et la Microanalyse, Orsay, 120 (Hermann Paris 1966).

[7] Fano, U., Phys. Rev. 33, 117 (1954).

[8] Goudsmit, S. and Saunderson J. L., Phys. Rev. 57, 24 (1940).

[9] Green, M., Proc. Phys. Soc. 82, 204, (1963).

[10] Heinrich, K. F. J., The Electron Microprobe, 296 (John Wiley, New York, 1966).

[11] Hénoc, J. and Maurice, F., Proceedings of the 6th International Conference on X-Ray Optics and Microanalysis, Osaka, 113 (University of Tokyo Press, Tokyo 1972).

[12] Hénoc, J. and Maurice, F., Rapport CEA N°4615 (1975).

[13] Humbert, P. and Colombo, S., Introduction Mathématique à l'étude des théories électromagnétiques, 1, 81 (Gauthiers-Villars, 1949).

[14] Landau, L., J. Phys. USSR 8, 201, (1944).

[15] Sevely, J., Perez, J. and Jouffrey, B., High Voltage Electron Microscopy Proceedings of the 3rd International Conference, Oxford, 32, Academic Press, London 1974).

[16] Philibert, J., 3rd International Symposium on X-Ray Optics and Microanalysis, Stanford, 379 (Academic Press, New York, 1963).

[17] Schiff, L.I., Quantum Mechanics, 162 (McGraw-Hill, New York, 1955).

[18] Shimizu, R, et al., 4é Congrès International sur l'Optique des Rayons X et la Microanalyse, Orsay, 127 (Hermann Paris, 1966).

[19] Shimizu, R., et al., J. of Phys. D (Appl. Phys.) 8, 1 (1975).

[20] Spencer, L. V., Phys. Rev. 98, 1597, (1955).

Appendix I

Electron Deceleration - Landau Theory (1944)

Let us consider an electron of initial energy E traversing the path length s. Let $f(s,\Delta)$ be the probability that this electron suffers an energy loss between Δ and $\Delta + d\Delta$ along this path length s.

Let $\omega(\varepsilon)$ be the probability of an energy loss ε per unit path length.

The relative number of electrons having the energy $E-\Delta$ after traveling through the distance ds is the difference between the number of electrons of energy $E-\Delta+\varepsilon$ which lose the energy ε along the path length ds and those whose energy was originally $E-\Delta$, but have similarly lost energy ε in traversing the same path. The resulting integral equation is the following:

$$\frac{\partial f(s,\Delta)}{\partial s} = \int_0^\infty \omega(\varepsilon)\,[f(s,\Delta-\varepsilon) - f(s,\Delta)]\,d\varepsilon. \tag{1}$$

The Laplace transform of the function $f(s,\Delta)$ is written:

$$\phi(s,p) = \int_0^\infty e^{-p\Delta}\, f(s,\Delta)\, d\Delta.$$

The inverse transform gives:

$$f(s,\Delta) = \frac{1}{2\pi i} \int_{-i\infty+\sigma}^{+i\infty+\sigma} e^{p\Delta}\, \phi(s,p)\, dp$$

a - General solution for $\phi(s,p)$

The derivative of the expression $\phi(s,p)$ with respect to s gives:

$$\frac{\partial \phi(s,p)}{\partial s} = \int_0^\infty \frac{\partial f(s,\Delta)}{\partial s}\, e^{-p\Delta}\, d\Delta \tag{2}$$

Upon multiplying the integral equation (1) by $e^{-p\Delta}$ and then integrating with respect to Δ, we obtain:

$$\int_0^\infty e^{-p\Delta}\, \frac{\partial f(s,\Delta)}{\partial s}\, d\Delta = \int_0^\infty \omega(\varepsilon) \left[\int_0^\infty e^{-p\Delta} [f(s,\Delta-\varepsilon)-f(s,\Delta)]\, d\Delta \right] d\varepsilon.$$

Comparing with (2), $\frac{\partial \phi(s,p)}{\partial s}$ appears in the left-hand side of the above equation.

The innermost integral of the right-hand side is calculated by using the characteristics of the Laplace transform for a linear change of the variable.

Let us calculate $\int_0^\infty e^{-p\Delta}\, [f(\Delta-\varepsilon) - f(\Delta)]\, d\Delta$

(In the calculation of this integral the parameter s is omitted in order to simplify the notation.)

Upon a change of variable $\Delta = t - \varepsilon$, $d\Delta = dt$, we have:

$$\int_0^\infty e^{-p\Delta} f(\Delta)\, d\Delta = \int_\varepsilon^\infty e^{-p(t-\varepsilon)} f(t-\varepsilon)\, dt$$

$$\int_0^\infty e^{-p\Delta} f(\Delta)\, d\Delta = e^{+p\varepsilon} \int_\varepsilon^\infty e^{-pt} f(t-\varepsilon)\, dt$$

since $f(\Delta) = 0$ for $\Delta < 0$, it follows that $f(t-\varepsilon) = 0$ for $t < \varepsilon$.

Thus, we can replace the lower limit by 0.

By multiplying both sides of the equation by $e^{-p\varepsilon}$, we obtain:

$$e^{-p\varepsilon} \int_0^\infty e^{-p\Delta} f(\Delta)\, d\Delta = \int_0^\infty e^{-pt} f(t-\varepsilon)\, dt$$

thus: $\int_0^\infty e^{-p\Delta} [f(s,\Delta-\varepsilon) - f(s,\Delta)]\, d\Delta = (e^{-p\varepsilon}-1) \int_0^\infty e^{-p\Delta} f(s,\Delta)\, d\Delta = (e^{-p\varepsilon}-1)\, \phi(s,p)$

It remains to perform the last integration:

$$\int_0^\infty \omega(\varepsilon)\, (e^{-p\varepsilon} - 1)\, \phi(s,p)\, d\varepsilon = \phi(s,p) \int_0^\infty \omega(\varepsilon)\, (e^{-p\varepsilon} - 1)\, d\varepsilon$$

Let us come back to the initial equation:

$$\frac{\partial \phi(s,p)}{\partial s} = - \phi(s,p) \int_0^\infty \omega(\varepsilon)\, (1 - e^{-p\varepsilon})\, d\varepsilon \qquad (3)$$

$$\frac{d\phi(s,p)}{\phi(s,p)} = - ds \int_0^\infty \omega(\varepsilon)\, (1 - e^{-p\varepsilon})\, d\varepsilon$$

We obtain by integrating with respect to s

$$\ln \phi(s,p) - \ln K = - s \int_0^\infty \omega(\varepsilon)\, (1 - e^{-p\varepsilon})\, d\varepsilon \qquad (4)$$

The boundary conditions give:

$$f(0,\Delta) = \delta(\Delta)$$

since all the electrons have the initial energy E_0 at the surface of the thin foil, and we can deduce:

$$\phi(o,p) = \int_0^\infty f(o,\Delta) e^{-p\Delta}\, d\Delta = \int_0^\infty e^{-p\Delta}\, \delta(\Delta)\, d\Delta = 1 \qquad (5)$$

By comparing (4) and (5), we find K = 1 and finally:

$$\phi(s,p) = e^{-s \int_0^\infty \omega(\varepsilon)\,(1 - e^{-p\varepsilon})\,d\varepsilon} \tag{6}$$

b - Approximation for a particular solution of $\phi(s,p)$

We intend to evaluate $\int_0^\infty \omega(\varepsilon)\,(1 - e^{-p\varepsilon})\,d\varepsilon$. (7)

The solution of the problem requires the knowledge of $\omega(\varepsilon)$. $\omega(\varepsilon)$ has been determined only for losses which are large with respect to the binding energy of atomic electrons. With the trick used by Landau, a complete knowledge of $\omega(\varepsilon)$ is not necessary. Let us set:

ε_o - the characteristic energy of the atom, of the same order of magnitude as the binding energy of the atomic electrons.

ε_{max} - the maximum energy which can be transferred in an ionization.

In the integral (7) under consideration, we suppose that only the values of p for which $p\varepsilon_o \ll 1$ and $p_{max} \gg 1$ are important.

Then, we can define ε_1 such that:

$$\varepsilon_1 \gg \varepsilon_0$$

$$p\varepsilon_1 \ll 1$$

The integral is written:

$$\int_0^\infty \omega(\varepsilon)\,(1 - e^{-p\varepsilon})\,d\varepsilon = \int_0^{\varepsilon_1} \omega(\varepsilon)\,(1 - e^{-p\varepsilon})\,d\varepsilon + \int_{\varepsilon_1}^\infty \omega(\varepsilon)\,(1 - e^{-p\varepsilon})\,d\varepsilon$$

Resolution of the first integral

$$e^{-p\varepsilon} = 1 - p\varepsilon \quad \text{since} \quad p\varepsilon_1 \ll 1$$

$$\int_0^{\varepsilon_1} \omega(\varepsilon)\,(1-e^{-p\varepsilon})\,d\varepsilon = \int_0^{\varepsilon_1} \omega(\varepsilon)\,(1-1+p\varepsilon)\,d\varepsilon = p \int_0^{\varepsilon_1} \omega(\varepsilon)\varepsilon \; d\varepsilon$$

$\int_0^{\varepsilon_1} \omega(\varepsilon)\,\varepsilon\,d\varepsilon$ expresses the mean energy loss along the path length ds. Then, we can apply the Bethe formula; consequently, we have:

$$\int_0^{\varepsilon_1} \omega(\varepsilon)\,\varepsilon\,d\varepsilon = \frac{\pi N e^4}{E}\,\rho\,\frac{Z}{A}\,\ln\left(\frac{4E}{J^2}\,\varepsilon_1\right)$$

Resolution of the second integral

For $\varepsilon_o << \varepsilon << \varepsilon_{max}$, we can use for $\omega(\varepsilon)$ the familiar expression:

$$\omega(\varepsilon) = \frac{\pi N e^4}{E} \rho \frac{Z}{A} \frac{1}{\varepsilon^2}$$

$$\int_{\varepsilon_1}^{\infty} \omega(\varepsilon) (1-e^{p\varepsilon}) d\varepsilon = \frac{\pi e^4 N}{E} \rho \frac{Z}{A} \int_{\varepsilon_1}^{\infty} \frac{1 - e^{-p\varepsilon}}{\varepsilon^2} d\varepsilon$$

$$= \frac{\pi e^4 N}{E} \rho \frac{Z}{A} \left[\left| \frac{1}{\varepsilon} \right|_{\varepsilon_1}^{\infty} - \int_{\varepsilon_1}^{\infty} \frac{e^{-p\varepsilon}}{\varepsilon^2} d\varepsilon \right]$$

$$= \frac{\pi e^4 N}{E} \rho \frac{Z}{A} \left[\frac{1}{\varepsilon_1} (1 - e^{-p\varepsilon_1}) + p \int_{\varepsilon_1}^{\infty} \frac{e^{-p\varepsilon}}{\varepsilon} d\varepsilon \right]$$

$e^{-p\varepsilon_1} = 1 - p\varepsilon_1$ because $p\varepsilon_1 << 1$

$$= \frac{\pi e^4 N}{E} \rho \frac{Z}{A} p \left[1 + \int_{\varepsilon_1}^{\infty} \frac{e^{-p\varepsilon}}{p\varepsilon} dp\varepsilon\right]$$

$$= \frac{\pi e^4 N}{E} \rho \frac{Z}{A} p \left[1 + Ei (p\varepsilon_1)\right]$$

The expansion of Ei (x) gives:

$$Ei (x) = - C - \ln x + \sum_{n=1}^{10} (-1)^{(n-1)} \frac{x^n}{x \cdot x!}$$

where C is the Euler constant.

The expansion can be limited to the two first terms where $x << 1$

$$= \frac{\pi e^4 N}{E} \rho \frac{Z}{A} p \left[1 - C - \ln (p\varepsilon_1) \right]$$

Finally: $\int_0^{\infty} \omega(\varepsilon) (1 - e^{-p\varepsilon}) d\varepsilon$

$$= \frac{\pi N e^4}{E} \rho \frac{Z}{A} p \left[\ln \frac{4E}{J^2} + \ln \varepsilon_1 + 1 - C - \ln \varepsilon_1 - \ln p\right]$$

Upon returning to the expression (6) of $\phi(s,p)$, we obtain:

$$\phi(s,p) = e^{-\left[\frac{\pi N e^4}{E} \frac{Z}{A} \rho s p \left(1 - C - \ln \left(\frac{J^2 p}{4E}\right)\right)\right]} \qquad (8)$$

c -Probability density

Replacing $\phi(s,p)$ by (8) in the expression of the inverse Laplace transform, we obtain the probability density $f(s,\Delta)$.

$$f(s,\Delta) = \frac{1}{2\pi i} \int_{-i\infty+\sigma}^{+i\infty+\sigma} e^{p\left[\Delta - \frac{\pi N e^4}{E} \frac{Z}{A} \rho s \left(1 - C - \ln\left(\frac{J^2 p}{4E}\right)\right)\right]} dp$$

setting $u = \xi p$ with $\xi = \frac{\pi N e^4}{E} \frac{Z}{A} \rho s$

$$\boxed{f(s,\Delta) = \frac{1}{2\pi i} \frac{1}{\xi} \int_{-i\infty+\sigma}^{+i\infty+\sigma} e^{u(\ln u + \lambda)} du = \frac{1}{\xi} P(\lambda)}$$

where: $$\lambda = \frac{\Delta - \xi\left(1 - C + \ln\left(\frac{4E}{J^2}\xi\right)\right)}{\xi} .$$

By introducing the Bethe mean energy loss written according to the Landau notation:

$$\frac{\overline{\Delta}}{\xi} = 2 \ln\left(1.166 \frac{E}{J}\right)$$

we obtain: $$\lambda = \frac{\Delta - \overline{\Delta}}{\xi} + \ln\left(\frac{E}{\xi}\right) - 1.502$$

The constant 1.502 is different from that of Spencer as reported by Bishop. The origin of this difference is due to the fact that the deceleration function used by Spencer is applied to energies of a different order of magnitude.

Borsh-Supan [3] has given another form of $P(\lambda)$ which is more convenient for computation. Detailed calculations are given in Appendix III.

$$P(\lambda) = \frac{1}{2 i \pi} \int_{-i\infty+\sigma}^{+i\infty+\sigma} \exp\left(u(\ln u + \lambda)\right) du$$

is plotted in the figure.

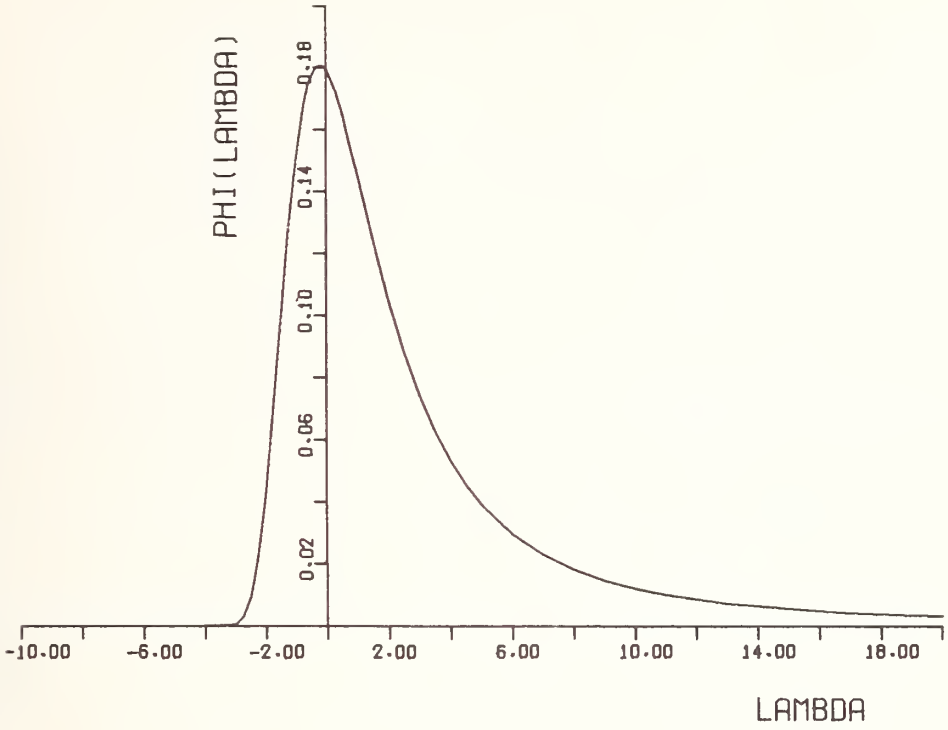

d - Distribution function for the energy loss

The distribution function $F(\lambda)$ is obtained by integrating the probability density $P(\lambda)$

$$F(\lambda) = \int_{\lambda_o}^{\lambda} P(\lambda)\, d\lambda$$

for $\lambda_o < \lambda < +\infty$

where λ_o is the value of λ corresponding to $\Delta = 0$.

This integral is calculated numerically according to Gauss method. The figure below is the plot of $F(\lambda)$.

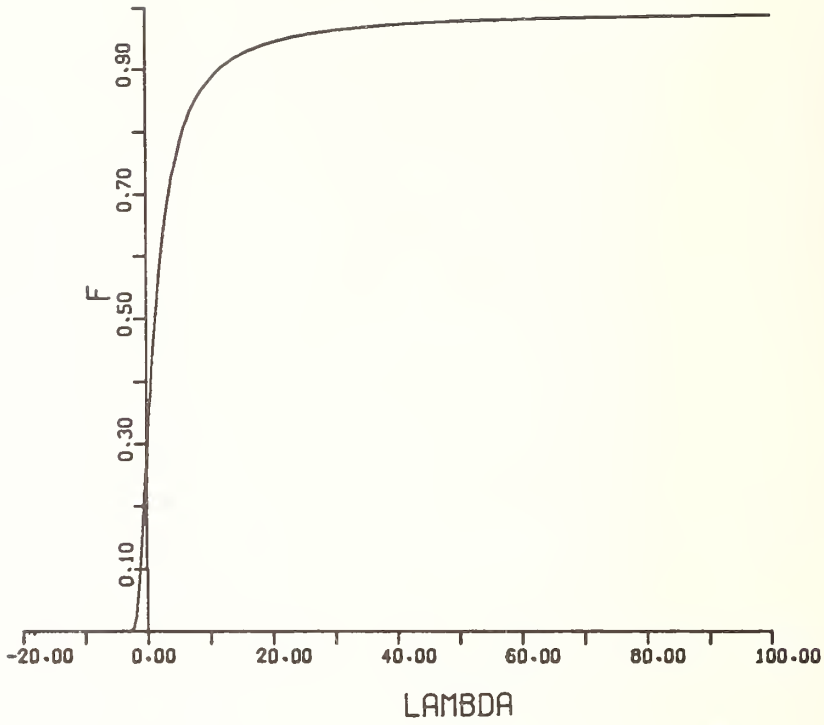
F
0.90
0.70
0.50
0.30
0.10
-20.00
0.00
20.00
40.00
60.00
80.00
100.00
LAMBDA

Appendix II

Electron Scattering

As it has been pointed out above, the elementary path length we have used for practical purposes is roughly an order of magnitude larger than the mean free path. Consequently a multiple scattering theory must be employed. The multiple scattering is derived from the single scattering by a convolution process; the aim of this appendix is to give an outline of this theory.

1 - Elastic single scattering cross-section

In quantum mechanics, the incident particle is represented by a plane wave $\psi_o(\vec{r})$; this plane wave is scattered by the atoms of the medium into a wave which behaves as a spherical wave at a great distance r from the scattering center. The total electron wave function is

$$\psi(\vec{r}) = \psi_o(\vec{r}) + f(\theta,\phi)\ \frac{\exp\ (i\vec{k}\cdot\vec{r})}{r}$$

where $f(\theta,d)$ is the scattering factor. The density of scattered particles at $M(r,\theta,\phi)$ is then

$$\frac{1}{r^2}\ |f(\theta,\phi)|^2$$

The differential scattering cross-section σ is the probability for an electron to be scattered into the direction (θ,ϕ) in the solid angle $d\Omega$ thus:

$$\sigma(\theta,\phi) = \frac{1}{r^2}\ |f(\theta,\phi)|^2\ r^2\ d\Omega = |f(\theta,\phi)|^2$$

Scattering obviously has a cylindrical symmetry, so that we can write

$$\sigma(\theta) = |f(\theta)|^2$$

For elastic scattering, the conservation law implies that the moduli of the incident and scattered wave vectors $\vec{k}$ and $\vec{k}'$ are equal. The scattering wave vector $\vec{q} = \vec{k}' - \vec{k}$ is related to the scattering angle by

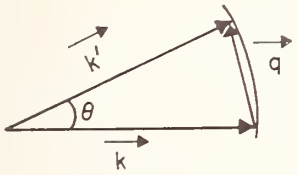

$$|\vec{q}| = 2\ |\vec{k}|\ \sin\frac{\theta}{2}\ ,\ \text{with}\ |\vec{k}| = \frac{2\pi}{\lambda}$$

where λ is the wavelength associated with the particle.

Under typical experimental conditions of microanalysis, the perturbing potential introduced by the scattering atom is small with respect to the energy of the incident electron. The diffusion amplitude is calculated according to the Born approximation and it can be shown that $f(\theta)$ is the Fourier transform $v(q)$ of the interaction potential $v(r)$ between the incident electron and the atom (Schiff, [17]):

$$f(\theta) = \frac{m}{2\pi\hbar^2} v(\vec{q})$$

where m is the electron mass and $\hbar = \frac{h}{2\pi}$, with h the Planck constant

$$v(\vec{q}) = \int v(r) \exp (i \vec{q}\cdot\vec{r}) \, d_3 r$$

To take into account the screening of the nuclear charge Z by atomic electrons, a screened coulomb potential is chosen for $v(\vec{r})$

$$v(\vec{r}) = \frac{Z e^2}{r} \exp (- \frac{r}{R})$$

The screening parameter R is essentially the atomic radius

$$R = k \, a_H^{-1/3}$$

a_H = first Bohr radius of the hydrogen atom

$$k = 1$$

The Fourier transform calculations of the $v(r)$ potential can be found in Appendix IV. The final result is:

$$v(\vec{q}) = \frac{4 \pi Z e^2}{\frac{1}{R^2} + q^2}$$

Then:

$$f(\theta) = -\frac{m}{2\pi\hbar^2} \frac{4\pi Z e^2}{(\frac{1}{R^2} + q^2)}$$

and

$$\sigma(\theta) = \frac{4 m^2 Z^2 e^4}{\hbar^4 (\frac{1}{R^2} + q^2)^2}$$

By substituting $2\ k \sin\frac{\theta}{2}$ for q and factoring $4\ k^2$ in the denominator, the electron kinetic energy E can be introduced as

$$E = \frac{\hbar^2\ k^2}{2\ m}$$

$$\sigma(\theta) = \frac{4\ m^2\ Z^2\ e^4}{16\ \hbar^4 k^4\ \left(\frac{1}{4R^2k^2} + \sin^2\frac{\theta}{2}\right)^2} = \frac{Z^2\ e^4}{16E^2\ \left(\sin^2\frac{\theta}{2} + \frac{1}{4R^2k^2}\right)^2}$$

setting $\theta_o = \frac{\lambda}{2\ \pi\ R}$ or $\theta_o = \frac{2\pi}{k}\ \frac{1}{2\pi R} = \frac{1}{kR}$

$$\boxed{\sigma(\theta) = \frac{Z^2\ e^4}{16\ E^2\ \left(\sin^2\frac{\theta}{2} + \frac{\theta_o^2}{4}\right)^2}}$$

$\sigma(\phi)$ is the differential single scattering cross-section. The total cross-section σ_E is obtained by integrating $\sigma(\theta)$ over the whole solid angle 4π

$$\sigma_E = \int_\Omega \sigma(\theta)\ d\Omega = \int_o^\pi \sigma(\theta)\ 2\pi\ \sin\theta\ d\theta$$

$$\sigma_E = \int_o^\pi \frac{2\pi\ Z^2\ e^4}{16\ E^2}\ \frac{\sin\ \theta}{\left(\sin^2\frac{\theta}{2} + \frac{\theta_o^2}{4}\right)^2}\ d\theta$$

setting $\alpha = \frac{\theta_o^2}{4}$. Then:

$$\int_o^\pi \frac{\sin\theta\ d\theta}{\left(\sin^2\frac{\theta}{2} + \alpha\right)^2} = \int_o^\pi \frac{2\ \sin\frac{\theta}{2}\cos\frac{\theta}{2}}{\left(\sin^2\frac{\theta}{2} + \alpha\right)^2}\ d\theta$$

setting $u = \frac{\theta}{2}$.

The integral becomes:

$$\int_o^{\pi/2} \frac{4\ \sin\ u\ \cos\ u}{\left(\sin^2\ u + \alpha\right)^2}\ du$$

setting v = sin u

$$\int_o^1 \frac{4\ v\ dv}{(v^2+\alpha)^2} = 2\left|-\frac{1}{(v^2+\alpha)}\right|_o^1 = \frac{2}{\alpha(1+\alpha)}$$

$$\sigma_E = \left(\frac{Ze^2}{2E}\right)^2 \frac{\pi}{\alpha(1+\alpha)}$$

the ratio $\frac{\sigma(\theta)}{\sigma_E}$ gives the scattering form factor

$$f(\theta) = \frac{\alpha(1+\alpha)}{\pi} \frac{1}{(1+2\alpha - \cos\theta)^2}$$

According to Spencer [20] and Fano [7], the total cross-section σ_E is multiplied by the factor $\frac{Z+1}{Z}$ in order to take into account the contribution of inelastic scattering.

2 - Distribution function for multiple scattering

The calculation is performed according to the Goudsmit and Saunderson method [8] using the convolution of the single scattering cross-section expanded in terms of Legendre polynomials.

2.1 - Expansion of the single scattering cross-section

The $f(\theta)$ expansion as a Legendre series can be written:

$$f(\theta) = \frac{1}{4\pi} \sum_{n=0}^{\infty} (2n+1)\, a_n\, P_n(\cos\theta)$$

with:
$$a_n = \int_0^{\pi} 2\pi\, f(\theta)\, P_n(\cos\theta)\, \sin\theta\, d\theta$$

in which:
$$f(\theta) = \frac{\alpha(1+\alpha)}{\pi} \frac{1}{(1+2\alpha-\cos\theta)^2}$$

with:
$$\alpha = 3.4 \cdot 10^{-3}\, Z^{2/3}/E$$

$$a_n = \int_0^{\pi} 2\pi \frac{\alpha(1+\alpha)}{\pi} \frac{1}{(1+2\alpha-\cos\theta)^2} P_n(\cos\theta)\, \sin\theta\, d\theta$$

$$a_n = 2\alpha(1+\alpha) \int_{\pi}^{0} \frac{1}{(1+2\alpha-\cos\theta)^2} P_n(\cos\theta)\, d(\cos\theta) = 2\alpha(1+\alpha) \int_{-1}^{+1} \frac{1}{(1+2\alpha-u)^2} P_n(u)\, du$$

setting $x = 1 + 2\alpha$

$$a_n/2\alpha\,(1+\alpha) = \int_{-1}^{+1} \frac{1}{(x-u)^2} P_n(u)\, du$$

but:

$$\frac{1}{(x-u)^2} = -\frac{d}{dx}\frac{d}{(x-u)}$$

then:

$$a_n/2\alpha\,(1+\alpha) = -\frac{d}{dx}\int_{-1}^{+1}\frac{P_n(u)}{x-u}\,du = -2\left[\frac{d}{dx}\int_{-1}^{+1}\frac{P_n(u)}{2(x-u)}\,du\right]$$

so that $a_n/2\alpha(1+\alpha) = -2\frac{d}{dx}Q_n(x)$ where $Q_n(x)$ is the second kind Legendre function. The $Q_n(x)$ functions are linked by the two relations (Humbert and Colombo, [13]):

$$\left\|\begin{array}{l} n\,Q_n = x\,Q_n' - Q_{n-1}' \\ (n+1)\,Q_n = Q_{n+1}' - x\,Q_n' \end{array}\right.$$

by multiplying the first of these by (n+1), the second one by -n, and by then adding

$$n\,Q_{n+1}' = (2n+1)\,x\,Q_n' - (n+1)\,Q_{n-1}' \ .$$

Then sucessive Q_n' are deduced by recurrence from the first two;

from $Q_0(x) = \frac{1}{2}\,L\,(\frac{x+1}{x-1})$ we get $Q_0'(x) = -\frac{1}{(x+1)(x-1)} = -\frac{1}{4\alpha(1+\alpha)}$

from $Q_1(x) = \frac{x}{2}\,L\,(\frac{x+1}{x-1}) - 1$ we get $Q_1'(x) = \frac{1}{2}\,ln\,(\frac{x+1}{x-1}) - \frac{x}{(x+1)(x-1)}$

$$Q_1'(x) = \frac{-1}{4\alpha(1+\alpha)}\left(1+2\alpha+2\alpha(1+\alpha)\,ln\,(\frac{\alpha}{1+\alpha})\right)$$

$a_0 = -4\alpha\,(1+\alpha)\,Q_0' = 1$

$a_1 = -4\alpha\,(1+\alpha)\,Q_1' = 1 + 2\alpha + 2\alpha\,(1+\alpha)\,ln\,(\frac{\alpha}{1+\alpha})$.

The different a_n can be defined from the same recurrent law:

$$n\,a_{n+1} = (2n+1)\,(1+2\alpha)\,a_n - (n+1)\,a_{n-1}$$

the initial value of n being 1.

2.2 - Convolution of two functions expanded in terms of Legendre series - Generalizations

Let us consider an electron beam with the given angular distribution

$$f_1(\theta_1) = \frac{1}{4\pi} \sum_{n=o}^{\infty} (2n+1)\ a_n\ P_n\ (\cos\ \theta_1)$$

After one collision (see figure), the angular distribution is

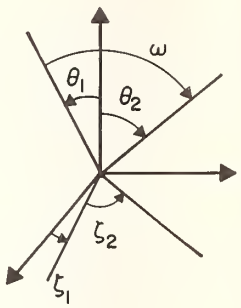

$$F(\theta_2)\ d\Omega_2 = \int f_1(\theta_1)\ d\Omega_1\ f_2(\omega)\ d\Omega_2$$

where:

$$f_2(\omega) = \frac{1}{4\pi} \sum_{n=o}^{\infty} (2n+1)\ b_n\ P_n\ (\cos\omega)$$

denotes the single scattering cross-section after one collision; by substituting this expression for $f_2(\omega)$ we get:

$$F(\theta_2) = \int f_1(\theta_1)\ d\Omega_1\ \frac{1}{4\pi} \sum_{n=o}^{\infty} (2n+1)\ b_n\ P_n\ (\cos\omega)$$

from the addition theorem of Legendre polynomials:

$$P_n(\cos\omega) = P_n(\cos\theta_1)\ P_n(\cos\theta_2) + 2 \sum_{k=1}^{n} \frac{(n-k)!}{(n+k)!}\ p_n^k(\cos\theta_1)\ p_n^k(\cos\theta_2)\ \cos\ k(\phi_2 - \phi_1)$$

the last term vanishes when the summation is performed over all the possible values of $(\phi_2 - \phi_1)$

thus:

$$F(\theta_2) = \frac{1}{4\pi} \sum_{n=o}^{\infty} (2n+1)\ b_n P_n(\cos\theta_2) \int_o^{\pi} f_1(\theta_1)\ P_n(\cos\theta_1)\ 2\pi\ \sin\theta\ d\theta$$

but $\int_o^{\pi} f_1(\theta_1)\ P_n(\cos\theta_1)\ 2\pi\ \sin\theta\ d\theta = a_n$; then

$$F\ (\theta_2) = \frac{1}{4\pi} \sum_{n=o}^{\infty} (2n+1)\ a_n\ b_n\ P_n\ (\cos\theta_2)$$

Generalizing, we can say that, when the primary beam distribution is:

$$f_o(\theta) = \frac{1}{4\pi} \sum_{n=o}^{\infty} (2n+1)\ a_n\ P_n\ (\cos\theta)$$

and when the single scattering cross-section after the i^{th} collision is:

$$f_i(\theta) = \frac{1}{4\pi} \sum_{n=o}^{\infty} (2n+1)\ i_n\ P_n\ (\cos\theta)$$

the angular distribution after m collisions will be:

$$f_m(\theta) = \frac{1}{4\pi} \sum_{n=o}^{\infty} (2n+1)\ a_n\ b_n\ c_n\ .....\ i_n\ P_n\ (\cos\theta)$$

In the following particular case, when the primary beam is a $\delta(\theta)$ Dirac distribution:

$$a_n = \int \delta(1-u)\ P_n(u)\ du = 1$$

and when after any number of collisions the single scattering cross-section is the screened Rutherford expression: $b_n = c_n = ... = i_n$, we obtain the simpler form:

$$\boxed{f_m(\theta) = \frac{1}{4\pi} \sum_{n=o}^{\infty} (2n+1)\ b_n^m\ P_n\ (\cos\theta)}$$

2.3 - Scattering distribution function

The mean number p of collisions suffered by an electron which has traveled through $\Delta(\rho s)$ is $p = \frac{N}{A}\ \sigma_E\ \Delta(\rho s)$. If we assume that the distribution $\Pi(m)$ of the collision number m obeys the Poisson law, we can write:

$$\Pi(m) = \frac{p^m}{m!}\ \exp\ (-p)$$

The scattering probability density function is then:

$$\boxed{F(p,\theta) = \sum_{m=o}^{\infty} f_m(\theta)\ \Pi(m)} = \frac{1}{4\pi} \sum_{n=o}^{\infty} (2n+1) \left[\sum_{m=o}^{\infty} \frac{p^m\ \exp\ (-p)}{m!}\ b_n^m \right] P_n\ (\cos\theta)$$

$$= \frac{1}{4\pi} \sum_{n=o}^{\infty} (2n+1)\ \exp\ (p\ b_n)\ \exp\ (-p)\ P_n\ (\cos\theta)$$

$$= \frac{1}{4\pi} \sum_{n=o}^{\infty} (2n+1)\ \exp(-p(1-b_n))\ P_n\ (\cos\theta)$$

$$= \exp\ (-p) \left[\frac{1}{4\pi} \sum_{n=o}^{\infty} (2n+1)\ \exp\ (p\ b_n)\ P_n\ (\cos\theta) \right]$$

According to Bishop, the unscattered fraction of the electron beam must be taken separately in order to get a faster convergence:

$$F(p,\theta) = \exp(-p)\left[\delta(\theta) + \frac{1}{4\pi}\sum_{n=0}^{\infty}(2n+1)\,(\exp(p\,b_n)-1)\,P_n(\cos\theta)\right]$$

with

$$\delta(\theta) = \frac{1}{4\pi}\sum_{n=0}^{\infty}(2n+1)\,P_n(\cos\theta)$$

The distribution function $G(\theta)$ is obtained by integrating the above scattering probability density $F(p,\theta)$

$$G(\theta) = 2\pi\int_0^{\theta} F(p,\theta)\,\sin\theta\,d\theta$$

2.3.1 - Distribution function related to a Legendre series probability density function

It will now be shown that in this case the distribution function can be simply written in terms of the Legendre coefficients.

Setting:

$$F(\theta) = \frac{1}{4\pi}\sum_{n=0}^{\infty}(2N+1)\,b_n\,P_n(\cos\theta)$$

as the Legendre series, the distribution function $G'(\theta)$ becomes:

$$G'(\theta) = \frac{1}{4\pi}\int_0^{\theta}\sum_{n=0}^{\infty}(2n+1)\,b_n\,P_n(\cos\theta)\,2\pi\,\sin\theta\,d\theta$$

$$G'(\theta) = \frac{1}{2}\sum_{n=0}^{\infty} b_n\int_0^{\theta}(2n+1)\,P_n(\cos\theta)\,\sin\theta\,d\theta$$

$$= \frac{1}{2}\left[b_0\int_0^{\theta}P_0(\cos\theta)\,\sin\theta\,d\theta + \sum_{n=1}^{\infty}\int_0^{\theta} b_n(2n+1)\,P_n(\cos\theta)\,\sin\theta\,d\theta\right]$$

$$= \frac{1}{2}\left[b_0\int_0^{\theta}\sin\theta\,d\theta + \sum_{n=1}^{\infty} b_n\int_0^{\theta}(2n+1)\,P_n(\cos\theta)\,\sin\theta\,d\theta\right]$$

setting $u = \cos\theta$

$$= \frac{1}{2}\left[b_0\,(1-P_1(u)) - \sum_{n=1}^{\infty} b_n\int_0^{\cos\theta}(2n+1)\,P_n(u)\,du\right]$$

The recurrence formulae give:

$$- P'_{n-1}(u) + uP'_n(u) = n\, P_n(u)$$

$$+ P'_{n+1}(u) - uP'_n(u) = (n+1)\, P_n(u)$$

by adding: $(2n+1)\, P_n(u) = P'_{n+1}(u) - P'_{n-1}(u)$

by integrating $(2n+1) \int P_n(u) = P_{n+1}(u) - P_{n-1}(u)$

by substituting in the above value of $G'(\theta)$, we get:

$$G'(\theta) = \frac{1}{2} \left[b_0 \left(1 - P_1(u)\right) - \sum_{n=1}^{\infty} b_n \left(P_{n+1}(u) - P_{n-1}(u)\right) \right]$$

by adding term to term

$$G'(\theta) = \frac{1}{2} \left[b_0 \left(1 - P_1(u)\right) + b_1 P_0(u) + b_2 P_1(u) + \sum_{n=1}^{\infty} \left(b_{n+2} - b_n\right) P_{n+1}(u) \right]$$

$$= \frac{1}{2} \left[b_0 + b_1\, P_0(u) + \left(b_2 - b_0\right) P_1(u) - \sum_{n=1}^{\infty} \left(b_n - b_{n+2}\right) P_{n+1}(u) \right]$$

$$= \frac{1}{2} \left[b_0 + b_1\, P_0(u) - \sum_{n=1}^{\infty} \left(b_{n-1} - b_{n+1}\right) P_n(u) \right]$$

2.3.2 - Numerical computation

By replacing the b_n coefficients by their expressions while taking into account the unscattered part of the beam, we get:

$$G(\theta) = \exp(-p) \left[1 + \frac{1}{2}\left(\exp(pa_0) - 1\right) + \frac{1}{2}\left(\exp(pa_1) - 1\right) - \sum_{n=1}^{\infty} \frac{1}{2}\left(\exp(pa_{n-1}) - \exp(pa_{n+1})\right) P_n(\cos\theta) \right]$$

$$\boxed{G(\theta) = \frac{1}{2} + \frac{1}{2} \exp\left(pa_1 - p\right) - \sum_{n=1}^{\infty} \frac{1}{2} \left[\exp\left(pa_{n-1} - p\right) - \exp\left(pa_{n+1} - p\right) \right] P_n(\cos\theta)}$$

This form is particularly well adapted to computation.

Appendix III

Calulation of: $$P(\lambda) = \frac{1}{2\,i\,\pi} \int_{-i\infty+\sigma}^{+i\infty+\sigma} e^{u(\ln u + \lambda)}\, du$$

σ may have any value provided that the singularities of the integrand are located on the left of the vertical axis going through σ. According to Borsh-Supan [3], we may take for σ the real value of the variable for which the integrand has an extremum. The derivative of the function equals zero for $u = e^{-(1+\lambda)}$.

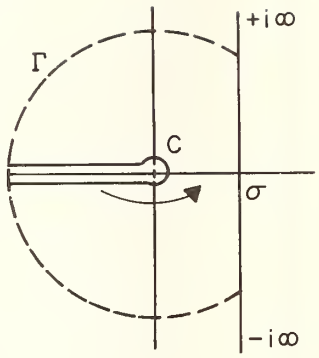

Then we set: $\sigma = e^{-(1+\lambda)}$.

The following change of variable is made:

$$u = \sigma + i\,y \qquad \text{or} \qquad u = \rho\, e^{i\theta}$$

$$P(\lambda) = \frac{1}{2\pi} \int_{-\infty}^{+\infty} e^{(\sigma+iy)(\ln\rho e^{i\theta}+\lambda)}\, dy$$

The integral is separated into two parts

$$P(\lambda) = \frac{1}{2\pi} \left[\int_{-\infty}^{0} e^{(\sigma+iy)(\ln\rho e^{i\theta}+\lambda)}\, dy + \int_{0}^{+\infty} e^{(\sigma+iy)(\ln\rho e^{i\theta}+\lambda)}\, dy \right]$$

In the first integral, transforming y into - y, ρ into ρ and θ into - θ, we obtain:

$$P(\lambda) = \frac{1}{2\pi} \int_{0}^{+\infty} \left[e^{(\sigma-iy)(\ln\rho e^{-i\theta}+\lambda)} + e^{(\sigma+iy)(\ln\rho e^{i\theta}+\lambda)} \right]$$

since $\sigma = e^{-(1+\lambda)}$, $\ln\sigma = -(1+\lambda)$ and $\lambda = -1 - \ln\sigma$

$$P(\lambda) = \frac{1}{2\pi} \int_{0}^{+\infty} \left[e^{(\sigma-iy)(\ln\rho-i\theta)-(1+\ln\sigma)(\sigma-iy)} + e^{(\sigma+iy)(\ln\rho+i\theta)-(1+\ln\sigma)(\sigma+iy)} \right] dy$$

We separate the real and imaginary exponents of e

$$P(\lambda) = \frac{1}{2\pi} \int_{0}^{+\infty} \left[e^{(\sigma\ln\rho-y\theta-\sigma-\sigma\ln\sigma)} e^{-i(y\ln\rho+\theta\sigma-y-y\ln\sigma)} + e^{(\sigma\ln\rho-y\theta-\sigma-\sigma\ln\sigma)} e^{+i(y\ln\rho+\theta\sigma-y-y\ln\sigma)} \right] dy$$

We set: $\ln\sigma = \frac{1}{2}\ln\sigma^2$, $\theta = \operatorname{arctg}\frac{y}{\sigma}$, $\ln\rho = \frac{1}{2}\ln(\sigma^2 + y^2)$

$$P(\lambda) = \frac{1}{2\pi} \left\{ e^{-\sigma} \int_{0}^{\infty} e^{\left(\frac{\sigma}{2}\ln\left(\frac{\sigma^2+y^2}{\sigma^2}\right) - y \operatorname{arctg}\frac{y}{\sigma}\right)} \left[e^{iy\left(\frac{1}{2}\ln\left(\frac{\sigma^2+y^2}{\sigma^2}\right)-1\right)+\sigma\operatorname{arctg}\frac{y}{\sigma}} + e^{-i\left(\frac{1}{2}\ln\left(\frac{\sigma^2+y^2}{2}\right)-1\right)+\sigma\operatorname{arctg}\frac{y}{\sigma}} \right] \right\} dy$$

The first form for $P(\lambda)$ is:

$$P(\lambda) = \frac{e^{-\sigma}}{\pi} \int_0^{+\infty} e^{\left(\frac{\sigma}{2} \ln\left(1+\frac{y^2}{\sigma^2}\right) - y \operatorname{arctg} \frac{y}{\sigma}\right)} \cos \left\{ y\left[\frac{1}{2} \ln\left(1+\frac{y^2}{\sigma^2}\right)-1\right] + \sigma \operatorname{arctg} \frac{y}{\sigma} \right\} dy$$

This form is particularly well-suited for large negative values of λ. On the contrary, for large positive values, the vertical axis through the point σ approaches the origin; in this case it is better to follow the equivalent path of integration shown on the scheme. In fact, the integral on the external arc of the circle equals zero.

On the lower part of the cut, we may write $u = |u| e^{-i\pi}$.

On the upper part $u = |u| e^{i\pi}$

and on the circle C $u = \varepsilon e^{i\theta}$.

Then, the integral is decomposed into three parts.

$$P(\lambda) = \frac{1}{2i\pi}\left[\int_{-\infty}^{0} e^{u(\ln|u|-i\pi)+\lambda u}\, du + \int_0^{-\infty} e^{u(\ln|u|+i\pi)+\lambda u}\, du + \int_C e^{u(\ln|u|+i\theta)+\lambda u}\, du\right]$$

$\int_C e^{u(\ln u+\lambda)} du = 0$: since the quantity under the integral sign is bounded

$$P(\lambda) = \frac{1}{2i\pi}\left[\int_{-\infty}^{0} e^{-i\pi u}\, e^{u\ln|u|+\lambda u}\, du + \int_0^{-\infty} e^{i\pi u}\, e^{u\ln|u|+\lambda u}\, du\right].$$

Upon substituting v for - u

$$P(\lambda) = \frac{1}{2i\pi}\left[-\int_{+\infty}^{0} e^{-i\pi v}\, e^{v\ln|v|-\lambda v}\, dv + \int_0^{+\infty} e^{-i\pi v}\, e^{-v\ln|v|-\lambda v}\, dv\right]$$

$$P(\lambda) = \frac{1}{2i\pi}\left[\int_0^{+\infty} (e^{+i\pi v} - e^{-i\pi v})\, e^{-v(\ln v+\lambda)} dv\right] = \frac{1}{\pi}\int_0^{\infty} e^{-v(\ln v+\lambda)} \sin \pi v\, dv \ .$$

A second form of $P(\lambda)$ is:

$$P(\lambda) = \frac{1}{\pi} \int_0^{+\infty} e^{-v(\ln v+\lambda)} \sin \pi v\, dv \ .$$

In practice, in the calculation of $P(\lambda)$, we shall take the first form for $\lambda \leq -1$ and the second one for $\lambda > -1$.

Appendix IV

Fourier Transform of the v (r) Potential: $v(r) = \frac{Ze^2}{r} e^{-\frac{r}{R}}$

The transform $v(\vec{q})$ of $v(\vec{r})$ is defined by:

$$v(\vec{q}) = \int_{r,\theta,\Phi} \frac{Ze^2}{r} e^{-\frac{r}{R}} e^{i\vec{q}\cdot\vec{r}} \, d_3 \vec{r}$$

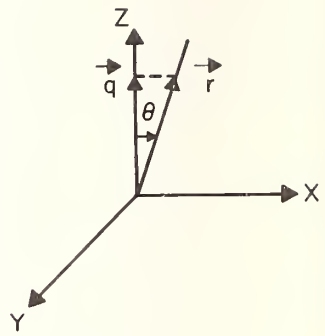

with $\begin{cases} \vec{q}.\vec{r} = q.r\cos\theta \\ d_3 \vec{r} = r^2 \sin\theta \, d\theta \, d\Phi \, dr \end{cases}$

$$v(\vec{q}) = \int_0^\infty \frac{Ze^2}{r} r^2 e^{-\frac{r}{R}} dr \int_0^\pi e^{iqr\cos\theta} \sin\theta \, d\theta \int_0^{2\pi} d\Phi \, .$$

1 - Integration with respect to Φ

$$v(\vec{q}) = 2\pi Ze^2 \int_0^\infty r e^{-\frac{r}{R}} dr \int_0^\pi e^{iqr\cos\theta} \sin\theta \, d\theta$$

2 - Integration with respect to θ

by writing $\cos\theta = u$,

$$\int_0^\pi e^{iqr\cos\theta} \sin\theta \, d\theta = \int_{-1}^{+1} e^{iqru} du = \left| \frac{-i}{qr} e^{iqru} \right|_{-1}^{+1}$$

$$= \frac{i}{qr} (e^{-iqr} - e^{+iqr}) = \frac{2 \sin qr}{qr}$$

the integral becomes:

$$v(\vec{q}) = \frac{4\pi Ze^2}{q} \int_0^\infty e^{-r/R} \sin qr \, dr$$

3 - Integration with respect to r

We integrate twice by parts:

First integration

$$\int_0^\infty e^{-r/R} \sin qr \, dr = \left| - \sin qr \, \frac{e^{-r/R}}{1/R} \right|_0^\infty + qR \int_0^\infty e^{-r/R} \cos qr \, dr$$

$$= qR \int_0^\infty e^{-r/R} \cos qr \, dr$$

Second integration

$$\int_0^\infty e^{-r/R} \cos qr \, dr = \left| - \frac{e^{-r/R}}{1/R} \cos qr \right|_0^\infty - qR \int_0^\infty e^{-r/R} \sin qr \, dr$$

$$= R - qR \int_0^\infty e^{-r/R} \sin qr \, dr$$

Coming back to the initial integral

$$\int_0^\infty e^{-r/R} \sin qr \, dr = qR \left(R - qR \int_0^\infty e^{-r/R} \sin qr \, dr \right)$$

$$\int_0^\infty e^{-r/R} \sin qr \, dr = qR^2 - q^2R^2 \int_0^\infty e^{-r/R} \sin qr \, dr$$

$$\int_0^\infty e^{-r/R} \sin qr \, dr = \frac{qR^2}{1 + q^2R^2} \quad .$$

Finally, the Fourier transform of the potential is:

$$v(\vec{q}) = \frac{4\pi \, Ze^2}{q} \quad \frac{qR^2}{1 + q^2R^2}$$

$$\boxed{v(\vec{q}) = \frac{4\pi \, Ze^2}{\frac{1}{R^2} + q^2}}$$

National Bureau of Standards Special Publication 460. Proceedings of a Workshop on the Use of Monte Carlo Calculations in Electron Probe Microanalysis and Scanning Electron Microscopy held at NBS, Gaithersburg, Maryland, October 1-3, 1975. Issued December 1976.

EVALUATION OF FORMULAS FOR INNER-SHELL IONIZATION CROSS SECTIONS[1]

C. J. Powell

National Bureau of Standards
Washington, DC 20234

An evaluation is presented of various formulas that can be used to describe cross sections for inner-shell ionization by electron impact in the electron-probe microanalyzer. Owing to lack of experimental data, most of the discussion pertains to the case of K-shell ionization. For incident energies greater than four times threshold ($U_K > 4$), the Bethe equation can describe adequately the observed cross-sections and recommended values are given for the two Bethe parameters. For ($U_K < 4$), the classical result of Gryzinski or the expressions of Lotz or Fabre should be useful.

Key Words: Cross sections; electron-probe microanalysis; electrons; inner-shell; ionization.

1. Introduction

The models and procedures for converting x-ray intensities observed with the electron-probe microanalyzer (EPMA) into elemental concentrations have been described in a number of recent reviews [1-10][2] and in other papers included in these proceedings. Although, in practice, x-ray intensities from a sample are often compared with those from a standard with known composition (ideally approximately that of the sample), the accuracy of the analysis will depend in detail on the chemical similarity of sample and standard, the degree of validity of the correction procedures for the particular analytical situation, and on the accuracy of the parameters used in the correction procedure [4].

The purpose of this paper is to evaluate formulas for one parameter used in the so-called atomic-number correction, the cross section Q_{nl} for ionization of electrons in the nl shell by electron impact. This parameter is often thought to be not important in the simpler analytic approaches [1] because the cross-section term "cancels out" when intensities from sample and standard are compared. The inaccuracy introduced by this apparent cancellation depends upon the implicit assumption that the rate of ionization can be related to the average electron energy in the sample and standard through the electron stopping power; in practice, the rate of ionization will depend on the distribution of electron energies in sample and standard. The variation of Q_{nl} with electron energy should be known, however, for Monte Carlo calculations of x-ray generation as a function of depth [11]. Absolute values of Q_{nl} are required when fluorescent emission is significant [4] and when the sample has an unusual topography (e.g., when particulates are being analyzed) [12].

A detailed intercomparison of calculated, semi-empirical and experimental inner-shell ionization cross-section data has been presented elsewhere [13]. We will review in Section 2 some of the cross-section formulas that have been used previously in EPMA procedures and others that have been proposed recently. Measurements of Q_K will be discussed briefly in Section 2 and a comparison will be made in Section 4 between this data and the formulas presented in Section 2.

---

[1]Work carried out at the National Bureau of Standards under the partial sponsorship of the U.S. Energy Research and Development Administration, Division of Biomedical and Environmental Research.

[2]Figures in brackets indicate the literature references at the end of this paper.

2. Review of Formulas

The most widely used formula for Q_{nl} is that due to Bethe [14]:

$$Q_{nl} = \frac{\pi e^4}{E \cdot E_{nl}} Z_{nl} b_{nl} \ln\left[\frac{c_{nl} E}{E_{nl}}\right] . \qquad (1)$$

In this equation, E is the electron energy, E_{nl} the binding energy of electrons in the nl shell, and Z_{nl} the number of electrons in the nl shell. The parameters b_{nl} and c_{nl} are often assumed to be constants for a particular subshell but they could be a function of Z. Finally, eq. (1) is expected to be valid only when $E >> E_{nl}$, but a satisfactory lower limit for E has not been defined previously.

It is convenient to rewrite eq. (1) as a function of $U_{nl} = E/E_{nl}$ so that cross-section data for different elements can be readily compared:

$$Q_{nl} E_{nl}^2 = 6.51 \times 10^{-14} Z_{nl} b_{nl} \ln(c_{nl} U_{nl})/U_{nl} \ cm^2 eV^2 . \qquad (2)$$

The problem now is to determine optimum values of the parameters b_{nl} and c_{nl}. Mott and Massey [15] analyzed some calculations of Q_{nl} by Burhop [16] and concluded that $b_K \approx 0.35$, $b_L \approx 0.25$, and $c_K = c_L \approx 2.42$. These values of b_{nl} and c_{nl} have been widely used in EPMA, but as we will point out later, further analysis of Burhop's results leads to appreciably different values for these two parameters.

Equations (1) and (2) are not only invalid near threshold ($U_{nl} = 1$), but also do not give a zero cross-section in this limit (unless $c_{nl} = 1$). To circumvent both difficulties, Worthington and Tomlin [17] modified the Bethe equation in an arbitrary, but plausible way, as follows:

$$Q_{nl} E_{nl}^2 = \frac{6.51 \times 10^{-14} Z_{nl} b_{nl}}{U_{nl}} \ln\left[\frac{4U_{nl}}{1.65+2.35\exp(1-U_{nl})}\right] cm^2 eV^2 . \qquad (3)$$

For large U_{nl}, eq. (3) becomes identical to eq. (2) (with $c_{nl} = 2.42$). The Worthington and Tomlin equation with the Mott and Massey values of b_{nl} has also been used extensively in EPMA.

Green and Cosslett [18] assumed for simplicity that $c_K = 1$ and modified the value of b_K to agree with experimental cross-section data for Ni and Ag in the vicinity of $U_K = 3$. Their result,

$$Q_K E_K^2 = 7.92 \times 10^{-14} \ln(U_K)/U_K \ cm^2 eV^2 , \qquad (4)$$

corresponds to $b_K = 0.61$. Equation (4) has been used by Brown [19] as the basis of a more general formula:

$$Q_{nl} E_{nl}^2 = 7.92 \times 10^{-14} d_{nl} \ln(U_{nl})/U_{nl} \ cm^2 eV^2 . \qquad (5)$$

The parameter d_{nl} was determined from absolute measurements of x-ray intensities for six elements and with electron transport in the sample being described by a Boltzmann equation. Brown's values of d_{nl} were

$$d_K = 0.85 + 0.0047 \ Z$$

and

$$d_{L_{23}} = 2.19 + 0.0098 \ Z$$

which correspond to

$$b_K = 0.52 + 0.0029\ Z$$

and

$$b_{L_{23}} = 0.44 + 0.0020\ Z$$

in eq. (2).

Hutchins [5] has used a variation of eq. (4):

$$Q_{nl}E_{nl}^2 \propto \ln(U_{nl})/U_{nl}^m\ , \tag{6}$$

where the exponent m was stated to be between 0.7 and 1.

The formulas listed above are those which have been used in EPMA correction procedures. Although various simplifications and modifications have been made to the original Bethe formula (eqs. (1) and (2)) and have been found useful, it is often difficult to judge the validity of particular expressions for particular shells and ranges of U_{nl} and to select the most suitable parameters.

Other calculations of Q_{nl} have been made, and other formulas for Q_{nl} have been proposed [13]. We quote here the result of a calculation by Rudge and Schwartz [20] for a fictitious hydrogenic ion with Z = 128:

$$Q_{nl}E_{nl}^2 = \frac{1.626\times10^{-14}\ Z_{nl}S_{nl}\ln(U_{nl})}{U_{nl}}\ ,\quad cm^2eV^2 \tag{7a}$$

where

$$S_K(U_K) = 2.799 - \frac{0.218}{U_K} + \frac{0.047}{U_K^2} \tag{7b}$$

and

$$S_{L_1}(U_{L_1}) = 2.168 + \frac{1.147}{U_{L_1}} - \frac{0.212}{U_{L_1}^2}\ . \tag{7c}$$

These results for Q_K and Q_{L_1} have been obtained from calculations for U_{nl} between 1.25 and 4. Kolbenstvedt [21] has derived a simple approximate formula for K-shell ionization applicable to relativistic electrons and heavy atoms. His result can be simplified for nonrelativistic energies to become:

$$Q_KE_K^2 = \frac{3.590\ \times\ 10^{-14}\ \ln(2.38\ U_K)}{U_K} + \frac{1.293\ \times\ 10^{-13}}{U_K}\left[1 - \frac{(1+\ln\ U_K)}{U_K}\right] cm^2eV^2\ . \tag{8}$$

McGuire [22] has calculated K-shell and L-shell ionization cross-sections for low-Z atoms and his numerical results can be fitted to the Bethe formulas, as described in Section 4.

Drawin [23] has proposed the semiempirical formula

$$Q_{nl}E_{nl}^2 = 4.32\ \times\ 10^{-14}\ Z_{nl}\ f_1(U_{nl} - 1)\ln(1.25\ f_2\ U_{nl})/U_{nl}^2\quad cm^2eV^2\ , \tag{9}$$

where f_1 and f_2 are parameters estimated to have values in the ranges 0.7 to 1.3 and 0.8 to 3.0, respectively, but which are often assumed to be unity. For $U_{nl} \gg 1$, eq. (8) reduces to eq. (2) with $b_{nl} = 0.66$ and $c_{nl} = 1.25$. Another semiempirical formula has been proposed by Lotz [24]:

$$Q_{nl}E_{nl}^2 = a_{nl}\, Z_{nl}\, \ln U_{nl} \left\{ 1 - b_{nl} \exp[-c_{nl}(U_{nl} - 1)] \right\} / U_{nl} \ . \qquad (10)$$

The parameters a_{nl}, b_{nl} and c_{nl} (which should not be confused with the Bethe parameters in eq. (2)) were selected to fit cross-section data for the removal of outer-shell electrons of atoms to produce ions and may not be appropriate for inner-shell ionization.

Finally, Gryzinski [25] has derived a formula for the inner-shell ionization cross-section based on a classical argument. His result is:

$$Q_{nl}E_{nl}^2 = 6.51 \times 10^{-14}\, Z_{nl}\, g(U_{nl}) \quad \mathrm{cm^2 eV^2} \ , \qquad (11a)$$

where

$$g(U_{nl}) = \frac{1}{U} \left(\frac{U-1}{U+1} \right)^{3/2} \left[1 + \frac{2}{3} \left(1 - \frac{1}{2U} \right) \ln \left[2.7 + (U-1)^{1/2} \right] \right] \ . \qquad (11b)$$

3. Experimental Data

Various measurements of inner-shell ionization cross-sections have been reviewed elsewhere [13]. Quite a few measurements have been made of cross-sections for K-shell ionization, but relatively few measurements exist for L-shell ionization.

Figure 1(a) shows some recent measurements of K-shell ionization cross-sections for C, N, O, and Ne by Mehlhorn and his students [26,27]. These cross-sections are plotted in the form suggested by eq. (2) and it can be seen that there is good internal consistency, in shape and absolute magnitude, in the data for these four elements. These cross-sections, which are based on absolute measurements of Auger-electron yields from gas-phase targets under electron bombardment, agree well with most of the previous x-ray yield measurements for $Z \lesssim 29$. (For medium- and high-Z atoms, relativistic corrections to the formulas for Q_K become necessary.) The Auger-yield measurements cover a range of U_K from near theshold to 25, and it is convenient to use this data for comparison with the formulas presented in the previous section.

4. Comparison of Formulas with Experiment

Figure 1 shows a graphical comparison of the various formulas presented in Section 2 with experiment. A smooth curve has been drawn through the experimental data shown in figure 1(a) and this curve has been replotted in the other panels as a solid line. For $U_K > 4$, this curve also represents eq. (2) with $b_K = 0.9$ and $c_K = 0.65$.

Figure 1(b) shows a comparison of the experimental curve with plots of the Worthington-Tomlin relation (eq. (3)), using the Mott and Massey value of $b_K = 0.35$, and the Green and Cosslett result (eq. (4)). The experimental curve peaks at a larger value of U_K than for these two formulas; also, the experimental cross-section is appreciably greater than those predicted by the formulas for $U_K \gtrsim 6$.

Plots of the Drawin (eq. (9)), Lotz (eq. (10)), and Gryzinski (eq. (11)) expressions are shown in figure 1(c). The Gryzinski expression gives a good fit to the experimental curve for $U_K < 6$. All three expressions give similar cross-section values for $U_K > 10$. The Lotz expression would agree well with experiment if the parameter a_K was increased by about 25%.

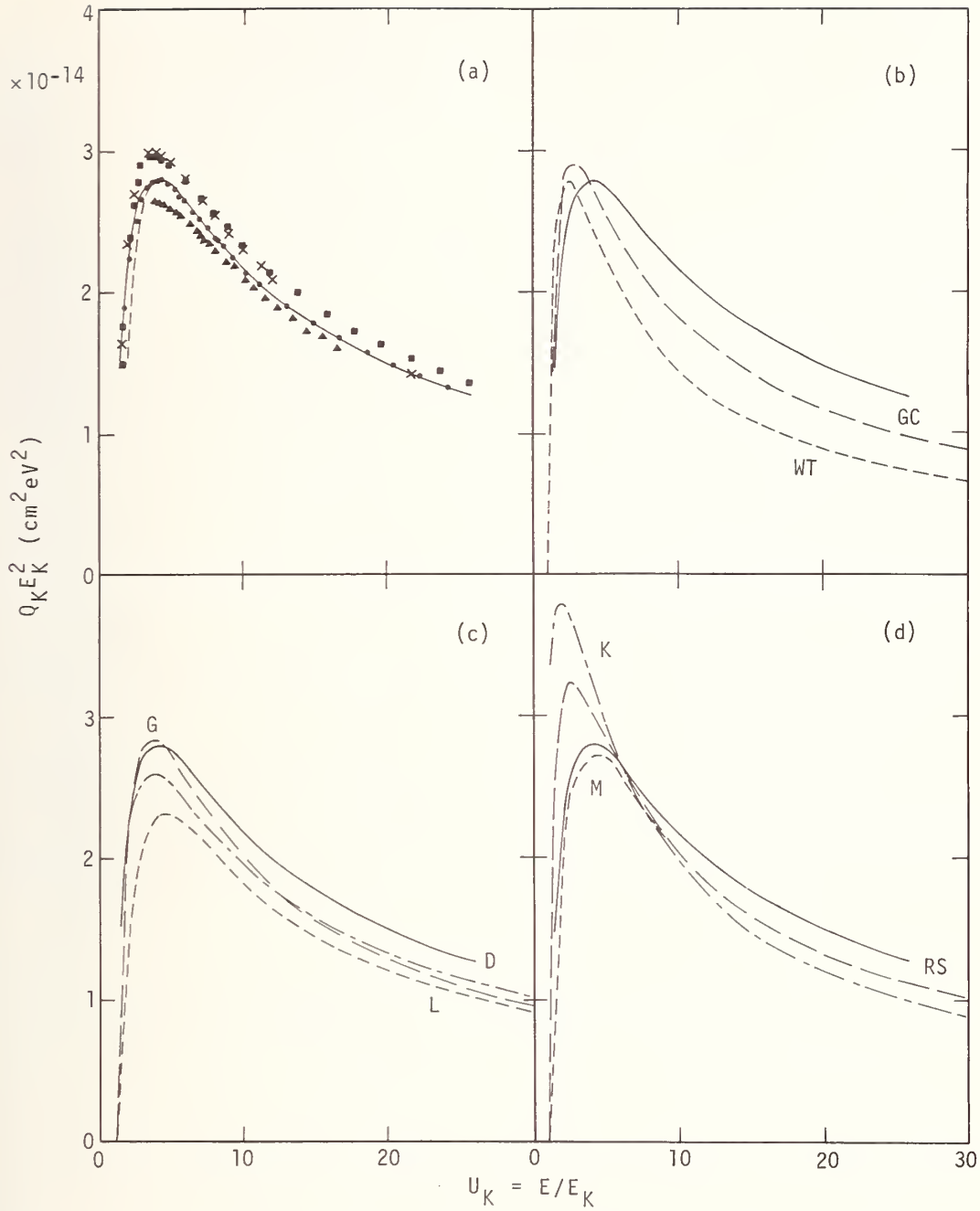

Figure 1. Plot of $Q_K E_K^2$ against $U_K = E/E_K$. (a) Measurements of Glupe and Mehlhorn and Bekk [26] for C (▲), Ne (×), N (■), and O (●). The solid line is a smooth curve through the experimental points and has been redrawn in the other three panels. The dashed curve is the Bethe equation (eq. (2)) with $b_K = 0.9$ and $C_K = 0.65$. (b) The short-dashed curve denoted WT is the Worthington-Tomlin equation (eq. (3)), and the long-dashed line denoted GC is the Green and Cosslett equation (eq. (4)). (c) The short-dashed line denoted L is the result of Lotz (eq. (10)) with $a_K = 4 \times 10^{-14}$ cm^{2}eV^2, $b_K = 0.75$, and $c_K = 0.5$), the long-dashed curve denoted G is the result of Gryzinski (eq. (11)), and the dot-dashed curve denoted D is the result of Drawin (eq. (9)). (d) The short-dashed curve denoted M is the result of calculations by McGuire [13,22] for Be, C, and O, the long-dashed line denoted RS is the result of Rudge and Schwartz (eq. (7)), and the dot-dashed curve denoted K is the result of Kolbenstvedt (eq. (8)).

Figure 1(d) shows a smooth curve based on McGuire's [13,22] calculations for Be, C, and O, the Rudge and Schwartz result (eq. (7)), and the Kolbenstvedt relation (eq. (8)). McGuire's result agrees moderately well with experiment, particularly near threshold. There is reasonable agreement of the Rudge and Schwartz equation with experiment for $U_K \gtrsim 5$, but closer to threshold (the specific region for which the calculations were made), the agreement is less satisfactory. Kolbenstvedt's result does not agree as well with experiment as the other two calculations.

Similar comparisons can be made with L_{23}-shell cross-section data [13]. The data base is here rather limited, but it also appears that the Worthington-Tomlin relation (eq. (3) with $b_{L_{23}} = 0.25$) again underestimates the ionization cross section (by at least 50%). The Drawin (eq. (9)) and Gryzinski (eq. (11)) results agree well with each other and with Christofzik's [27] cross-section measurements for Ar. Lotz's result (eq. (10)), with $a_{L_{23}} = 2.6 \times 10^{-14}$ cm^{2}eV^2, $b_{L_{23}} = 0.92$, and $c_{L_{23}} = 0.19$, however, differs substantially in shape and magnitude when compared with the other data.

Tests have been made to determine whether the inner-shell ionization cross-section data can be fitted to a linearized form of the Bethe equation (eq. (2)) in order to find the region of U_{nl} over which the equation is valid and to derive values for the Bethe parameters b_{nl} and c_{nl} [13]. Almost all of the cross-section data could be satisfactorily fitted over the range $4 \lesssim U_{nl} \lesssim 30$. (It is interesting to note here that analysis of Burhop's [16] calculated cross-sections yields results [13] (e.g., $b_K = 0.50$ and $c_K = 1.41$ for Ni, and $b_{L_3} = 0.32$ and $c_{L_3} = 1.85$ for Hg) appreciably differ from those quoted by Mott and Massey [15]). These fits indicated that the parameters $b_K \approx 0.9$ and $c_K \approx 0.60$-0.75 could describe Q_K adequately for light atoms in the range $4 \lesssim U_K \lesssim 25$; the dashed curve in figure 1(a) shows eq. (2) plotted with $b_K = 0.9$ and $c_K = 0.65$. The situation for L_{23}-shell ionization is less certain, but the values $b_{L_{23}} \approx 0.5$-0.6 and $c_{L_{23}} \approx 1$ appear to be reasonable for $U_{L_{23}} \gtrsim 20$ while the values $b_{L_{23}} \sim 0.6$-0.9 and $c_{L_{23}} \sim 0.6$ seem appropriate for $4 < U_{L_{23}} \lesssim 20$. No attempt has been made here to fit the cross section data to analytic formulas near threshold in the manner described by Green and Stolarski [28].

Values of the parameter b_{nl} have also been derived from photoabsorption data and were found to be consistent with the ionization data if account was taken of the expected distribution of differential oscillator strength with respect to excitation energy. Specifically, b_{nl} should, in principle, be regarded as a function of U_{nl} for $U_{nl} \lesssim 20$. The values of b_{nl} and c_{nl} derived from the fits to the cross-section data should therefore be considered as empirical parameters and should not be used outside the range of each fit.

5. Summary

The foregoing comparison of experimental data with the predictions of various cross-section formulas together with the previous analysis [13] of inner-shell ionization cross-section data can be used to draw the following conclusions.

(1) Useful empirical fits of cross-section data can be made with the Bethe equation (eqs. (1) and (2)) over a wide range of U_{nl} (typically from 4 to 30).

(2) The present data base does not indicate a significant variation of the Bethe parameters with Z. This conclusion, which differs from that of Brown [19], has also been independently reached by Quarles [29] for K-shell ionization.

(3) A better choice of the Bethe parameters can now be made than those recommended many years ago by Mott and Massey [15]. Recent calculations and measurements show that the inner-shell ionization cross-sections are appreciably (at least 40 to 50%) higher than those calculated with the Mott and Massey parameters. Specifically, it is suggested that the values $b_K \sim 0.9$ and $c_K \sim 0.65$ are appropriate for $4 < U_K < 25$.

(4) The results of Lotz (eq. (10)) when increased by 25% (that is, $a_K = 5 \times 10^{-14}$ cm^{2}eV^2, $b_K = 0.75$, and $c_K = 0.5$ and of Gryzinski (eq. (11)) for Q_K agree well with experiment near threshold ($1 < U_K < 4$). These expressions could therefore be useful for improved atomic-number correction procedures in EPMA; see also, Note Added in Proof.

(5) More experimental measurements are required to establish cross-section formulas (particularly near threshold) for shells other than the K shell.

Note Added in Proof:

Fabre [30] has derived a modification to the Bethe formula [eq. (1)] that could be useful near the threshold for ionization. His formula is:

$$Q_{nl}E_{nl}^2 = \frac{6.51 \times 10^{-14} Z_{nl} \ln(U_{nl})}{k_{nl}(U_{nl} + \chi_{nl})} \ cm^2 eV^2 , \qquad (12)$$

where k_{nl} and χ_{nl} are parameters; k_{nl} is equivalent to $1/b_{nl}$ in eqs. (1) and (2), and χ_{nl} is expected to be greater than 1. Fabre has fitted eq. (12) to the K-shell ionization cross-section data [26] shown in figure 1 and finds that $k_K = 1.18$ and $\chi_K = 1.32$. Equation (12) fits these measurements of Q_K within 6%, with these values of k_K and χ_K, in the range $1.5 < U_K < 25$.

References

[1] *Quantitative Electron Probe Microanalysis*, K. F. J. Heinrich, ed. (National Bureau of Standards Special Publication 298, Washington, DC, 1968).

[2] Birks, L. S., *Electron Probe Microanalysis* (Wiley-Interscience, New York, second edition, 1971).

[3] Reuter, W., *Surface Sci.* 25, 80 (1971).

[4] Heinrich, K. F. J., *Anal. Chem.* 44, 350 (1972).

[5] Hutchins, G. A., in *Characterization of Solid Surfaces*, P. F. Kane and G. B. Larrabee, eds., p. 441 (Plenum Press, New York, 1974).

[6] Lifshin, E., in *Scanning Electron Microscopy*, by O. C. Wells, A. Boyde, E. Lifshin, and A. Rezanowich, p. 243 (McGraw-Hill Book Co., New York, 1974).

[7] Yakowitz, H., in *Practical Scanning Electron Microscopy, Electron and Ion Microprobe Analysis*, J. I. Goldstein and H. Yakowitz, eds., p. 373 (Academic Press, New York, 1974).

[8] Ogren, J. R., in *Systematic Materials Analysis*, J. H. Richardson and R. V. Peterson, eds., Vol. 1, p. 143 (Academic Press, New York, 1974).

[9] Philibert, J. and Tixier, R., in *Physical Aspects of Electron Microscopy and Microbeam Analysis*, B. M. Siegel and D. R. Beaman, eds., p. 333 (Wiley, New York, 1975).

[10] Reed, S. J. B., *Electron Microprobe Analysis* (Cambridge University Press, London, 1975).

[11] Bishop, H. E., private communication.

[12] Heinrich, K. F. K., private communication.

[13] Powell, C. J., *Rev. Mod. Phys.* 48, 33 (1976).

[14] Bethe, H., *Ann. Physik* 5, 325 (1930).

[15] Mott, N. F. and Massey, H. S. W., *The Theory of Atomic Collisions*, 2nd edition, p. 243 (Oxford University Press, London, 1949).

[16] Burhop, E. H. S., *Proc. Camb. Phil. Soc.* 36, 43 (1940).

[17] Worthington, C. R. and Tomlin, S. G., *Proc. Phys. Soc. (London)*, A69, 401 (1956).

[18] Green, M. and Cosslett, V. E., *Proc. Phys. Soc. (London)*, 78, 1206 (1961).

[19] Brown. D. B., in *Handbook of Spectroscopy*, Vol. 1, J. W. Robinson, ed., p. 248 (CRC Press, Cleveland, 1974).

[20] Rudge, M. R. H. and Schwartz, S. B., *Proc. Phys. Soc. (London)*, 88, 563 (1966).

[21] Kolbenstvedt, H., *J. Appl. Phys.* 38, 4785 (1967).

[22] McGuire, E. J., *J. de Phys.* C4, 37 (1971); *Phys. Rev. A* 3, 267 (1971); private communication.

[23] Drawin, H.-W., *Z. Physik* 164, 513 (1961); *ibid.*, 172, 429 (1963).

[24] Lotz. W., *Z. Physik* 232, 101 (1970).

[25] Gryzinski, M., *Phys. Rev.* 138, A336 (1965).

[26] Glupe, G. and Mehlhorn, W., *Phys. Lett.* 25A, 274 (1967); Glupe, G. and Mehlhorn, W., *J. de Phys.* C4, 40 (1971); Bekk, K.-J., Diplom-Thesis, University of Freiburg (1974).

[27] Christofzik, H.-J., Diplom-Thesis, University of Münster (1970).

[28] Green, A. E. S. and Stolarski, R. S., *J. Atmos. Terr. Phys.* 34, 1703 (1972).

[29] Quarles, C. A., in *Electronic and Atomic Collisions*, Proceedings of the Ninth International Conference on the Physics of Electronic and Atomic Collisions, Seattle, 1975, J. S. Risley and R. Geballe, eds., p. 898 (University of Washington Press, Seattle, 1975); *Phys. Rev. A* 13, 1278 (1976).

[30] M. Fabre de la Ripelle, *J. Phys. (Paris)*, 10, 319 (1949); private communication; and to be published.

National Bureau of Standards Special Publication 460. Proceedings of a Workshop on the Use of Monte Carlo Calculations in Electron Probe Microanalysis and Scanning Electron Microscopy held at NBS, Gaithersburg, Maryland, October 1-3, 1975. Issued December 1976.

NBS MONTE CARLO ELECTRON TRAJECTORY CALCULATION PROGRAM

Robert L. Myklebust, Dale E. Newbury and Harvey Yakowitz

Institute for Materials Research
National Bureau of Standards
Washington, D. C. 20234

A number of Monte Carlo programs for obtaining information of interest to x-ray microanalysts and scanning electron microscopists have been developed; the outputs from many of these programs are discussed elsewhere in this volume [1][1]. The purpose of this paper is to present the Monte Carlo program for microanalysis currently in use at the National Bureau of Standards. This program is a considerably extended treatment of the Curgenven-Duncumb formulation [2]. A large number of electron trajectories can be simulated rapidly--about 1200 per minute of central processing unit time--at a reasonable cost. The electron scattering calculation is an approximation to multiple elastic electron scattering in an amorphous solid. Details of other assumptions made in constructing the program, as well as a number of comparisons of calculated and experimental data, are given in the text.

Key Words: Electron trajectories; magnetic effects; Monte Carlo calculations; multiple scattering x-ray generation; particle analysis; quantitative x-ray microanalysis; thin films; x-ray emission.

1. Introduction

In 1971, our group acquired a copy of the compact Monte Carlo electron trajectory program devised by Curgenven and Duncumb [2]. In adapting this program for use with our computer, we introduced a number of changes necessary to facilitate the execution of the program. Moreover, in subsequent studies, it became necessary to make further extensive changes to the program. The resulting program, hereafter referred to as the NBS Monte Carlo Program, has been adapted to the study of a proposed mechanism of Type II magnetic contrast in the scanning electron microscope, to the study of x-ray emissions from particles, and to problems of quantitative x-ray microanalysis from tilted specimens.

While the NBS Monte Carlo program uses the basic structure devised by Curgenven and Duncumb [2], the extensive changes made in the original program necessitate a detailed description, which is the subject of this paper. Modification of the step length between elastic collisions and the elastic scattering angle distribution will be discussed. The techniques of adapting the program to the particular applications will be described in this paper and in a second paper in these proceedings. The results of the testing of the program against experimental determinations of electron-solid interaction parameters will be given.

2. NBS Monte Carlo Program

We will describe a typical trajectory calculation to illustrate the computational techniques in the NBS Monte Carlo program. Prior to impact on the specimen, the electron beam parameters are its direction cosines, beam diameter, energy, and the intensity distribution within the beam. The right-handed, orthogonal, coordinate system used in the program is shown in figure 1. The Z-axis is defined to be normal to the surface of the specimen and

[1]Figures in brackets indicate the literature references at the end of this paper.

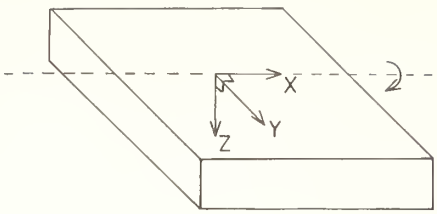

Figure 1. Coordinate system used in Monte Carlo electron trajectory calculations.

the positive sense is into the specimen. The X-axis is further defined to be the axis of specimen tilt. All tilt angles are specified about the X-axis, and 0° tilt corresponds to normal beam indcidence. The Y-axis lies in the plane of the surface of a flat specimen; the positive sense is downward from the beam impact point for a tilted specimen.

The beam diameter is a variable which is important primarily for the characterization of small particles. The intensity distribution within the beam depends on the beam focus. An ideal finely focused beam has a Gaussian intensity distribution along its diameter [3]. A defocused beam may have a nearly constant intensity distribution along its diameter. Both cases are considered in the NBS program through the selection of either a Gaussian or linear random number generator for intensity distributions along the beam diameter.

For the case of a Gaussian intensity distribution, the beam diameter is arbitrarily defined, in accordance with the convention used in electron microscopy, as the diameter of the circle containing 80 percent of the current [4]. To scale the Gaussian distribution, the chosen beam diameter is divided by 2.56 to give the radius corresponding to one standard deviation, σ, of the distribution. This radius then serves to scale the electron impact points along a given diameter vector. All of the electrons are used in the calculations except that electron impacts at a distance from the center greater than 4σ are disregarded. A linear random number generator is used to rotate the diameter vector through 2π radians. For normal beam incidence on a flat specimen, the coordinates of the beam impact points are given by:

$$X = \cos(R_L \pi)\ R_G\ \sigma \tag{1}$$

$$Y = \sin(R_L \pi)\ R_G\ \sigma \tag{2}$$

$$Z = 0 \tag{3}$$

where R_L is a random number from a linear distribution ($-1 \leq R_L \leq +1$) and R_G is a random number from a Gaussian distribution ($-4 \leq R_G \leq +4$).

A plot of a typical Gaussian beam cross-section produced by this procedure is shown in figure 2. A uniform beam density is obtained by substituting a linear random distribution (R_L) for R_G in eqs. (1) and (2) and replacing the scaling factor, σ, by the specified beam radius. For a non-planar surface, the Z-coordinate of impact is calculated according to the form of the surface of the specimen. For spheres, the equation is:

$$Z = r - \sqrt{r^2 - x^2 - y^2} \tag{4}$$

and for cylinders oriented with the cylinder axis along the X-axis:

$$Z = r - \sqrt{r^2 - y^2} \tag{5}$$

where r is the radius of the sphere or cylinder.

The electron trajectory within the specimen is defined as follows. The total length of electron travel within the specimen is assumed to be the Bethe range, R_B, computed by integrating the Bethe energy loss law [5,6]

Figure 2. Distribution of electron impact points generated by Gaussian random number scheme. The beam diameter contains 80 percent of the impact points. For calculations, all impacts with radii up to 4σ are used.

$$R_B = \int_{1.03J}^{E_o} \left(-\frac{1}{dE/ds}\right) dE \tag{6}$$

$$\frac{dE}{ds} = \frac{-78{,}500\ Z}{EA} \ln\left(\frac{1.166\ E}{J}\right), \frac{keV\ cm^2}{g} \tag{7}$$

where E_o is the initial beam energy (keV), E is the instantaneous energy (keV), s is the mass length (g/cm^2), Z is the atomic number, A is the atomic weight (g/mol), and J is the mean ionization energy (keV). J may be obtained from either the Duncumb equation [7]:

$$J = Z\left[14\left(1-e^{-0.1Z}\right) + \frac{75.5}{Z(Z/7.5)} - \frac{Z}{100+Z}\right] \tag{8}$$

or the Berger-Seltzer equation [8]:

$$J = 9.76Z + 58.5Z^{-0.19}. \tag{9}$$

The lower limit of integration of eq. (6) was arbitrarily selected as 1.03J following Curgenven and Duncumb [2], since the integration of eq. (6) cannot be evaluated when $E \leq J$.

At present, we are using a multiple scattering model in which the electron step length varies directly as the electron energy. This is a modification of the first Monte Carlo program used at NBS based on the Curgenven-Duncumb program [2], which used equal step-lengths regardless of the electron energy. These step-lengths were computed by arbitrarily dividing the calculated Bethe range of the electron into 60 equal steps. Each step contains a number of scattering acts depending on the electron energy. The energy of an electron anywhere within a given step is assumed to be equal to that at the mid-point of the step. A table of these energies is calculated from Bethe's continuous energy-loss relation by a fourth order Runge-Kutta solution [9] of the differential eq. (7).

The Curgenven-Duncumb program used an empirical Rutherford-type expression to describe the electron scattering within the solid. This expression is based on the path of a charged particle passing near to an atomic nucleus and assumes that the energy of the particle is not appreciably altered as it passes through the atom. The particle is subjected to a repulsive force which varies inversely as the square of the distance between the nucleus and the particle. The path of the particle is then a hyperbola having the nucleus as its external focus [10]. Under these conditions, Rutherford showed that

$$\cot(\beta/2) = \frac{2p}{b} \tag{10}$$

where β is the scattering angle,

p is the impact parameter (i.e., the distance of closest approach of the particle to the nucleus), and

b is equal to $2ZeQ/mv^2$, Z being the atomic number, e, m, and v being the electron charge, mass and velocity, respectively, and Q the charge on the nucleus.

Curgenven and Duncumb [2] modified the expression given by Rutherford, and introduce the concept of a statistical variation in β as follows:

$$\tan(\beta/2) = \frac{F_i}{E}\left(\frac{1}{\sqrt{R_L}}\right) \tag{11}$$

where E is the instantaneous energy and $F_i = 0.0072\ Z_i/E_0P_i$. F_i embodies the parameters p and b in eq. (10), and R_L is a random number such that $(0 < R_L \leq 1)$. P_i is a function of Z ($P_i = 0.263Z_i^{0.4}$) where the coefficient and exponent are adjusted such that the program will compute the correct backscatter coefficient for a flat specimen.

The energy distribution of the backscattered electrons which results from this model is shown in figure 3, curve A. Its shape is in reasonable agreement with experimental determinations of the energy distribution [11], curve B, except for the electrons of highest energy. Because the initial scattering point in this model was assumed to be at the surface, and because the multiple scattering distribution produces too many scattering angles greater than 90°, the model overestimates the number of backscattered electrons of high energy in the first step.

Equation (11) truncates the angular distribution of β to a minimum value of about 10° to 15°, depending on the parameter P_i, since as R_L approaches unity, $\tan(\beta/2)$ approaches F_i/E_i rather than zero. While the results obtained with this program generally agree with the available experimental data, the energy distribution deviates considerably from that observed experimentally. To overcome this deficiency, an energy-dependent variable step-length was introduced. With the table of energies obtained for the case of equal step lengths, the Bethe range was calculated for each of these energies. The variable step length was then defined as 1/31 of the Bethe range appropriate to each energy. This fraction was selected because with it, the sum of sixty steps would approximately equal the Bethe range for the incident beam energy. The energy for each step was again computed to be equal to the energy at the mid-point of the step, and P_i was also adjusted to give the correct backscatter coefficients. The energy distribution of the backscattered electrons in this case is, however, quite different from the experimental values (see fig. 3, curve C).

The statistical variation in the angle β used by Curgenven and Duncumb (see eq. (11)) was then modified to allow small-angle scattering as follows:

$$\tan(\beta/2) = \frac{F_i}{E_i}\left(\frac{1}{\sqrt{R_L}} - 1\right). \tag{12}$$

When the random number (R_L) approaches one, the angle β approaches zero. This scattering model produces an energy distribution of backscattered electrons with a shape similar to the experimental results, but still too many electrons backscatter in the first step (see fig. 3, curve D). In addition, we can now reproduce the angular distribution of low-loss backscattered electrons as measured by Wells [12] (see fig. 4). Only electrons backscattered during the first multiple scattering step are counted as low-loss electrons.

The initial scattering point has been moved from the surface to a variable depth within the solid. This depth is an exponential function of the step-length which allows only 0.1 percent of the incident electrons to travel a full step length before scattering.

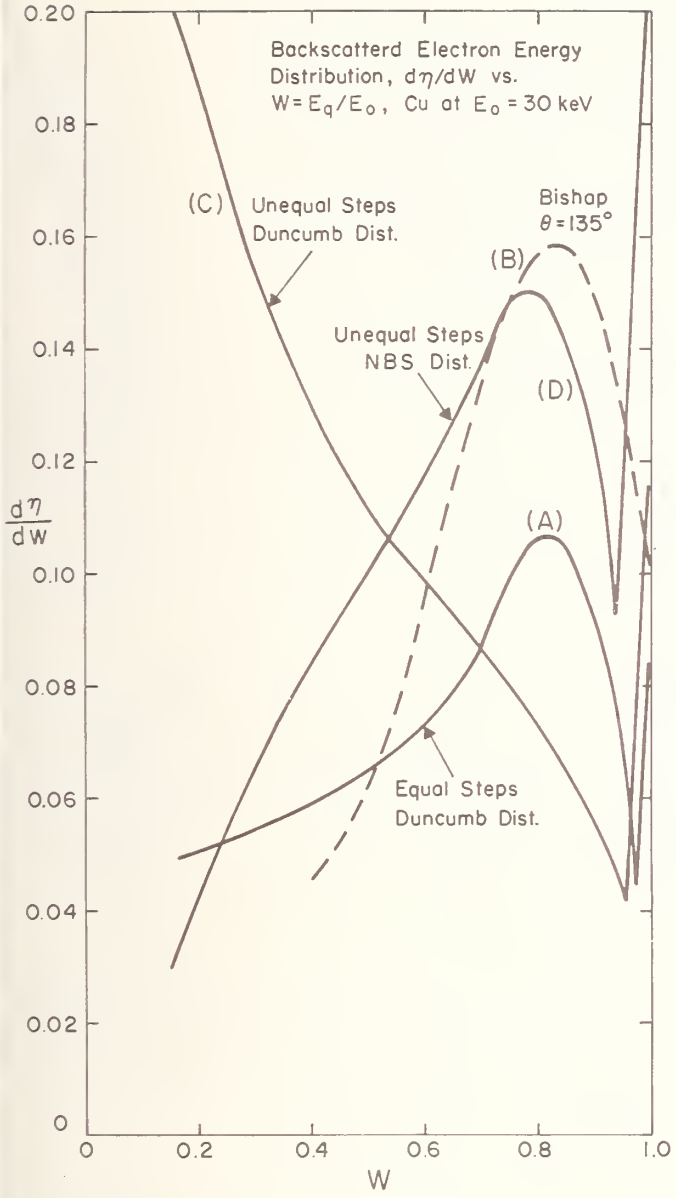

Figure 3. Backscattered electron energy distributions calculated with various step lengths and scattering parameters; experimental data of Bishop [11].

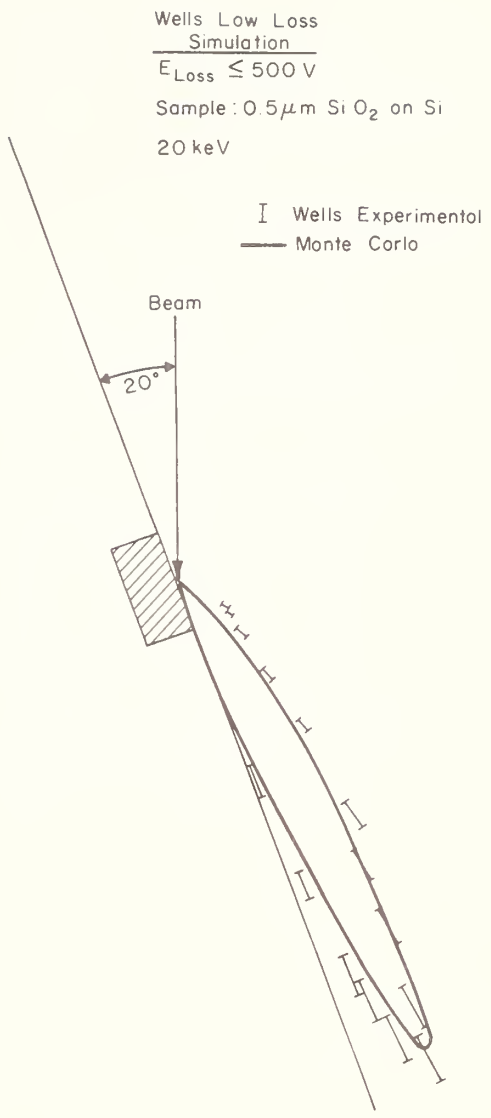

Figure 4. Angular distribution of low energy-loss electrons as measured by Wells [12]; Monte Carlo calculations for electrons emitted after the first multiple scattering interaction.

In reality, an absorbed electron will undergo from several hundred to several thousand elastic scattering events. Since these events are all combined in our multiple scattering model into 60 steps, the modification of the single-scattering model must be made so that all scattering acts within each step will be replaced by an equivalent scatter through an angle larger than that corresponding to a single scattering event. A frequency histogram of scattering angles generated by our modified scattering function is shown in figure 5 for aluminum with E_o = 20 keV, curve A. In the same figure is the distribution of angles of electrons transmitted through a thin foil calculated by the program, curve B, and compared with the data of Thomas [13], curve C. The calculated distribution is similar to the experimental distribution, i.e., Gaussian, but is shifted to higher angles (see curve D). The

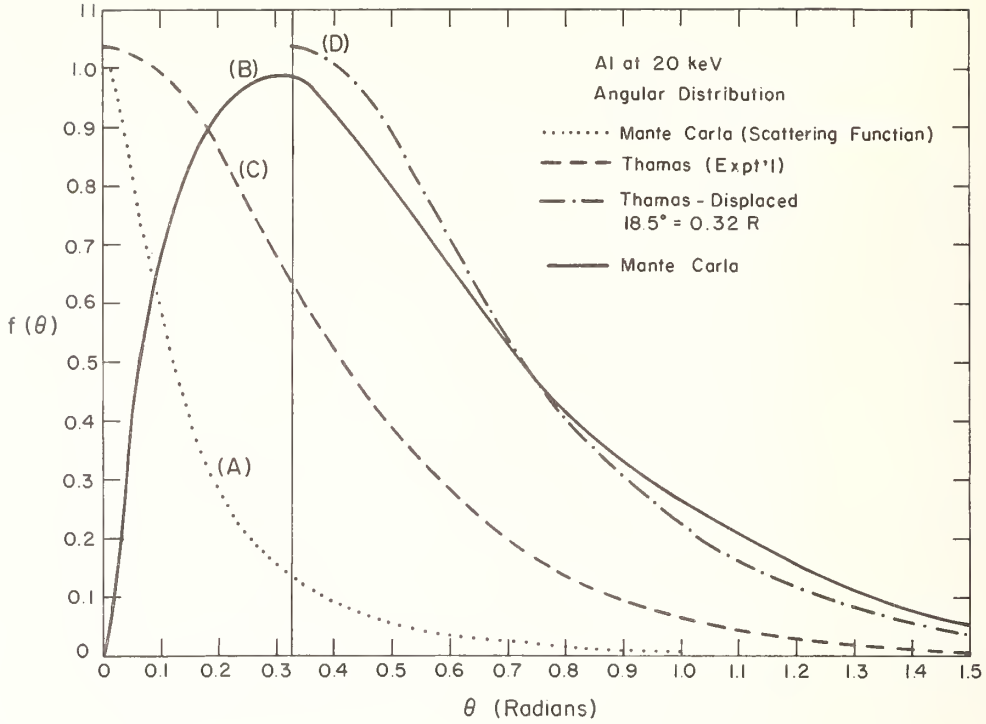

Figure 5. Angular distribution of electrons transmitted through an aluminum film (0.56 μm thick); experimental data of Thomas [13]. The angular distribution generated by the scattering law used in the Monte Carlo calculation is shown, along with the angular distribution calculated for the film.

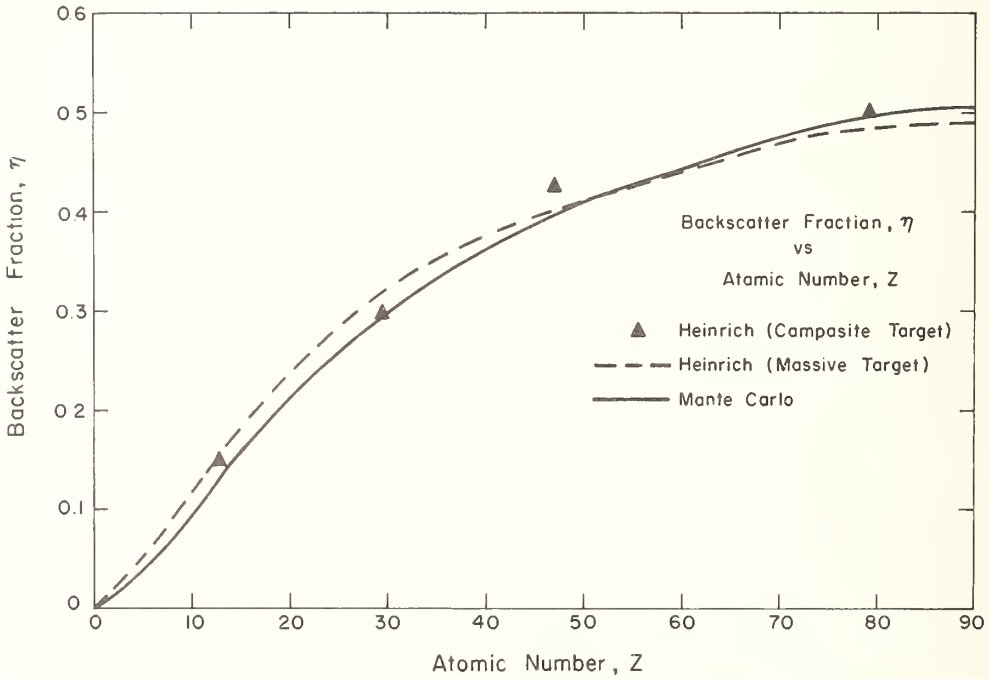

Figure 6. Backscattering coefficient versus atomic number for a beam energy of 30 keV; data of Heinrich [14].

magnitude of this shift is related to the number of single scattering events combined in a multiple scattering step and controlled by the impact parameters, eq. (10). Selection of the impact parameters is made so that the relationship of the backscatter coefficient vs. atomic number agrees with measured values. Such a fit was made for the experimental values at aluminum and gold, and very good agreement was obtained at intermediate atomic numbers (see figure 6). Tests of other electron properties with the selected impact parameters are described in a later section.

The Bethe range, rate of energy loss, step-lengths, and the scattering angles determine the behavior of the electrons within the specimen. The exact calculation of the spatial coordinates of the electron within the specimen is shown in Appendix A.

Since the exact position of the electron (X,Y,Z) is known after each scattering act, backscattering can be determined by comparing the electron coordinates with the equation of the locus of the free surface of the specimen. The current program can accommodate flat, semi-infinite specimens at any tilt, and simple shapes such as spheres and cylinders. Other shapes could be handled through the appropriate surface locus equations. Films on substrates can also be studied, with the electron behavior controlled by the material in which the electron is instantaneously located.

The effect of a magnetic field within the specimen can be simulated through the use of the Lorentz force equation. A detailed discussion of magnetic studies is presented elsewhere in this volume.

3. X-Rays

In addition to the various electron signals produced by the Monte Carlo program, information concerning x-ray signals also is computed. The generation of x-rays by electrons is a relatively inefficient process yielding only one characteristic photon for every 1,000 to 10,000 primary electrons. For Monte Carlo computations, however, this inefficiency may be avoided by considering the probabilities of x-ray excitation as appropriate fractions of a photon to be excited for each electron scattering event. For K- or L-shell ionizations, this probability may be written, according to Bethe as:

$$Q_{K,L} = q_{K,L} \frac{\ln U_i}{U_i} \frac{1}{E_{K,L}^2} \tag{13}$$

where $Q_{K,L}$ is the ionization cross-section for K- or L-shell electrons, $E_{K,L}$ is the minimum ionization potential, $q_{K,L}$ is a constant, and U_i is the instantaneous overvoltage ($E_i/E_{K,L}$). The x-ray generation in our program is normalized by dividing the probability at any step by the probability at E_o:

$$Q_{K_o} E_K^2 = q_K \frac{\ln U_o}{U_o} \tag{14}$$

which results in:

$$\frac{Q_K}{Q_{K_o}} = \frac{\ln U_i}{E_i} \frac{E_o}{\ln U_o} . \tag{15}$$

(Note that this equation is strictly applicable only at large U. In the present calculations, we need to calculate the ionization cross-section down to the excitation energy, and in the absence of a definitive cross-section at $U \sim 1$, we employed eq. (15).)

The cross-sections are first summed at the depths in the specimen where they are generated. This summation produces a distribution in depth of x-ray generation, i.e., a plot of $\phi(Z)$ versus Z (where Z is depth). The number of photons generated per electron is then computed by numerical integration of the distribution $\phi(Z)$ and division of the result by E_K. If the specimen contains several elements, the cross-section for each element is multiplied by its mass fraction before summing so that x-rays are computed for all elements at each electron scattering. When the specimen is a film on a substrate of a different material, the generated x-rays for either the film or the substrate are computed depending on

whether the electron is in the film or the substrate. Otherwise, the x-ray generation is computed in the same way for all specimens irrespective of their shape as long as the electron is within the specimen. The second summation of the same cross-sections is performed versus the path length for an x-ray leaving the specimen in the direction of the detector. The probability of generation of x-rays in each increment of the path length is multiplied by the factor which indicates the loss through absorption along the path:

$$I' = I\, e^{-\mu_l s} \tag{16}$$

where I' is the emitted x-ray intensity, I is the generated x-ray intensity at each increment of the path length, μ_l is the linear absorption coefficient for the x-rays, and s is the path length out of the specimen in the direction of the detector. This procedure produces a distribution in depth of emitted x-rays which is then numerically integrated to obtain the number of photons emitted per electron. The shape of the specimen and the x-ray emergence angle determine the intensity of x-ray emission to a large extent since the path lengths vary as a function of these parameters. The effect of emergence angle on a sphere is shown in figure 7. It is easily seen that for low emergence angles, the path becomes very long for spheres of large diameter. If the specimen is a film on a substrate, both the x-ray emission from the film and from the substrate are computed.

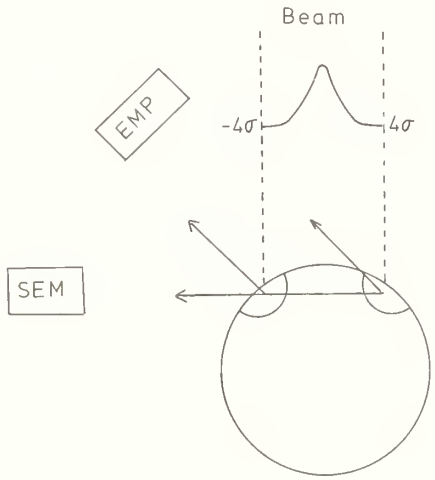

Figure 7. Emergence effects on the x-ray path length for a particle of intermediate size (1-20 μm diameter); typical x-ray detector positions for the scanning electron microscope and the electron probe microanalyzer are shown.

The absorption in the specimen, f_p, is then computed by dividing the number of emitted x-ray photons by the number of those which were generated. In the case of flat specimens, it is also possible to compute the absorption function, f_p vs. χ, where $\chi = (\mu/\rho)\csc \Psi$, (μ/ρ) being the mass absorption coefficient and Ψ the x-ray emergence angle, by calculating the x-ray emission at various values of Ψ in the expression:

$$I' = I\, e^{-\chi z} dz. \tag{17}$$

The ratio of the the x-rays emitted from a specimen and from a pure element standard can also be computed by the Monte Carlo technique. Relative emitted x-ray intensities (k) obtained in this way are only corrected for absorption. No corrections for secondary fluorescence have, as yet, been programmed into our Monte Carlo program.

4. Comparison of Results of the NBS Monte Carlo Procedure and Experiment

A number of tests of the NBS Monte Carlo program have been carried out. Both the properties of electron interaction and x-ray generation have been examined. The variation of the coefficient of backscattering, η, as a function of atomic number, specimen tilt, specimen shape and internal magnetic field in the specimen has been studied. In addition, the transmission of electrons through thin films and the energy distribution of backscattered electrons have been computed.

The x-ray computation tests include the calculation of photons generated per incident electron, the distribution in depth of electron-excited x-rays in the specimen, the absorption of x-rays, the construction of analytical calibration curves for both normal and oblique electron beam incidence, and of x-ray intensities from thin films and particles.

Considering the potential for errors in the model itself, as well as in input parameters (e.g., mean ionization potentials required for the model), the agreement with experimental findings was good in each of these tests.

4.1 Electron Interactions with the Target

The program is constrained by providing a fit to the experimental backscatter coefficients at normal electron beam incidence. This condition was set for aluminum and gold, with reference to Heinrich's measured η values [14]. Agreement over the entire range of atomic numbers is good, as shown in figure 6.

A further series of tests of the applicability of the Monte Carlo procedure to electron backscattering was carried out. Heinrich showed that the backscatter fraction, η, varied discontinuously with atomic number, Z, in the range of $22 \leq Z \leq 29$ [15]. The effect was especially pronounced for an incident electron beam energy of 40 keV. A comparison of the measured and calculated results is shown in figure 8. The Monte Carlo results reproduce the observed trend very well, and the magnitude of the backscatter fraction is within a few percent of the measured data.

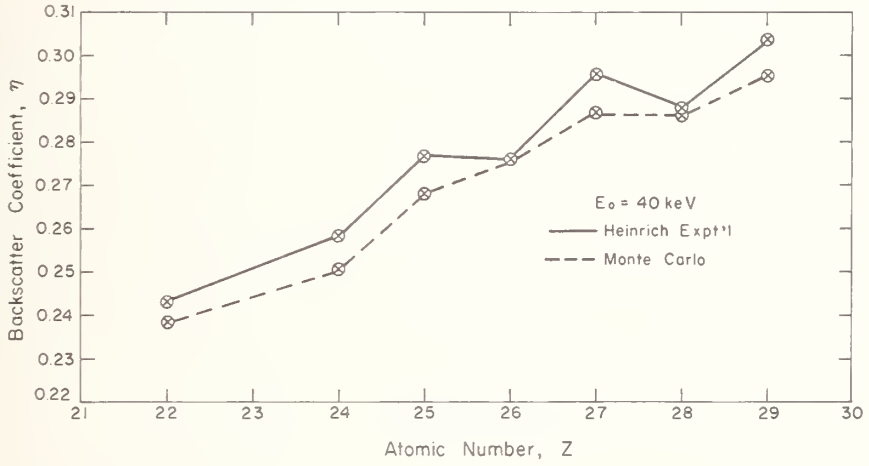

Figure 8. Backscatter coefficient versus atomic number for the elements at the end of the first transition series; experimental data of Heinrich [14].

The backscatter fraction increases as the specimen tilt angle increases from zero, i.e., normal beam incidence. At 90° specimen tilt, the value of η should be unity since the electrons skim the surface without penetrating. The value of η as a fraction of specimen tilt, θ, was measured for an iron-3.22 weight percent silicon alloy. The measurements were made with the specimen current signal. The incident current and absorbed current were measured using a high-stability current amplifier. The specimen was biased to +30 V in order to suppress secondary electron escape. The region of the scanning electron microscope specimen chamber above the specimen was covered with a carbon-coated plastic shield so as to minimize re-backscattering onto the sample. Measurements were carried out at 10° intervals in the range 0° to 70° of specimen tilt. The corresponding curve was calculated by the Monte Carlo method. The comparison of experimental and calculated values is shown in figure 9; the curves are in reasonable agreement.

Electron backscattering from tapered needles of pure nickel and from a homogeneous alloy of 40 weight percent gold-copper (SRM-482) [10] was measured as a function of needle diameter. Figure 10 shows the comparison of the calculated and measured results for the gold-copper alloy.

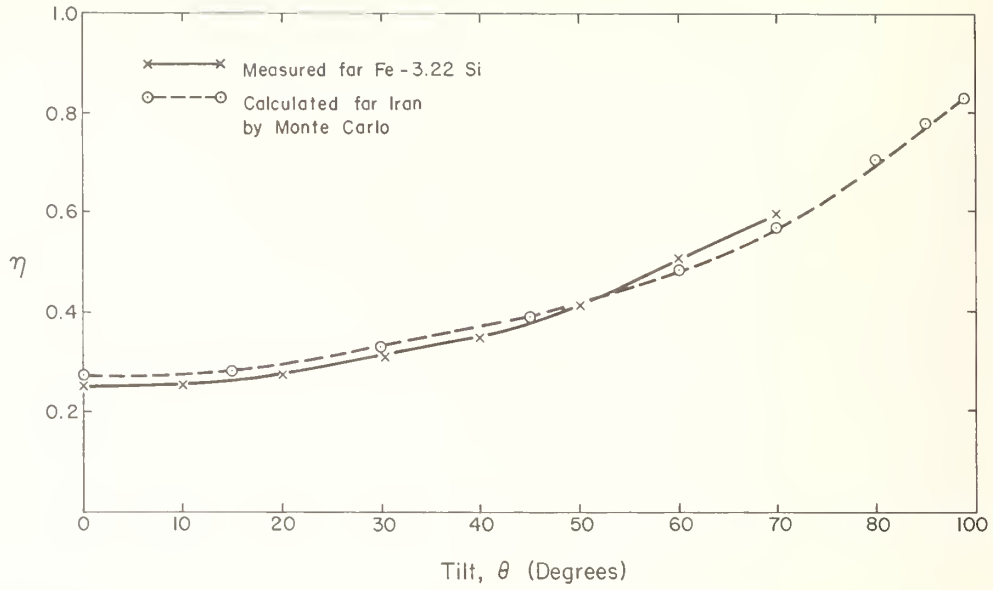

Figure 9. Backscatter coefficient versus specimen tilt (beam energy 30 keV); experimental data for Fe-3.22% Si; Monte Carlo calculations for iron.

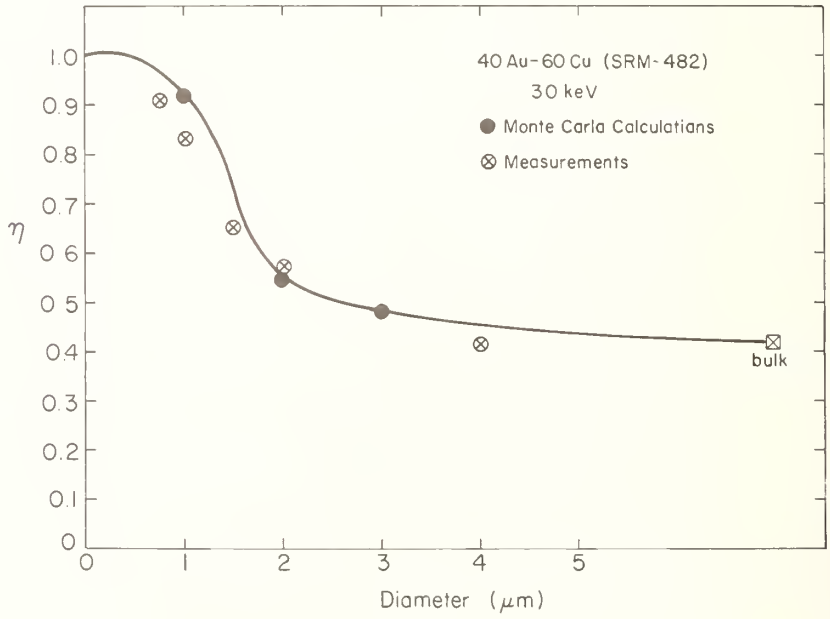

Figure 10. Backscatter coefficient (all emitted beam electrons) versus diameter for a copper-gold alloy needle.

The relationship for the electron backscattering fraction as a function of specimen composition has been shown experimentally to be [11]:

$$\eta^* = \sum_{i=1}^{m} C_i \eta_i$$

where C_i is the weight fraction of element i,

η_i is the backscatter fraction of element i, and

η^* is the backscatter fraction of the specimen which consists of m components.

The backscatter coefficients for gold-copper and gold-silver alloys and the pure elements were calculated. Experimentally, the backscatter coefficient follows a simple rule of mixtures, so that the Monte Carlo method should yield a straight line through each composition point connecting the pure end members. As figure 11 shows, the computational scheme correctly predicts the electron backscattering fraction as a function of composition.

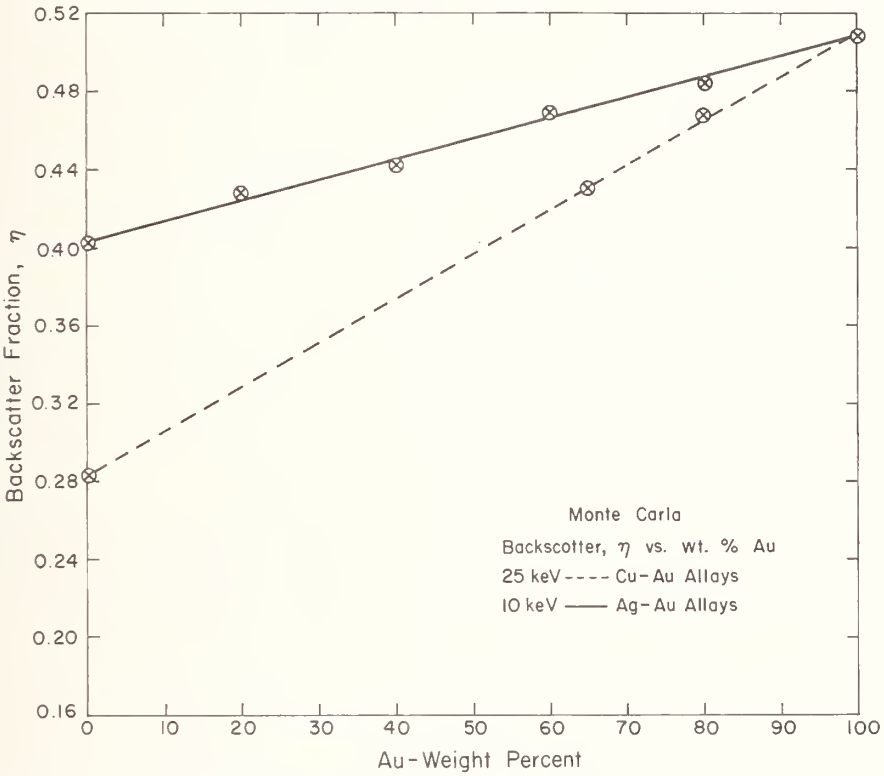

Figure 11. Calculated backscatter coefficients versus composition for copper-gold and silver-gold alloys.

The effect of a magnetic field within the specimen on the incoming electron beam has been investigated exhaustively with this Monte Carlo procedure. The details can be found elsewhere in this volume [17]. We comment here that agreement of predicted and observed results is very good.

Cosslett reported a series of measurements of electron transmittance and backscatter fractions as a function of thickness for copper films bombarded with 10 keV electrons [18]. The agreement between these fractions and those predicted by Monte Carlo calculations is shown in figure 12.

Wells' technique of energy filtering the backscattered electron signal so as to accept only those electrons which have suffered a low energy loss provides better effective resolution in scanning electron microscopy [20]. In order to obtain these low-loss electrons, the specimen is tilted 50° to 70° with respect to the electron beam. Then, many electrons strike the surface and re-emerge having lost only a small fraction of their initial energy. Wells has measured the angular distribution of the low-loss electrons [3]. The Monte Carlo computed distribution agrees well with the experimental results as is shown in figure 4.

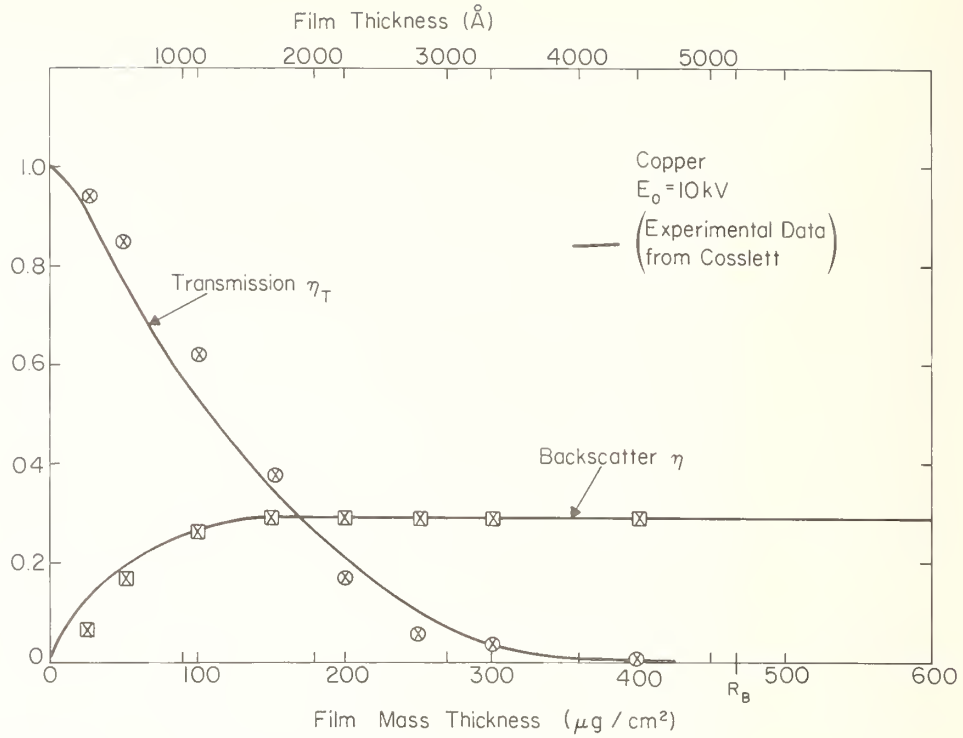

Figure 12. Transmission and backscattering coefficients for copper films; experimental data by Cosslett [18].

For all of the many cases subjected to testing, the agreement between predicted and measured electron properties is satisfactory. Such agreement indicates that the electron-solid interaction is adequately modeled by the described form of the Monte Carlo procedure.

4.2 X-Ray Production

The first test of the x-ray portion of the program involves calculation of the number of photons generated per electron. If the program fails to correctly predict the x-ray generation, then all x-ray computations become suspect. As a consequence of the good fit of the backscattering parameters, there is very good agreement between the calculated and measured values for K x-ray lines as a function of atomic number and beam energy (figures 13 and 14). For L x-ray lines, agreement is not as good. We believe that this may be due to the use of an incorrect ionization cross-section for the L series. Powell has pointed out that these cross-sections seem to be in substantial error [21]. We intend recalculating our L series data with Powell's suggested cross-sections.

Castaing and Hénoc have measured the x-ray generation distribution as a function of depth, $\phi(z)$, in aluminum for several incident beam energies [22]. Figure 15 shows the comparison of these data to those calculated by the Monte Carlo method. The Monte Carlo model appears to predict the distribution $\phi(z)$ quite well. However, the x-ray calculation is sensitive to input parameters such as mean ionization potential [23] and x-ray mass attenuation coefficients [24]. The effect of varying the mean ionization potential J on a predicted $\phi(z)$ curve for Au-Mα (beam energy of 10 keV) is shown in figure 16.

We have compared Monte Carlo calculations of $1/f(\chi)$ vs. χ for a wide variety of elements and incident beam energies with empirical results [16]. A comparison is shown in figure 17; however, the agreement is not always this good. The effect of the uncertainty of J on one set of results is shown in figure 18, showing one such difficulty. Effects of the model and details of input parameters cannot be clearly separated, and until the input parameters are better known, this situation will be difficult to resolve. Moreover, the uncertainty in the experimental data is not known.

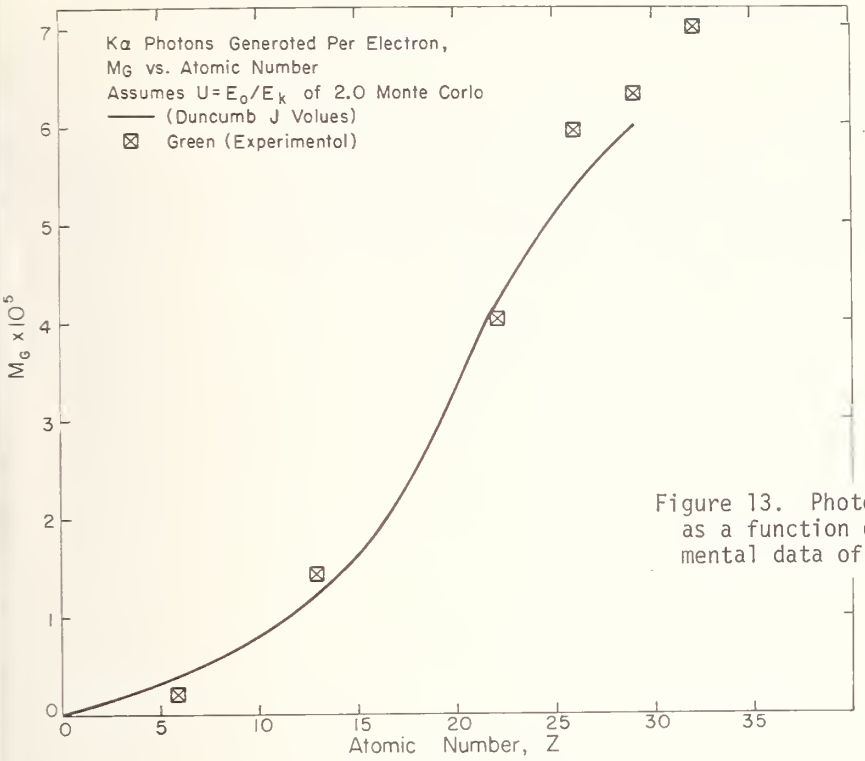

Figure 13. Photons generated per electron as a function of atomic number; experimental data of Green [19].

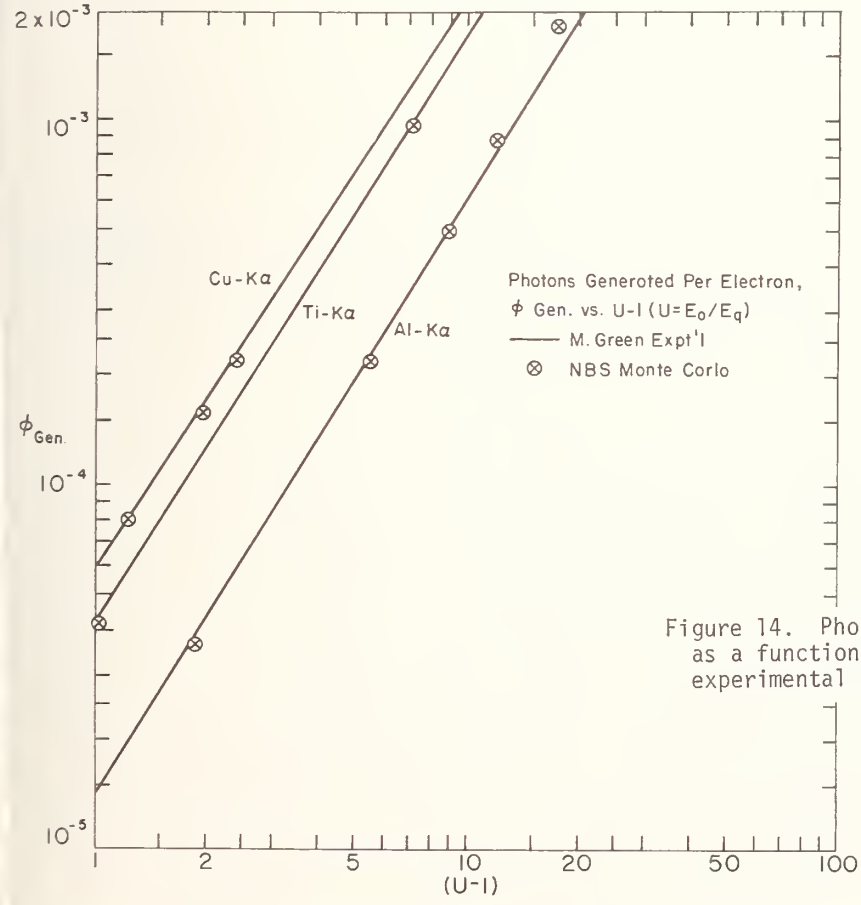

Figure 14. Photons generated per electron as a function of beam over-voltage; experimental data of Green [19].

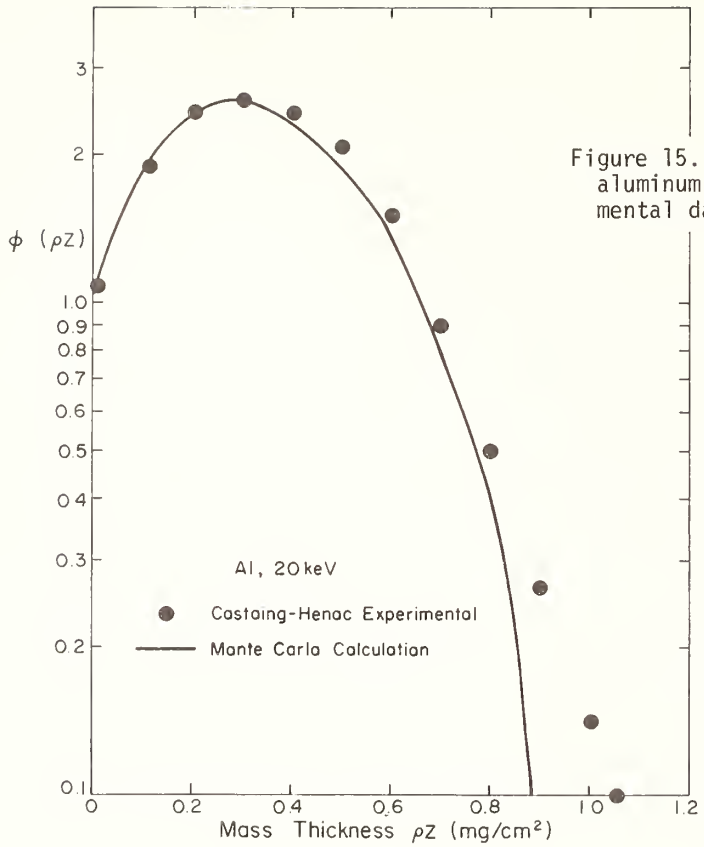

Figure 15. Depth distribution, $\phi(z)$ versus z for aluminum with a beam energy of 20 keV; experimental data of Castaing and Hénoc [22].

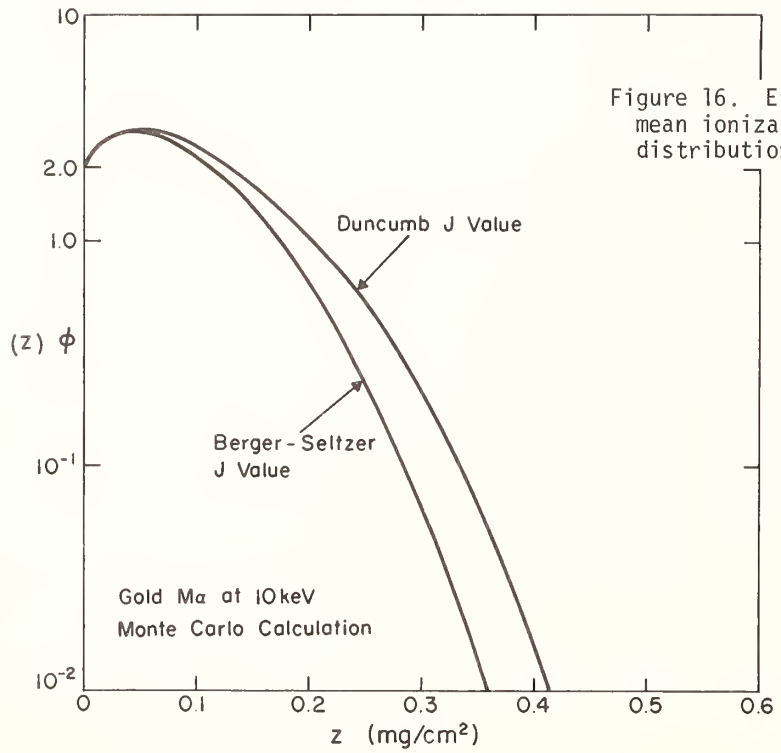

Figure 16. Effect of varying the value of the mean ionization potential, J, on the depth distribution of generated x-rays.

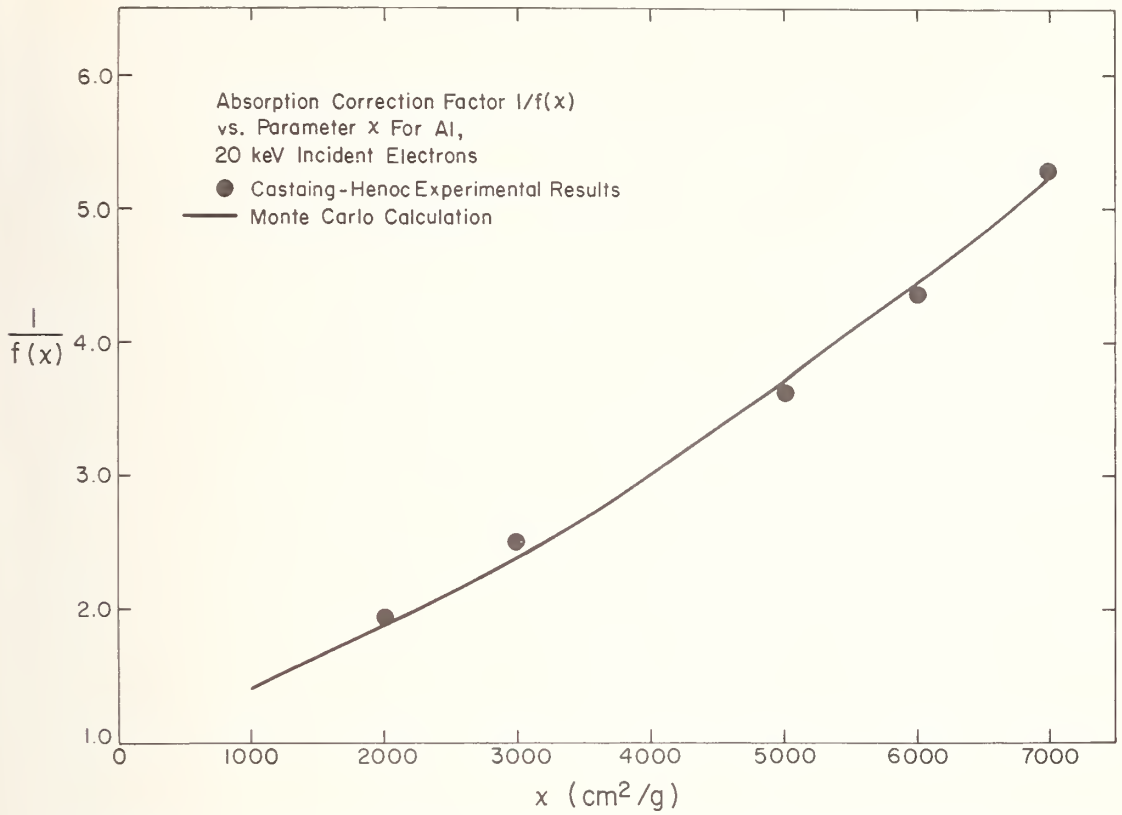

Figure 17. Absorption correction factor $1/f(\chi)$ versus χ (absorption coefficient multiplied by the cosecant of the take-off angle (Ψ) for aluminum, beam energy 20 keV; experimental data of Castaing and Hénoc [22].

The effect of uncertainties in the mean ionization potential on the analysis of gold in gold-silver alloys (SRM 481) was tested. The Monte Carlo program was given certified alloy compositions (homogeneity is also certified) [16], and the expected intensity ratio I_{BINARY}/I_{PURE} was calculated (k_A). The calculated value was then compared with the measured value obtained from the Au-Mα line for analysis with Ψ = 52.5° and an incident beam energy of 10 keV. Two sources for mean ionization potentials were utilized. Results are shown in table 1. The urgent need for accurate input parameters is clearly pointed out by these and similar results testing effects of different x-ray mass attenuation coefficients [25].

We carried out a set of measurements on copper-gold alloys (SRM 482) with tilted specimens. The ratio of the intensities of CuKα and AuLα in alloys of 20, 40, 60 and 80 weight percent copper in gold to the intensity of CuKα and AuLα from pure copper and gold was measured. The experiment was performed in a commercial scanning electron microscope equipped with an energy-dispersive x-ray spectrometer (EDS). Specimen tilts of 30°, 45°, and 60° with respect to the normal position of the electron beam were used. Integrated peak intensities were taken; the region of interest was the full peak. At least 5×10^4 counts were recorded for peaks of interest. Background substraction was carried out by the method described by Fiori, et al. [26]. The electron beam energy was 20 keV. The specimen-detector configuration was carefully arranged so that the x-ray emergence angle was equal to the tilt angle; specimen height was not changed between sample and standard. The beam current was checked between each analysis with the aid of a Faraday cup. Stability within two percent was maintained throughout the course of the experiment. The total count rate into the EDS system was maintained well within the linear input-output region. Standards were measured before and after analysis of the alloys; two regions on each sample were analyzed. The intensity ratios for copper and gold, called k_{Cu} and k_{Au}, respectively, were plotted against the ratio k/C. The results for the 45° tilt are shown in figure 19. If the plot of k/C against k is scattered, then the experimental results are internally inconsistent [16]. The

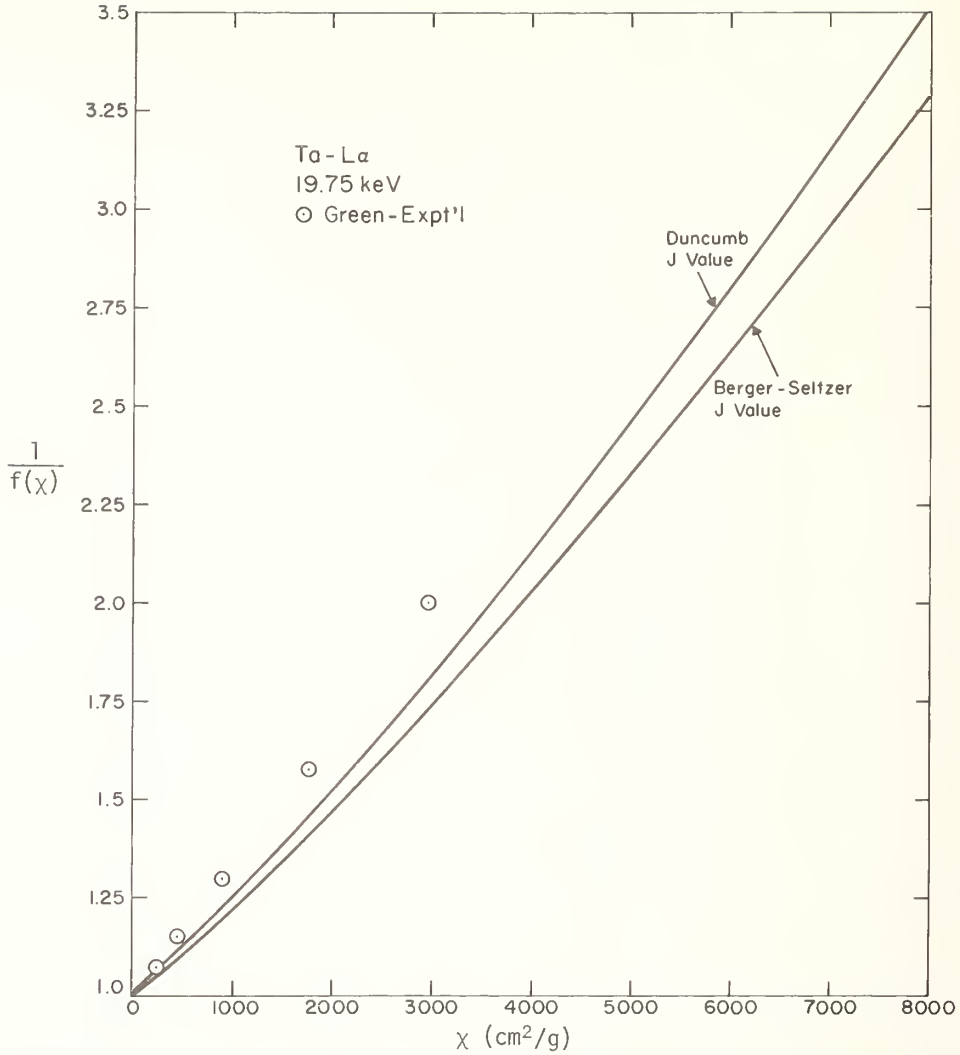

Figure 18. Effect of varying the value of the mean ionization potential, J, on $1/f(\chi)$ versus χ.

Table 1. Comparison of intensity ratios (K) calculated by Monte Carlo with measured values.

Au-Mα in Au-Ag at 10 kV				Cu-Lα in Cu-Au at 25 kV			
C	K_M	K(D-S)	K(B-S)	C	K_M	K(KFJH)	(KAMEN)
0.2243	0.201	0.221	0.200	0.1983	0.097	0.083	0.073
.4003	.362	.349	.363	.3964	.219	.188	.178
.6005	.599	.549	.563	.5992	.387	.345	.337
.8005	.771	.759	.771	.7985	.632	.561	.584

KAMEN: M(Cu,CuLα) = 1907; M(Au,CuLα) = 8181

KFJH: M(Cu,CuLα) = 2079; M(Au,CuLα) = 7030

C is concentration, K_M is measured intensity ratio, K(K-S) is calculated with the Duncumb-Shields mean ionization potential (J), K(B-S) is calculated with the Berger-Seltzer J.

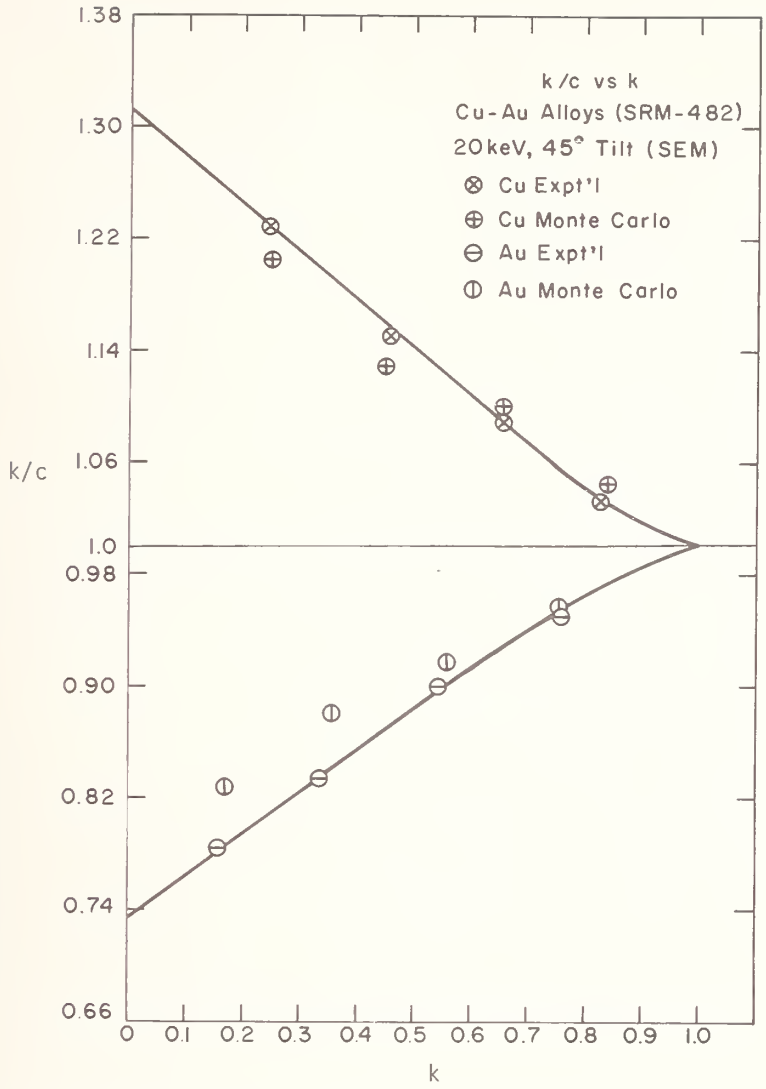

Figure 19. Intensity ratio, k, divided by certified concentration, c, plotted against k for copper-gold alloys.

lack of such scattering implies that these results are internally consistent. The corresponding Monte Carlo results are shown in figure 19 as well. The largest relative difference between the measured and Monte Carlo results is about five percent. Considering the input parameter uncertainties, this agreement is satisfactory. Similar results were obtained at 30° and 60° tilt.

Quantitative analysis of particulates is not feasible with conventional electron probe microanalysis data reduction schemes. However, the Monte Carlo procedure is capable of dealing with the geometric configurations prevalent in particulate analysis. We have tested the NBS Monte Carlo program by calculation for both spherical and cylindrical shapes.

Bayard measured the ratio of AlKα x-ray intensity from spheres ranging in diameter from 1 to 10 μm to that of pure bulk aluminum. The nominal x-ray emergence angle was 52.5° with respect to the substrate; the incident beam energy was 17 keV [27]. Calculations of the intensity ratio were made with the Monte Carlo program and the ratio of emitted intensities was computed. The results are shown in figure 20; agreement of Monte Carlo calculations with Bayard's experimental results is very good.

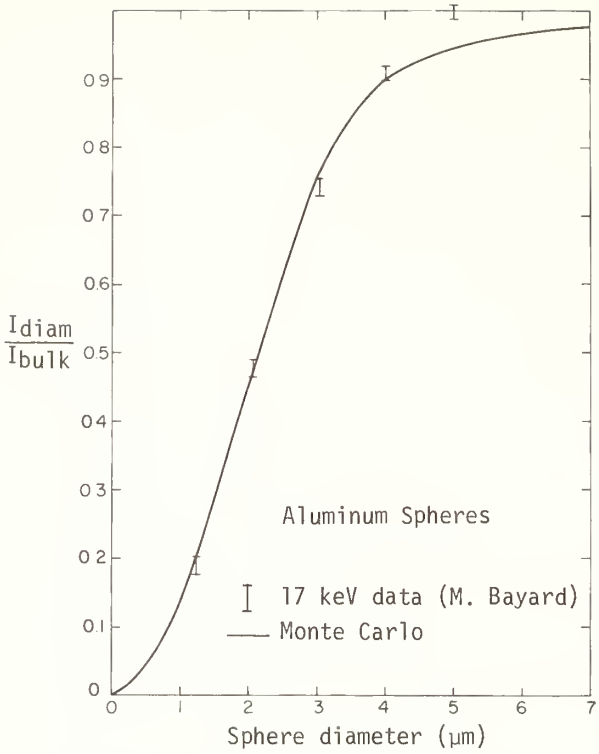

Figure 20. Intensity ratio I_{diam}/I_{bulk} versus diameter for aluminum spheres, beam energy 17 keV; experimental data of Bayard [27].

A needle consisting of a 40 weight percent gold-copper alloy was fashioned from SRM 482. The intensity ratios for CuKα and AuLα were measured with pure copper and gold as standards. The experiment was performed with a scanning electron microscope in which the standards were tilted with respect to normal electron beam incidence by 30°. The x-ray emergence angle was 30°. Incident beam energy was 30 keV. Apparent cylinder diameters were determined assuming that the magnification indicator on the scanning electron microscope was correct. The comparison of experimental and Monte Carlo results are shown in figure 21. The agreement for the gold is excellent, but the copper results show a systematic deviation.

The analysis of a thin film on a bulk substrate is important in many instances. Several techniques have been devised to carry out such analyses [28,29]. The Monte Carlo method is well suited to deal with such cases [30]. For our test, the data of Bishop and Poole for a copper film on a nickel substrate [31] were selected. The nominal copper film thickness was 0.035 mg/cm^2 or 390 Å. The ratios of CuKα and NiKα line intensities from this specimen to pure bulk CuKα and NiKα intensities were measured. The incident electron beam energy was 10.75 keV; the x-ray emergence angle was 75°. For copper, the experimental result was 0.476 and the Monte Carlo result was 0.445. For nickel, the experimental result was 0.570 and the Monte Carlo result was 0.560.

We conclude from the foregoing series of tests that the Monte Carlo program described here reproduces a wide variety of experimental findings with good agreement usually within ten percent relative to experimental values. Therefore, this program can be used to predict, to a good approximation, similar data under a wide variety of conditions. Since the cost of the Monte Carlo procedure is relatively high, the ultimate use of the Monte Carlo method will probably be to determine if empirical tests can be employed in explaining observed phenomena. In other words, the Monte Carlo results will be used as a referee test for empirical formulae. When the results of both agree, then the empirical formula may be considered as being reliable. Monte Carlo methods have already been used for such purposes, e.g., the testing of an analytical expression for $\phi(z)$ and an analytical method for thin film analysis [32]. The Monte Carlo procedure can also be used to decide on experimental conditions. An example is shown in figure 22, which shows the predicted SiKα intensity ratio for a cylinder measured under the two conditions illustrated. Clearly, the geometrical effect of a 0° emergence angle produces undesirable results due to high absorption; hence, for particle analysis, one requires a high effective emergence angle, Ψ. Other possible experimental configurations may be first tested by the Monte Carlo procedure.

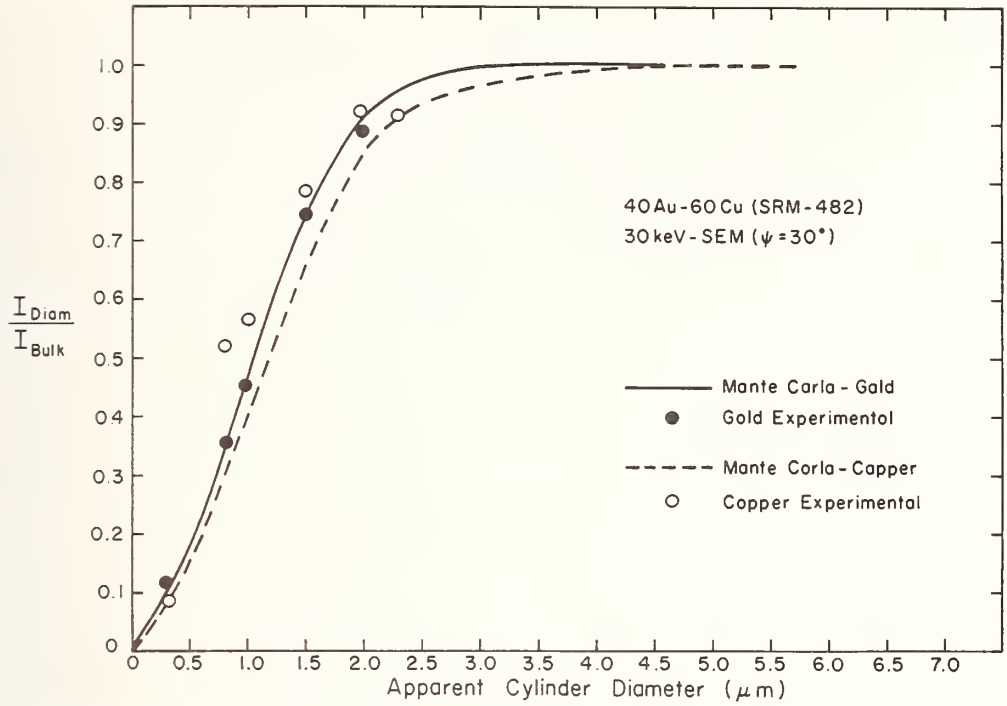

Figure 21. Intensity ratio I_{diam}/I_{bulk} versus diameter for a copper-gold alloy needle.

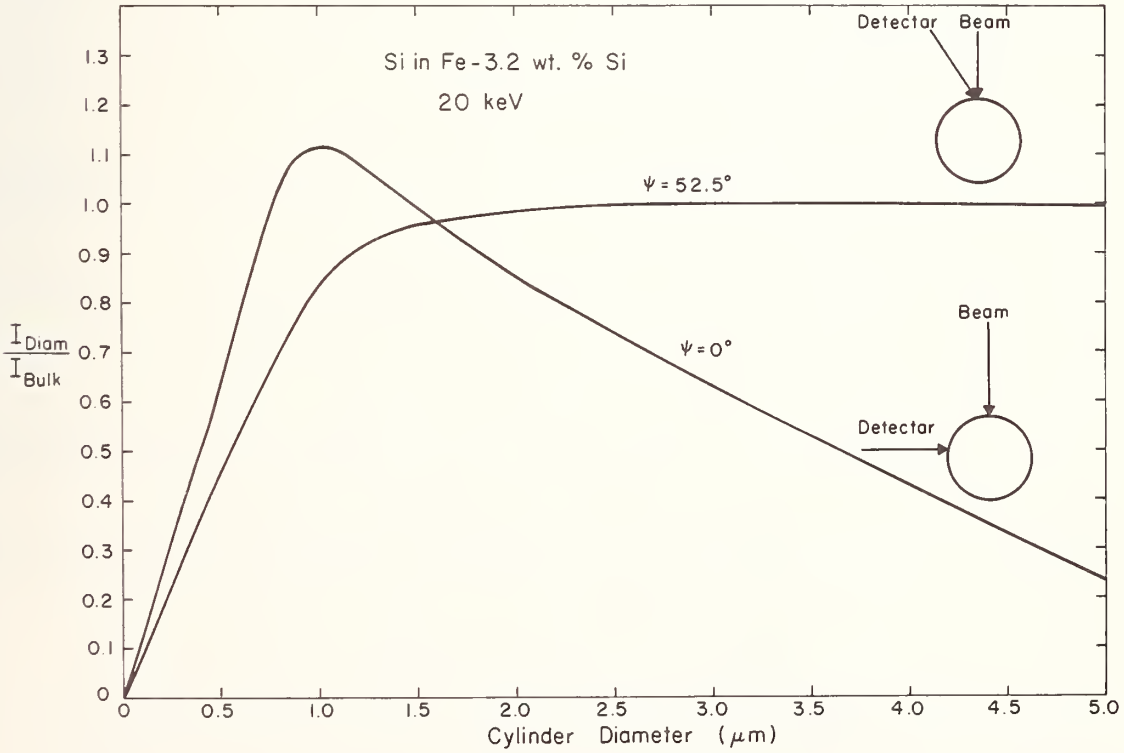

Figure 22. Effect of take-off angle on the intensity ratio I_{diam}/I_{bulk} for silicon K-radiation from an iron-3.22% Si alloy needle.

References

[1] Heinrich, K. F. J., Yakowitz, H., and Newbury, D. E., eds., *Monte Carlo Calculations in Electron Probe Microanalysis and Scanning Electron Microscopy*, this publication (p. 105).

[2] Curgenven, L. and Duncumb, P., Simulation of Electron Trajectories in a Solid Target by a Simple Monte Carlo Technique, Tube Investments Research Laboratories, Report No. 303 (Hinxton Hall, Saffron Walden, Essex, England, 1971).

[3] Wells, O. C. *Scanning Electron Microscopy*, p. 71 (McGraw Hill, New York, 1974).

[4] Broers, A. N., in *Microprobe Analysis*, C. A. Anderson, ed., p. 88 (Wiley, New York, 1973).

[5] Bethe, H., *Annalen der Phys. LPZ.* 5, 325 (1930).

[6] Bethe, H., Rose, M., and Smith, L., *Proc. Am. Phil. Soc.* 78, 573 (1938).

[7] Duncumb, P., Shields-Mason, P. K., and daCasa, C., *Proc. Fifth International Congress on X-ray Optics and Microanalysis, p.* 146 (Springer-Verlag, Berlin, 1969).

[8] Berger, M. J. and Seltzer, S. M., Natl. Acad. Sci., Natl. Res. Council Publ. 1133, p. 205 (Washington, D. C., 1964).

[9] Southworth, R. W. and Deleeuw, S. L., *Digital Computation and Numerical Methods*, p. 455 (McGraw-Hill, New York, 1965).

[10] Rutherford, E., *Phil. Mag.* 21, 669 (1911).

[11] Bishop, H. E., in *X-ray Optics and Microanalysis*, IV International Congress on X-ray Optics and Microanalysis, Orsay, 1965, R. Castaing, P. Deschamps, and J. Philibert, eds., p. 153 (Hermann, Paris, 1966).

[12] Wells, O. C. in SEM/1975, *Proc. of the 8th Annual SEM Symp.*, O. Johari, ed., p. 43 (IITRI, Chicago, 1975).

[13] Thomas, R. N., Ph.D. thesis, Cambridge University (1961).

[14] Heinrich, K. F. J. in *X-ray Optics and Microanalysis*, IV International Congress on X-ray Optics and Microanalysis, Orsay, 1965, R. Castaing, P. Deschamps, and J. Philibert, eds., p. 159 (Hermann, Paris, 1966).

[15] Heinrich, K. F. J., in *Quantitative Electron Probe Microanalysis*, K. F. J. Heinrich, ed. Natl. Bur. Stds. Spec. Publ. 298, p. 5 (NBS, Washington, D. C., 1968).

[16] Heinrich, K. F. J., Myklebust, R. L., Rasberry, S. D., and Michaelis, R. E., Natl. Bur. Stds. Spec. Publ. 260-28 (NBS, Washington, D. C., 1971).

[17] Newbury, D. E., Yakowitz, H., and Myklebust, R. L., A Study of Type II Magnetic Domain Contrast in the SEM by Monte Carlo Electron Trajectory Simulation, this publication (p. 151).

[18] Cosslett, V. E., in *X-ray Optics and Microanalysis*, IV International Congress on X-ray Optics and Microanalysis, Orsay, 1965, R. Castaing, P. Deschamps, and J. Philibert, eds., p. 85 (Hermann, Paris, 1966).

[19] Green, M., Ph.D. thesis, University of Cambridge (1962).

[20] Wells, O. C., in SEM/1974, *Proc. of the 7th Annual SEM Symposium*, O. Johari, ed., p. 1 (IITRI, Chicago, 1974).

[21] Powell, C. J., Evaluation of Formulas for Inner-Shell Ionization Cross-Sections, this publication (p. 97).

[22] Castaing, R. and Hénoc, J., in *X-ray Optics and Microanalysis*, IV International Congress on X-ray Optics and Microanalysis, Orsay, 1965, R. Castaing, P. Deschamps, and J. Philibert, eds., p. 120 (Hermann, Paris, 1966).

[23] Heinrich, K. F. J and Yakowitz, H., *Mikrochim. Acta* 123 (1970).

[24] Yakowitz, H. and Heinrich, K. F. J., *Mikrochim. Acta* 182 (1968).

[25] Yakowitz, H., in *Practical Scanning Electron Microscopy*, J. I. Goldstein, and H. Yakowitz, eds., p. 327 (Plenum, New York, 1975).

[26] Fiori, C. E., Myklebust, R. L., Heinrich, K. F. J., and Yakowitz, H., *Anal. Chem.* 48, 172 (1976).

[27] Bayard, M., in *Microprobe Analysis*, C. A. Anderson, ed., p. 323 (Wiley, New York, 1973).

[28] Colby, J. W., in *Advances in X-ray Analysis*, Vol. II, p. 287 (Plenum, New York, 1968).

[29] Oda, Y. and Nakajima, K., *J. Jap. Inst. Met.* 37, 673 (1973).

[30] Kyser, D. F. and Murata, K., *IBM J. Res. and Dev.* 18, 352 (1974).

[31] Bishop, H. E. and Poole, D. M., *J. Phys. D: Appl. Phys.* 6, 1142 (1973).

[32] Yakowitz, H. and Newbury, D. E., in SEM/1976, *Proc. of the 9th Annual SEM Symposium,* O. Johari, ed. p. 151 (IITRI, Chicago, 1976).

The specimen surface is contained in the X-Y plane, with the positive direction of the Y-axis pointing down a tilted specimen and away from the beam impact point.

The exact technique of calculating the point coordinates is as follows (figure 23):

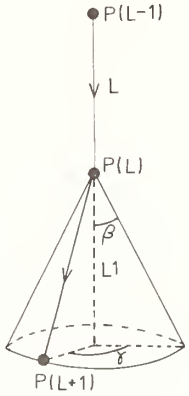

Figure 23. Schematic of Monte Carlo calculation.

With the electron at a known point P(L), having come from a known point P(L-1), calculate P(L+1).

The electron has traveled from P(L-1) to P(L) along a line (L) whose direction cosines (a,b,c) can be calculated from the coordinates (X,Y,Z) (L-1) and (X,Y,Z) (L). If the electron were not scattered at point P(L), it would continue along line (L). The act of scattering the electron through an angle β, calculated from the screened Rutherford model, sends the electron to some point P(L+1) on the perimeter of the base of a cone whose altitude is the extension of line L1, (fig. 23).

To calculate P(L+1), the point (X_o,Y_o,Z_o) at which the extended line L1 intersects the plane containing the base of this cone is first determined: the path on the same surface that the electron travels from P(L) to P(L+1) has a length equal to the step-length for that scattering act, D(L), which is known. The altitude of the cone, H, is given by:

$$H = D(L) \cos\beta. \tag{A-1}$$

Similarly, the radius of the base of the cone is:

$$R = D(L) \sin\beta. \tag{A-2}$$

The coordinates of the center of the cone base (X_o,Y_o,Z_o) are given by:

$$X_o = X(L) + (H \cdot a) \tag{A-3}$$

$$Y_o = Y(L) + (H \cdot b) \tag{A-4}$$

$$Z_o = Z(L) + (H \cdot c). \tag{A-5}$$

We next establish a new set of coordinate axes, X',Y',Z' (fig. 24) with X'Y' plane containing the base of the cone, and the Z' axis coincident with extended L'.

The direction cosines of the primed axes in terms of the original axes must be determined. For the Z' axis, the direction cosines are the same as line L1:

$$a_{Z'} = a,\ b_{Z'} = b,\ c_{Z'} = c. \tag{A-6}$$

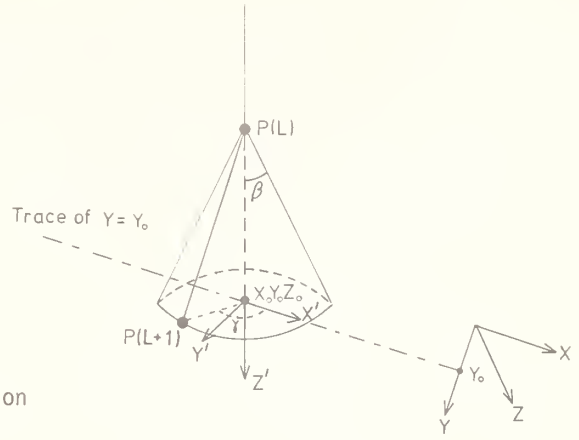

Figure 24. Schematic of Monte Carlo calculation showing choice of coordinate axes.

The X' axis is arbitrarily chosen to be the line of intersection of the plane of the base of the cone with the plane $Y = Y_0$. From the knowledge of a point in the plane of the cone base, (X_0,Y_0,Z_0), and the direction cosines of the normal to the plane, i.e., those of line L1, the equation of the cone base is:

$$aX + bY + cZ - (aX_0+bY_0+cZ_0) = 0. \tag{A-7}$$

The line of intersection with the plane $Y = Y_0$ is:

$$aX + cZ - (aX_0+cZ_0) = 0. \tag{A-8}$$

Thus, the line has the form:

$$Z = \frac{-a}{c} X + K \; ; \quad K = \frac{aX_0}{c} + Z_0 \tag{A-9}$$

and the direction cosines of the X' axis with respect to the original axes are:

$$a_{X'} = \cos (\arctan (-a/c)) \tag{A-10}$$

$$b_{X'} = \cos 90° = 0 \tag{A-11}$$

$$c_{X'} = \cos (\arctan (-c/a)). \tag{A-12}$$

Knowing the direction cosines of X' and Z', we can obtain the direction cosines of Y' by the "direction number device." Since the original X,Y,Z axes were chosen to form a right-handed coordinate system, we maintain parity, making X',Y',Z' right-handed by forming the cross product $(Z'\overline{X}X')$:

$$a_{Y'} = b_{Z'} \cdot c_{X'} \tag{A-13}$$

$$b_{Y'} = c_{Z'} \cdot a_{X'} - c_{X'} \cdot a_{Z'} \tag{A-14}$$

$$c_{Y'} = -a_{X'} \cdot b_{Z'} . \tag{A-15}$$

In the coordinate system X,Y,Z, the point P(L+1) on the base perimeter of the cone is chosen randomly. The azimuthal angle is calculated with a random number RN such that $0.0 \leq RN \leq 1.0$. The coordinates of the point P(L+1) are

$$X'(L+1) = R \cdot \cos (RN \cdot 2\pi) \tag{A-16}$$

$$Y'(L+1) = R \cdot \sin (RN \cdot 2\pi) \tag{A-17}$$

$$Z'(L+1) = 0. \tag{A-18}$$

The coordinates X',Y',Z'(L+1) can be transformed back to the space X,Y,Z to give the desired point P(L+1) since we have the direction cosines of the X',Y',Z' axes:

$$X = a_{X'} \cdot X'(L+1) + a_{Y'} \cdot Y'(L+1) + X_o \tag{A-19}$$

$$Y = b_{X'} \cdot X'(L+1) + b_{Y'} \cdot Y'(L+1) + Y_o \tag{A-20}$$

$$Z = c_{X'} \cdot X'(L+1) + c_{Y'} \cdot Y'(L+1) + Z_o. \tag{A-21}$$

National Bureau of Standards Special Publication 460. Proceedings of a Workshop on the Use of Monte Carlo Calculations in Electron Probe Microanalysis and Scanning Electron Microscopy held at NBS, Gaithersburg, Maryland, October 1-3, 1975. Issued December 1976.

APPLICATION OF MONTE CARLO SIMULATION TO ELECTRON MICROPROBE ANALYSIS OF THIN FILMS ON SUBSTRATES

David F. Kyser

IBM Research Laboratory
San Jose, California 95193

and

Kenji Murata

University of Osaka Prefecture
Osaka, Japan

A Monte Carlo simulation procedure has been developed for high-energy (1-50 keV) electron beam scattering, energy loss, and x-ray production in targets consisting of thin alloy films on thick substrates. The method utilizes experimental x-ray intensities referenced to thick standards, and avoids the problems associated with preparation and characterization of thin film standards. The chemical analysis C_i (weight percent) and mass thickness ρt (g/cm^2) of the alloy film can be deduced separately; specific examples are given of alloy films Mn_xBi_{1-x} and CO_xPt_{1-x} on SiO_2 substrates. The chemical analysis obtained with the Monte Carlo procedure is correlated with that obtained from nuclear backscattering energy analysis.

Monte Carlo-generated calibration curves of total electron backscatter yield η are presented for the case of Al films on Au substrates and Au films on Al substrates. These curves show a smooth transition of η versus ρt between the asymptotic limits of η(Al) and η(Au). The shape of the curve depends on the electron beam voltage E_0 (keV). Further experimental work is necessary to confirm the accuracy of these calculations for η, and then the method may be useful for a nondestructive, localized thickness measurement of thin films on substrates.

Key Words: Electron probe microanalysis; Monte Carlo electron trajectory calculations; nuclear backscattering analysis; scanning electron microscopy; thin films; x-ray analysis.

1. Introduction

Quantitative electron microprobe analysis of thin alloy films on thick substrates is an important and challenging problem for which there are two procedures available. If the film is sufficiently thick to stop the electron beam before it penetrates into the substrate, then the conventional "ZAF" model [1][1] can be utilized to transform the measured x-ray intensities into chemical weight fraction. This approach often requires low overvoltages ratios, $U_0 = E_0/E_c$, where E_c is the critical excitation energy or extremely low beam energy, E_0, coupled with soft x-ray measurements. These operating conditions can lead to serious quantitative errors due to surface effects (roughness, corrosion) or due to limitations in correction procedures (e.g., absorption, atomic number).

Another approach is to maintain high beam energy and high overvoltage U_0 coupled with hard x-ray measurements and thick standards. However, corrections must still be made for: (a) atomic number effects in the film sample and thick standards, (b) loss of x-ray inten-

[1]Figures in brackets indicate the literature references at the end of this paper.

sity from the film sample due to electron penetration into the substrate, and (c) enhanced x-ray intensity from the film due to electrons backscattered from the substrate. There may also be some absorption and fluorescence corrections. In traditional style, these corrections for thin film targets could be called the "ZAP" model (Z = atomic number, A = absorption, P = penetration). Due to the complex target configuration and variety of experimental parameters, it is very difficult to write an analytic function and separate solution for these effects without numerous assumptions. We have instead, attacked this problem with a Monte Carlo simulation of electron scattering, energy loss, and subsequent ionization distribution with depth into the film. We calculate an intensity ratio, k, for each characteristic x-ray line from the film, referenced to a thick standard target. This ratio k is conceptually the same as that utilized for electron microprobe analysis of thick targets. No film standards are required. The method assumes that there are no elements common to the film and substrate, and that the substrate composition is specified. Specific examples of Mn_xBi_{1-x} and Co_xPt_{1-x} alloy films on SiO_2 substrates will be described.

In the second part of this paper, we present some calculations of electron backscatter yield from thin films on thick substrates. The backscatter yield is calculated with the same basic Monte Carlo simulation theory as that used for the x-ray calculations. This type of calculation would be useful for nondestructive and highly localized measurement of thin film thickness. The method can be utilized even when there are elements common to the film and substrate, but requires the film and substrate composition to be specified. The usefulness of this technique lies in the unique dependence of backscatter yield on atomic number of the target, and the thickness sensitivity depends upon the difference in atomic number between the film and substrate. Specific calculations are made for thin films of Al or Au on substrates of Au or Al, respectively.

2. Quantitative Microprobe Analysis of Thin Alloy Films on Substrates

In this paper, we restrict ourselves to analysis of thin alloy films on substrates, and exclude freestanding foils. Foils are also an important application which requires quantitation but that was not the primary emphasis in this work. The special case of foil targets can easily be treated by elimination of the substrate within the present model.

Quantitative analysis of alloy films on substrates with the electron microprobe has received some attention already [2-11]. These references can be separated into two broad classes, namely those dealing with analytic function techniques [2,4,6,8,10], and those dealing with Monte Carlo simulation techniques [3,5,7,9,11]. The technique of Monte Carlo simulation is ideally suited for application to complex target configurations such as a thin film on a thick substrate. The boundary conditions of the particular target can be easily accommodated within a single model for electron scattering and energy loss, in contrast to the analytic techniques which require additional assumptions and approximations to treat the interface effects. The following treatment describes our success with Monte Carlo electron simulation and quantitative analysis of thin alloy films on thick substrates.

2.1 Monte Carlo Simulation

The details of the Monte Carlo simulation for electron scattering, atomic ionization, and x-ray production have been described previously [9]. A single-scattering model is used which has been described by Murata et al. [12,13], in applications to thick targets. The single-scattering model utilizes the Rutherford equation to describe elastic angular scattering of the primary electrons by the (screened) atomic nuclei in the target. The Bethe equation is used to describe continuous energy loss between the elastic scattering events. The energy-dependent mean free path of the electron (for elastic scattering) is the step length between angular scattering points. When the electron path being simulated crosses the prescribed boundary between film and substrate, the ionization rate for elements within the film is set equal to zero unless the electron is subsequently backscattered into the film. Scattering and energy loss, characteristic to the substrate, continues as the primary electrons decelerate in the substrate.

Because the angle of scattering is chosen by a computer-generated random number and analytic probability distribution with angle, no two simulated electrons will have identical three-dimensional trajectories in the target. To simulate a real electron beam, a large number of electrons paths (typically 10^3-10^4) are obtained in order to permit a meaningful statistical analysis. The target is divided into differential volumes or layers, and a

histogram of energy deposition and x-ray production is then produced by the Monte Carlo technique. This is possible because the computer program maintains the energy and spatial coordinates of each simulated electron. The computer program also generates the energy distribution, angular distribution, and total yield of backscattered electrons. The program also generates the absorption correction $f(\chi)$ where $\chi = (\mu/\rho)\csc\psi$ and $f(\chi)$ is the Laplace transform of the ionization depth distribution $\Phi(\rho z)$. This same procedure is utilized for a specified film thickness $\rho t(\mu g/cm^2)$ and specified film-substrate composition, as well as for each thick elemental standard target required. The final result is a set of calibration curves (k value) for each x-ray line, with ρt as a parameter. The calibration curves (drawn through a series of calculated points) apply to only one set of parameters such as beam energy E_0, x-ray take-off angle ψ, and substrate. An example of these theoretical calibration curves is shown in figures 1 and 2 for MnBi and CoPt films on SiO_2 substrates.

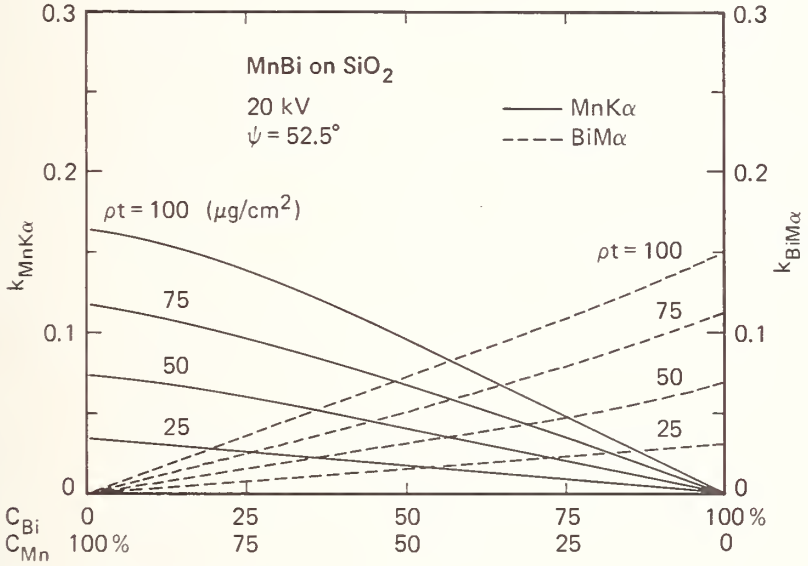

Figure 1. Theoretical calibration curves for MnKα and BiMα x-ray emission from thin films on SiO_2.

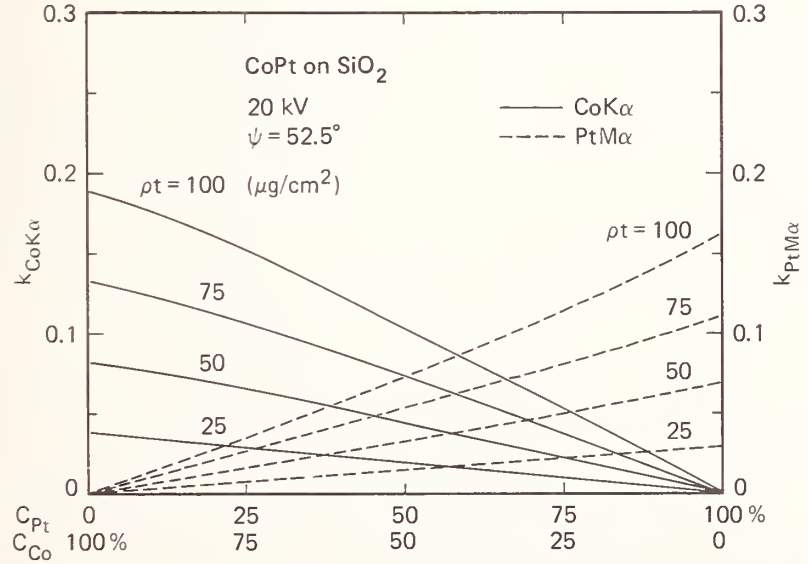

Figure 2. Theoretical calibration curves for CoKα and PtMα x-ray emission from thin films on SiO_2.

2.2 Experimental Measurements

Two sets of alloy films were obtained for test cases of binary analysis. Alloy films of Mn_xBi_{1-x} and Co_xPt_{1-x} were fabricated on SiO_2 substrates. All x-ray measurements were made at E_0 = 20 keV in an ARL electron probe microanalyzer with $\psi = 52.5°$ and normal beam incidence. The k-values were formed after correction of the observed intensities from sample and standard for spectral background and detector dead-time. These particular alloy systems were chosen because of insignificant secondary fluorescence effects and the current technical interest in their magnetic properties. The thickness range of these films was approximately 200-600Å. The experimental k-values are given in tables 1 and 2.

Table 1. Experimental k values for MnBi films on SiO_2 at 20 kV.

Sample	k(MnKα)	k(BiMα)
X115-1	0.0	0.0766
X115-3	0.0226	0.0515
X115-5	0.0293	0.0220
X115-7	0.0329	0.0067
X115-9	0.0610	0.0

Table 2. Experimental k values for CoPt films on SiO_2 at 20 keV.

Sample	k(CoKα)	k(PtMα)
10-2	0.0177	0.0581
11-2	0.0305	0.114
12-2	0.0148	0.0675
13-2	0.0067	0.0465

2.3 Analysis of Binary Films with Theoretical Calibration Curves

The analysis procedure requires that we iterate the experimental data of tables 1 and 2 within the theoretical calibration curves of figures 1 and 2, respectively, for each film sample in order to converge to a unique solution for composition C_i and total mass thickness ρt. There can be only one unique solution for each film, and a graphical procedure for convergence is described in reference 9. The results of this graphical procedure are shown in tables 3 and 4, along with some results of chemical analysis by a nuclear backscattering energy analysis method [14]. The chemical analyses agree within 5% relative, but the total mass thickness differs in a systematic fashion, i.e., the nuclear backscattering analysis results for ρt are consistently low compared to the Monte Carlo results. The source of this difference is not known at the present, and further work is required to establish the accuracy limits for both of these analysis methods.

2.4 Discussion

The Monte Carlo simulation can also be applied to ternary alloy films and even higher order systems. However, then a graphical procedure for iteration and convergence is no longer practical, and a computer method must be used after the theoretical calibration curves have been generated. One suggestion is to curve-fit the binary film calibration curves with α-coefficient expressions such as those utilized for thick targets, and then combine the binary α-coefficients for application to high-order systems such as ternary alloys [15,16]. After the theoretical calibration curves have been generated for a particular alloy system and substrate, they can be re-used to decrease the computer cost per analysis. The initial cost of a calibration curve depends on many factors such as statistical precision desired (i.e., number of trajectories simulated), concentration and thickness

Table 3. Monte Carlo and nuclear backscattering analysis of MnBi films.

	Monte Carlo		Nuclear Backscattering	
Sample	C_{Mn}(%)	ρt($\mu g/cm^2$)	C_{Mn}(%)	ρt($\mu g/cm^2$)
X115-1	0.0	54	0.0	49
X115-3	25.5	53	26.6	48
X115-5	51.0	38	53.5	34
X115-7	80.0	29	80.1	26
X115-9	100.0	42	100.0	40

Table 4. Monte Carlo and nuclear backscattering analysis of CoPt films.

	Monte Carlo		Nuclear Backscattering	
Sample	C_{Co}(%)	ρt($\mu g/cm^2$)	C_{Co}(%)	ρt($\mu g/cm^2$)
10-2	18.5	53	19.4	49
11-2	16.3	89	---	--
12-2	14.0	56	---	--
13-2	10.1	40	9.6	34

resolution desired, beam energy E_0, and cutoff energy in the trajectory termination. For a typical point on the calibration curves of figures 1 or 2, 1200 electron trajectories were simulated on our IBM S/360-model 195 computer. In figure 1, five concentrations C_i and four thicknesses ρt were chosen, in addition to the two thick standards. The total CPU time was under 30 minutes. Improvements in the computer code have now reduced this by a factor of 2.

3. Monte Carlo Calculation of Electron Backscatter Yield

The Monte Carlo computer program used for quantitative chemical analysis with x-ray production can also be used to generate theoretical calibration curves of electron backscatter yield. The electron backscatter yield η from thick targets has a unique relationship with atomic number Z of the target [17-19]. At small values of Z, $\eta \tilde{=} Z/100$ and is not very sensitive to incident beam energy E_0. At large Z, η approaches an asymptotic limit for normal (90°) beam incidence.

If the target is composed of a thin film with average atomic number Z_1 and mass thickness $\rho_1 t_1$ on top of a thick substrate with average atomic number Z_2, then the effective backscatter yield η will depend on: (a) the relative value of $\rho_1 t_1$ and the total electron range R_e in the complex target, and (b) the relative value of Z_1, Z_2. The dependence of η on E_0 is contained in R_e, and this dependence can be strong if the difference $|Z_1-Z_2|$ is large. If $\rho_1 t_1 >> R_e$, then η will be representative of Z_1, and if $\rho_1 t_1 << R_e$, η will be representative of Z_2. At intermediate values of $\rho_1 t_1$, η will also be intermediate and vary smoothly with $\rho_1 t_1$ between the limits $\eta = \eta(Z_1)$ and $\eta = \eta(Z_2)$. It is just this sensitivity of η to $\rho_1 t_1$ and E_0 which can be used for a local, nondestructive measurement of $\rho_1 t_1$, if a continuous calibration curve can be obtained theoretically without the need for experimental calibration standards.

The special case of a freestanding foil can easily be simulated by elimination of the substrate backscattering or assigning a very low value to Z_2. However, the primary interest

was in films on substrates, and hence, we will not discuss the Monte Carlo simulation of results from foils.

The subject of electron backscatter yield from thin films on thick substrates has already been of some interest [20-24], primarily from an experimental viewpoint. References [21] and [23] propose a simple analytic expression for η based on semi-empirical reasoning. Reference [25] deals with freestanding foils without a substrate and shows that good agreement was obtained between experimental values of η and theoretical values calculated with a similar Monte Carlo model. As discussed in previous sections of this paper, Monte Carlo simulation is a very powerful tool for application to discontinuous targets such as thin films on thick substrates, with a minimum of assumptions. The following describes some calculations of η for Al films on Au and Au films on Al.

3.1 Theoretical Calibration Curves with Monte Carlo Simulation

The Monte Carlo computer program was used to calculate η for thin films of Al on Au substrates and Au films on Al substrates with normal (90°) beam incidence. The results of these calculations are shown in figures 3 and 4. As described previously, the Monte Carlo program calculates one value of η for a particular target configuration $(\rho_1 t_1, Z_1, Z_2)$ and beam energy (E_0). The continuous curves shown in figures 3 and 4 have been drawn through a series of calculated points. For each point, a total of 10^4 incident electrons were simulated, and hence the statistical precision of the calculation is given by the variance $\sigma^2 = \eta(1-\eta)/N$, where N = number of electrons simulated [26]. Bulk values of mass density $\rho(g/cm^3)$ for Al and Au were used to convert mass thickness ρt to thickness t.

There are several things to notice in these theoretical calibration curves. For the case of Al films on Au substrates shown in figure 3, the asymptotic limits of η at large ρt are 0.161 (10 kV) and 0.154 (30 kV). This magnitude and weak energy-dependence of $\eta = \eta(Al)$ is in good agreement with that measured by Bishop [17], Heinrich [18], and Wittry [19] independently on thick targets of Al. As $\rho t(Al)$ becomes vanishingly small, the calculated asymptotic limit of $\eta = \eta(Au)$ becomes 0.520 (10 kV) and 0.482 (30 kV). The average value of $\eta(Au)$ is in good agreement with that measured on thick Au [17-19], but the weak energy dependence of $\eta(Au)$ is not. At large Z, experimental results on thick targets show that η increases slowly with increasing E_0, and at small Z it decreases slowly with increasing E_0. At intermediate values of Z, η is experimentally found to be independent of E_0. The wrong

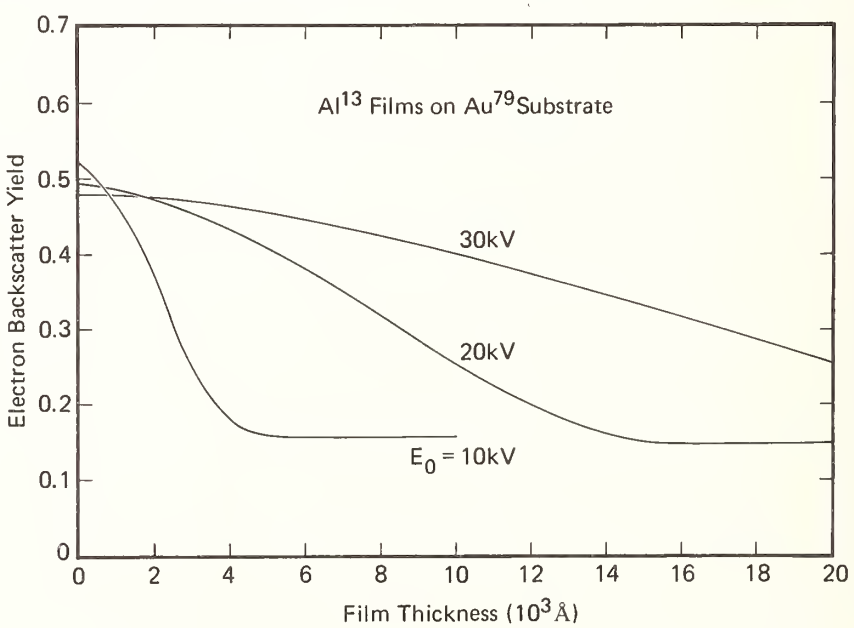

Figure 3. Monte Carlo calculations of electron backscatter yield from Al films on Au substrate.

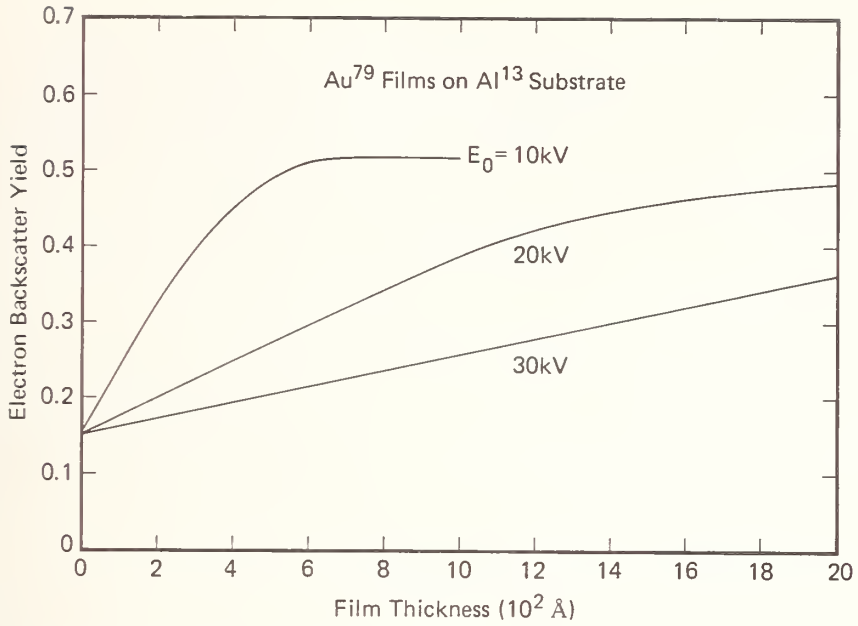

Figure 4. Monte Carlo calculations of electron backscatter yield from Au films on Al substrate.

energy-dependence predicted for η(Au) is probably due to the failure of the Born approximation in the Bethe energy-loss equation of the Monte Carlo model, with decreasing E_0 and high Z targets such as Au.

For the case of Au films on Al substrates shown in figure 4, the dependence of η (calculated) versus t is linear with t for $t \leq 250$Å (10 kV), $t \leq 1{,}000$Å (20 kV), and $t \leq 2{,}000$Å (30 kV). For the case of Al films on Au, there is not a large range of linear dependence. However the calibration curves, if they are accurate, can be used in the nonlinear range also. Such a technique depends upon a large value of $|Z_1-Z_2|$ for maximum sensitivity, but can accommodate elements which are common to both the film and substrate in compound targets. The latter case cannot be treated as easily with x-ray measurements described earlier in this paper.

3.2 Experimental Results and Comparison with Theory

Holliday and Sternglass [20] have measured η for Al and Au films on Au and Al substrates. Their experiment was performed with the use of bias grids placed between the target and the collecting electrodes for backscattered electrons. Holliday and Sternglass (H-S) made no correction for secondary electron emission or backscattering from the grids, and hence, their results are in error. Bishop [17] has discussed the experimental errors introduced to the measurement of η when grids are used, and he proposed the use of a double target without grids for which the experimental errors due to secondary electrons and electrons scattered from sample chamber walls can be eliminated. For the experimental configuration which H-S used, the experimental errors should result in a low value for η, and that is observed in the comparison between the present Monte Carlo calculations and their experimental values. The asymptotic limits of the H-S data for thick films show $\eta(\text{Al}) \tilde{=} 0.13$ and $\eta(\text{Au}) \tilde{=} 0.45$. These values are also too low compared to those measured by Bishop [17], Heinrich [18], and Wittry [19], in which the secondary electrons and rescattered electrons were taken into account. Hence, the discrepancy between the Monte Carlo calculations and the experimental data of H-S can be explained qualitatively. The asymptotic limits of the Monte Carlo calculations (i.e., thick films) are approximately correct, with η(Al) being more exact than η(Au) for the reasons already given.

3.3 Discussion

There is a need for more measurements of η obtained in a systematic fashion and for a variety of films and substrates in order to compare with, and fully confirm or modify, the existing Monte Carlo model. The angular and energy distribution of backscattered (or transmitted) electrons would allow us to make another valuable comparison. The general accuracy of the Monte Carlo model will probably be indicated better through direct electron distribution measurements rather than x-ray emission measurements or other atomic relaxation processes. This is due to the additional modeling and input parameters required for the calculation of atomic relaxation processes (e.g., ionization cross-sections, fluorescent yield, absorption, etc.) versus calculation of the primary electron scattering and energy loss alone.

The experimental results of reference [21] are not complete enough for comparison with the Monte Carlo theory and, in addition, they differ significantly from those of H-S for the same target configuration. The experimental results of references [22] and [24] were obtained at very low values of E_0 ($\leq$ 2 keV). The present Monte Carlo model cannot accurately simulate target behavior at electron energies in that range and, hence, that information is not useful to us now. In the future, we plan to extend the simulation model to lower energies, perhaps by switching (at some particular value of electron energy along the trajectory) from the Bethe equation for energy loss to an equation such as that proposed by Rao-Sahib and Wittry [27].

If η is quantitatively measured in an electron probe microanalyzer (EPMA) or scanning electron microscope (SEM), great care must be taken to eliminate the effects of secondary electrons and rescattered electrons. We have attempted to utilize the technique of Heinrich [18], which employs a measurement of collected target current and incident beam current for calculating η. However, in our EPMA [28], the target current is found to be a complex function of target bias, target elevation (i.e., distance below final magnetic lens), and also final lens current. These observations strongly suggest that secondary electrons from the target and chamber walls, as well as rescattered electrons backscattered originally from the target, are producing extraneous collected target currents. We are continuing to search for an accurate method of measuring η in our EPMA.

4. Conclusions

Monte Carlo simulation of electron beam scattering, energy loss, and x-ray production has been developed and experimentally verified for targets consisting of thin alloy films on thick substrates. Theoretical calibration curves of intensity ratio k_i versus weight fraction C_i were generated for alloy films Mn_xBi_{1-x} and Co_xPt_{1-x} on SiO_2 substrates, with total mass thickness ρt as a parameter. Experimental data from alloy films were graphically iterated; the results converged within the calibration curves to provide a unique analysis of both C_i and ρt. These elemental analyses agreed well with analyses obtained from nuclear backscattering energy analysis. The Monte Carlo model provides a general procedure for quantitative and nondestructive elemental analysis of thin films on thick substrates, while retaining the high lateral spatial resolution provided by the electron microprobe.

The Monte Carlo simulation model is set up to utilize measured x-ray intensities from the film that are referenced to thick standard targets and, hence, does not require thin standard films. The use of thick standards greatly simplifies the experimental procedure, and also eliminates a potential source of error due to thickness uncertainties if film standards are utilized [29].

If the average atomic number of the film and substrate are sufficiently different, then a measure of total electron backscatter yield η can also provide information about total mass thickness ρt of the film. The Monte Carlo model was used to generate calibration curves of η versus ρt for Au films on Al substrates and Al films on Au substrates as an example. The asymptotic limits of these curves are approximately correct, with η(Al) in better agreement with experiment than η(Au). Further work is necessary to fully confirm the Monte Carlo prediction of η at intermediate thickness values. This work will require careful elimination of experimental uncertainties due to secondary and re-scattered electrons

We thank IBM, Japan, Ltd., and the IBM World Trade Corporation for financial support of one of the authors (KM) as a WTC Post-Doctoral Fellow during 1973. J. Baglin (IBM Watson Research Center) performed the nuclear backscattering energy analysis, and K. Lee and T. Jacobs (IBM San Jose Research Laboratory) provided the MnBi and CoPt films, respectively. Stimulating and helpful discussions about parts of this work were held with K. Heinrich, W. Reuter, and E. Sternglass.

References

[1] Beaman, D. and Isasi, J., *ASTM Special Technical Publication No. 506* (1972).

[2] Colby, J. W., *Advances in X-ray Analysis,* Vol. 11, p. 287 (Plenum Press, New York, 1968).

[3] Henoc, J., *J. de Microscopie* 15, 289 (1972).

[4] Warner, R. and Coleman, J., *Micron* 4, 61 (1973). Also see *Micron* 6, 79 (1975).

[5] Bishop, H. and Poole, D., *J. Phys.* D6, 1142 (1973).

[6] Oda, Y. and Nakajima, K., *J. Japan Inst. Metals* 37, 673 (1973).

[7] Bolon, R. and Lifshin, E., *Proceedings of Sixth Annual SEM Symposium,* p. 285 (IITRI, Chicago, 1973).

[8] Stine, P., and Hruska, S. and Liedl, G., *Advances in X-Ray Analysis,* Vol. 17, p. 487 (Plenum Press, New York, 1974).

[9] Kyser, D. and Murata, K., *IBM J. Res. Develop.* 18, 352 (1974).

[10] Eshel, A., *Micron* 5, 41 (1974).

[11] Yakowitz, H. and Newbury, D., *Proceedings of Ninth annual SEM Symposium,* p. 151 (IITRI, Chicago, 1976).

[12] Murata, K., Matsukawa, T., and Shimizu, R., *Japan J. Appl. Phys.* 10, 678 (1971).

[13] Murata, K., Matsukawa, T. and Shimizu, R., *Proceedings of Sixth International Conferences on X-Ray Optics and Microanalysis,* p. 105 (Univ. of Tokyo Press, Tokyo (1972).

[14] Nicolet, M., Mayer, J., and Mitchell, I., *Science* 177, 844 (1972).

[15] Ziebold, T. and Ogilvie, R., *Anal. Chem.* 36, 322 (1964).

[16] Laguitton, D., Rousseau, R., and Claisse, F., *Anal. Chem.* 47, 2178 (1975).

[17] Bishop, H., *Proceedings of Fourth International Conference on X-Ra Optics and Microanalysis,* p. 153 (Hermann, Paris, 1966).

[18] Heinrich, K., *ibid.,* p. 159.

[19] Wittry, D., *ibid.,* p. 168.

[20] Holliday, J. and Sternglass, E., *J. Appl. Phys.* 30, 1428 (1959).

[21] Nakhodkin, N., Ostroukhov, A., and Romanovskii, V., *Sov. Phys.-Solid State* 4, 1112 (1962).

[22] Thomas, S. and Pattinson, E., *J. Phys.* D3, 349 (1970).

[23] Reuter, W., *Proceedings of Sixth International Conference on X-Ray Optics and Microanalysis,* p. 121 (Univ. of Tokyo Press, 1972).

[24] Goto, K., Ishikawa, K., Koshikawa, T., and Shimizu, R., *Surface Science* 47, 477 (1975).

[25] MacDonald, I., Lamki, A., and Delaney, C., *J. Phys.* D4, 1210 (1971).

[26] Bishop, H., *Brit. J. Appl. Phys.* 18, 703 (1967).

[27] Rao-Sahib, T. and Wittry, D., *J. Appl. Phys.* 45, 5060 (1974).

[28] Applied Research Laboratories model EMX-SM, equipped with magnetic beam deflection and a "pancake" style magnetic objective lens.

[29] Philibert, J. and Tixier, R., *Physical Aspects of Electron Microscopy and Microbeam Analysis*, Ch. 21 (Wiley, New York, 1975).

National Bureau of Standards Special Publication 460. Proceedings of a Workshop on the Use of Monte Carlo Calculations in Electron Probe Microanalysis and Scanning Electron Microscopy held at NBS, Gaithersburg, Maryland, October 1-3, 1975. Issued December 1976.

CALCULATION OF TYPE II MAGNETIC CONTRAST IN THE LOW-LOSS IMAGE IN THE SCANNING ELECTRON MICROSCOPE

Oliver C. Wells

IBM Thomas J. Watson Research Center
P. O. Box 218
Yorktown Heights, New York 10598

The backscattered electrons which are often most useful in the scanning electron microscope (SEM) are those which have lost the least energy. (We have called these the "low-loss" electrons.) The question is whether they can be analyzed by a simple electron scattering model, or whether the Monte Carlo method must be used. Previously, it has been shown that a simple model based jointly on the Bethe energy loss law and a single Rutherford wide-angle scattering event can account for both the angular distribution and the absolute magnitude of the low-loss electron emission from amorphous SiO_2 with oblique incidence with an accuracy of a few percent provided that the energy loss is less than about 1%. This simple model has been extended to allow for curvature of the electron trajectories in the specimen, so as to calculate the contribution to Type II magnetic contrast in a suitable specimen caused by those backscattered electrons which have been scattered by a single wide-angle scattering event. Some preliminary theoretical results are given.

Key words: Contrast calculations; energy filtering; low-loss electron image; magnetic contrast; Monte Carlo electron trajectory calculations; scanning electron microscopy.

1. Introduction

Type II magnetic contrast arises in the backscattered electron image from a solid specimen because the incident electrons are deflected inside the specimen by the internal magnetic field of the material [1-12][1]. The magnitude of Type II magnetic contrast calculated has been explained by two different theoretical models. First, both the magnitude of the contrast and the way in which it depends on the angle of incidence have been successfully analyzed by the Monte Carlo method [3,9]. Also, Fathers, et al. [2], have analyzed the problem by means of a simplified electron scattering model.

In this paper, the electron scattering model approach is followed, with particular emphasis on calculating the angular distribution of the backscattered electrons, and on predicting the dependence of Type II magnetic contrast on the angle of incidence. The model used here is an extension of one which had previously been successful in explaining the scattering of low-loss electrons from an amorphous SiO_2 target [13-17]. This is referred to below as "The Simple Model." This model has now been extended to calculate the contribution to Type II magnetic contrast which arises from backscattered electrons which have been scattered by only a single wide-angle event (in addition to small-angle inelastic events, of course). The extent to which there will also be a contribution from electrons which have suffered more than one wide-angle event is not covered by this theory. (This is a point which may need to be investigated by the Monte Carlo method.)

[1]Figures in brackets indicate the literature references at the end of this paper.

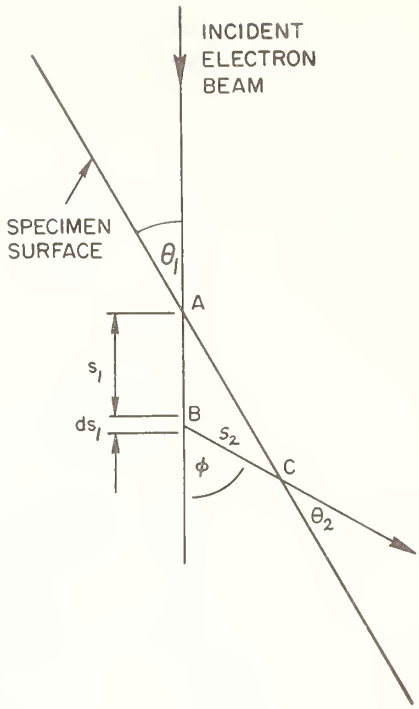

Figure 1. Penetration model for the escape of low-loss electrons [15].

The three results which must be explained by this model were reported by Newbury, Yakowitz, and Myklebust [6], and are the following:

(1) type II magnetic contrast calculated by Monte Carlo technique to be in iron is 0.18% at 30 kV when the glancing angle of incidence Θ_1 is 30° (see fig. 1 for the definition of Θ_1) (compared to an experimental value of 0.3%);

(2) the contrast varies as $E^{1.5}$ (calculation and experiment) (the "three-halves power law"); and

(3) the contrast is zero for Θ_1 = 0° and 90°, with a broad maximum between Θ_1 = 20° and 60° (calculation and experiment).

2. The Simple Model

This is the model which was originally developed to explain the scattering of low-loss electrons from a solid, amorphous target [13-17]. It is based on the idea that the distance which an electron can travel in the target before losing too much energy to be accepted by the energy filter is limited, in a typical case, to 1000 Å or less. Under these conditions, it can be shown that the deflection of typically 30° or more which it must acquire to escape from the target within such a short total penetration path is most likely to occur as a result of a single wide-angle event rather than as the sum of two or more deflections through a small angle. (The question of how long the penetration path can be before multiple wide-angle scattering will become significant is discussed in Appendix 2.) In the simple model, therefore, it is assumed that the electron penetrates in a straight line into the specimen while losing energy by small-angle inelastic events at an average rate given by the Bethe's energy loss law and with a single wide-angle Rutherford's event to bring the electron out of the target before it has lost too much energy to be accepted by the energy filter. The properties of the simple model will be briefly described before discussing how it must be modified to allow for the internal magnetic field of the Type II sample.

In the simple model, the incident electrons are assumed to penetrate straight into the specimen along the line AB in figure 1. The energy loss is assumed to be constant and given

by the Bethe's energy loss law. At a distance s_1, along AB, there is a probability $P(\phi)ds d\Omega$, as given by the Rutherford's scattering law, that the electron will be scattered in the incremental distance ds into an incremental solid angle $d\Omega$ in the direction BC. The distance AB + BC must be smaller than some value L_{max} or the electron will have lost too much energy and will be rejected by the energy filter. This gives rise to the following formula for the low-loss conversion efficiency [13]:

$$d\eta = ds_1 \int_{\Omega} P(\phi)\ F(E_{loss})\ d\Omega \qquad (1)$$

where $P(\phi)ds_1 d\Omega$ is the scattering probability defined above, and where $F(E_{loss})$ will be, for a perfect energy filter, unity or zero depending on whether AB + BC is less than or greater than L_{max}. The numerical evaluation of this integral for a practical energy filter is discussed in Appendix 1. A comparison between the theoretical and the measured low-loss angular distribution curve is shown in figure 2. The bars show the measurements for an energy loss of less than 1%, while the full line was calculated numerically from eq. (1). (The measured values were reduced by 6% to improve the fit with the calculated curve.) Certainly, for this low-loss region and for this particular specimen, the agreement between the theory and the measurements is very encouraging. Some further calculated results are shown in figure 3.

The agreement between the simple model and the measurements is not so good if the energy loss is increased. The effect of increasing the energy loss on the observed angular distribution is shown in figure 4. The experimental curve becomes wider and the peak lifts away from the surface as the acceptable energy loss is increased. (According to the simple model, it would be expected that the angles in figure 1 should not change as the energy loss is increased, so that the geometric form should scale and these curves should all have the same shape.) The energy distribution curve for the electrons which leave the specimen in three different directions is shown in figure 5. (According to the simple model these curves should be flat.) In both of these sets of measurements, there is a departure from

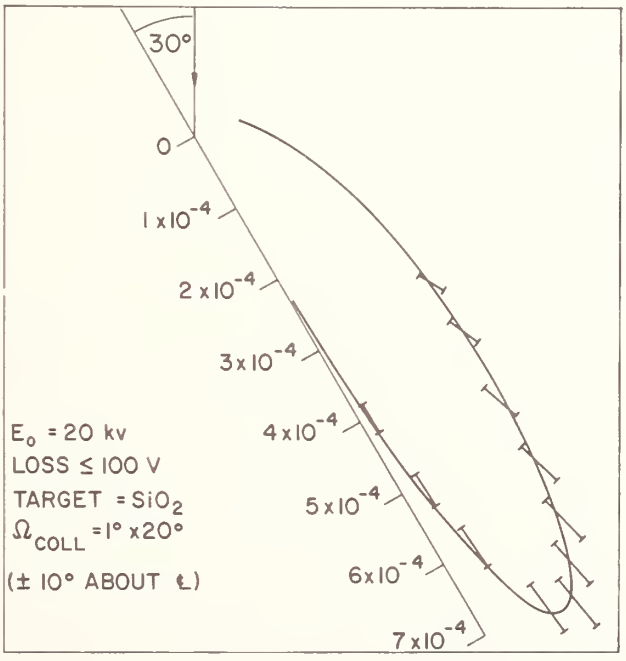

Figure 2. Comparison between theory (full line) and experiment (bars) for low-loss emission from amorphous SiO_2. The experimental values were all reduced by 6% to obtain the best fit with the theoretical curve [16].

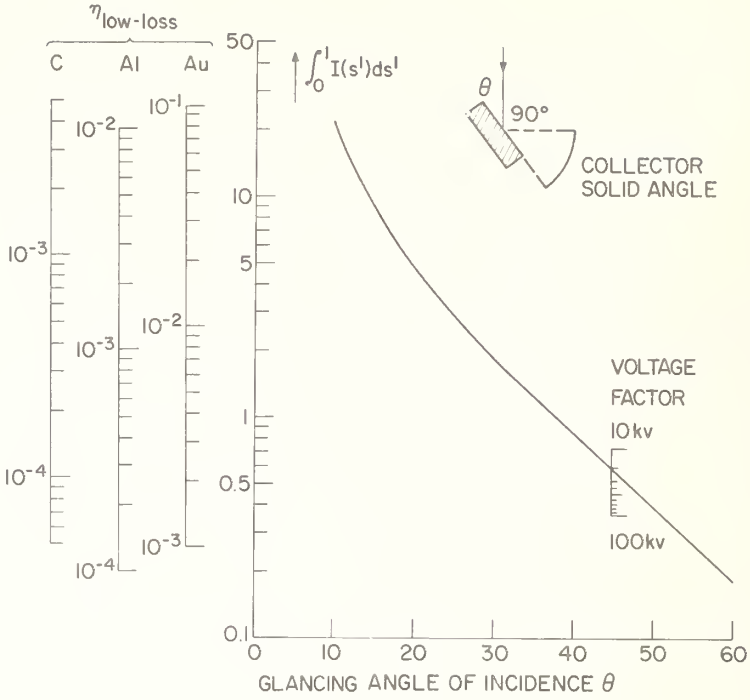

Figure 3. Theoretical low-loss conversion efficiency for flat amorphous targets calculated for the takeoff angle shown and $n_0 = 0.5$; $E_0 = 20$ kV; $E_{filter} = E_{resn} = 200$ V [13].

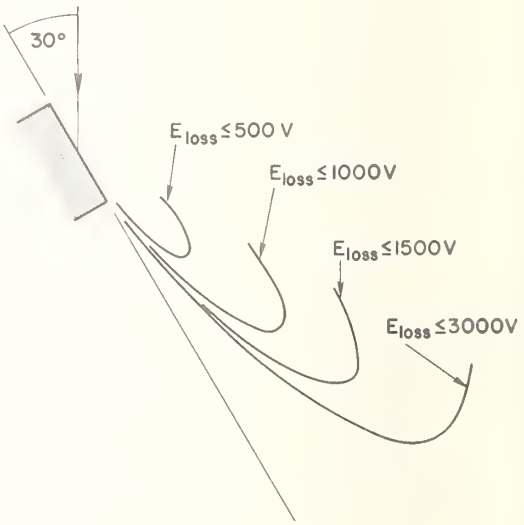

Figure 4. Experimental angular distribution curves from flat amorphous SiO_2 target as E_{loss} is increased: $E_0 = 20$ kV [17].

the predicted values as the acceptable energy loss rises above about 1%, and it is presumed that this is caused by additional wide-angle scattering events. At present, it is not clear whether the simple model can be modified to allow for these extra events, or whether the Monte Carlo approach must be used. This model can, however, be modified in a simple way to allow for curvature of the electron trajectories in the specimen, and it was therefore decided to calculate the contribution to Type II magnetic contrast which can be expected from electrons which have suffered only a single wide-angle event.

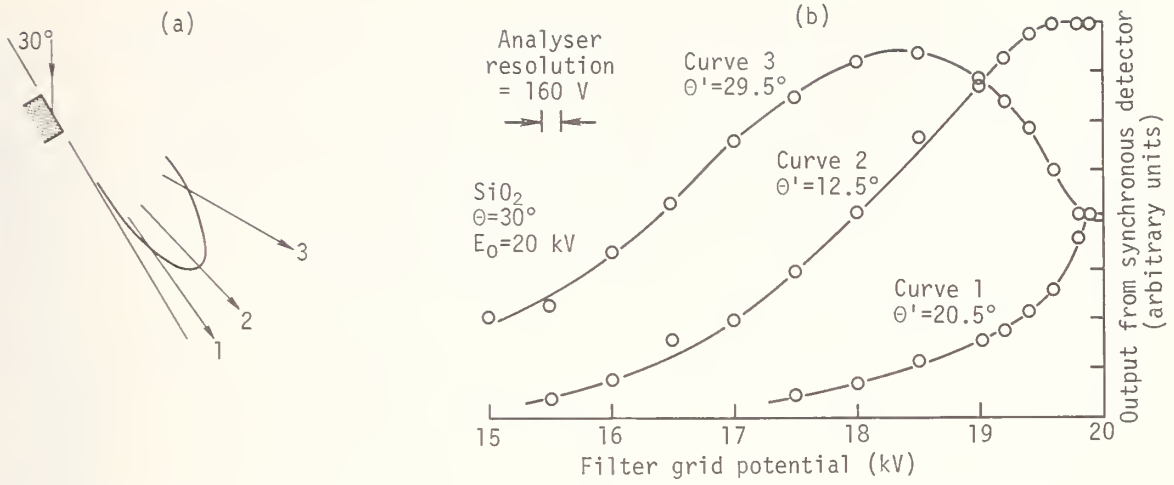

Figure 5. (a) Directions in which the energy distributions were measured. (b) Observed energy distributions from SiO_2 with E_0 = 20 kV [17].

3. Electron Scattering Model with Curvature of the Electron Trajectories in the Specimen

The modified model is shown in figure 6. The electron trajectories in the specimen have a radius of curvature which can be negative (fig. 6a), infinite (fig. 6b), or positive (fig. 6c). In a practical magnetic material, the radius of curvature is quite large; for example, with 21,000 Gauss in iron and E_0 = 30 kV, then R = 277 μm.

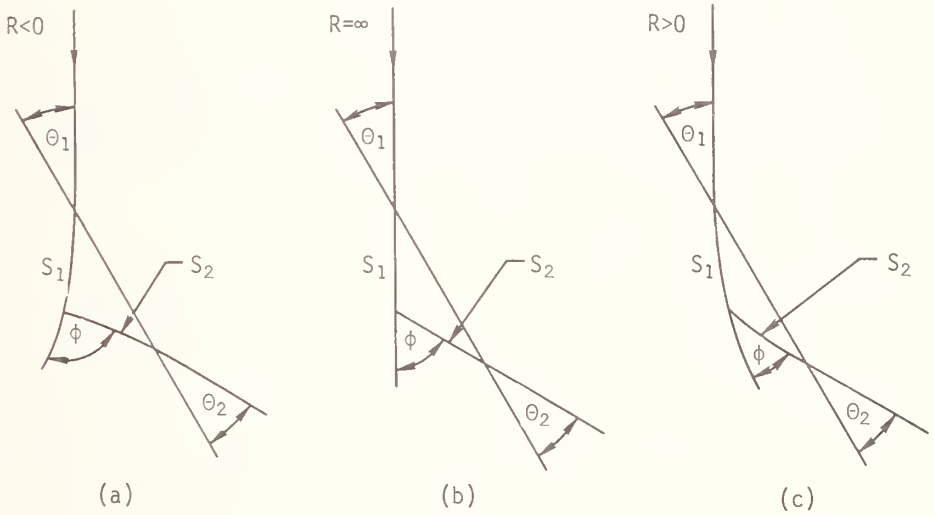

Figure 6. Extension to the electron scattering model to allow for curvature of the electron trajectories in the specimen.

For a given s_1 and Δs_1, the contribution to the low-loss conversion efficiency, $d\eta$, which arises within a specified range of exit angles, θ_2, is given by

$$d\eta = ds_1 d\phi_t \int_{\Theta_2} P(\phi) \frac{\partial \phi}{\partial \Theta_2} F(E_{loss}) \, d\Theta_2 \qquad (2)$$

where $d\phi_t$ is a specified small acceptance angle at right angles to the paper plane, and where the term $\partial\phi/\partial\Theta_2$ allows for the fact that the elemental collector solid angle $d\Omega$ as measured outside the specimen is no longer the same as the solid angle into which the scattering event occurs.

The numerical evaluation of eq. (2) is discussed in Appendix 1. Some calculated results are shown in figures 7 and 8, where the three curves shown for each value of incident angle in figure 7 correspond to values of L_{max}/R of -0.1, zero, and + 0.1. Unexpectedly perhaps, the shape of the angular distribution curve is not greatly affected even by such a severe curvature, and the major change is in the absolute magnitude rather than the shape of these curves.

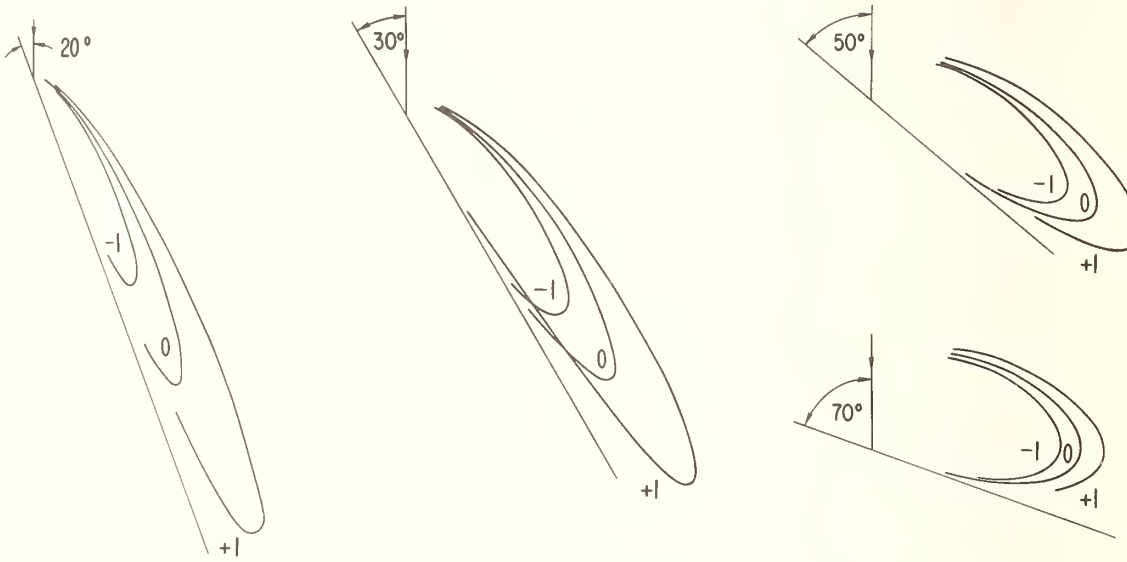

Figure 7. Calculated angular distributions of low-loss electrons as modulated by type-2 magnetic contrast for Θ_1 = 20°, 30°, 50° and 70°. For each value of incident angle the three curves corresponds to L_{max}/R = -0.1 (inner curve), 0.0 (middle curve) and +0.1 (outer curve). The areas inside the four middle curves are shown here as being equal; in practice they would vary with the incident angle as shown in figure 3.

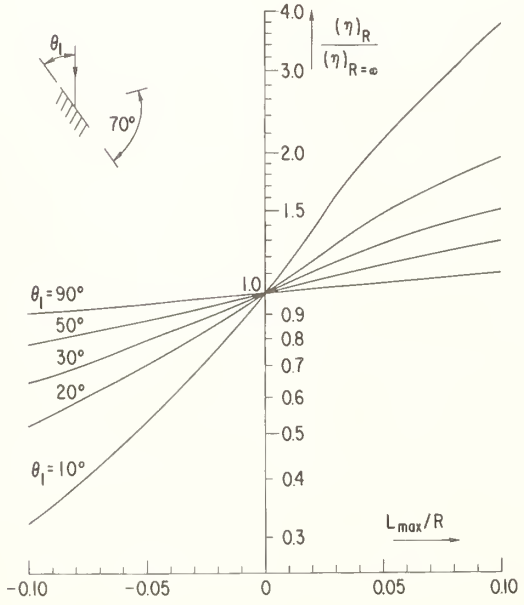

Figure 8. Showing the modulation to be expected from type-2 magnetic contrast as a function of the glancing angle of incidence Θ_1 and the curvature of the electron trajectory in the specimen.

The calculated modulation of the low-loss conversion efficiency by the curvature parameter L_{max}/R is shown as a function of the glancing angle of incidence Θ_1 in figure 8. The vertical axis shows the ratio of the areas inside the calculated angular distribution curves for the value of L_{max}/R as shown on the horizontal axis to the value when $R = \infty$. These curves were plotted by running the program for $L_{max}/R = \pm 0.1, \pm 0.08, \pm 0.06, \pm 0.04, \pm 0.03, \pm 0.02, \pm 0.01$, and zero. For L_{max}/R less than about 0.04, these curves can be approximated by the equation

$$\frac{(\eta)_R}{(\eta)_{R=\infty}} = 1 + k \cdot \frac{L_{max}}{R} \qquad (3)$$

where the numerical values for k are shown by one of the curves in figure 9. Thus, according to this model, if L_{max} is fixed, then Type II magnetic contrast will progressively

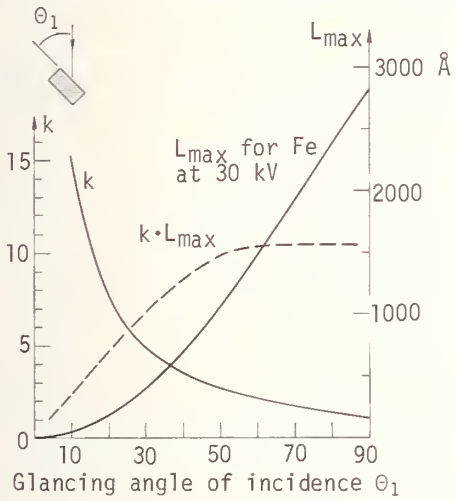

Figure 9. Showing the dependence of k, L_{max} and the product $k \cdot L_{max}$ on the glancing angle of incidence Θ_1 (see text).

increase as the angle of incidence becomes more nearly glancing. One thing must be noticed in figure 9. These results were obtained with a collector angle of 70° relative to the specimen surface, and it is the asymmetry of the collector which accounts for the modulation of the collected signal when $\Theta_1 = 90°$. With a symmetrical collector solid angle, k will be zero at $\Theta_1 = 90°$.

4. Discussion of Results

In the low-loss situation, L_{max} is determined by the maximum energy loss as given by the potential on the filter grid of the energy filter. For low-loss topographic studies, an energy loss of 1% is appropriate, which leads to $L_{max} = 590$ Å for iron bombarded by 30 keV electrons. (This number was calculated using the slowing-down value of 0.056 ev/Å for iron at 30 kV as given by Berger and Seltzer [18].) The radius of curvature R at 30 kV in iron is 277 μm. The Type II magnetic contrast as calculated from eq.(3) for a 1% energy loss and $\Theta_1 = 30°$ is therefore 0.106%. In other words, it should only be necessary to increase the energy loss of the collected electrons to 1.7% for the modulation depth as given by eq. (3) to equal the value of 0.18% as specified by Newbury, Yakowitz and Mykelbust [6]. (This corresponds to $L_{max} = 1000$ Å at 30 kV.)

Of course, it must be noted that the contrast given by eq. (3) will be reduced by the presence of an unmodulated background of slower backscattered electrons. The present model gives data that is relevant either to the filtered case or, alternatively, the model should predict the conversion efficiency between the incident beam current and the maximum-to-minimum current swing in the collected signal.

To analyze the non-filtered case, it is necessary to define an "equivalent" value for L_{max} in the case when all of the backscattered current is collected. For example, in the case of electrons scattered from SiO_2 with $\Theta_1 = 30°$, the energy distribution curve of electrons

in the forward peak shows that these electrons have lost, at most, only 2 or 3 keV energy with E_0 = 20 keV, as is shown in figure 5. A natural filtering action is therefore taking place for the electrons in the forward lobe.

As a hypothesis, we can define the equivalent value of L_{max} as being the path distance within which a wide-angle Rutherford scattering event through an angle greater than Θ_1 is equal to the probability of two consecutive scattering events, each through an angle greater than half of that amount. It is shown in Appendix 2 that this gives rise to

$$L_{max} = 1.07 \times 10^{-12}\, C(\Theta_1) E_0^2 \qquad (4)$$

where

$$C(\Theta) = \frac{\cot^2(\Theta/2)}{\cot^4(\Theta/4)} \qquad (5)$$

(L_{max} is in cm if E_0 is in eV). This, therefore, gives a value for L_{max} which will depend on both the incident energy and angle of incidence. Physically, it corresponds to the case when the majority of the escaping backscattered electrons have suffered only a single wide-angle scattering event.

The values of L_{max} as calculated from eqs. (4) and (5) for iron with a beam at 30 keV are plotted as a function of Θ_1 in figure 9. The general tendency is for L_{max} to become larger as the beam comes closer to normal incidence. When Θ_1 = 30°, then L_{max} = 403 Å as calculated from eqs. (4) and (5). This is smaller than the 1000 Å which was calculated above as being needed to provide the observed contrast, so presumably a higher degree of multiple scattering can be tolerated in comparison with the present hypothesis.

The 3/2 power law follows immediately from eq. (4). Thus, in the Monte Carlo results obtained by Newbury, Yakowitz, and Myklebust [6], it was found that Type II magnetic contrast varied as $E_0^{1.5}$. From eq. (3), we would expect it to vary as L_{max}/R while L_{max} will vary as E_0^2 from eq. (4) and R will vary as $E_0^{0.5}$. The ratio L_{max}/R will therefore vary as $E_0^{1.5}$. The dependence of Type II magnetic contrast on Θ_1 is illustrated in figure 9. According to eq. (3), the contrast is proportional to $k \cdot L_{max}$. The values for k as measured from figure 8 decrease from k = 15.0 at Θ_1 = 10° to k = 1.1 at Θ_1 = 90°. The variations of L_{max} with Θ_1 are given by eq. (5), and these are also plotted in figure 9. Here, L_{max} increases from 46 Å at Θ_1 = 10° to 2,840 Å at Θ_1 = 80°. The product kL_{max} increases from a low value at Θ_1 = 10° to a flat maximum for Θ_1 > 50°. As noted above, if the collector solid angle was to be symmetrical about the incident beam, then this would make k = 0 at Θ_1 = 90°, and the curve of kL_{max} would then be zero for Θ_1 = 0 and Θ_1 = 90°, in agreement with the published curve of Newbury, Yakowitz, and Myklebust [6].

5. Conclusions

This model has correctly predicted both the approximate magnitude of the contrast and the way in which it depends on both the incident electron energy and angle of incidence. This model cannot, however, be fully evaluated until some further numerical data can be obtained using an energy filter.

I would like to thank D. J. Fathers of the Metallurgy Department at Oxford University for discussions concerning his model, and to acknowledge that this paper was put into final form following helpful discussions with the other participants at the Monte Carlo Workshop.

References

[1] Philibert, J. and Tixier, R., Effects of crystal contrast in scanning electron microscopy, (in French), *Micron*, 1, 174 (1969).

[2] Fathers, D. J., Jakubovics, J. P., and Joy, D. C., Magnetic domain contrast from cubic materials in the scanning electron microscope, *Phil. Mag.* 27, 765 (1973).

[3] Fathers, D. J., Jakubovics, J. P., Joy, D. C., Newbury, D. E., and Yakowitz, H., A new method of observing magnetic domains by scanning electron microscopy, I. Theory of the image contrast, *Phys. Stat. Sol (a)*, 20, 535 (1973). Also, same authors and main title, ...II Experimental confirmation of the theory of image contrast, *Phys. Stat. Sol (a)*, 22, 609 (1974).

[4] Fathers, D. J., Joy, D. C., and Jakubovics, J. P., Magnetic contrast in the SEM, *IITRI/SEM/1973*, 259 and 242 (1973).

[5] Newbury, D. E. and Yakowitz, H., Magnetic domain studies in iron - 3.25 weight percent silicon transformer sheet using the scanning electron microscope, in *Proc. 19th Conf. on Magnetism and Magnetic Materials*, (AIP, Boston, Nov. 1973).

[6] Newbury, D. E., Yakowitz, H., and Myklebust, R. L., Monte Carlo calculations of magnetic contrast from cubic materials in the scanning electron microscope, *Appl. Phys. Lett.*, 23, 488 (1973).

[7] Newbury, D. E., Yakowitz, H., and Yew, N. C., Observation of magnetic domains in nickel using the scanning electron microscope, *Appl. Phys. Lett.*, 24, 98 (1974).

[8] Shimizu, R., Ikuta, T., Yamamoto, T., Kinoshita, M., and Murayama, T., Direct observation of the magnetic domain structure in Mn-Zn ferrite using the 200 kV high voltage scanning electron microscope, *Phys. Stat. Sol. (a)*, 26, K87 - K89 and 2 plates (1974).

[9] Ikuta, T. and Shimizu, R., Magnetic domain contrast from ferromagnetic materials in the scanning electron microscope, *Phys. Stat. Sol. (a)*, 23, 605 (1974).

[10] Ikuta, T., Dynamic and high resolution observations of the magnetic domain, PhD Diss., Osaka Univ. (1974).

[11] Yamamoto, T., Nishizawa, H., and Tsumo, K., High voltage scanning electron microscopy for observing magnetic domains, *J. Phys. D: Appl. Phys.*, 8, L113-L114 and 1 plate (1975).

[12] Yamamoto, T., Tsuno, K., and Nishizawa, H., Utilizability of high voltage SEM for observing magnetic domains, *JEOL News*, 13e, No. 1, Z(1975).

[13] Wells, O. C., Boyde, A., Lifshin, E., and Rezanowich, A., *Scanning Electron Microscopy*, (McGraw Hill, New York, 1974). Since this book was written, some additional data on the low-loss image has been published as follows: first, in ref. [16] below, some additional micrographs have shown that the topographic information for the smallest surface features is contained in the low-loss electrons that leave the specimen with $\Theta_2 < 20°$. Second, in the proceedings entitled, *Ninth Annual Conference, Microbeam Analysis Society, July, 1974, Ottawa, Canada*, pp. 2A-2E, it is shown that a low-loss image can be obtained with a loss energy of only 25 eV, which corresponds to an escape depth of $\sim$ 10 Å (This final result was obtained by C. G. Bremer.)

[14] Wells, O. C., Low-loss image for surface SEM, *Appl. Phys. Lett.*, 19, 232 (1971).

[15] Wells, O. C., Explanation of the low-loss image in the SEM in terms of electron scattering theory, *IITRI/SEM/1972*, 169 (1972). (This material is more extensively analyzed in reference [13] above.)

[16] Wells, O. C. and Bremer, C. G., Low-loss image from a solid specimen, Eighth Internat. Cong. El. Mic., *Canberra, Aus. Acad. Sci.*, 1, 216 (1974).

[17] Wells, O. C., Measurements of low-loss electron emission from amorphous targets, *IITRI/SEM/1975*, 43 and 132 (1975).

[18] Berger, M. J. and Seltzer, S. M., Tables of energy losses and ranges of electrons and positrons, NASA Report number SP-3012 (Washington, D. C., 1964.)

Appendix 1

Numerical Evaluation of Integrals

The procedures used to evaluate the integrals given in eqs. (1) and (2) were the following. In each case, the expression for $P(\phi)$ was

$$P(\phi) = n \frac{d\sigma}{d\Omega}$$

$$= 1.29 \times 10^{-15} \frac{nZ^2}{E_o^2} \qquad \text{(A-1)}$$

where n = number of atoms/cm^3,

= 0.852×10^{23} for iron,

Z = atomic number,

= 26 for iron, and

E_o = incident electron energy, eV.

$P(\phi)$ is expressed above in $sterad^{-1} \cdot cm^{-1}$. The expression for $F(E_{loss})$ was the same in each case:

$$F(E_{loss}) = 0 \qquad \text{for } E_{loss} > E_{filter}$$

$$= k_o \left(\frac{E_{filter} - E_{loss}}{E_{resn}} \right)^{n_o} \qquad \text{for } E_{loss} < E_{filter} \leq E_{resn} \qquad \text{(A-2)}$$

where E_{loss} = energy lost by the electron in the specimen, eV;

E_{filter} = potential of energy filter grid relative to the SEM cathode, expressed in equivalent eV;

E_{resn} = resolution of the energy filter, expressed in equivalent eV; and

k_o and n_o are constants of the energy filter (typically $k_o = n_o = 0.5$).

The equations used for the simple model were

$$\cos\phi' = \cos\phi \cdot \cos\phi_t \qquad \text{(A-3)}$$

where ϕ' is the actual deflection angle which was submitted into eq. (A-1) and ϕ_t is the angle of the exit ray in figure 1 above or below BC at right angles to the paper plane.

$$L = s_1 + s_2 = s_1 + s_1 \frac{\sin \Theta_1}{\sin (\phi - \Theta_1) \cos\phi_t} \qquad \text{(A-4)}$$

where Θ_1, s_1, and ϕ are defined in figure 1 and L is the total path length of the electron in the specimen.

For the simple model, this leads to

$$\eta_{\text{low-loss}} = 5.2 \times 10^{-15} L_{max} n k_o \frac{Z^2}{E_o^2} \left(\frac{E_{filter}}{E_{resn}} \right)^{n_o} \int_o^1 I(s')\, ds' \qquad \text{(A-5)}$$

where $s' = s_1/L_{max}$,

$$I(s') \equiv \iint_{\phi} \int_{\phi t} \left(1 - s' - s' \frac{\sin \theta_1}{\sin(\phi - \theta_1) \cos \phi_t} \right)^{n_o} \frac{\cos\phi_t \, d\phi \, d\phi_t}{(1 - \cos \phi \cos\phi_t)^2} \qquad \text{(A-6)}$$

(L_{max} is in cm; E_o is in eV; see eq. (3.29) in ref [13]).

In the model with curvature, the integral on ϕ_t was not carried out (eq. (2)). The values of ϕ and s_2 were given by

$$\left.\begin{aligned} \phi &= \theta_1 + \theta_2 && \text{if } R = \infty \\ &= \theta_1 + \theta_2 - \frac{s_1 + s_2}{R} && \text{if } R \neq \infty \end{aligned}\right\} \qquad \text{(A-7)}$$

$$\left.\begin{aligned} s_2 &= s_1 \frac{\sin \theta_1}{\sin \theta_2} && \text{if } R = \infty \\ &= R\theta_2 - R \arccos \Gamma && \text{if } R \neq \infty \end{aligned}\right\} \qquad \text{(A-8)}$$

where $\Gamma = \cos \theta_2 - \cos \theta_1 + \cos \left(\theta_1 - \frac{s_1}{R} \right)$,

$$\frac{\partial \phi}{\partial \theta_2} = \frac{\sin \theta_1}{\sqrt{1 - \Gamma^2}}. \qquad \text{(A-9)}$$

In evaluating this integral, an addition boundary condition based on the need to establish the existence of a solution for s_2 is $|\Gamma| \leq 1$. The numerical values shown in figures 7 and 8 were obtained by substituting the above expressions into eq. (2).

Appendix 2

Derivation of Equations (4) and (5)

In the simple model, it is assumed that the total penetration path AB + BC in figure 1 is sufficiently small so that the probability of a second wide-angle event also occurring can be ignored. The value L_{max} at which rejection occurs is determined by the energy filter. If there is no energy filter present, then the forward lobe of the backscattered electron distribution will still consist of electrons which have lost only 2 keV or 3 keV of energy when the take-off angle lies close to the specimen surface (fig. 5). This presumably occurs because the slower backscattered electrons have been scattered by additional wide-angle events. In the present calculation, it is desired to find an "equivalent" value of L_{max} such that the simple model can be applied even though there is no energy filter present. Accordingly, as a hypothesis, it is required to find the path length L_{max} for which the probability of single wide-angle Rutherford deflection through an angle greater than Θ_1 is equal to two consecutive deflections through angles which are greater than half of this amount. (It is presumably at about this point that multiple wide-angle scattering will become the dominant process.) The probability of a Rutherford deflection through an angle $>\Theta$ in a path length L (where L is small) is given by

$$\text{Prob}\ (>\Theta) = \frac{kL}{E_o^2} \cot^2 \frac{\Theta}{2} \tag{A-10}$$

where $k = 1.62 \times 10^{-14}\ nZ^2 = 9.33 \times 10^{-11}$ for iron, if E_o is in eV and L is in cm (see also equation (3.6a) in reference [13]). The relationship

$$\text{Prob}\ (>\Theta) = [\text{Prob}(>\Theta/2)]^2 \tag{A-11}$$

then leads to

$$L = \frac{0.617 \times 10^{14}}{nZ^2} \cdot E_o^2 \cdot \frac{\cot^2(\Theta/2)}{\cot^4(\Theta/4)} . \tag{A-12}$$

For iron, $n = 0.852 \times 10^{23}$ atoms/cm^3 and Z = 26, which gives rise to the numerical coefficient given in eq. (5).

National Bureau of Standards Special Publication 460. Proceedings of a Workshop on the Use of Monte Carlo Calculations in Electron Probe Microanalysis and Scanning Electron Microscopy held at NBS, Gaithersburg, Maryland, October 1-3, 1975. Issued December 1976.

A STUDY OF TYPE II MAGNETIC DOMAIN CONTRAST IN THE SEM BY MONTE CARLO ELECTRON TRAJECTORY SIMULATION

D. E. Newbury, H. Yakowitz, and R. L. Myklebust

Institute for Materials Research
National Bureau of Standards
Washington, DC 20234

Magnetic contrast in the scanning electron microscope occurs by two distinct mechanisms: Type I magnetic contrast arises from the interaction of secondary electrons which have exited the specimen with leakage magnetic fields above the surface and Type II magnetic contrast arises from the interaction of beam electrons with the internal magnetic field. The observed properties of Types I and II magnetic contrast are reviewed. The proposed mechanism of Type II magnetic contrast, that of internal beam-magnetic field interactions, is modeled with the Monte Carlo electron trajectory technique. Details of the modifications to the standard Monte Carlo technique to account for magnetic deflection are given. Monte Carlo results are given for the following cases: contrast as a function of specimen magnetization, tilt, rotation, beam energy and energy fraction. The spatial resolution of domain edges is also considered. Calculated results are compared with experimental values, and the correspondence is excellent.

Key Words: Iron-silicon transformer steel; magnetic contrast; magnetic domain images; magnetic domains; Monte Carlo electron trajectory calculations; scanning electron microscope.

1. Introduction

Magnetic domains were first observed in the scanning electron microscope (SEM) by Dorsey [1][1], who studied magnetic signatures written on ordinary iron oxide recording tape. Such a material has a magnetic structure similar to that illustrated in figure 1(a). The chief characteristic of these materials is the existence of a magnetic field outside the specimen--the leakage field. The contrast discerned by Dorsey, which is now referred to as Type I magnetic contrast by reason of chronology, arises because of the interaction of the secondary electrons which have exited the specimen with the exterior leakage magnetic field (fig. 2(a)). Deflection of secondary electrons either toward the Everhart-Thornley detector of the SEM or away, depending on the sense of the magnetic field, produces a black-white contrast. Extension of this technique to crystalline materials of uniaxial magnetic character, such as cobalt and yttrium orthoferrite, was accomplished by Joy and Jakubovics [2] and by Banbury and Nixon [3]. Such materials have a structure similar to figure 1(a). An example of a Type I image of a magnetic signature on recording tape is shown in figure 2(b).

The characteristics of Type I magnetic contrast may be summarized as follows [4]:

1. Type I magnetic contrast is obtained with secondary electrons only. No contrast is obtained with the high-energy primary (backscattered) electrons or specimen current signals.

2. The contrast is a form of pure trajectory contrast, arising from the deflection of emitted secondary electrons by leakage magnetic fields external to the specimen.

[1]Figures in brackets indicate the literature references at the end of this paper.

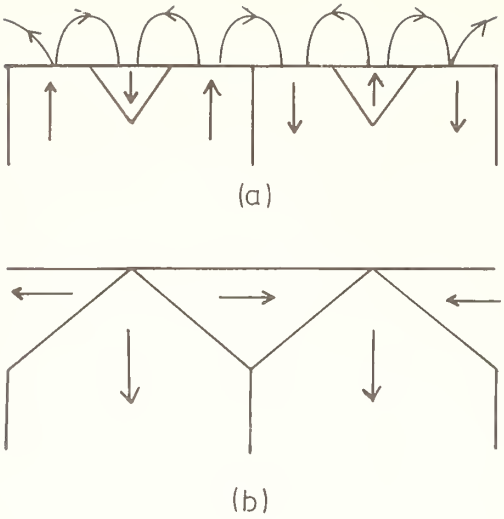

Figure 1. Schematic diagram of: (a) uniaxial magnetic domain structure, and (b) cubic magnetic domain structure.

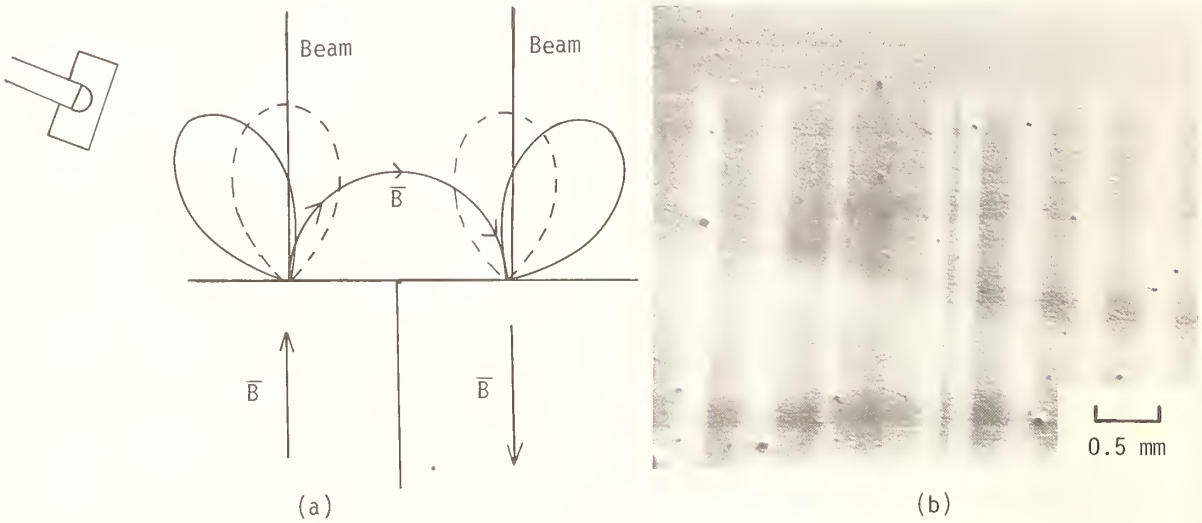

Figure 2. (a) Mechanism of Type I magnetic contrast, and (b) SEM Type I magnetic contrast image of magnetic signatures in recording tape.

3. The magnetization vector must be out of the plane of the specimen.

4. The magnitude of the contrast can be as high as $\Delta S/S = 20\%$, where S is the signal at the specimen, and is dependent on the geometry of secondary electron collection as well as the magnetization strength.

5. The contrast is dependent on specimen (magnetization direction) rotation relative to the Everhart-Thornley detector.

6. The contrast is independent of accelerating voltage, although an improved signal-to-noise (S/N) ratio may be obtained at low accelerating voltage due to enhanced secondary electron production.

7. The resolution limit is determined primarily by characteristics of the contrast mechanism rather than probe size; the limit is typically several micrometers due to the diffuseness of the leakage fields above domain walls.

8. The contrast across the domain is a function of the magnetic field integral

$$\int_0^\infty H_x dz$$

and is non-uniform with respect to position.

Attempts to obtain Type I magnetic contrast from anisotropic magnetic materials of cubic symmetry, such as iron and nickel, were unsuccessful. Due to the multiplicity of possible magnetization directions in such cubic materials, the material can establish a low-energy configuration by forming surface closure domains in which the magnetic field lies parallel to the surface (figure 1(b)). Such a state is characterized by a negligible leakage field, thus virtually eliminating the possibility of Type I magnetic contrast.

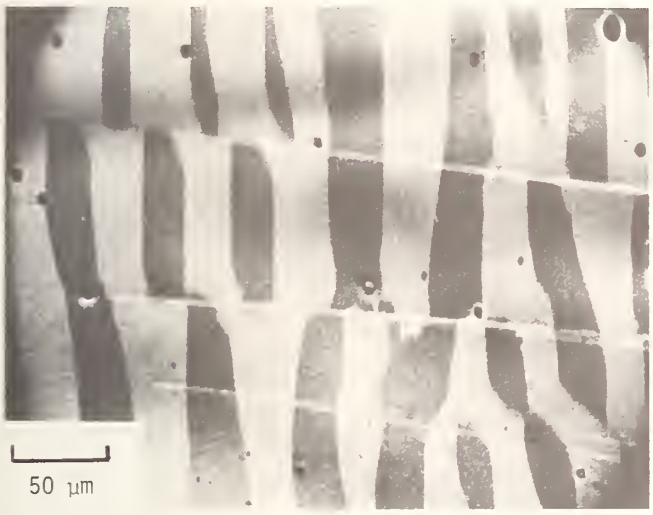

Figure 3. SEM Type II magnetic contrast image of Fe-3 1/4% Si; beam conditions: 30 keV, 2 x 10^{-7} A, specimen tilt: 55°.

Nevertheless, characteristic fir-tree magnetic domains were observed in iron by Philibert and Tixier by means of a scanning electron beam instrument [5]. The characteristics of this new form of magnetic contrast, shown in figure 3 and now referred to as Type II magnetic contrast, were elucidated by Fathers, et al. [6,7], and can be summarized as follows [4]:

1. Type II magnetic contrast is obtained with the primary (backscattered) electron and specimen current signals. No appreciable contrast is obtained with secondary electrons.

2. The contrast is pure number contrast, i.e., different numbers of electrons are backscattered from domains of opposite magnetization. Since the contrast can also be obtained with the specimen current signal, the origin of the contrast is clearly associated with events inside the specimen.

3. The magnetization vector must lie in the plane of the specimen or have a significant component resolved in that plane.

4. The contrast is strongly dependent on the specimen tilt, with zero contrast at a tilt of 0° (i.e., specimen normal to the beam) and a maximum at about 55° tilt.

5. The contrast is dependent on the specimen magnetization direction relative to the beam; the maximum contrast occurs when the magnetization vector is parallel to the tilt axis.

6. The contrast increases with increasing accelerating voltage.

7. The contrast is very weak; e.g., for an optimum situation in a conventional SEM (iron, beam energy 30 keV, 55° tilt, magnetization parallel to the tilt axis), the measured contrast is $\Delta S/S = 0.3\%$.

Fathers, et al., proposed a possible mechanism for the contrast [6]; the contrast formation occurs because of the deflection of the primary beam electrons by the internal magnetic field during scattering within the specimen (fig. 4). Thus, the deflection by the magnetic field results in the electrons remaining closer to the surface in a domain with one magnetization sense, and further from the surface in the domain of opposite magnetization. A difference in the backscattering coefficient would therefore be observed between the two domains. An analytic model was developed in an attempt to explain characteristics of the contrast and, simultaneously, a Monte Carlo electron trajectory simulation study including magnetic field effects was carried out [7,8]. We shall be concerned here with the Monte Carlo calculations only.

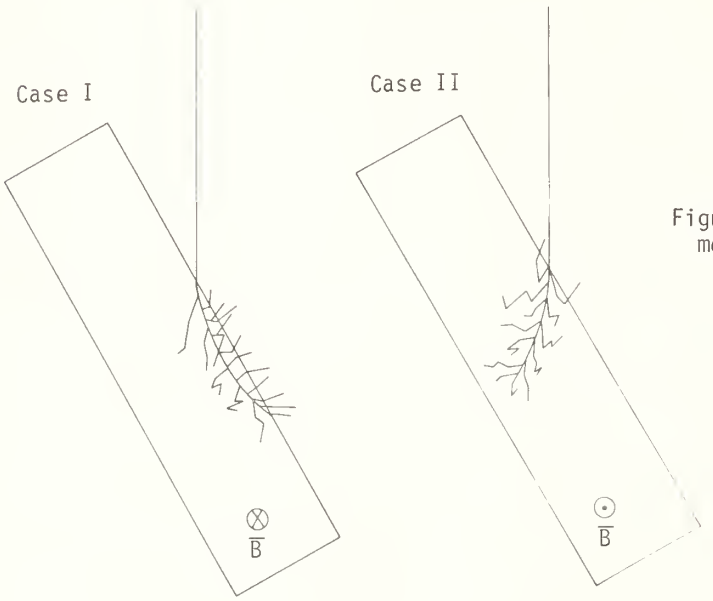

Figure 4. Schematic diagram of proposed mechanism of Type II magnetic contrast.

2. Monte Carlo Trajectory Simulation in the Presence of a Magnetic Field

The specific details of the general Monte Carlo calculation program used in the present study are given elsewhere in this volume [9]. Briefly, the general model makes use of an empirical Rutherford model of elastic scattering and the Bethe continuous energy loss approximation. The energy is fully depreciated in 60 scattering acts. The step length, or distance between elastic scattering events, is variable and related to the instantaneous electron energy in such a way that the total distance traveled in 60 steps is equal to the Bethe range for the incident beam energy. The program has been extensively tested with satisfactory results with regard to experimentally observed electron properties; e.g., backscattering coefficient as a function of atomic number, specimen tilt, and beam energy; transmission, backscattering, and absorption in thin foils and particles; and angular distributions of scattered electrons.

The coordinates (X,Y,Z) after each scattering act are calculated relative to a right-handed set of coordinate axes centered on the beam impact point. The coordinate system, figure 5, consists of the positive-going Z axis into the specimen and normal to the surface, the X-axis parallel to the tilt-axis, the specimen surface contained in the X-Y plane, and the positive-going Y-axis pointing down a tilted specimen and away from the beam impact point.

The exact technique of calculating the point coordinates is as follows (fig. 6). With the electron at a known point P(L), having come from a known point P(L-1), we must calculate

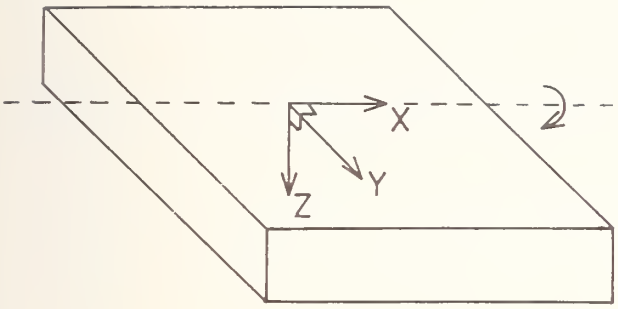

Figure 5. Schematic diagram of coordinate system used in Monte Carlo calculations.

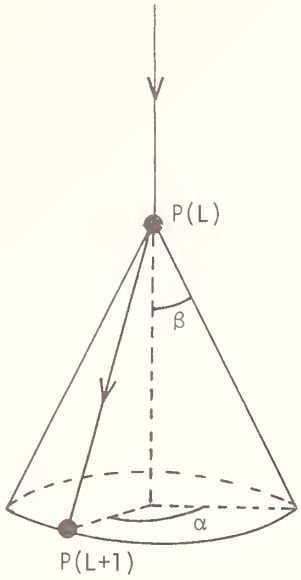

Figure 6. Illustration of coordinate values used in calculation of point P(L+1) from point P(L).

P(L+1). The electron traveled from P(L-1) to P(L) along a line (L) whose direction cosines (a,b,c) can be simply calculated from the coordinates $(X,Y,Z)_{L-1}$ and $(X,Y,Z)_L$. If the electron were not scattered at point P(L), it would continue along line (L). The act of scattering the electron through an angle β, calculated from the Rutherford relation, sends the electron to some point P(L+1) on the perimeter of a cone whose altitude Ll is the extension of line L, figure 6. To calculate P(L+1), the point (X_o,Y_o,Z_o) where the extended line Ll intersects the plane containing the base of this cone is first determined. The path on this cone surface that the electron travels from P(L) to P(L+1) has a length equal to the step length for that scattering act, D(L), which is known. The altitude of the cone, H, is given by:

$$H = D(L) \cos\beta. \tag{1}$$

Similarly, the radius of the base of the cone is:

$$R = D(L) \sin\beta. \tag{2}$$

The coordinates of the center of the cone base (X_o, Y_o, Z_o) are given by:

$$X_o = X(L) + (H \cdot a) \tag{3}$$

$$Y_o = Y(L) + (H \cdot b) \tag{4}$$

$$Z_o = Z(L) + (H \cdot c). \tag{5}$$

We next establish a new set of coordinate axes, X', Y', Z' (fig. 7) with the X'Y' plane containing the base of the cone, and the Z' axis parallel to extended Ll. The direction cosines of the primed axes in terms of the original axes must be determined. For the Z' axis, the direction cosines are the same as line Ll:

$$a_{Z'} = a, \; b_{Z'} = b, \; c_{Z'} = c. \tag{6}$$

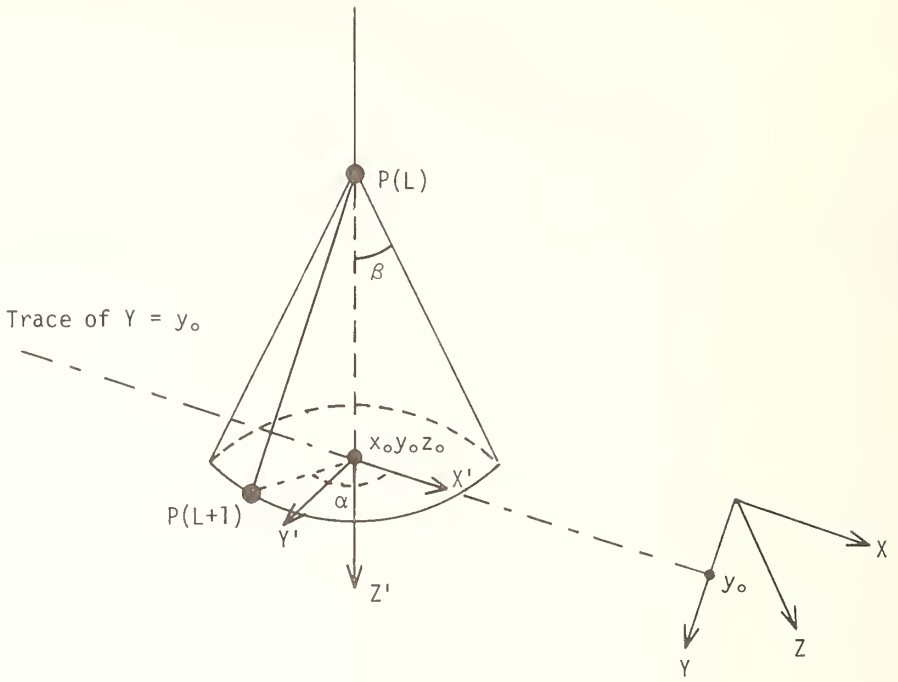

Figure 7. Primed coordinate system used in the point calculation scheme.

The X' axis is arbitrarily chosen to be parallel to the line of intersection of the plane of the base of the cone with the plane $Y = Y_0$. From the knowledge of a point in the plane of the cone base, (X_0, Y_0, Z_0) and the direction cosines of the normal to the plane, i.e., those of line L1, the equation of the cone base is:

$$aX + bY + cZ - (aX_0 + bY_0 + cZ_0) = 0. \tag{7}$$

The line of intersection with the plane $Y = Y_0$ is:

$$aX + cZ - (aX_0 + cZ_0) = 0. \tag{8}$$

Thus, the line has the form

$$Z = (-a/c)X + K;\ K = (a/c)X_0 + Z_0 \tag{9}$$

and the direction cosines of the X' axis with respect to the original axes are:

$$a_{X'} = \cos(\arctan(-a/c)) \tag{10}$$

$$b_{X'} = \cos 90° = 0 \tag{11}$$

$$c_{X'} = \cos(\arctan(-c/a)). \tag{12}$$

Knowing the direction cosines of X' and Z', we can obtain the direction cosines of Y' by the "direction number device" [10]. Since the original X, Y, Z, axes were chosen to form a right-handed coordinate system, we maintain parity, making X', Y', Z' right-handed by forming the cross product $(Z'\bar{k} \times X'\bar{i})$:

$$a_{Y'} = b_{Z'} \cdot c_{X'} \tag{13}$$

$$b_{Y'} = c_{Z'} \cdot a_{X'} - c_{X'} \cdot a_{Z'} \tag{14}$$

$$c_{Y'} = -a_{X'} \cdot b_{Z'}. \tag{15}$$

In the X', Y', Z' coordinate system, a point P'(L+1) (identical with P(L+1)) on the cone base perimeter is chosen randomly. The azimuthal angle is calculated with a uniformly distributed random number RN chosen such that $0.0 \leq RN \leq 1.0$. The coordinates of the point P'(L+1) are

$$X'(L + 1) = R * \cos(RN * 2\pi) \tag{16}$$

$$Y'(L + 1) = R * \sin(RN * 2\pi) \tag{17}$$

$$Z'(L + 1) = 0. \tag{18}$$

The coordinates $(X', Y', Z')_{L+1}$ can be transformed back to X, Y, Z space to give the desired point P(L+1) since we have the direction cosines of the X', Y', Z' axes:

$$X = a_{X'} \cdot X'(L + 1) + a_{Y'} \cdot Y'(L + 1) + X_o \tag{19}$$

$$Y = b_{X'} \cdot X'(L + 1) + b_{Y'} \cdot Y'(L + 1) + Y_o \tag{20}$$

$$Z = c_{X'} \cdot X'(L + 1) + c_{Y'} \cdot Y'(L + 1) + Z_o. \tag{21}$$

Effect of a Magnetic Field:

The effect of an internal magnetic field on the electron trajectory is simulated as follows. The trajectory calculation is first performed as described above to obtain the scattering step from P(L) to P(L+1) without the influence of the magnetic field. The effect of a magnetic field will result in a deflection of the electron trajectory so that a curved path of flight is followed, bringing the electron to a point $P_M(L+1)$ instead of P(L+1) (fig. 8). The magnetically-deflected trajectory is determined through the action of the

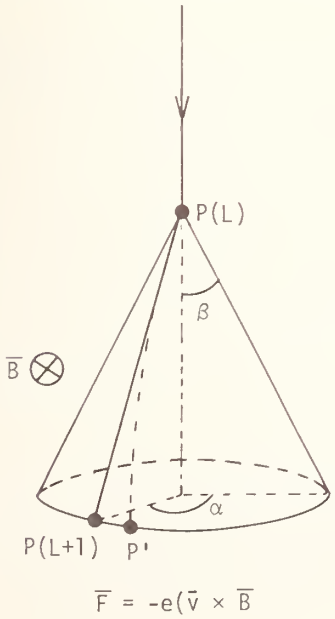

Figure 8. Effect of a magnetic field on the electron trajectory during a single scattering step.

Lorentz force, $\bar{F}$, on the electron:

$$\bar{F} = -e\bar{V} \times \bar{B} = m_e\bar{a} \tag{22}$$

where $\bar{V}$ is the electron velocity, $\bar{B}$ is the magnetic field vector, $\bar{a}$ is the acceleration, e is the electron charge, and m_e is the mass of the electron. The direction cosines of the line of flight from P(L) to P(L+1) in the nonmagnetic case are used to give the initial velocity components for the magnetic calculation. Thus, the velocity vector $\bar{V}$ is:

$$\bar{V} = aV\bar{i} + bV\bar{j} + cV\bar{k} \tag{23}$$

where V is the magnitude of the electron velocity which is determined from the electron energy for the particular scattering step. The Lorentz acceleration vector $\bar{a}$ becomes:

$$\bar{a} = \left(\frac{-e}{m_e}\right)\bar{V} \times \bar{B} = \left(\frac{-eV}{m_e}\right)\left[(bB_z - B_y c)\bar{i} + (cB_x - B_z a)\bar{j} + (aB_y - B_x b)\bar{k}\right]. \tag{24}$$

The magnetic deflection of an electron under the conditions used for the calculation is small; hence the time-of-flight will be virtually the same as in the nonmagnetic trajectory. This time-of-flight is

$$t = D(L)/V \tag{25}$$

where D(L) is the step length for the particular step being calculated. This time-of-flight is then used to calculate the displacement components, ΔS_i, under magnetic deflection:

$$\Delta S_i = V_{oi}t + (1/2)a_{oi}t^2 \tag{26}$$

where i represents the component along X, Y, or Z. Thus, in the absence of a magnetic field, the acceleration term is zero and the displacement components calculated by eq. (26) would place the electron at point P(L+1). When a magnetic field is present, the acceleration term acts to deflect the electron to a new point P_M(L+1). For the next step, the direction cosines are calculated from P(L) and P_M(L+1). For the field strengths used (up to 50 times the saturation value of iron, as described below), the adjustment due to magnetic deflection on a given step is small.

3. Characteristics of Type II Contrast Predicted by the Monte Carlo Model

To apply the Monte Carlo program described above to study Type II magnetic contrast, the backscattering coefficient was calculated for selected conditions of beam energy, specimen tilt, and magnetization direction. However, since the experimentally observed magnetic contrast has a maximum of only about 0.3%, definite statistical limitations are imposed on the Monte Carlo calculations. To obtain adequate statistical confidence, at least 10^6 electron trajectories would have to be calculated. However, the backscattering coefficient must be calculated for each of two senses of magnetization in order to calculate the contrast, C, observed between domains of opposite magnetization. Thus, between two domains, $C = (\eta_1 - \eta_2)/\eta_{ave}$ where η is the backscattering coefficient. Such Monte Carlo calculations proved to be prohibitively expensive. Therefore, to reduce the number of necessary trajectories, use was made of the fact that the complementary analytic model [6,7] predicted a linear contrast dependence on magnetization strength. This suggested that a valid calculation could be performed using a higher value of magnetization than actually found in iron so that the "contrast" was of the order of 5%. The contrast value appropriate to iron (or another material) could then be obtained by appropriate scaling.

To check the validity of this procedure, a series of Monte Carlo trajectory calculations was carried out with the induction, $\bar{B}$, as high as 100 Wb/m^2 ($\bar{B}$ at saturation for iron is 2.16 Wb/m^2). A linear relation between contrast and magnetization was indeed observed (fig. 9). Calculations for other conditions of beam energy and specimen tilt were performed with B = 60 Wb/m^2 giving adequate statistical confidence with 20,000 to 75,000 trajectory calculations for the conditions of interest. In the figures that follow, the calculated contrast has been reduced to that appropriate for iron.

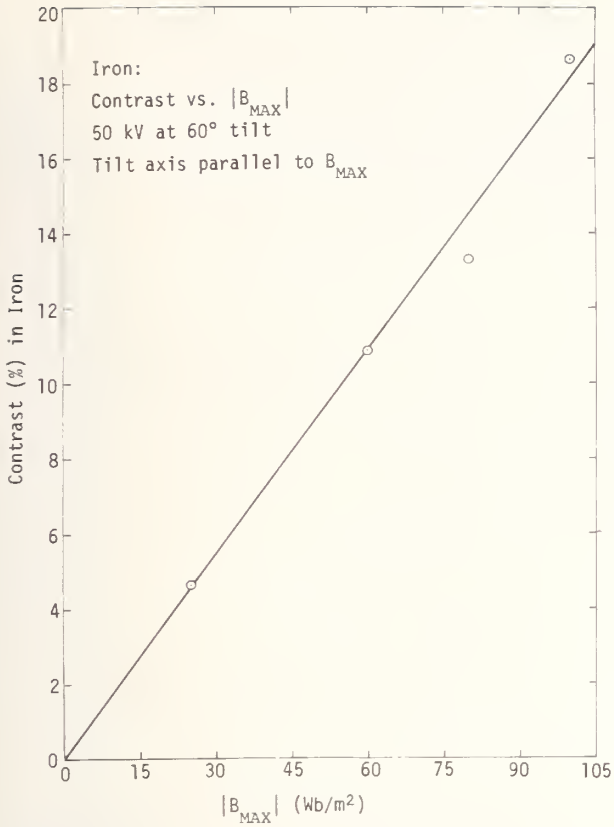

Figure 9. Calculated magnetic contrast versus magnetic field.

The behavior of the contrast as a function of tilt was calculated for an accelerating voltage of 50kV (fig. 10). As the tilt increases from 0° (normal beam incidence) the contrast increases, reaching a maximum between 50°-60°, and then decreases as the tilt is further increased toward grazing incidence. This behavior can be understood according to

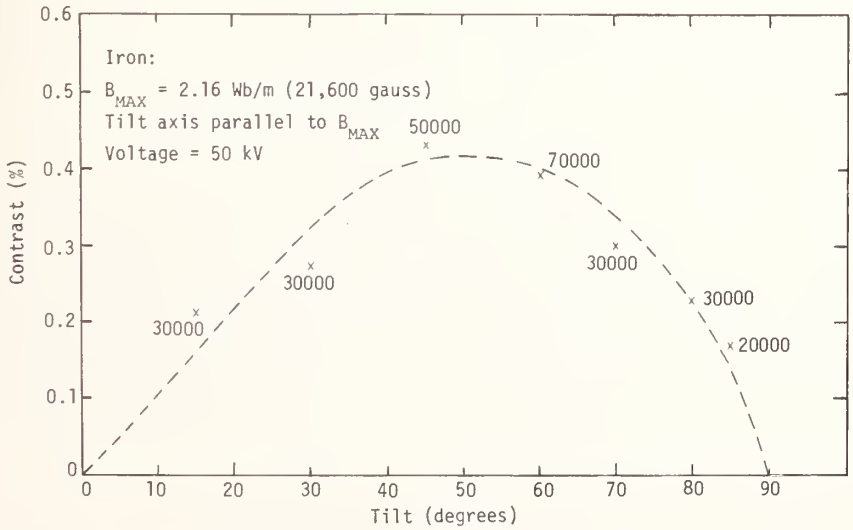

Figure 10. Calculated and observed magnetic contrast versus tilt angle, θ.

the model (fig. 11). At 0° tilt, the effect of the magentic field of opposite sense is simply to change the direction of the curving path of the electrons, i.e., either clockwise or counterclockwise (fig. 11(a)). There is no effective difference in depth of the electron distribution between the two domains, and therefore no contrast. As the tilt increases, the clockwise or counterclockwise curvature does result in a difference in the depth of the electrons (fig. 11(b)). At high tilts, the electrons tend to scatter out of the specimen in a few scattering acts, thus minimizing the length of path within the specimen over which the internal magnetic field can act upon the electron. Experimental measurements of C show a similar behavior as a function of tilt [11].

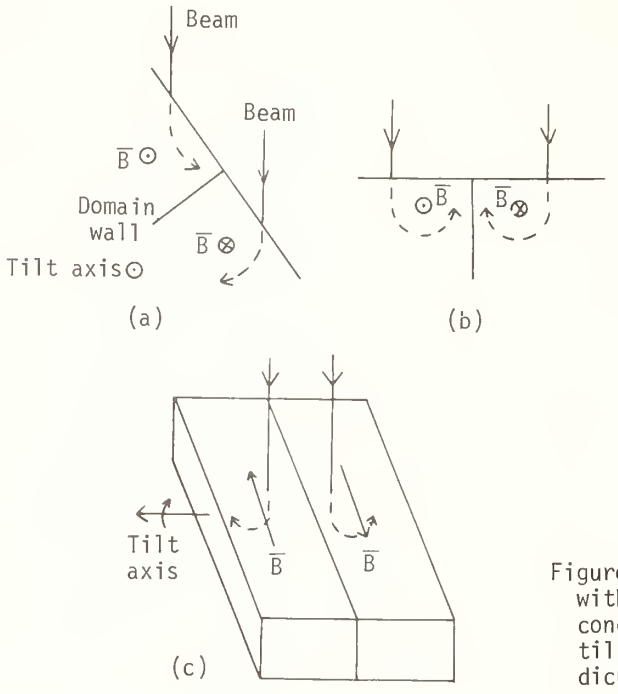

Figure 11. Electron interactions in a specimen with an internal magnetic field under special conditions: (a) 60° tilt and $\overline{B}$ parallel to tilt axis; (b) 0° tilt; (c) tilt and $\overline{B}$ perpendicular to tilt axis.

The absolute value of the calculated contrast falls below that measured experimentally by approximately a factor of two. Thus, for iron at 30 keV and a tilt of 60°, the calculated contrast is 0.15% and the measured contrast is 0.35%. This discrepancy may occur because of errors in the simplified model of electron interaction used in the Monte Carlo calculation, as well as experimental errors in the measurement arising due to the considerable difficulties in measuring such low contrast values.

The behavior of the contrast as a function of the accelerating voltage is shown in figure 12. The contrast increases as the 1.44 power of the accelerating voltage. Experimental measurements performed at voltages up to 30 keV supported this trend with an observed voltage exponent of approximately 1.4 [10]. Recent measurements performed on a high voltage SEM gave measured contrast values of 1.3% (100 keV), 2.8% (150 keV), and 5.2% (200 keV) [12]. These values correspond reasonably well to 1.1% (100 keV), 2.1% (150 keV) and 3.1% (200 keV) predicted by the Monte Carlo calculations. In addition, the recent measurements were made with a detector for emitted electrons, which is both somewhat directional and energy-selective, and therefore might produce higher measured values. The increase in contrast with increased accelerating voltage is understandable since the Lorentz force is given by $e\overline{V} \times \overline{B}$. As the electron energy, and hence, velocity increases, the Lorentz force increases.

One of the most interesting results obtained with the Monte Carlo calculation concerned the distribution of contrast as a function of the energy of the backscattered electrons. A histogram of backscattered electron energy for the domains of opposite magnetization is shown in figure 13. The contrast carried by each energy fraction is:

Energy	ΔS/S Total
45.4 - 50 keV	0.126
40.1 - 45.4	0.130
34.1 - 40.1	0.129
27.2 - 34.1	0.121
18.4 - 27.2	0.116
2.7 - 18.4	0.110

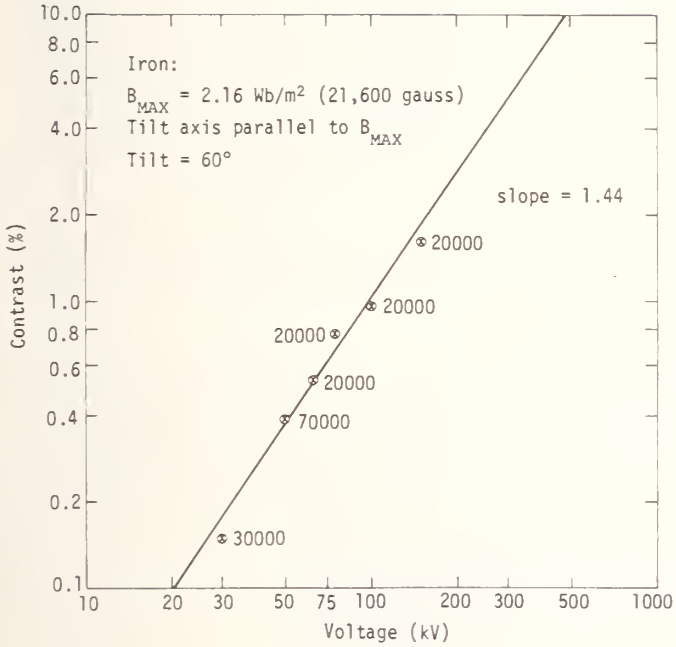

Figure 12. Calculated magnetic contrast versus beam energy.

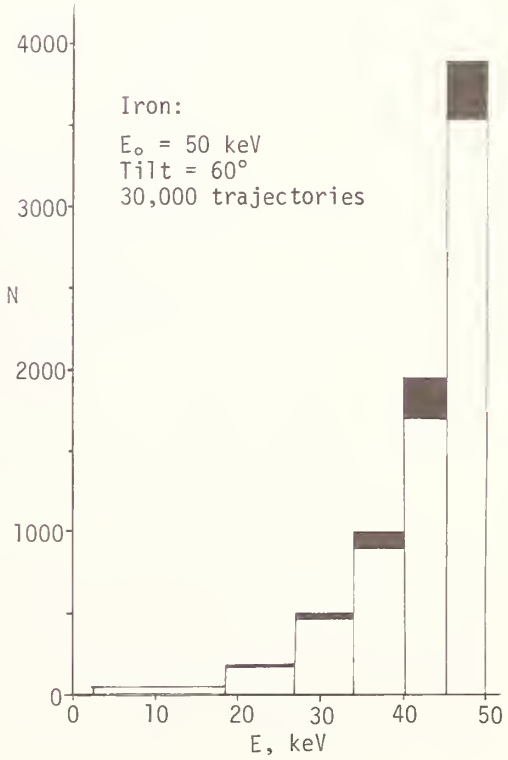

Figure 13. Histogram of the number of backscattered electrons versus energy from domains of opposite magnetization. (Black region gives difference between opposite domains.)

Thus, accepting electrons which have lost more than about 20% of the initial beam energy actually results in a decrease in contrast. This result implies that suitable energy filtering of the backscattered electron fraction should result in increased contrast. Experimental verification of this prediction has been obtained with a special forward scattering experiment [11]. The energy dependence can be explained by the following argument: When the magnetization vector is parallel to the tilt axis, the Lorentz force is greatest on those electrons traveling in the original beam direction, since the angle between the velocity and magnetization vectors is 90°. Electrons which have lost energy due to inelastic scattering are also likely to have been elastically scattered out of the incident direction. For these scattered electrons, the Lorentz force is decreased due to the reduced angle between $\overline{V}$ and $\overline{B}$ as well as the reduced magnitude of $\overline{V}$ which results from energy loss. However, the electron must spend some time under the influence of the internal magnetic field; and hence, those electrons which scatter out after only one or two elastic scattering steps are probably not carrying much contrast information. This requirement for some length of path within the specimen is apparent from the contrast behavior at high tilt. The decreasing contrast at tilts above 65° corresponds to decreasing path length within the specimen and higher backscatter.

Monte Carlo calculations of the 0° tilt case of figure 11(a) verify that no contrast occurs. Moreover, the situation illustrated in figure 11(c), where the magnetization vector is perpendicular to the tilt axis, i.e., $\overline{B}$ lies along the Y-axis, also is found to produce no contrast despite the optimum tilt.

Monte Carlo calculations also provided information on the edge resolution to be expected with Type II magnetic contrast. Figure 14 shows an image in which domain walls run parallel and perpendicular to the tilt axis. It can be observed that the domain walls which are perpendicular to the tilt axis appear more sharply defined than the walls parallel to the tilt axis (e.g., circled area in fig. 14). Plots of electron trajectories obtained with the Monte Carlo technique for a tilted iron specimen at 30 keV beam energy can be used

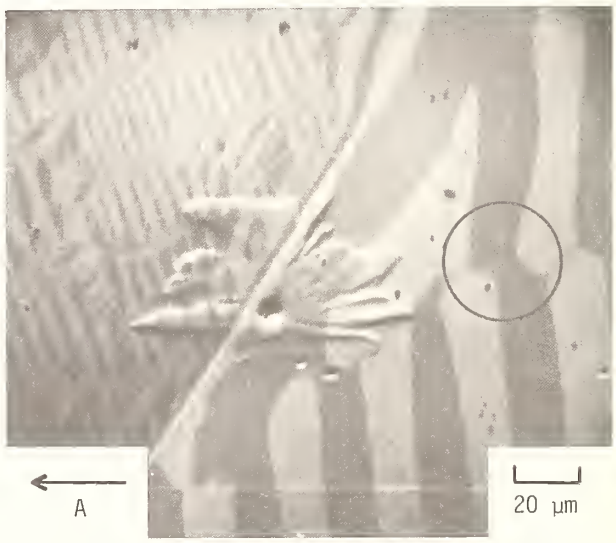

Figure 14. Image of magnetic domains in Fe-3 1/4% Si; specimen tilt 55° (axis $\overline{A}$); beam 30 keV; note domain wall resolution in circled area.

to understand this observation of differential wall resolution. The dense trajectory region of a plot showing a Y-Z section (fig. 15(a)) is larger and more elongated than the dense trajectory region of the X-Z section (fig. 15(b)). Thus, the difference in edge resolution is a result of the different dimensions of the interaction volume which sweeps across the domain walls during the scanning action. The image of a domain wall running perpendicular to the tilt axis is affected by the smaller dimensions of the interaction volume in the X-Z plane; and thus, the wall position is more sharply defined than the case of a wall parallel to the tilt axis which is affected by the dimensions of the Y-Z section.

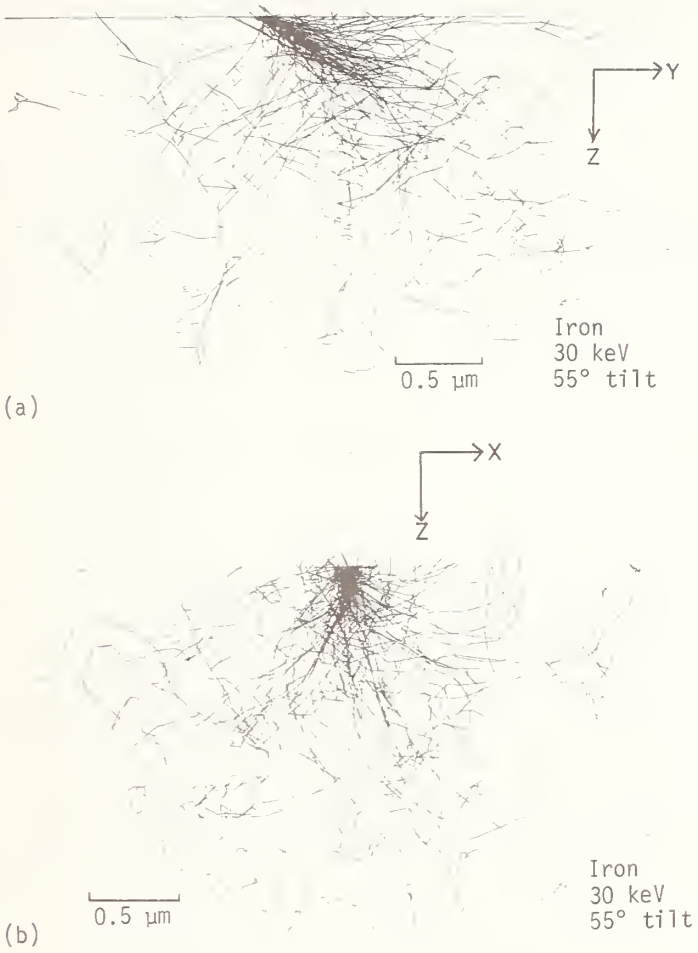

Figure 15. Monte Carlo trajectory plot for iron at 55° tilt, 30 keV beam energy: (a) Y-Z section, (b) X-Z section.

4. Conclusions

Monte Carlo simulations of electron trajectories under the influence of an internal magnetic field verify all aspects of the proposed mechanism for Type II magnetic contrast. The contrast arises from the action of the Lorentz force of the internal magnetic field on the scattering electrons. Contrast is maximized by three conditions: (1) a specimen tilt of 50° to 60°, (2) high accelerating voltage, and (3) magnetization direction lying in the plane of the specimen and parallel to the specimen tilt axis.

References

[1] Dorsey, J. R., *Proc. 1st National Conference on Electron Probe Microanalysis* (College Park, Md., 1966); *Adv. Electronics and Electron Phys. Suppl. 6,* "Electron Probe Microanalysis," A. J. Tousimis, and L. Marton, eds. p. 291 (Academic Press, 1969)

[2] Joy, D. C. and Jakubovics, J. P., *Phil Mag.*, 17, 61 (1968).

[3] Banbury, J. R. and Nixon, W. L., *J. Sci. Instrum.* 44, 889 (1967).

[4] Goldstein, J. I., Yakowitz, H., Newbury, D. E., Lifshin, E., Colby, J. W., and Coleman, J. R., *Practical Scanning Electron Microscopy*, Chapter 5 (Plenum Press, New York, 1975).

[5] Philibert, J. and Tixier, R., *Micron*, 1, 174 (1969).

[6] Fathers, D. J., Jakubovics, J. P., and Joy, D. C., *Phil. Mag.* 27, 765 (1973).

[7] Fathers, D. J., Jakubovics, J. P., Joy, D. C., Newbury, E. D., and Yakowitz, H., *Phys. Stat. Sol. (A)* 20, 535 (1973).

[8] Newbury, D. E., Yakowitz, H., and Myklebust, R. L., *Appl. Phys. Lett.* 23, 488 (1973).

[9] Myklebust, R. L., Yakowitz, H., Newbury, D. E., and Heinrich, K. F. J., this publication (p. 105).

[10] C. H. Lehmann, *Analytic Geometry* p. 289 (Wiley, New York, 1942).

[11] Fathers, D. J., Jakubovics, J. P., Joy, D. C., Newbury, D. E., and Yakowitz, H., *Phys. Stat. Sol. (A)*, 22, 609 (1974).

[12] Yamamoto, T., Nishizawa, H., and Tsuno, K., *J. Phys. D. Appl. Phys.* 8, L113 (1975).

NBS-114A (REV. 7-73)

U.S. DEPT. OF COMM. BIBLIOGRAPHIC DATA SHEET	1. PUBLICATION OR REPORT NO. NBS SP-460	2. Gov't Accession No.	3. Recipient's Accession No.

4. TITLE AND SUBTITLE
Use of Monte Carlo Calculations in Electron Probe Microanalysis and Scanning Electron Microscopy

Proceedings of a workshop held at the National Bureau of Standards, Gaithersburg, Maryland, October 1-3, 1975

5. Publication Date: December 1976

6. Performing Organization Code

7. AUTHOR(S)
K. F. J. Heinrich, D. E. Newbury, H. Yakowitz (eds.)

8. Performing Organ. Report No.

9. PERFORMING ORGANIZATION NAME AND ADDRESS

NATIONAL BUREAU OF STANDARDS
DEPARTMENT OF COMMERCE
WASHINGTON, D.C. 20234

10. Project/Task/Work Unit No.

11. Contract/Grant No.

12. Sponsoring Organization Name and Complete Address *(Street, City, State, ZIP)*

Same as No. 9.

13. Type of Report & Period Covered

14. Sponsoring Agency Code

15. SUPPLEMENTARY NOTES

Library of Congress Catalog Card Number: 77-608002

16. ABSTRACT *(A 200-word or less factual summary of most significant information. If document includes a significant bibliography or literature survey, mention it here.)*

This book is the formal report of the Workshop on the Use of Monte Carlo Calculations in Electron Probe Microanalysis and Scanning Electron Microscopy held at the National Bureau of Standards, October 1-3, 1975. The papers cover a wide range of topics within the field: the history and development of Monte Carlo methods for use in x-ray microanalysis; the study of the distribution of electron and x-ray signals by Monte Carlo techniques; the effect of the choice of scattering models on the calculations; techniques for considering the distribution of energies of the beam electrons propagating in the specimen; evaluation of ionization cross-section models; and applications of Monte Carlo techniques to the study of particles, thin films, and magnetic domain images. The contributions include reviews of general interest as well as papers treating specific topics. The volume should be of wide interest to workers in the fields of scanning electron microscopy, electron probe microanalysis, electron physics, and other fields involving the interaction of electrons with solids.

17. KEY WORDS *(six to twelve entries; alphabetical order; capitalize only the first letter of the first key word unless a proper name; separated by semicolons)* Electron probe microanalysis; electron-solid interactions; magnetic domains; Monte Carlo electron trajectory calculations; particle analysis; scanning electron microscopy; thin film analysis.

18. AVAILABILITY

[X] Unlimited

[ ] For Official Distribution. Do Not Release to NTIS

[X] Order From Sup. of Doc., U.S. Government Printing Office Washington, D.C. 20402, SD Cat. No. C13.10:460

[ ] Order From National Technical Information Service (NTIS) Springfield, Virginia 22151

19. SECURITY CLASS (THIS REPORT): UNCLASSIFIED

21. NO. OF PAGES: 169

20. SECURITY CLASS (THIS PAGE): UNCLASSIFIED

22. Price: $2.35

USCOMM-DC 29042-P74

make color work for you

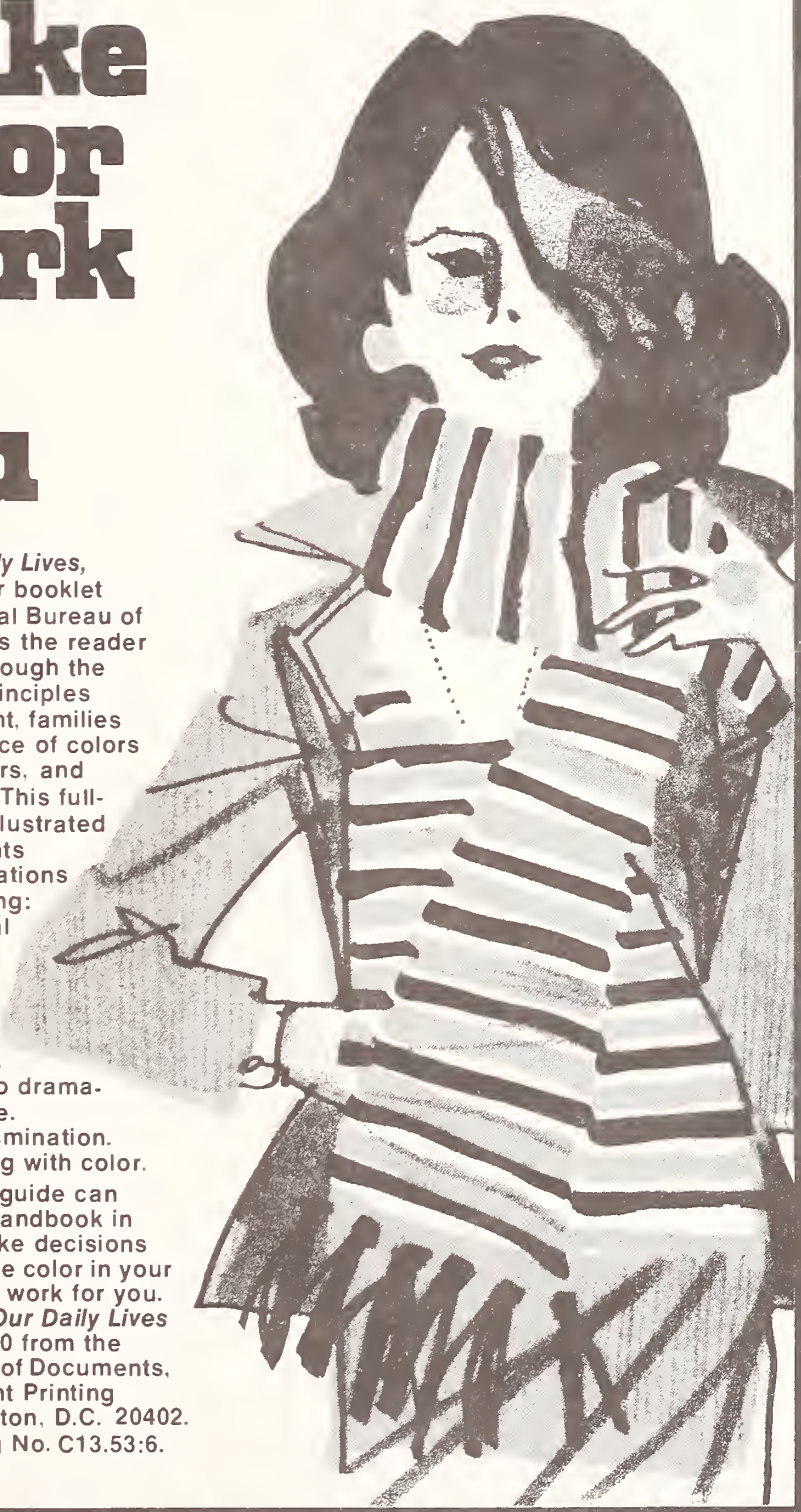

Color in our Daily Lives, a new consumer booklet from the National Bureau of Standards, takes the reader step by step through the fundamental principles of color and light, families of color, influence of colors upon other colors, and color harmony. This full-color, 32-page illustrated booklet highlights practical applications of color, including:

- Your personal color plan.
- Your color environment.
- Color plans for the home.
- Using color to dramatize or to hide.
- Color and illumination.
- Experimenting with color.

This new basic guide can serve as your handbook in helping you make decisions about how to use color in your life and make it work for you. Order *Color in Our Daily Lives* prepaid for $1.70 from the Superintendent of Documents, U.S. Government Printing Office, Washington, D.C. 20402. Use SD Catalog No. C13.53:6.

☆ U.S. GOVERNMENT PRINTING OFFICE : 1977 0-328-72

NBS TECHNICAL PUBLICATIONS

PERIODICALS

JOURNAL OF RESEARCH reports National Bureau of Standards research and development in physics, mathematics, and chemistry. It is published in two sections, available separately:

• Physics and Chemistry (Section A)

Papers of interest primarily to scientists working in these fields. This section covers a broad range of physical and chemical research, with major emphasis on standards of physical measurement, fundamental constants, and properties of matter. Issued six times a year. Annual subscription: Domestic, $17.00; Foreign, $21.25.

• Mathematical Sciences (Section B)

Studies and compilations designed mainly for the mathematician and theoretical physicist. Topics in mathematical statistics, theory of experiment design, numerical analysis, theoretical physics and chemistry, logical design and programming of computers and computer systems. Short numerical tables. Issued quarterly. Annual subscription: Domestic, $9.00; Foreign, $11.25.

DIMENSIONS/NBS (formerly Technical News Bulletin)—This monthly magazine is published to inform scientists, engineers, businessmen, industry, teachers, students, and consumers of the latest advances in science and technology, with primary emphasis on the work at NBS. The magazine highlights and reviews such issues as energy research, fire protection, building technology, metric conversion, pollution abatement, health and safety, and consumer product performance. In addition, it reports the results of Bureau programs in measurement standards and techniques, properties of matter and materials, engineering standards and services, instrumentation, and automatic data processing. Annual subscription: Domestic, $9.45; Foreign, $11.85.

NONPERIODICALS

Monographs—Major contributions to the technical literature on various subjects related to the Bureau's scientific and technical activities.

Handbooks—Recommended codes of engineering and industrial practice (including safety codes) developed in cooperation with interested industries, professional organizations, and regulatory bodies.

Special Publications—Include proceedings of conferences sponsored by NBS, NBS annual reports, and other special publications appropriate to this grouping such as wall charts, pocket cards, and bibliographies.

Applied Mathematics Series—Mathematical tables, manuals, and studies of special interest to physicists, engineers, chemists, biologists, mathematicians, computer programmers, and others engaged in scientific and technical work.

National Standard Reference Data Series—Provides quantitative data on the physical and chemical properties of materials, compiled from the world's literature and critically evaluated. Developed under a world-wide program coordinated by NBS. Program under authority of National Standard Data Act (Public Law 90-396).

NOTE: At present the principal publication outlet for these data is the Journal of Physical and Chemical Reference Data (JPCRD) published quarterly for NBS by the American Chemical Society (ACS) and the American Institute of Physics (AIP). Subscriptions, reprints, and supplements available from ACS, 1155 Sixteenth St. N.W., Wash. D. C. 20056.

Building Science Series—Disseminates technical information developed at the Bureau on building materials, components, systems, and whole structures. The series presents research results, test methods, and performance criteria related to the structural and environmental functions and the durability and safety characteristics of building elements and systems.

Technical Notes—Studies or reports which are complete in themselves but restrictive in their treatment of a subject. Analogous to monographs but not so comprehensive in scope or definitive in treatment of the subject area. Often serve as a vehicle for final reports of work performed at NBS under the sponsorship of other government agencies.

Voluntary Product Standards—Developed under procedures published by the Department of Commerce in Part 10, Title 15, of the Code of Federal Regulations. The purpose of the standards is to establish nationally recognized requirements for products, and to provide all concerned interests with a basis for common understanding of the characteristics of the products. NBS administers this program as a supplement to the activities of the private sector standardizing organizations.

Consumer Information Series—Practical information, based on NBS research and experience, covering areas of interest to the consumer. Easily understandable language and illustrations provide useful background knowledge for shopping in today's technological marketplace.

Order above *NBS publications from: Superintendent of Documents, Government Printing Office, Washington, D.C. 20402.*

Order following *NBS publications—NBSIR's and FIPS from the National Technical Information Services, Springfield, Va. 22161.*

Federal Information Processing Standards Publications (FIPS PUBS)—Publications in this series collectively constitute the Federal Information Processing Standards Register. Register serves as the official source of information in the Federal Government regarding standards issued by NBS pursuant to the Federal Property and Administrative Services Act of 1949 as amended, Public Law 89-306 (79 Stat. 1127), and as implemented by Executive Order 11717 (38 FR 12315, dated May 11, 1973) and Part 6 of Title 15 CFR (Code of Federal Regulations).

NBS Interagency Reports (NBSIR)—A special series of interim or final reports on work performed by NBS for outside sponsors (both government and non-government). In general, initial distribution is handled by the sponsor; public distribution is by the National Technical Information Services (Springfield, Va. 22161) in paper copy or microfiche form.

BIBLIOGRAPHIC SUBSCRIPTION SERVICES

The following current-awareness and literature-survey bibliographies are issued periodically by the Bureau:

Cryogenic Data Center Current Awareness Service. A literature survey issued biweekly. Annual subscription: Domestic, $20.00; Foreign, $25.00.

Liquified Natural Gas. A literature survey issued quarterly. Annual subscription: $20.00.

Superconducting Devices and Materials. A literature survey issued quarterly. Annual subscription: $20.00. Send subscription orders and remittances for the preceding bibliographic services to National Bureau of Standards, Cryogenic Data Center (275.02) Boulder, Colorado 80302.

U.S. DEPARTMENT OF COMMERCE
National Bureau of Standards
Washington, D.C. 20234

OFFICIAL BUSINESS

Penalty for Private Use, $300

POSTAGE AND FEES PAID
U.S. DEPARTMENT OF COMMERCE
COM-215

SPECIAL FOURTH-CLASS RATE
BOOK